



University Library

Author/Filing Title GAZIS, A.

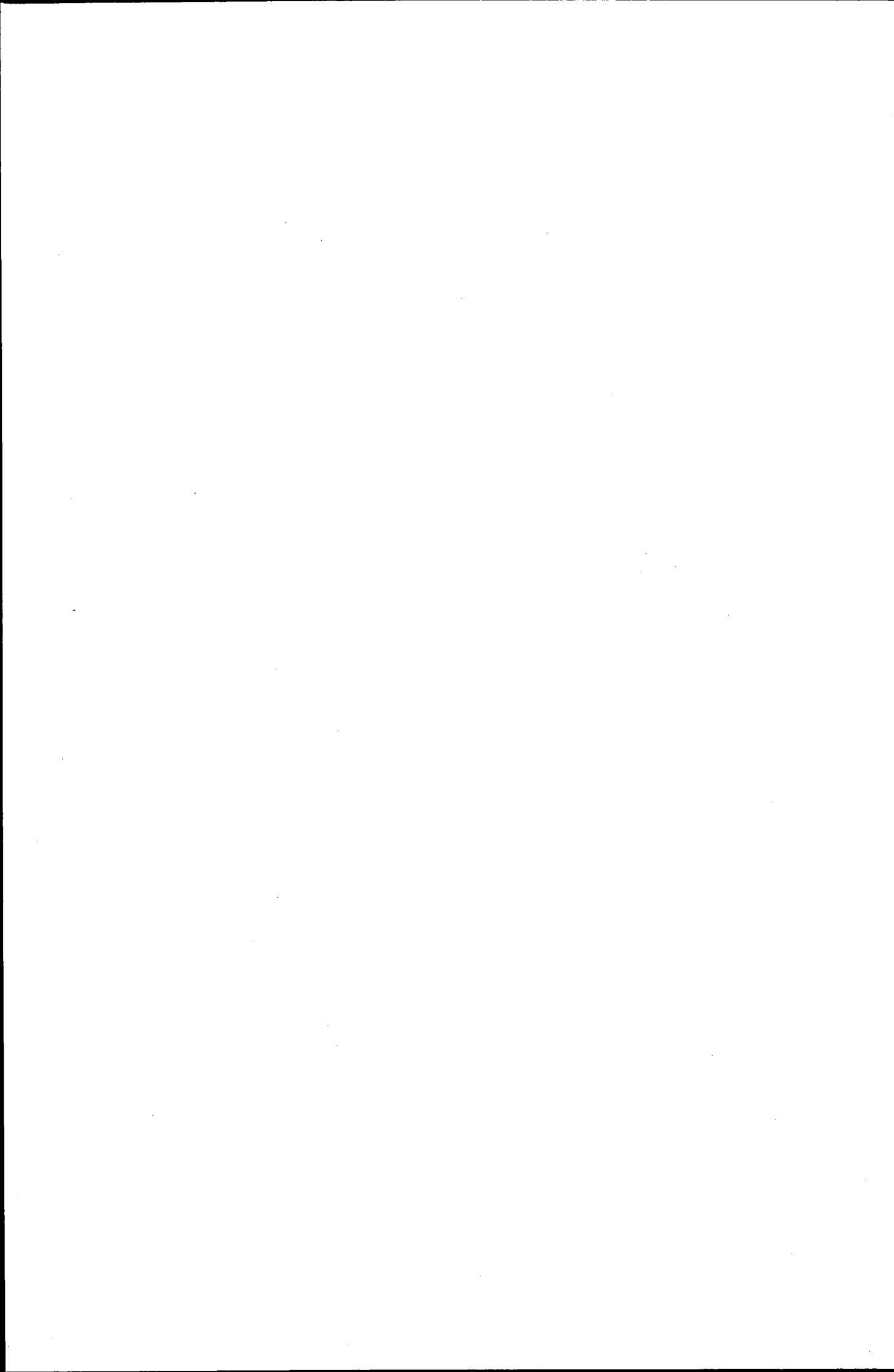
Class Mark T

**Please note that fines are charged on ALL
overdue items.**

FOR REFERENCE ONLY

0403600464





**Algorithm development on the
use of feedback signals in the
context of gasoline HCCI
combustion**

by

Andreas Gazis


Doctoral Thesis

Submitted in partial fulfilment of the
requirements for the award of Doctor of
Philosophy of Loughborough University

November 2006

Faint, illegible text at the top of the page, possibly a header or title.

Faint, illegible text in the middle of the page.

 Loughborough University Bislington Library
Date 8/2008
Class T
Acc No. 040360044

To my friend,
Andreas Kalpatsekas,
who will never get to read this.

ACKNOWLEDGMENTS

A completed PhD thesis is usually a task involving the efforts of many parties and this one is by no means an exception. I would like therefore to list just a few of those who helped me produce this work.

First of all my supervisors. Wen-Hua Chen for his ongoing support, resourcefulness and enthusiasm, often in the face of horrendous adversity. Rui Chen for his orchestrating the research team both inside and outside of the university.

Also, my fellow research students: Dimitris Panousakis, Andrew Heather, Paul Osei-Owusu and Jill Patterson for helping with technical matters but, perhaps most importantly, making life as a researcher fun.

Outside the university, Lotus Engineering for providing data, resources and support without which this work would not have been possible.

Finally, Michalis Gregoriadis, Theodoros Mortis, Somya Joshi, Karthik Bhargavan and my parents Kakia Karvounidou and Antonis Gazis for providing a reasonably calm refuge in times of general mayhem.

The research presented in this thesis is the result of a collaboration of Loughborough University and Lotus Engineering Ltd on the subject of Homogeneous Charge Compression Ignition (HCCI) combustion. More specifically, it covers research conducted between 2002 and 2005 in Loughborough University by myself and research partner Dimitris Panousakis, under the supervision of Dr Wen-Hua Chen and Dr Rui Chen.

The general idea behind the research has been the control of HCCI combustion. More specifically, it has focused on methods of using some form of feedback signal for this purpose. Thus both pressure transducers and ion current sensors have been used in experimental investigations and subsequent analysis of the results. The engineering/technical component of the research has been primarily the field of Dimitris Panousakis and Dr Rui Chen, while the theoretical/computational component has been the field of Dr Wen-Hua Chen and myself. Hence, the work presented in this thesis mainly focuses on the algorithm development based on experimental signals.

Contents

Abbreviations	vii
1 Introduction	1
1.1 Global Outlook	1
1.2 Internal Combustion engines	2
1.2.1 Spark Ignition Engines	3
1.2.2 Compression Ignition Engines	4
1.3 Homogeneous Charge Compression Ignition engines	5
1.3.1 HCCI history	6
1.4 Aim of this work	10
1.4.1 Thesis Map	11
2 Present Status	13
2.1 HCCI Implementations	15
2.1.1 Intake Air Heating	16
2.1.2 Variable Compression Ratio	17
2.1.3 Dual Fuels	17
2.1.4 Use of Residual Gases	18
2.2 Ion Current Research	20
2.3 Modeling Approaches	20

3	Experimental Setup and Strategies Employed	24
3.1	Experimental Engine	24
3.2	Experimental strategies	27
3.2.1	SI	27
3.2.2	HCCI with constant EVO and IVC	27
3.2.3	HCCI with constant duration	28
3.2.4	HCCI-SACAI nature of experimental data	29
3.3	Ion Current Signal Acquisition	29
4	Ion Current	32
4.1	Ion Current as a diagnostic tool in SI operation	33
4.1.1	Introduction to Ion Current Measurement	33
4.1.2	Experimental Setup for SI Ion Current investigation	36
4.1.3	Signal Interpretation	38
4.1.4	Pressure Measurant Prediction	48
4.1.5	Summary of ion current use in SI combustion	59
4.2	Ion Current as a diagnostic tool in HCCI operation	61
4.2.1	Ion Current Signal and Treatment in HCCI	62
4.2.2	Ion Current Measurant Extraction	62
4.2.3	The Wavelet Decomposition of the Ion Current Signal Procedure	71
4.2.4	Artificial Neural Network Based Predictions	72
4.2.5	Summary of ion current use in HCCI combustion	86
5	Combustion Analysis	88
5.1	Averaged Pressure Trace Treatment	89
5.1.1	Pegging	90

5.1.2	TRG Estimation and Pressure Trace Imbalance	99
5.1.3	Sensitivity Analysis of whole procedure to Trapped Residual Gas (TRG) temperature variation	110
5.2	Heat Exchange	113
5.2.1	Theory of Heat Exchange Calculation	113
5.2.2	TRG temperature sensitivity analysis	117
5.2.3	TRG Representation	119
5.3	Individual Cycle Combustion Analysis	121
5.3.1	Safeguards against Erroneous Data	124
5.3.2	Cycle to Cycle Heat Exchange Calculation Implementation	125
5.3.3	Cycle to Cycle Investigation Example	128
5.4	Summary	131
6	Modeling	133
6.1	Software Design	134
6.1.1	Governing equations	135
6.1.2	Model Architecture	145
6.1.3	Wall Heat Transfer Tuning	155
6.1.4	Combustion Profile Calculation	160
6.1.5	Modeling of single SI and HCCI cycles	164
6.1.6	Cycle to cycle coupling	165
6.2	Example Results	169
6.2.1	Simulated instability with fixed combustion phasing	170
6.2.2	Simulated instability with temperature triggered combustion phasing	173
6.3	Summary	174

7	Autoignition Study of Experimental Data	176
7.1	Search for an autoignition criterion	177
7.1.1	Data Analysis	179
7.2	The question of the heat addition mechanism	183
7.2.1	Potential mechanisms	183
7.2.2	Noteworthy engine characteristics	184
7.2.3	Proposed mechanism	184
7.3	Instability	187
7.3.1	Potential use of low tension coil as alternative in-cylinder sensor	196
7.4	Summary	199
8	Conclusion	202
8.1	In-cylinder Feedback Signals	202
8.2	Control	203
8.3	Future Work	204
8.3.1	Experimental	204
8.3.2	Theoretical	204
	Bibliography	205
	List of Tables	216
	List of Figures	217
A	Hardware Specifications	223
B	Publications	225
	Analysis of SI Combustion Diagnostics Methods Using Ion-Current Sensing Techniques (SAE 2006-01-1345)	226

Computationally inexpensive methods of ion current signal manipulation for predicting the characteristics of engine in-cylinder pressure (JER 04005)	239
Using Ion-current Sensing to Interpret Gasoline HCCI Combustion Processes(SAE 2006- 01-0024)	251
Ion Current Signal Interpretation via Artificial Neural Networks for Gasoline HCCI Control (SAE 2006-01-1088)	260

Abbreviations

ADALINE(s)	ADaptive LINear Element(s)
AFR	Air Fuel Ratio
ANN(s)	Artificial Neural Network(s)
ATDC	after Top Dead Centre
AVT	Active Valve Train
BDC	Bottom Dead Centre
BMEP	Brake Mean Effective Pressure
BTDC	before Top Dead Centre
CAD	Crank Angle Degrees
CAI	Controlled Auto Ignition
CFD	Computational Fluid Dynamics
CFV	Capillary Force Vaporizer
CO	Carbon Monoxide
CO ₂	Carbon Dioxide
CoC	Completeness of Combustion
CI	Compression Ignition
CR	Compression Ratio
DI	Direct Injection

DME	Dimethyl Ether
DWT	Discrete Wavelet Transform
EGR	Exhaust Gas Recirculation
EGT	Exhaust Gas Temperature
EVC	Exhaust Valve Closing time
EVO	Exhaust Valve Opening time
FVVT	Fully Variable Valve Timing
FMEP	Friction Mean Effective Pressure
GDI	Gasoline Direct Injection
GRNN(s)	Generalised Regression Neural Network(s)
HC	Hydrocarbons
HCCI	Homogeneous Charge Compression Ignition
IC	Internal Combustion
IEGR	Internal Exhaust Gas Recirculation
IMEP	Indicated Mean Effective Pressure
ITA	Ignition Timing Advance
IVC	Inlet Valve Closing time
IVO	Inlet Valve Opening time
LHV	Lower Heating Value

LMS	Least Mean Square
MAP	Manifold Air Pressure
MFB	Mass Fraction Burnt
MFB5	Location of 5% Mass Fraction Burnt
MFB50	Location of 50% Mass Fraction Burnt
MLP	Multi-Layer Perceptron
NO_x	Nitrogen Oxides
NVO	Negative Valve Overlap
PDF	Probability Density Function
PPP	Peak Pressure Position
PFJ	Pulsed Flame Jet
RASP	Rotating Ark Spark Plug
RBF(s)	Radial Basis Function(s)
RPM	Revolutions per minute
SACAI	Spark Assisted Controlled Auto Ignition
SI	Spark Ignition
SoC	Start of Combustion
TDC	Top Dead Centre
TRG	Trapped Residual Gas

TWC Three Way Catalyst

VVT Variable Valve Timing

WOT Wide Open Throttle

Abstract

Homogeneous Charge Compression Ignition (HCCI) combustion is a promising research subject due to its characteristics of high efficiency and low emissions. These are highly desirable, given the global picture of increased energy requirements coupled with serious environmental implications. However, one of the main considerations of HCCI implementation is its control strategies which are not straightforward as in conventional Spark Ignition (SI) or Compression Ignition (CI) engines.

In order for closed loop control strategies to be successful, appropriate signals must be selected. In this research, experimental in-cylinder signals have been collected for pressure and ion current. These have been processed and evaluated as regards their suitability for HCCI control. During this process, physical based models have been developed both for treating experimental data as well as simulating theoretical cases. Using these tools, the behaviour of unstable HCCI operation has also been explored.

Chapter 1

Introduction

1.1 Global Outlook

The lion's share of contemporary industrialised societies' energy needs is covered by burning fossil fuels. When considering transportation alone, burning fossil fuels in Internal Combustion (IC) engines is the norm. This is mainly because of the high energy density and proven service record of the IC engine. Unfortunately, there are many associated drawbacks, which are becoming increasingly pressing as societies become increasingly industrialised in a world of finite resources.

To begin with, there is the unsettled question to what extent a non renewable resource, like fossil fuels, can keep providing the ever growing energy needs of the global population. However, even assuming that the available supply is adequate, the problem of traditional pollution resulting from hydrocarbon combustion residues or Nitrogen Oxides (NO_x) leading to acid rain remains.

To compound this problem, any form of burning a hydrocarbon fuel results in the release of carbon dioxide, whose effects on global warming, though ferociously contested, are alarming.

A large amount of the pollution produced by IC engines comes from the road transport sector, an issue which is particularly problematic in cities where population density is greatest.

Hence, the automotive industry is faced with two main issues, first how to make more efficient

engines so as to make the increasing energy demands rely on less fuel and second, how to use the available fuel in such a way as to reduce pollution.

To that end, various alternatives have been proposed and are under development. Hybrid cars, fuel cells and the like are all attempts at downplaying or replacing the role of the IC engine. However, none of these are capable of offering a realistic alternative as yet. In the case of fuel cells, cost is still a big issue. However, hydrogen as a fuel is also problematic since, unlike fossil fuels, it must be produced, thus requiring energy. Burning a fossil fuel to produce energy to produce hydrogen is not a viable solution. Similarly, chemical extraction from fossil fuels still does not solve the fossil fuel dependency. Alternatives based on carbon neutral sources are also investigated but are still in very early stages of development. Nuclear power might provide a vast energy source, thus providing the energy to produce large quantities of hydrogen but does not come without major drawbacks of its own, like high cost and risk.

On the other hand, the IC engine has been developed continuously for a century, in fact, the history of the 20th century is in many levels interwoven with the history of the IC engine. Technology still advances in leaps and bounds, and IC engines have benefited immensely from technological advances (electronic control, catalysts, fuel injection to name but a few). However, the question still remains of how much more performance can be squeezed out of what is still, in effect, the same process. Although alternatives are still not particularly attractive, the amount of time and funding which have gone into their research is negligible compared to that of IC engines.

1.2 Internal Combustion engines

At present, IC piston engines used in road transport are divided into two main groups: Spark Ignition (SI) and Compression Ignition (CI).

In general, before looking at each individual engine type, it can be said that there are limited areas where improvements can be made. These are reduction in pumping losses, improvement in

the compression and expansion work (Atkinson Miller cycles), improvement in combustion duration (more efficient Otto cycle), improvement in chemical conversion efficiency (i.e. completeness of combustion) and reduction in mechanical friction.

1.2.1 Spark Ignition Engines

SI engines inhale a homogeneous mixture of air and fuel. A spark plug is used to ignite this mixture. Combustion then relies on the flame propagation to achieve as complete a chemical transformation of the fuel as possible. In order for this flame propagation to occur, stoichiometric or near stoichiometric mixtures have to be used. Stoichiometric mixtures also provide a means of using a Three Way Catalyst (TWC) as an exhaust after treatment method. The spark ignited engines at the moment achieve quite low emissions, however their efficiency is low thus a large amount of CO_2 is produced.

The limitation for the SI engines comes from two main sources: one is that throttling is needed in order to control the load, thus imposing pumping losses during the gas exchange process. In addition the resulting effective compression ratio is low thus decreasing thermodynamic efficiency. The second drawback comes from the reliance on flame propagation itself. Flame propagation, even at the pressures reached after the compression of the air-fuel mixture, attains speeds of around 30-40 m/s. In order to follow the Otto cycle more closely higher flame speeds are needed. However, the use of higher Compression Ratio (CR) which would promote higher flame speeds cannot be realized since knocking would occur. Knocking occurs when the mixture outside the "flame ball" propagating inside the combustion chamber, auto-ignites due to the higher ambient pressures and temperatures. When auto ignition occurs flame propagation reaches supersonic speeds (in the order of 2000 m/sec) and instead of achieving deflagration, detonation ensues.

An engine which accommodates all these considerations of allowable CR and throttling for the whole operating range, unfortunately compromises part load efficiency to a great extent.

Special cases

Gasoline Direct Injection (GDI) engines do not rely on an overall homogeneous mixture but use specially shaped turbulence to achieve a local ignitable mixture in the vicinity of the spark plug. Thus, the combustion occurs in a confined area, in a cylinder with an overall excess of air. This stratified combustion allows them to operate throttleless, thus achieving higher efficiencies.

However, due to the stratified combustion, high amounts of NO_x are created which require the use of a NO_x trap, since they cannot be used in direct conjunction with a TWC.

1.2.2 Compression Ignition Engines

CI engines can use very high compression ratios and also operate unthrottled throughout the operating range. This means that very high part-load efficiencies are achievable. This is because these engines operate on the principle of compressing the inhaled air to the point at which fuel, which is directly injected in the combustion chamber, ignites.

Again, it is this principle of operation that, although giving high efficiency potential, imposes limitations on emissions reduction. Since the fuel is ignited as it is injected inside the combustion chamber it is burnt through diffusion flame. This means that on the outside boundaries of the fuel jet very lean combustion occurs while inside the jet core very rich combustion occurs. Although this inadequate mixing is tackled through the use of swirl imposed on the intake air-streams by swirl pots or specially shaped inlet tracts the results can't match the emission levels of SI engines. In addition, due to the necessarily low air utilization, as stoichiometric mixtures would result in very high particulate emissions, specific power outputs of normally aspirated diesels is low.

However, CI engines can be perfectly complemented with turbochargers that further increase their efficiency and (recently in combination with common rail systems) put their power density on a par with SI engines. Most importantly, turbocharging can be used without the compression ratio reduction requirement which is necessary for turbocharged SI engines. Again this comes as a

direct result of the knock free operation of diffusion flame combustion.

1.3 Homogeneous Charge Compression Ignition engines

Homogeneous Charge Compression Ignition (HCCI) is an attempt at getting the advantages of both SI and CI engines in the same engine. As the name implies, the idea is to ignite a homogeneous charge through compression. There are many ways in which this can be achieved and HCCI-type combustion has been discovered in many different guises as will be discussed later on. However, the main theme is that the homogeneous mixture is diluted by a hot gas and then compressed. The increased starting temperature causes the mixture to combust. In normal circumstances, an autoigniting homogeneous mixture can result in a powerful detonation, damaging or destroying the engine. However, due to the presence of the hot gas, the released energy is distributed to a larger mass, which acts as a cushion. In this way, both the speed of the reaction and the maximum temperatures involved are moderated, leading to a manageable release of energy.

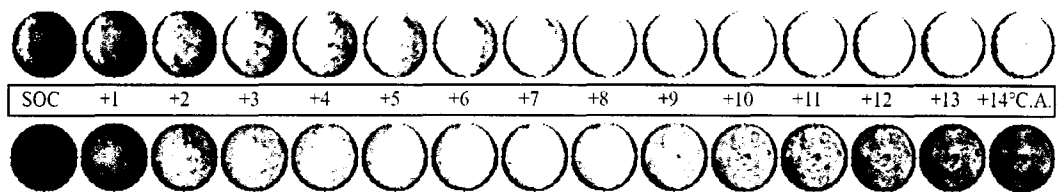


Figure 1.1: Comparison of SI (top) and HCCI (bottom) combustion duration, 1500rpm, 2.5 bar IMEP

The benefits of such an engine is that it can operate unthrottled, thus reducing pumping losses. Because it relies on autoignition, rather than flame propagation, combustion duration is shorter, resembling more closely an ideal Otto cycle as seen on figure 1.1 [1], where the white regions indicate the presence of flame. On the emissions side, due to the lower maximum temperatures reached, NO_x emissions are dramatically reduced as seen on figure 1.2, where HCCI engine emissions are compared to those of Direct Injection (DI) engines. Since the combustion is not stratified,

particulate emissions are also reduced. The drawbacks are that, due to these lower temperatures, unburnt Hydrocarbons (HC) and Carbon Monoxide (CO) levels rise.

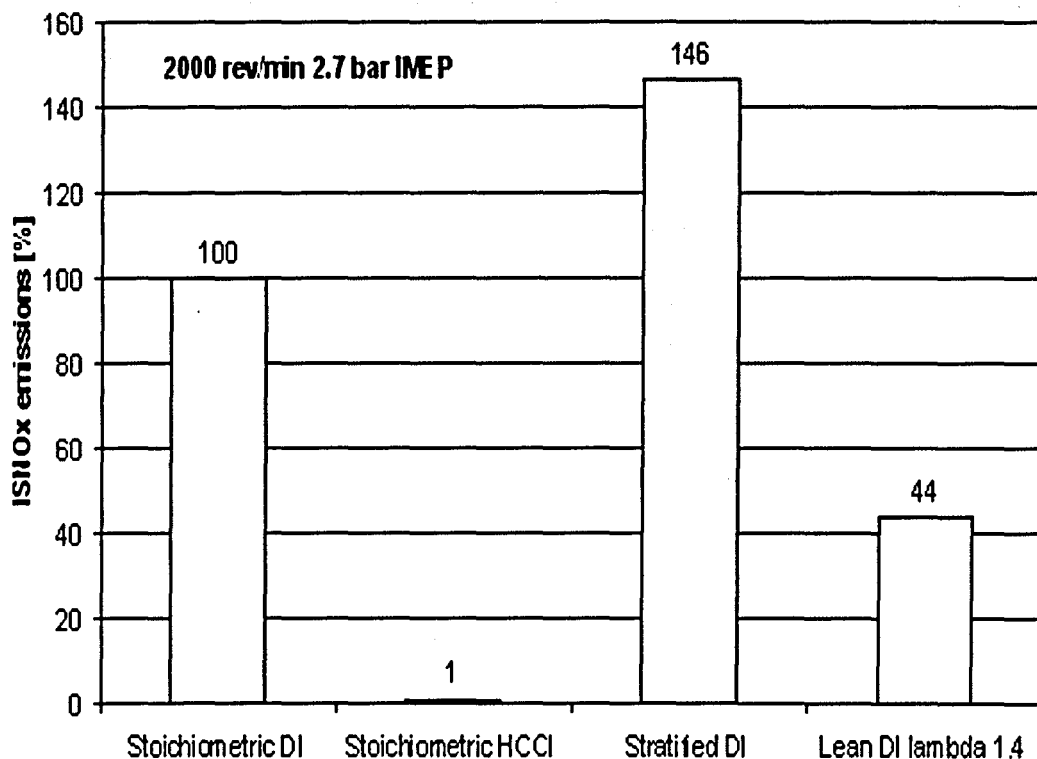


Figure 1.2: Comparison of NO_x emissions for different engines) combustion duration, 1500rpm, 2.5 bar IMEP

To implement an HCCI engine, the hot gas has to be present in the cylinder alongside the charge. This is done either by retaining or rebreathing an amount of exhaust gases or by introducing preheated air in the inlet.

1.3.1 HCCI history

While research interest in HCCI has grown in recent years, HCCI itself is not a new discovery. Over the years, similar processes have been recorded under various names:

- Active Thermo Atmosphere Combustion (ATAC) [2]

- Activated Radicals Combustion (AR, Honda) [3]
- Toyota Soken Combustion (TS, Toyota) [4]
- Premixed-Charge Compression Ignition (PCCI) [5]
- Homogeneous Charge Compression Ignition (HCCI)
- Controlled Auto-Ignition (CAI, Lotus, Ford)

The first four names are mostly used in Japan, while the term HCCI is mostly used in the USA. CAI appears to be the preferred name in the UK.

In 1958, experiments were performed with premixed charges of hexane and air, and n-heptane and air in a Diesel engine [6]. They found that under certain operating conditions their single cylinder engine would run quite well in a premixed mode with no direct fuel injection whatsoever.

A few years later, in 1979, HCCI combustion, a result of unscavenged exhaust gasses from the previous cycle, was recorded [2], in two stroke engines. It was termed "Active Thermo-Atmospheric Combustion" (ATAC). It was the tendency of the engine for run-on, after turning the ignition off, that gave away the fact that some form of autoignition was taking place. It was found that this was the result of the high levels of residuals at part load, in two stroke engines. By exploiting this unique feature, i.e. high initial charge temperatures due to high levels of residuals, the engine operation, fuel efficiency and refinement, were drastically improved. This came as a result of the cycle-to-cycle variability almost being eliminated in the "ATAC" combustion mode.

Observations in their optical engine showed a fine pattern of density variations and gradual combustion reactions throughout the entire chamber during combustion, instead of the normal flame front propagation as shown in figure 1.3.

The critical parameters of HCCI combustion were identified as:

1. high levels of dilution to obtain high enough temperatures for autoignition

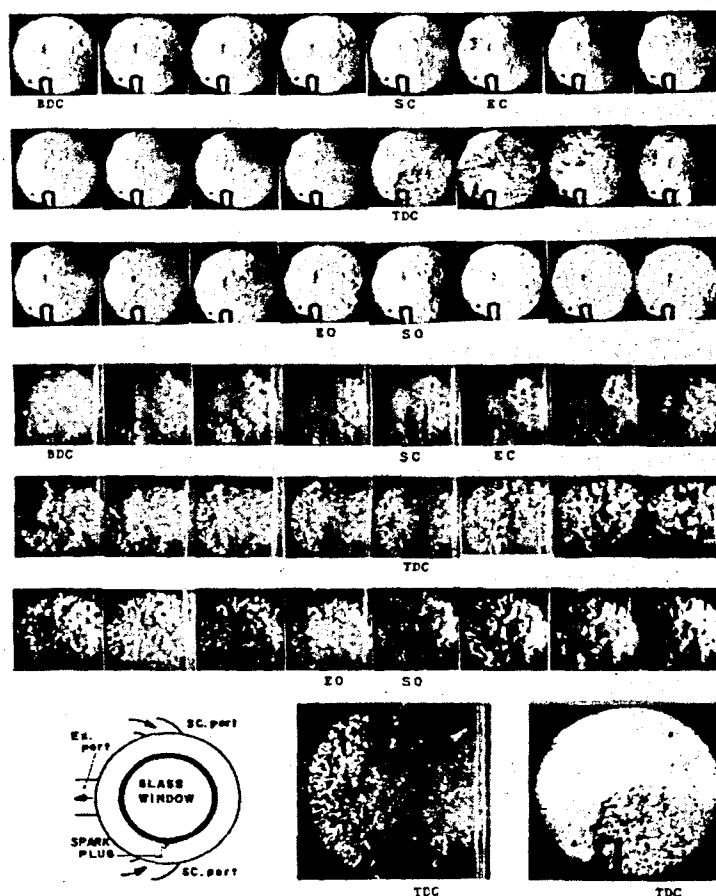


Figure 1.3: Schlieren photography of SI (top three rows) and HCCI (bottom three rows), and close ups. Taken from [2].

2. uniform mixing between residual and fresh charge
3. repeatable cycle-to-cycle scavenging

At the same time, experimental work performed by Toyota and Nippon Soken Inc. [4] revealed similar behavior again on two stroke engines. The authors concluded that HCCI combustion is very well suited for part load two stroke engine operation and that while the overall burn rates were very fast, combustion was smooth and fuel consumption and emissions were vastly improved.

From optical investigations during this research at Toyota, multiple sites of ignition and no discernible flame front propagation were evident. Spectroscopic analysis revealed high levels of

CH_2O , HO_2 , and O radicals well before autoignition. These species are characteristic of low-temperature autoignition chemistry of larger paraffinic hydrocarbon fuels. During combustion, high concentrations of CH , H and OH radicals were recorded, indicative of high-temperature chemistry during the bulk-burn. These measurements resembled concentrations found in end-gas autoignition and knock, thus confirming similarities between HCCI and combustion and knock while also justifying the use of the term Controlled Auto Ignition (CAI).

Work in four-stroke engines, [7], using blends of paraffinic and aromatic fuels over different engine speeds and loads (dilution), simulated internal residuals by heating the intake air. Chemical kinetic modeling and heat release analysis of experimental data showed that two semi-independent processes of ignition and bulk fuel combustion were present. HCCI autoignition is governed by the low-temperature chemistry (less than 1000K) that leads to knock in SI engines. The bulk energy release comes from high temperature (above 1000K) CO oxidation. Based on chemical kinetics alone, a correlation for the energy release that simulated the experimental results was developed that explained HCCI behavior to changes in compression ratio, equivalence ratio, dilution level, engine speed and fuel type. These results and the previous work on two-strokes concluded that HCCI is a chemical kinetic combustion process controlled by the temperature, pressure and composition (which can be time dependent) of the charge. This work, [7] concluded that HCCI is not a mixing-controlled process, but rather resembles a compression-ignited, stirred chemical reactor.

Further work [8] examined HCCI operation of a single-cylinder engine using fully blended gasoline. Again, air to fuel ratio and external Exhaust Gas Recirculation (EGR) rates were varied in an attempt to find the limits of this operating regime.

Much of our knowledge of knock chemistry has been based on experiments in shock tubes, constant pressure flow reactors, rapid compression machines and motored engine layouts. These experiments have highlighted the importance of low and intermediate temperature chemistry in

knock processes [9, 10]. The data have also been used to develop and validate detailed reaction mechanisms for higher carbon number fuels such as n-heptane and iso-octane [11, 12].

As with all of the above researchers, and unfortunately up to now, the limitations of speeds and loads that an HCCI engine can cover is always observed. A hybrid engine operating strategy was first suggested in 1989 [8], where part of the operation would be conventional SI, while HCCI could cover the more favorable, for this type of combustion, regions.

From all of the above, it can be concluded that HCCI is a process where mechanical means are used to control what is basically a chemically controlled process. Still, the implementation of HCCI engines is not straightforward. With current technology status, HCCI can only be used for hybrid electric powertrain applications. This is because electric power generation does not require operation over a wide range of speed/load conditions, which is where HCCI engines currently struggle. It is the control issues of HCCI engines over wide windows of operation that are holding them back presently.

1.4 Aim of this work

The inspiration for the work presented in this thesis is a result of the control issues surrounding gasoline HCCI. Due to the indirect nature of the combustion initiation, HCCI combustion is harder to control than more conventional methods. Hence, the question of closed loop strategies become more attractive.

However, for a well tuned closed loop implementation, a suitable feedback signal is required. Hence, the use of pressure and ion current sensors is central to this work.

The idea behind using both these kinds of signal come from the fact that, pressure sensors provide a reasonably good quality signal but are too costly and potentially unreliable to be used in mass production. The search for an alternative type of sensor indicates that ion current sensors can provide relevant combustion information that can substitute the information provided by the

pressure sensors at a much lower cost. The signals provided by both these two sensors have certain characteristics which need to be addressed in each case. Hence, the development of the algorithms dealing with each kind of signal and their correlations constitutes the core of this thesis.

There is both an experimental and a modeling component to this work. The experimental component has focused on collecting pressure and ion current data. The modeling component has then been designed in order to interpret the data and hence attempt to get an understanding of the mechanisms involved. The structure of the thesis is presented below.

1.4.1 Thesis Map

Chapter 1 gives an overview of the historic and practical reasons behind HCCI research.

Chapter 2 focuses on the practical methods involved in implementing HCCI combustion in hardware (Section 2.1) and software (Section 2.3). Also, outlines the present status of ion current research (Section 2.2).

Chapter 3 presents the hardware setup and strategies used in collecting the experimental data.

Chapter 4 introduces ion current as feedback signal. The chapter describes the ion current related research carried out, both in an SI and an HCCI context. The algorithms dealing with the ion current signal, as well as its use for matching it to the pressure signal through the use of Artificial Neural Network(s) (ANN(s)) is described and discussed.

Chapter 5 describes the techniques employed in dealing with the experimental data, finally yielding an algorithm which is useful for treating both SI and HCCI pressure traces in general.

Chapter 6 describes the implementation of the thermodynamic model developed for this research and offers some results which are useful in understanding the mechanisms of cycle to cycle

coupling in HCCI.

Chapter 7 deals with the issues of autoignition and unstable HCCI combustion. The failure of simple Arrhenius style models is discussed and a possible autoignition mechanism for the engine used is suggested.

Chapter 8 contains the final thoughts concerning the present work.

Chapter 2

Present Status

At present there are various ways to implement HCCI operation, though no HCCI powered production automobiles exist as yet. This chapter introduces the present status of HCCI research.

There are three potentially problematic areas where HCCI operation is concerned. The first one is a matter of mechanical complexity. In order for autoignition to occur, a hot gas must somehow be introduced to the cylinder. The various ways of doing this are examined further down but all of them add new levels of complexity to the classic design of an SI engine. The second problem is that some emissions, namely HC and CO rise. The third and arguably most important problem is that, unlike spark controlled SI or injection controlled CI engines, autoignition cannot be directly controlled but must arise as a consequence of chemical kinetics. This imposes a great uncertainty on what is probably the most important aspect of an IC engine, the manipulation of the heat release.

Emissions HC and CO emissions in homogeneous charge engines mainly arise from the crevices in the combustion chamber. This is due to the fact that the portion of the mixture that gets trapped in these fails to combust completely. The cooling of this mixture in the crevices is a lot more pronounced since it presents a greater surface to volume ratio and also due to the difficulty of the flame to propagate into these crevices.

However, in SI engines the temperatures in the cylinder are high enough to support the conversion of the hydrocarbons as the piston moves down and the trapped gasses are, mostly, released. This is not the case in HCCI engines where peak combustion temperatures are typically less than 1500K. At these temperatures, even the autoigniting mixture in the centre of the combustion chamber fails to complete the CO to Carbon Dioxide (CO_2) oxidation and the combustion efficiency deteriorates precipitously at lower loads where the lowest temperatures occur. High combustion temperatures in stoichiometric SI engines allow post combustion oxidation processes to continue into the expansion stroke and blowdown process. In HCCI this post combustion CO oxidation becomes inefficient due to the lower temperatures. Fuel and intermediate species cannot react into ultimate products and some hydrocarbons emitted from combustion chamber crevices only partially oxidize to CO [13].

One more issue that might arise is that the resulting exhaust gases temperature is low, which can result in reduced aftertreatment efficiency. This is because oxidation catalysts need to reach a certain operating temperature to function efficiently. However, studies have proven that the exhaust temperature remains between 450 and 560°C when air to fuel ratios are close to stoichiometric ($0.95 < \lambda < 1.15$) and for a standard SI compression ratio. This is sufficient for aftertreatment with an oxidation catalyst [1].

By having the low load operation limited due to the combustion inefficiencies that arise as a result of the low combustion temperatures, it immediately transpires that a multi-mode, or hybrid, engine is needed to serve the complete operating range.

When one also considers that the high loads, in diesel implementations of HCCI, are also limited by the large heat release rates that occur due to the low mixture dilution and enriched mixtures, the seamless transition between the modes of combustion appears as a fundamental issue for the implementation of such an engine. Transient behaviour of HCCI engines, be it within the auto-ignition operating region, or where mode switching is necessitated, is still an unresolved issue at

the centre of research attention.

Ignition Control Ignition timing control is the most important control parameter. It is governed by the chemical kinetic reaction rates of the mixture, which in turn are governed by time, temperature, pressure and mixture composition. If transient operation is considered, matters become considerably more complex due to the different timescales involved as these interlinked variables settle to new values.

If full flexibility over engine operation is desired, a simple engine map like the ones currently used for spark ignition timing in SI engines, or injection timing in CI engines is not adequate for ignition control. Some sort of closed-loop control must be employed in order to keep engine operation under control, avoiding driveability problems and, more importantly, engine damage.

2.1 HCCI Implementations

The methods used to induce autoignition can be divided in two main categories, “thermal control” and “chemical control”.

Thermal Control In the case of thermal control, parameters such as temperature, pressure and composition at Inlet Valve Closing time (IVC) are selected so that autoignition occurs close to Top Dead Centre (TDC). Thermal control methods include intake air heating, variable compression ratio or using residual gas.

Chemical Control Chemical control involves the use of dual fuels, where typically one fuel provides the energy needed to initiate combustion, while the other fuel provides the bulk of the heat release.

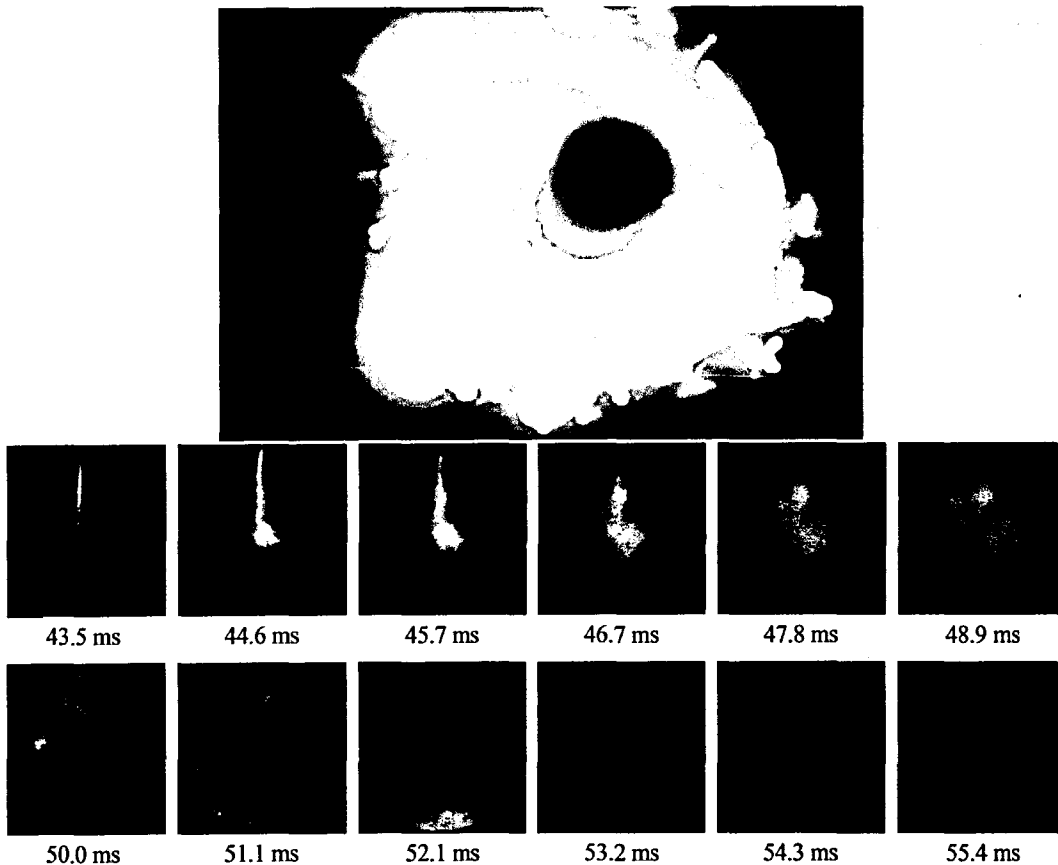


Figure 2.1: Rotating Ark Spark Plug (RASP) (top [14]) and Pulsed Flame Jet (PFJ) initiated HCCI combustion (bottom [15])

Other methods Auxiliary methods used in conjunction with the above may involve the use of ignition systems yielding energy in amounts far greater than a conventional spark plug, thus aggressively pushing the mixture towards autoignition. These include the Rotating Ark Spark Plug (RASP) [14], figure 2.1 top, Pulsed Flame Jet (PFJ) [15], figure 2.1 bottom, and Capillary Force Vaporizer (CFV) [16]. All of these increase the possibility of ignition at the desired point by providing energy, usually in the order of 100+ times that of a spark plug.

2.1.1 Intake Air Heating

The necessary temperature for promoting autoignition at the required crank angle can be achieved through intake air heating. Because the heated air is not inert, very violent rates of heat release

can be reached. To avoid damage to the engine, the mixtures must be kept very lean. A very lean mixture lowers the temperature, maintaining the heat release to acceptable rates [17].

This method suffers from a lot of drawbacks, the most notable of which is the large amount of energy needed to raise the temperature of the intake air, making overall efficiency suffer as a result [18]. Also, the slow transient response is a big issue if a real life implementation for this method is to be considered.

2.1.2 Variable Compression Ratio

For HCCI applications the variable compression ratio can influence the temperature level at the end of the compression stroke, thus affecting autoignition timing. However, typical compression ratios do not lead to a temperature that is high enough for autoignition at the end of the compression stroke. Thus this technique is usually used in conjunction with a heater or variable valve timing [19–22].

2.1.3 Dual Fuels

In this method, two fuels of different octane number are used. The low octane fuel is used to trigger combustion while the high octane fuel provides the bulk of the heat release.

Systems presented include Dimethyl Ether (DME) [23] in combination with methane, natural gas and naphtha fuel (gas and liquid) [24], ethanol and n-heptane [25], iso-octane and n-heptane [26] and also propane and ozone [27]. This last enhancer, ozone, has the added advantage of requiring only very small amounts of it to be added and also does not require a second fuel tank, since it is claimed that ozone can be produced on-board with a relatively inexpensive and fast response system. One more possibility is the use of natural gas and hydrogen, using hydrogen as the ignition improver. Again, hydrogen can be produced on board using a natural gas reformer [28].

2.1.4 Use of Residual Gases

Using residual gases is a combination of mainly thermal and arguably chemical control. Because the residual gases are hot, it raises the temperature of the mixture so that it reaches autoignition conditions towards the end of the compression, like in the case of preheated air. However, unlike in the case of preheated air, there is no excess oxygen to lead to a violent heat release, so there is no need to use very lean mixtures in order to avoid damaging the engine.

The chemical effects are under debate, however, it is possible that fresh residual gases contain radicals which attack the fuel molecules, thus promoting autoignition. The importance of active species was highlighted by experiments where preheated air or nitrogen, in quantities and temperatures similar to residuals was used to dilute the charge. In cases where autoignition was possible with residuals it was not possible with the other inert substitutes [29].

Strategies

The simplest way to introduce residual gases into the cylinder is to route them from the exhaust to the inlet manifold, hence the term Exhaust Gas Recirculation (EGR). While this is easy to implement, it incurs frictional and thermal losses.

More elaborate methods make use of Variable Valve Timing (VVT) in order to dynamically control residual amounts. There are two ways in which this can be implemented as described below.

Rebreathing [30]

In this case, the exhaust gases are expelled normally, but then the exhaust gas remains open for part of the induction, allowing some amount of residuals to be rebreathed. This allows for less losses than recirculating but still, the pumping loss must be "paid" both for getting the gases out and for getting them back in.

Early EVC and late IVO [31]

In this case, the exhaust valve closes before all the gases have been expelled. The trapped residual gases are then compressed and expanded during the remainder of the gas exchange cycle. In addition, the opening inlet valve is delayed until the pressure of the residual gases in the cylinder has reached that of the inlet in order to avoid backflow from the cylinder to the inlet. The compression and expansion of the residuals acts as a pneumatic spring, in theory requiring no net work. In practice, a small amount of energy is lost as heat to the walls.

In a normal SI engine, there is a certain amount of overlap between the inlet and exhaust valves. Because in this implementation, this overlap becomes negative, the region of compression and expansion of the residuals is termed Negative Valve Overlap (NVO).

Because the term EGR does not adequately describe this process, the term Internal Exhaust Gas Recirculation (IEGR) is sometimes used. However, there is no recirculation involved so the IEGR term might be misleading. Hence, throughout this work, the term Trapped Residual Gas (TRG) will be used to describe residuals trapped through early Exhaust Valve Closing time (EVC).

Trapping exhaust gasses, offers exceptional control and transient possibilities and is thus being used more and more by researchers [22, 30, 32–34]. It is argued that TRG has multiple effects on combustion. Apart from the obvious thermal effect, four others can be identified [35]. These are:

- **Heat Capacity** Due to the presence of large percentage of CO_2 and H_2O in TRG, the specific heat capacity of the mixture is increased, leading to lower temperatures compared to those reached in normal SI with the same amount of charge.
- **Dilution** The introduction of an arguably inert gas slows down the reaction rate.
- **Exhaust Gas Species Concentration Increase** The net production rate of CO_2 and H_2O is decreased due to the non negligible concentrations of these species even before combustion.

- **Radical Production and Destruction Influence** It is claimed that, “some exhaust gas species, particularly residual (active) radicals (such as H , OH , HO_2), may influence the production and destruction reactions of some radicals. Also, water vapour as an effective third body may affect reactions where a third body plays an important role, such as in termination reactions”.

2.2 Ion Current Research

Ion current has long been investigated as a combustion diagnostic tool [36,37] in SI engines. The principle of operation is based upon the fact that burning cylinder gases become ionized and can thus conduct a current when a voltage is applied to them.

The potential of ion current has been researched and used in production as a means of misfire detection (a task it is well suited for as a misfire produces no ion current) and knock detection [38–40]. More research has focused on the estimation of Air Fuel Ratio (AFR) from manipulation of ion current signals [41–46] and how to incorporate it into a closed loop control system [47–53].

Recent research has gone further trying to reproduce in-cylinder-pressure profile characteristics from ion current data [54–58]. This has often been accomplished through ANN(s) methods [53, 54, 59]. In the present work, the potential use of the ion current as a feedback signal has been investigated in both an SI and HCCI context, using a variety of ANN(s) designs.

2.3 Modeling Approaches

So far, the basics of hardware implementations of HCCI have been reviewed. However, experimentation is not the only tool available to the researcher. Modeling through computer simulation is an attractive proposition, mainly due to the low time and financial costs involved. This research is based upon both an experimental and a modeling part. Hence, a brief outline of modeling

techniques is presented here.

Designing a model is a balancing act between computational resources and required precision. Most of the relevant equations describing physical and chemical systems are available but implementing them in a form which can be tackled by finite computational resources is not always easy. In engine modeling relevant to HCCI combustion, the task is relatively easy to visualise at least, a moving part (the piston), changes the volume of a cylinder containing a mixture of gases undergoing chemical transformation. The system described can be thought of as consisting of three parts, a mechanical part (cylinder and piston), a fluid mechanical part (the gases) and a chemical part (the chemical reactions).

The mechanical part is fortunately trivial. The other two however are anything but. A complete description of the gases' variables in both space and time requires tracking a system of gases whose internal variables are not necessarily described by simple mathematical functions. To make matters more complicated, the chemical reactions must also be taken into account, changing both physical and chemical properties of the mixture.

The physical tracking of the gases can vary from a zero dimensional study [20, 60–62], where only intensive quantities are taken into account, to a detailed Computational Fluid Dynamics (CFD) study [63–65]. In the latter case, the space to be considered is discretised into many small control volumes, or cells, to which the equations that govern the fluid flow are applied. The equation set is usually solved in an iterative manner, from which the complex behaviour of the system under consideration can be studied as a function of both space and time. The finer the level of grid resolution the better resolved the underlying flow physics, provided that the model equations tend to the exact value in the limit as the cell size tends to zero. However, the computational cost rises rapidly with increasingly fine grids. To negate the effects of the rising computational burden, techniques such as localised grid refinement and adaptive meshing incorporate higher cell densities in the main regions of interest, or where the steepest gradients in the dependent variables

can be observed.

Similarly, the chemical modeling can be as simple as an instantaneous conversion from reactants to products or a detailed chemical model involving a host of intermediate steps [66, 67].

While an ultra-fine grid CFD study with detailed chemical kinetics might yield the best results, the computational resources required are considerable from a research point of view (both CFD and chemical kinetics models can run for days on conventional high end PCs) For control applications, this is simply impossible. Hence, shortcuts must be made to abstract the most important aspects of the physical system for the research under consideration into a computationally manageable mathematical description.

To that end, multi-zone [13, 68–72] or Probability Density Function (PDF) [73–75] models are bridging the gap between zero dimensional and CFD models. The idea behind these is similar to that employed in the dynamically changing grids in CFD described above. That is, to focus the computation at the most significant points. This is done by, for example, dividing space in shapes that capture vital aspects of the studied processes or using stochastic methods to identify important points.

Similarly for the reaction mechanisms, various models of reduced complexity can be employed which aim to capture the principal features of combustion. Depending on the focus of the research, more or less precision might be required in a particular aspect, hence appropriate hybridisation is at the discretion of the researcher.

Once implemented, a well tuned model will hopefully correspond well with experimental data. It can then give data not covered by experiment or give insights on aspects of the process not directly measurable through experiment. As a tool for control, a model can be invaluable by supplying advance knowledge of the expected behaviour of a system. However, if designed for control purposes, a model has to be fast enough in order to evaluate the future system state before the system actually reaches it itself. In practical terms, bearing engine modeling in mind, this

means that any but the most computationally inexpensive models are inadequate as regards speed of execution.

Chapter 3

Experimental Setup and Strategies

Employed

The early EVC - late Inlet Valve Opening time (IVO) method of TRG control has been employed for the experimental part of this work, due to its agreeable characteristics discussed on page 19.

From an engineering point of view, the main issue with such an implementation is how to change the valve timing. Since the present research has been carried out in collaboration with Lotus Engineering, the specially made test rig is described in this section.

3.1 Experimental Engine

An engine capable of operating in HCCI as well as SI was needed, hence, the engine employed was a single cylinder, gasoline port fuel injected, 4-stroke research engine based on a GM Family One, 1.8L series architecture (figure 3.1).

A standard 4-cylinder head is mounted on top of a water cooled barrel, with a custom made bottom end. Only the front cylinder of the head is operational, provided with a Fully Variable Valve Timing (FVVT) system named Active Valve Train (AVT) manufactured by Lotus Engineering. The

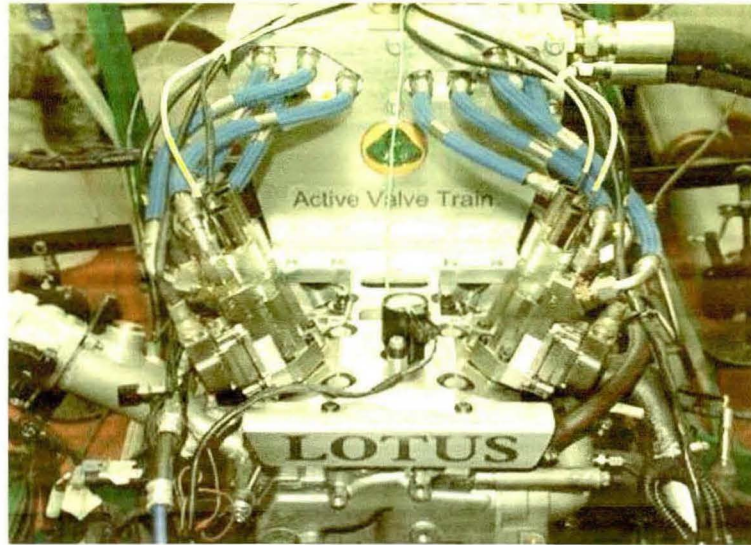


Figure 3.1: Research Engine with AVT system

AVT is a high pressure hydraulic valvetrain system that uses high speed digital valves to control the oil pressure in a hydraulic piston driving the valve stem. Details of the design are displayed in figure 3.2.

The AVT is computer controlled and can change valve profiles whilst the engine is running and within an engine cycle, thus facilitating the selection of TRG quantity. Because of this, switches between SI and HCCI can be performed while the engine is running.

The engine was equipped with an electronic throttle, in addition to a standard mechanical one, that was used for load control, especially keeping the load constant whilst switching from SI to HCCI and back.

The use of conventional parts in the combustion system, wherever possible, ensures that the cost of rebuild is low in case of any component failures (because of uncontrolled detonation, for example). The CR can easily be changed in this engine, both because of the separate barrel and, more importantly, because of the AVT system negating the need to consider modifications to belt runs etc. Any change in CR is achieved by means of the deck height being moved up and down by spacers or special short liners, or a combination of the two. The bottom end can accept various

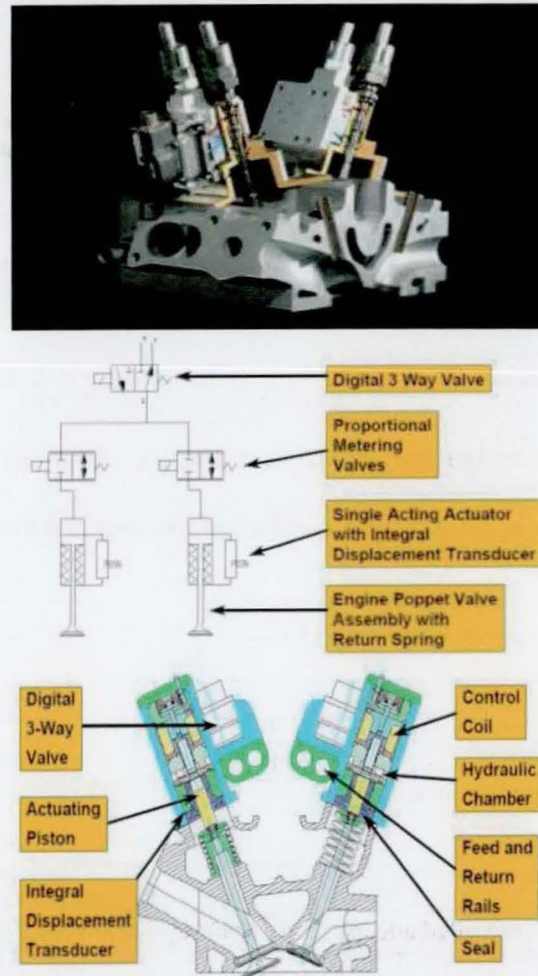


Figure 3.2: Details of the AVT design

strokes up to and including 100mm, and is capable of running to 7000rpm (depending on stroke).

For this research, the CR was set to 10.5 and the fuel used was commercial gasoline 95 ON.

The engine was connected to a Froude Hofmann AG30 eddy-current dynamometer. A redline ACAP data acquisition system from DSP Technologies Inc. was used, together with a Kistler 6123 piezoelectric pressure transducer. A Horiba MEXA 7100 DEGR analyzer was used for emissions measurement. Port fuel injection was employed, managed by a conventional Lotus V8 engine controller. Technical information on the dynamometer, pressure transducer and gas analyzer can be found in appendix A on page 223.

3.2 Experimental strategies

The experimental data presented throughout this research has been collected using this setup unless otherwise stated, as in the case of the SI data in section 4.1.

The data falls into three categories, one for SI and two for HCCI operation.

3.2.1 SI

For SI operation the standard profile used in the production engine equivalent was used which involves positive overlap, high lift (8-10mm) and a fixed duration and phasing.

3.2.2 HCCI with constant EVO and IVC

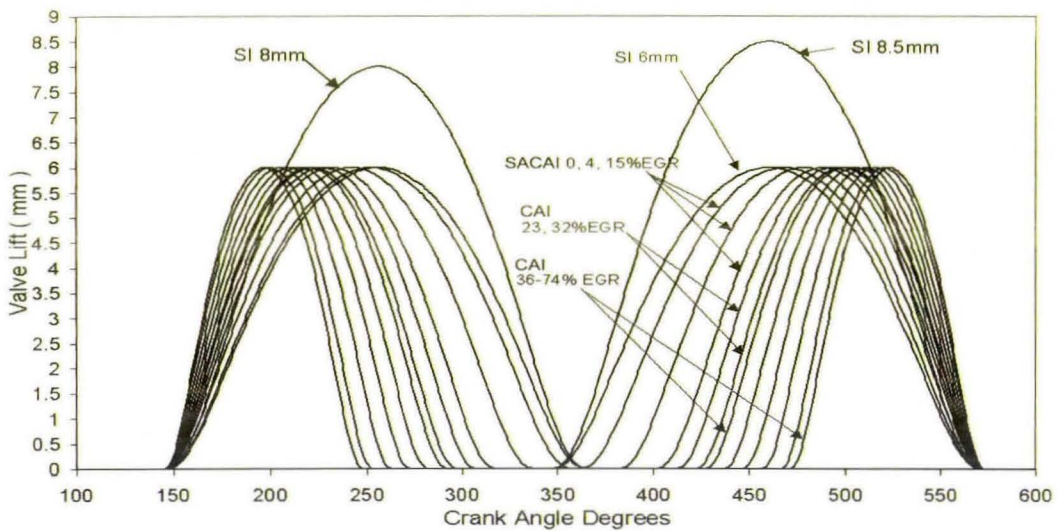


Figure 3.3: Valve lift traces in the constant EVO/IVC strategy

In the overall early EVC strategy, the deciding factor for the amount of TRG is in the selection of the EVC. This also dictates also IVO. Hence, having selected a TRG amount (effectively EVC-IVO), the Exhaust Valve Opening time (EVO) and the IVC are left to the discretion of the experimenter.

The constant EVO, IVC strategy hold these two constant at typical values. This has the implication that the duration of valve opening for both valves is variable and TRG dependent (figure

3.3).

3.2.3 HCCI with constant duration

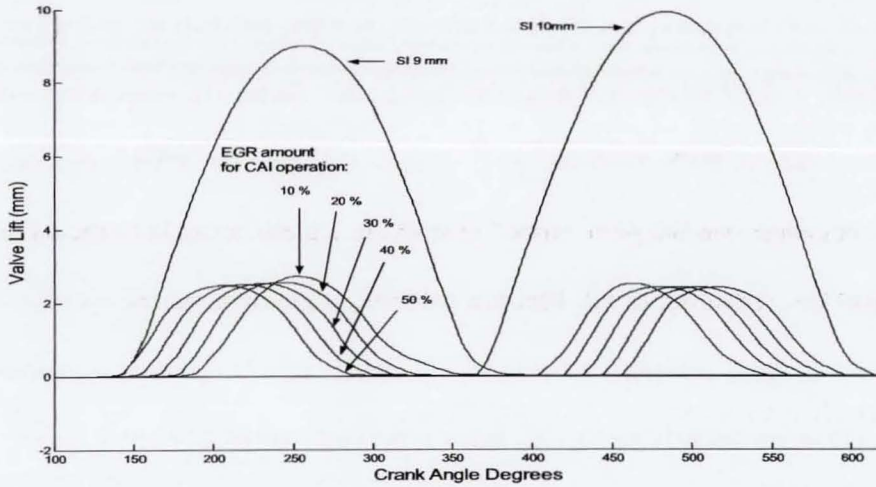


Figure 3.4: Valve lift traces in the constant duration strategy

In this case, again, TRG amount dictates EVC and subsequently IVO. However, the *duration* of the valve opening event is kept constant, thus dragging both EVO and IVC along (figure 3.4).

Although the AVT system can simulate any valve configuration, the second (constant duration) valve strategy has been tried in order to simulate an operation which can be easily be implemented by mechanical means (e.g. phaser). The problem with the constant duration strategy is that, as TRG is increased, EVO is occurring earlier and IVC later. Early EVO might be a problem due to premature venting leading to a loss of usable energy. However, the main problem is the late IVC. This leads to the compression stroke starting at a point where the volume has been reduced by non negligible amounts, thus altering the compression ratio. It is due to this reason that the autoignition behaviour of the engine is greatly dependent on the strategy as discussed in Chapter 7.

3.2.4 HCCI-SACAI nature of experimental data

One final point that needs clarification is that generally experimental data are collected with the spark plug firing unless otherwise stated. There are various reasons for this. The most obvious one is that, in HCCI (especially in a single cylinder engine where residuals are retained as opposed to rebreathed), a single misfire will make the engine stall. Hence, the spark firing, even when not needed in general, has a stabilising effect. However, there might be some controversy over what kind of combustion should be termed as HCCI. In a purist sense, HCCI should be able to operate sparkless. However, in gasoline, this requirement greatly limits the operating window of a combustion that is otherwise not pure SI. This non-pure HCCI operation is *initiated* by the spark but almost immediately autoignites, hence is not conventional flame propagation. A more appropriate name for it is Spark Assisted Controlled Auto Ignition (SACAI) (Lotus). Of course, the spark timing is a helper, rather than the orchestrator of the combustion as in pure SI and its influence is increasingly limited with increasing TRG. Since most but *not* all the data presented are SACAI, the term HCCI is used throughout the text.

3.3 Ion Current Signal Acquisition

The experiments also involved ion current signal acquisition. This was done by locating an ionization probe in the four-valve cylinder head between one of the inlet and one of the exhaust valves as shown in figure 3.5. The probe was electrically isolated from the cylinder head by means of a ceramic sleeve. The diameter of the sensing element was slightly less than 1mm, and the tip protrusion into the combustion chamber was approximately 3.5 mm.

Since the mass of positive ions, such as H_3O^+ , is approximately 30,000 times larger than that of an electron (negative charge), the light electrons can be accelerated much more easily towards the positive electrode than the heavy ions [76], when driven by an applied electromagnetic field.

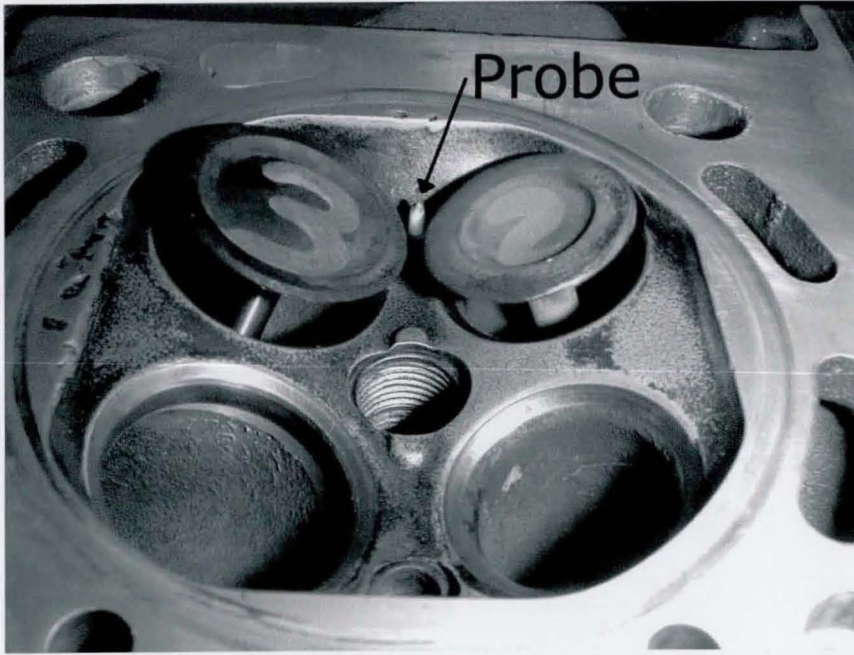


Figure 3.5: Cylinder head, showing the location of ionization probe

The voltage polarity at the gap of sensing spark plugs was therefore selected such that the small area centre electrode was positive, and the rest of the combustion chamber was negative. This coincides conveniently with the original engine polarity where the engine block is negative, earth.

A one-off DC voltage source, as shown in Figure 3.6, was used to power the measuring probe. The input to the DAQ board came from the voltage divider and was inversely proportional to the sensed ion current (i.e. 5V for zero ion current and 0V for infinite) to avoid the possibility of damage caused due to excessive voltage. The signal was then inverted during the post processing phase.

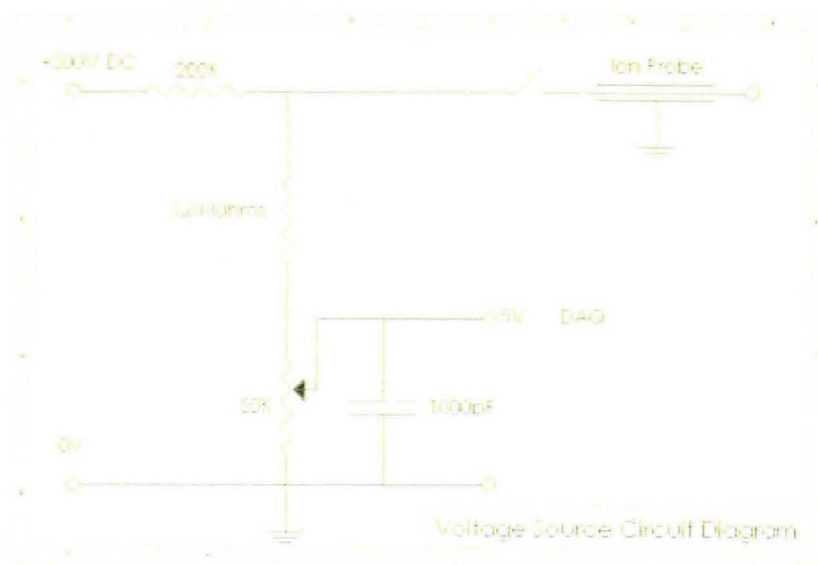


Figure 3.6: Voltage source circuit diagram

Chapter 4

Ion Current

The work presented in this thesis focuses on two main in-cylinder signals, pressure and ion current. Although pressure measurements via a piezoelectric transducer are standard practice, it can hardly be a realistic proposition for a production automotive engine. This is due to the high cost of piezoelectric pressure transducers as well as questionable long term performance. Hence, using an alternative signal, such as ion current, and trying to match its characteristics to those of the pressure transducer is a very promising line of research.

Ion current measurements are based upon the fact that the prevailing conditions inside the engine during combustion cause ionization of the gases in the cylinder. By applying a voltage, a current is produced since the ionized gases are conductive.

Ion current based measurements have been successfully used in this research, initially on an engine under SI operation and subsequently on the Lotus engine on which the rest of the HCCI data has been collected. The post processing of the ion current data lends itself very well to treatment through ANN(s). This chapter describes in detail how this has been implemented.

4.1 Ion Current as a diagnostic tool in SI operation

4.1.1 Introduction to Ion Current Measurement

In order to use ion current as a tool for in-cylinder engine diagnostics, suitable probes have to be situated inside the combustion chamber. The most obvious way to apply a voltage inside the cylinder is to use two existing electrodes; the spark plug tips [57], and a typical trace of data acquired by this method is shown in Figure 4.1, where the signal has been averaged over a number of engine cycles that were acquired with the firing plug. However, such averaging of signals is a compromise that might be considered unacceptable, depending on what level of performance is expected of the diagnostic tool.

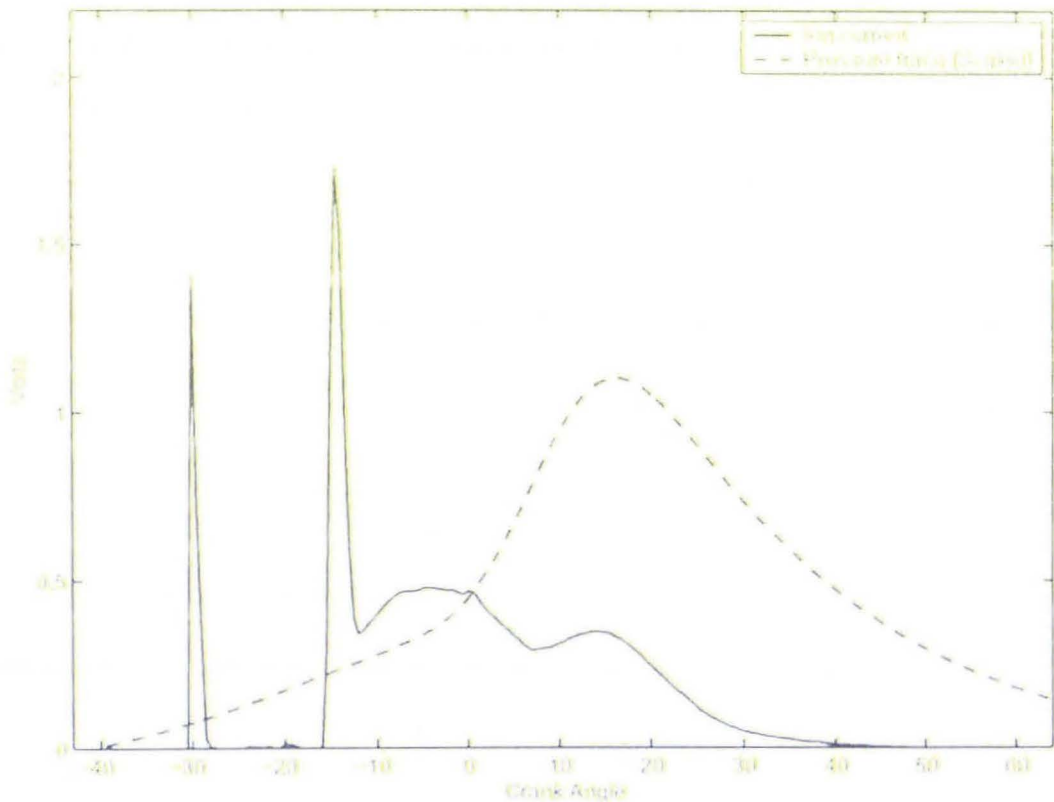


Figure 4.1: Typical ion-current signal (and pressure signal) recorded by a central plug [57]

It can be seen in Figure 4.1 that the ion-current signal can be generally divided into three

phases: the first phase consists of two sharp spikes located at 30 and 15 Crank Angle Degrees (CAD) before Top Dead Centre (BTDC). These are due to ignition and the measuring circuit ringing where the ion-current is measured most commonly from the low voltage side of the coil, and interference causes some spikes to appear in the ion-current signal. This problem also occurs even when the less common practice of measuring from the high voltage side of the coil is employed.

After the first two spikes, the second phase of the ion-current signal appears as a first hump at around 10 CAD BTDC. This is a result of the flame kernel development around the tips of the spark plug. The level of the ion-current within this region is generally high due to intense chemical reactivity in the vicinity of the tips.

After the establishment of the combustion kernel, flame propagation towards the rest of the mixture starts. The intensified heat energy release from the burning "flame ball" growing in the cylinder warms the burned gasses inside it and further increases their temperature. As a result, the internal energy of the burned gasses increases and the ion formation rate becomes strong in comparison to the ion recombination rate [57]. Overall, after a short period of decline due to the flame front moving away from the sensor, the ion signal starts to rise again due to energy addition from the surrounding burning mixture. This gives the second hump in the signal, and the third phase of the ion-current signal. As the piston moves away further from TDC, the volume of the combustion chamber increases and in-cylinder pressure and temperature of the burned gasses decline. The ion recombination rate increases, and the measured ion-current signal starts to decline. This third phase of the ion-current signal is a post-flame or thermal ionization induced signal [49, 53, 58, 77–79], and it is proportional to the cylinder pressure produced by combustion.

There are some inherent problems associated with using the spark plug as the ion-current sensor. In most engines there is one plug per cylinder which has to generate a spark as well as measure ion current. Because the spark generating voltage is substantially higher than the typical voltages

applied in the ion current measuring circuit, the latter has to be protected somehow. This has been accomplished for example by either measuring from the low voltage side of the ignition circuit or by switching the measuring circuit in and out of the high voltage side. Both these approaches complicate matters, the former because of increased noise and bandwidth filtering by the coils, the latter because of the intricacy of such a dedicated circuit. Furthermore, all approaches that measure ion current signals from the ignition spark plug suffer from the fact that no meaningful information can be gathered until the ignition circuit has been fully discharged. As a result, the initial stage of the combustion, which corresponds to the chemical phase of the ion current signal, cannot be recorded [51, 80].

The best signal is therefore derived from the thermal phase of the signal, but this second hump is not always very well pronounced thus making it a less than perfect feedback signal for engine diagnostic and control purposes. Moreover, cylinder pressures decrease as the engine load reduces, further reducing the signal strength of this second hump. Consequently, the diagnosable region of the engine loads are limited to a minimum of 75% of full load.

In order to address these issues, ion current sensing from dedicated sensors can be employed (remote sensing), introducing significant advantages. On the technical side, signal quality is greatly improved since data acquisition does not need to be interrupted. This continuous measurement allows for acquisition of ion current data throughout the combustion process. This allows for a much a greater volume of information to be extracted from the signal at higher signal to noise ratios. Since this signal potentially holds a lot of information to be extracted, sophisticated signal processing strategies need to be employed.

On the cost side, this approach offers the opportunity for simpler, more robust therefore more cost efficient designs for the measuring circuit, since there is no consideration of coupling with the ignition circuit to be taken into account.

Finally, signal quality is greatly improved using remote sensing, thus offering the potential for

true cycle to cycle engine diagnosis and control. Thus, the need for averaging is eliminated, which reduces computational and time requirements.

It might, at first, seem as a significant complication to introduce dedicated ion sensors on mass production engines. However, companies that already offer head gaskets with multiple ion collectors exist. This makes it modifications to the cylinder head and engine block unnecessary [81, 82].

4.1.2 Experimental Setup for SI Ion Current investigation

The engine used was a Renault research single cylinder 4-stroke research engine, full details of which are presented in Table 4.1. The engine featured variable compression ratio, variable ignition timing, variable air to fuel ratio and four access points in the cylinder head.

Table 4.1: Specification for engine used on SI ion current research

Bore	80 mm
Stroke	100 mm
Capacity	0.503 L
Inlet Valve Opening	12 CAD BTDC
Inlet Valve Closing	64 CAD ABDC
Exhaust Valve Opening	64 CAD BBDC
Exhaust Valve Closing	12 CAD ATDC
Compression Ratio	4.5:1 - 13:1
Ignition Timing	55 CAD BTDC - 20 CAD ATDC
Maximum Speed	4500 RPM
Maximum Power	16 bhp

Figure 4.2 shows the arrangement of the cylinder head and the spark plug locations. The firing

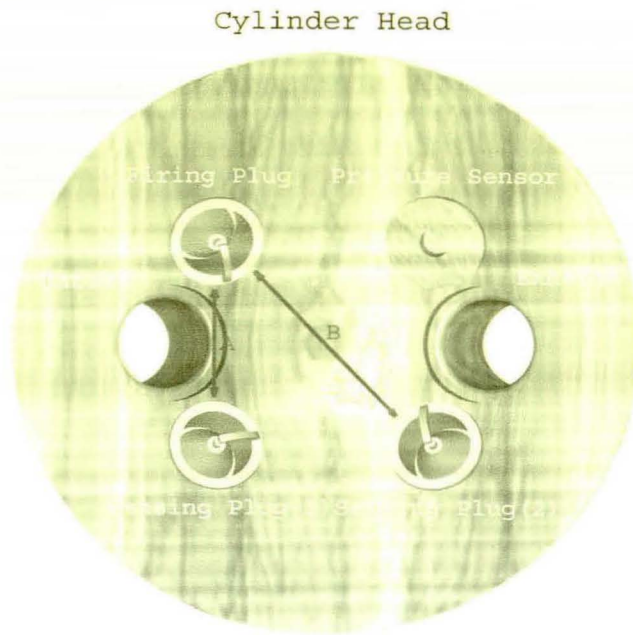


Figure 4.2: Cylinder head fitted with 1 spark plug and two remote ion sensors

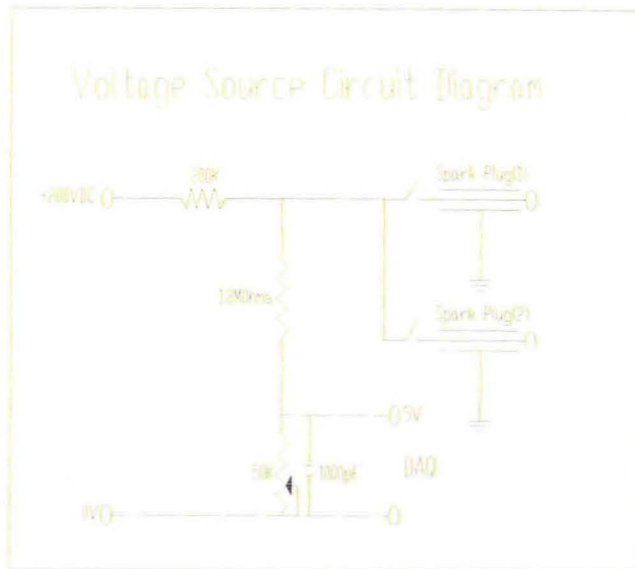


Figure 4.3: Circuit Diagram of DC Source

plug, which is located next to the inlet valve was used as the ignition source while one, or both, of the two remote sensing plugs were used as the ion-current sensing units. One was fitted on the

other side of the inlet valve opposite to the firing plug (sensing plug (1) in the diagram) whilst the other, (sensing plug (2)), was fitted next to the engine exhaust valve. The distance between sensing plug (1) and the firing plug was 42mm, and the distance between the sensing plug (2) and the firing plug was 55mm. The final access point was fitted with the pressure transducer.

A purpose built DC voltage source, (shown in figure 4.3), was used to power the measuring plugs. The output of the voltage divider was passed to a data acquisition board as the ion-current signal. The voltage divider would produce a voltage inversely proportional to the sensed ion-current (i.e. 5V for zero ion-current and 0V for infinite) to avoid the possibility of damage caused due to excessive voltage. The signal was inverted during the post processing phase. The data acquisition sampling rate was one sample per 2 CAD. Data were acquired using either a single sensing plug ((1) on figure 4.2) or both. When using both sensing plugs, these were connected in parallel, as shown in figure 4.3, which essentially results in the addition of the two ion-current signals.

Examples of Pressure and Ion Current logs using one or both sensors can be seen in Figure 4.4. Results obtained using both sensors contain more information, thus generally produce higher correlations. For this reason, the ion current research on SI combustion has focused solely upon twin ion current sensor data.

4.1.3 Signal Interpretation

The experimental data consists of two main signals. The first one is in-cylinder pressure, measured from the pressure transducer. The second one is the ion current signal as measured from the two measuring plugs. Both of these signals are sampled every 2 CAD. Figure 4.5 shows them together for a typical combustion event.

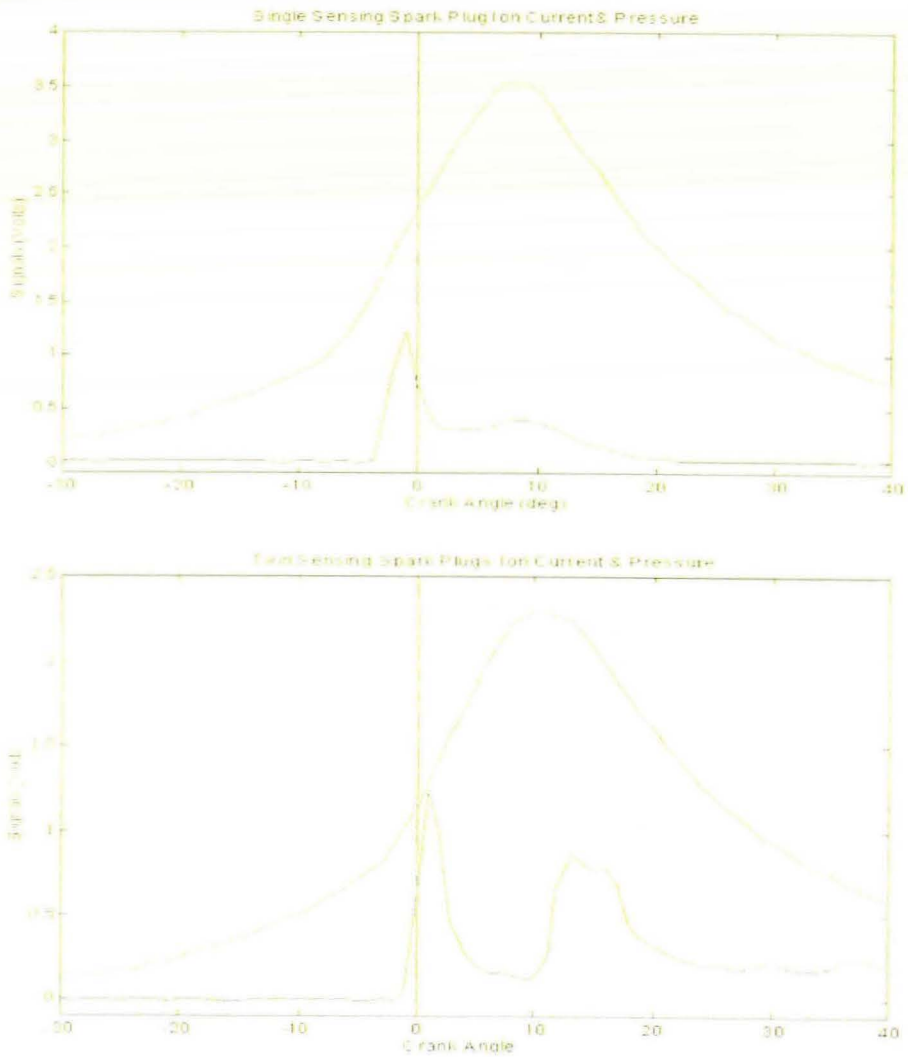


Figure 4.4: Pressure and ion current traces from single and twin sensor configurations

Measurants

In order to characterize the two signals, certain “measurants” have to be extracted that describe their features. This is done in the post processing phase of the signal manipulation and is carried out separately for pressure and ion current.

The pressure signal is the simplest of the two signals. In order to describe it numerically, four characteristics or measurants are extracted for every combustion event. Figure 4.6 shows a typical

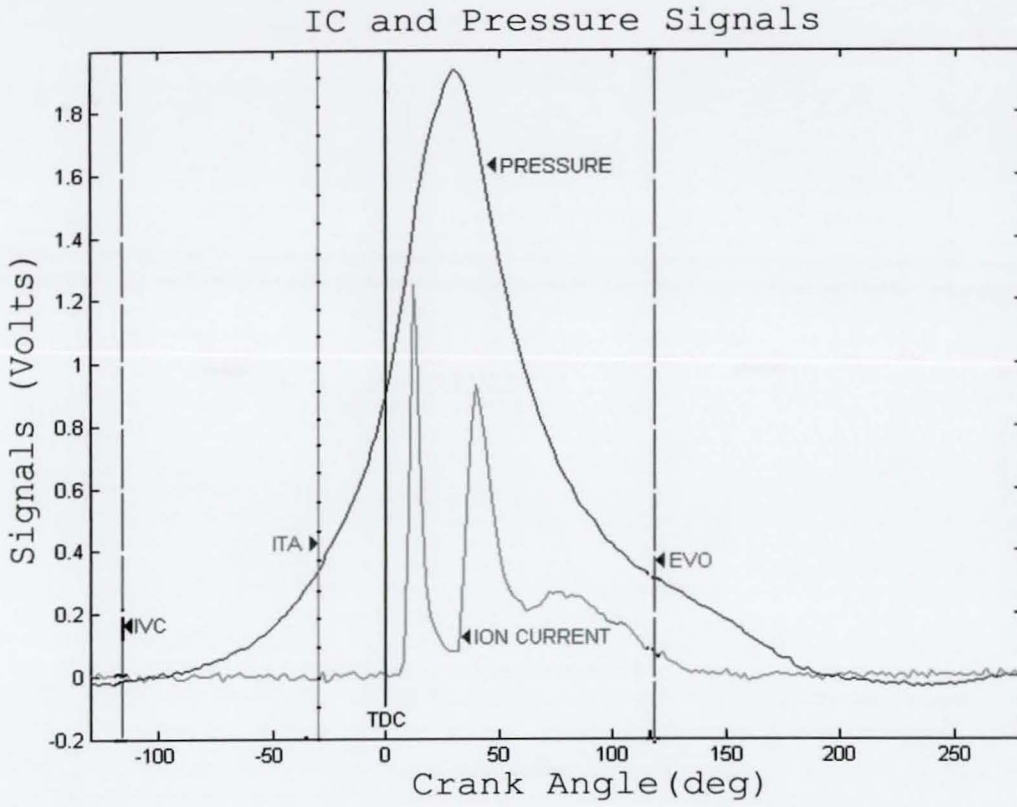


Figure 4.5: Typical pressure and ion current signals

pressure curve and associated measurants.

The measurants for the pressure curves are:

- The Peak Pressure Position (x-axis)
- The Peak Pressure Magnitude (y-axis)
- The width of the curve at half its height
- The area of the curve between IVC and EVO

The ion current is a more information rich signal. Because it is measured from two different plugs at different distances from the firing plug there are two distinct spikes. This is because

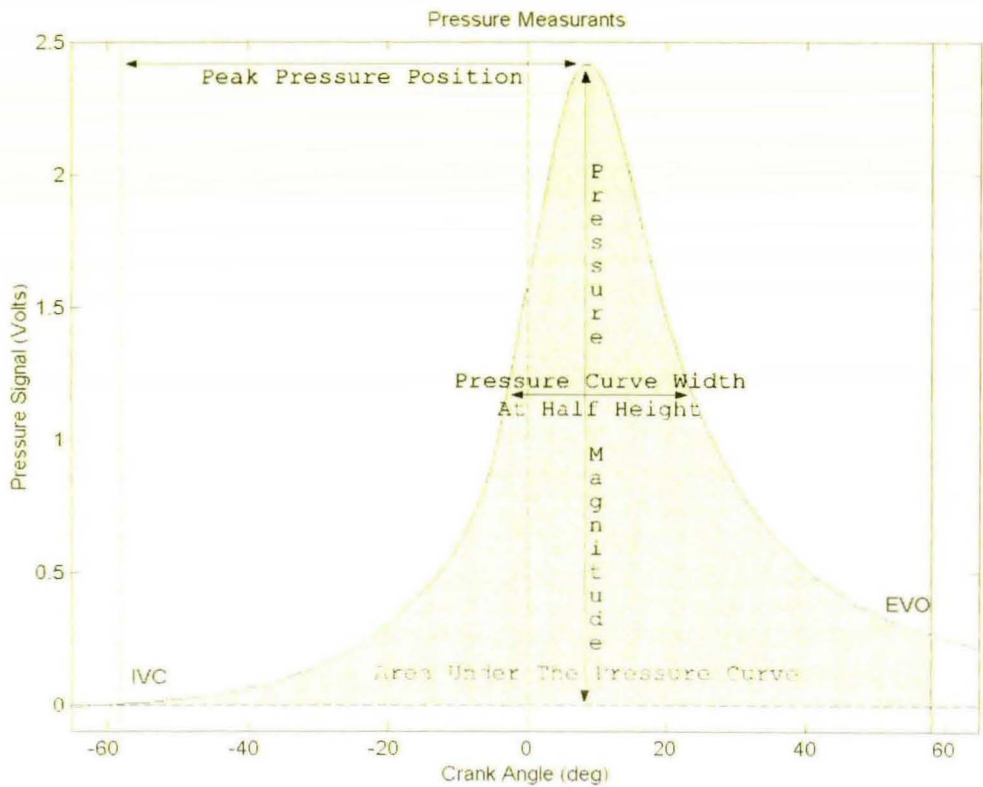


Figure 4.6: Typical pressure curve and associated measurants

the flame front will sweep through the measuring electrodes at slightly different times. After the second spike there is the hump associated with the post-flame phase.

One point to consider is how signals from two sensing plugs create a single trace. The circuit used simply adds up the two signals so what is seen is the sum of the ion current on both plugs. This would lead one to expect the second spike to be heavily affected by the post-flame phase, since both measuring plugs are registering at that time (whereas for the first spike, the flame has only reached the first plug), degrading its information content. This, however, is not the case. Figure 4.7 shows a close up of an ion current trace with only one measuring plug and the engine operating highly throttled so as to minimise the post flame hump. These are the conditions that create the most problems when measuring from the firing plug, as is the usual practice.

Hellring et al mention that the post flame peak essentially vanishes if the load is less than 20%

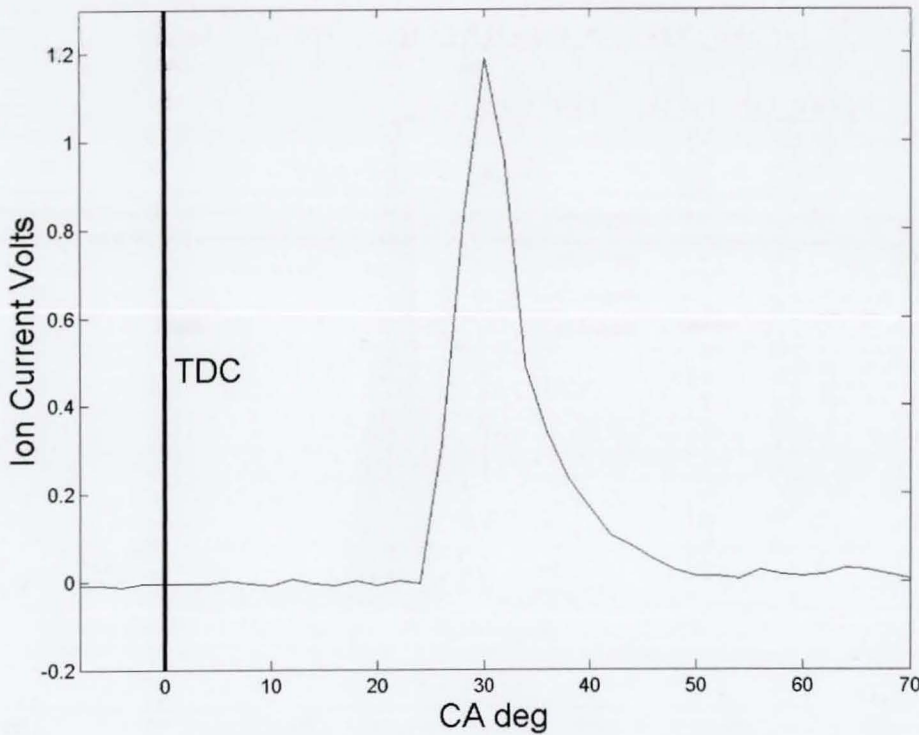


Figure 4.7: Single sensor trace

of the maximum load [58]. It is evident from Figures 4.4, 4.5 and 4.7 that the first spike only lasts for about 10 CA degrees. The post flame phase is either faint or missing completely since ionisation due to compression of the gases is low owing to the low load conditions. Employing remote sensing eliminates the dependence on the post flame signal. Employing two remote sensors adds further signal information.

The third phase (thermal, post-flame hump) is a less localised, lower magnitude event. Although the time window available for post flame signal acquisition is reduced when using the sum of the signal from the two sensors, the results obtained are superior.

As in the pressure curve, some measurants are needed to describe the ion current signal for a combustion event. In the case of ion current there are 13 such measurants. A typical ion current signal and its associated measurants is shown in Figure 4.8.

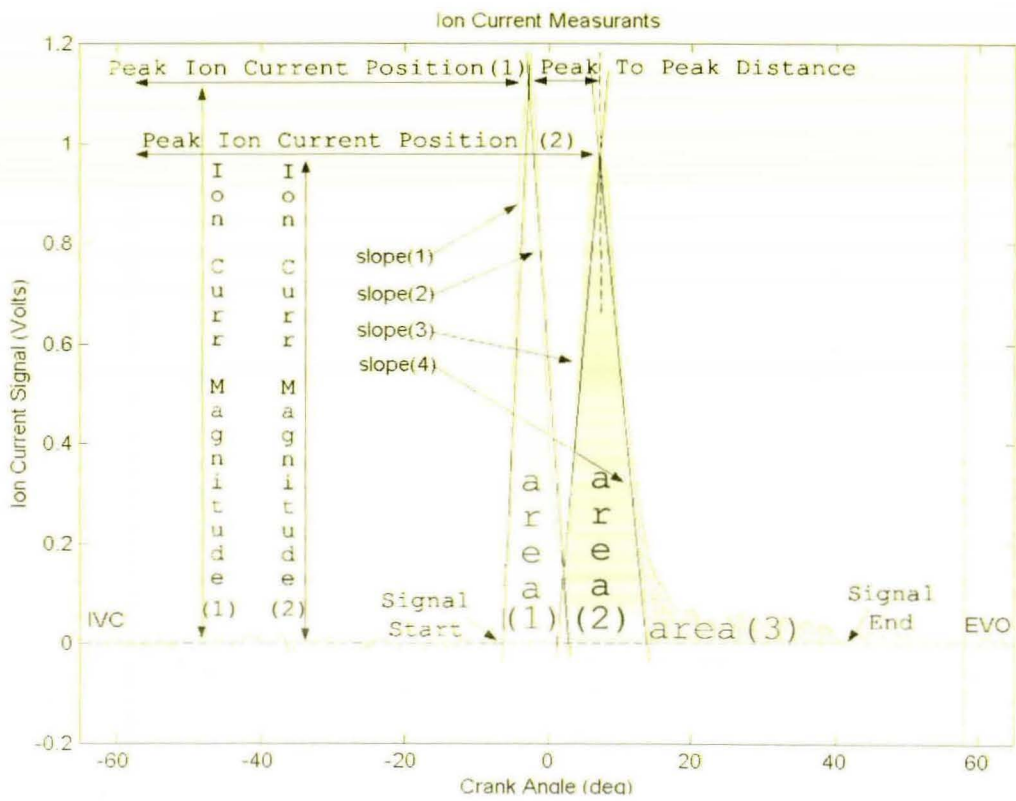


Figure 4.8: Typical Ion Current Signal and associated measurants

The measurants for the ion current signals are:

- The x-axis position of the start of the signal
- The x-axis position of the first spike
- The x-axis position of the second spike
- The magnitude of the first spike
- The magnitude of the second spike
- The slope of the curve between the signal start and the first spike peak
- The slope of the curve between the first spike peak and the minimum between the spikes
- The slope of the curve between the minimum between the spikes and the second spike peak

- The slope of the curve between the second spike peak and a point on the curve at the same x-axis distance as used for the previous slope
- The area under the first spike
- The area under the second spike
- The area under the post flame section
- The x-axis position of the end of the signal

After comparative tests, these measurants were chosen as carriers of adequate information to describe this signal. Of these, the various x-axis positions proved the most useful, since they are related to flame development. However, all selected measurants contribute in increasing the accuracy of the results.

Feature Relations

Given the measurants extracted, the easiest way to look for relations is to plot them against each other. Ideally, a strong relation between an ion current measurant and one or more pressure measurants will settle the case in favour of ion current. However, things are not that simple. There are conclusions to be drawn by averaging over a number of cycles which is the technique used routinely in treating such signals. These however are not helpful when it comes to developing a tool which should, in practice, be able to help control cycle-to-cycle engine operation.

Figures 4.9 to 4.11 show some cases of strongly related measurants. Ion Current measurants are on the x-axis, pressure measurants are on the y-axis. These data have been logged over a varying compression ratio loop, therefore each data point batch corresponds to a compression ratio between 4.5:1 and 11.2:1 as described in the figures' legends.

Figures 4.9 and 4.10 are matches for the Peak Pressure Position (PPP) with the positions of the first and second ion current spikes respectively. It shows good correlation with both measurants

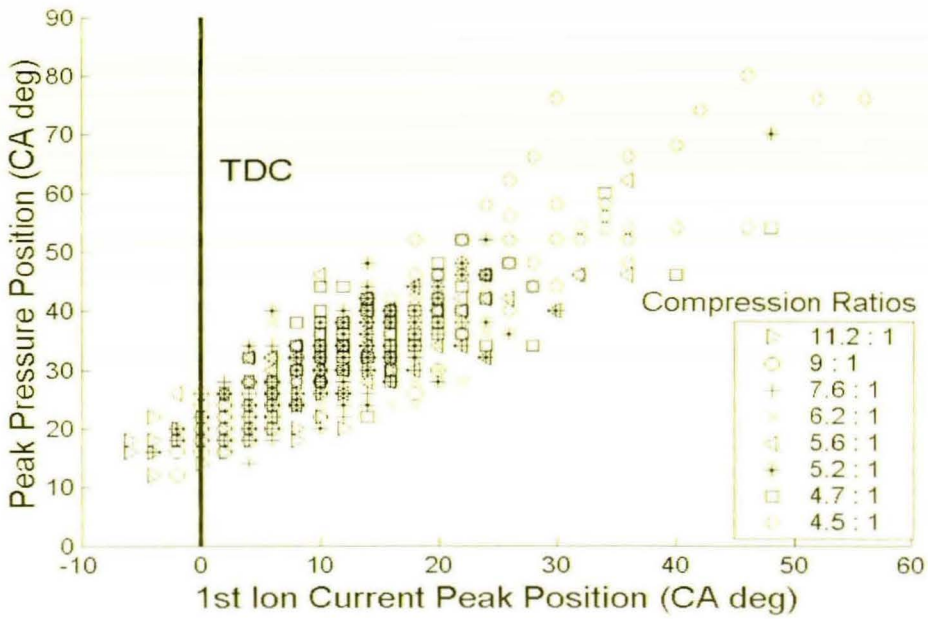


Figure 4.9: Relationship between 1st ion current peak position and peak cylinder pressure position

and that a delayed combustion event results in a late pressure peak position. Another point to notice is that delayed combustion results in a greater uncertainty in PPP. This is due to delayed combustion being more unstable, resulting in a higher cycle-to-cycle variation.

Figure 4.11 is a match between peak pressure magnitude and the position of the second ion current spike. It can be seen that the second peak ion current position has a strong relationship with the peak cylinder pressure magnitude, too. When the second ion current spike occurs late, the flame reaches the second sensing plug late which indicates late combustion. Therefore the peak cylinder pressure magnitude is reduced.

Although the relationships between the first and second ion current spikes with the combustion event are strong, as can be seen in figures 4.9 to 4.11, there is an uncertainty of the order of 10 CA degrees relating to the peak pressure position and of the order of 0.4 Volts relating to the peak pressure magnitude. These uncertainties are too large to be acceptable for an engineering implementation of ion current use as an alternative means of measuring cylinder pressure. For

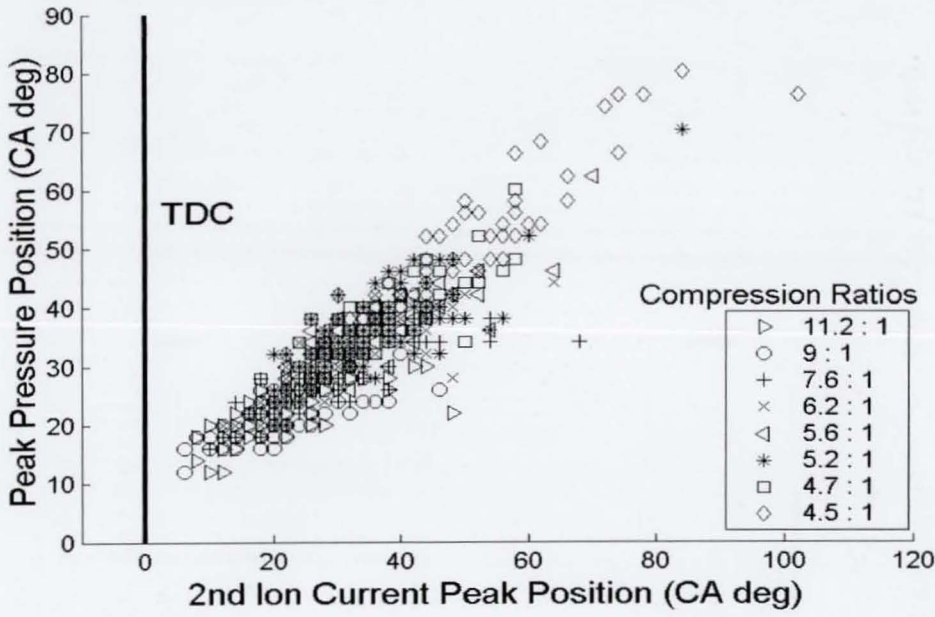


Figure 4.10: Relationship between 2nd ion current peak position and peak cylinder pressure position

this reason, a more sophisticated strategy has to be developed and employed for ion current signal interpretation in order to improve its correlation with the pressure signal.

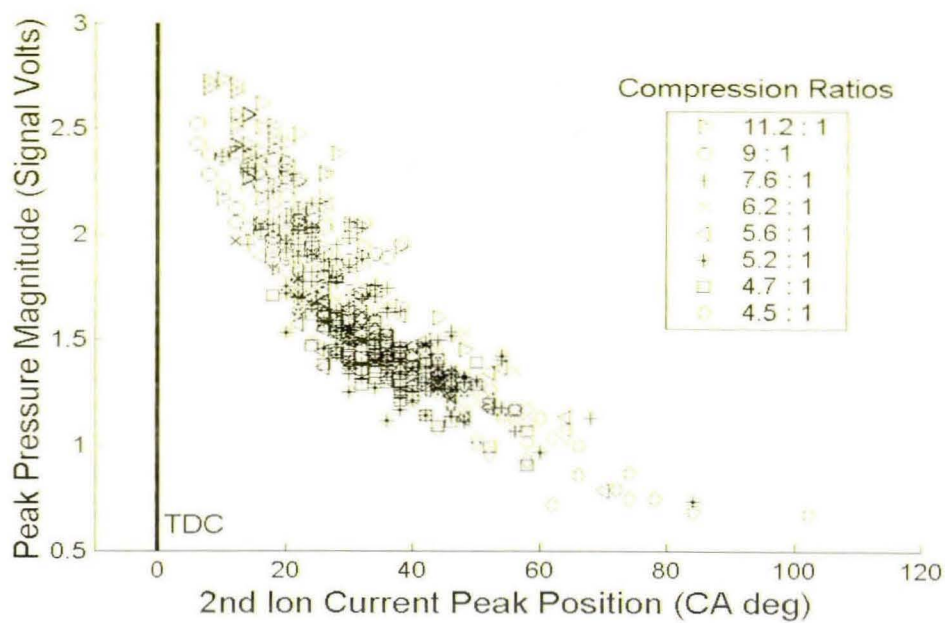


Figure 4.11: Relationship between 2nd ion current peak position and peak cylinder pressure

4.1.4 Pressure Measurant Prediction

Artificial Neural Networks

ANN(s) are a good candidate for tackling this kind of problem [44,53,54]. These are computational constructs, used in a variety of applications for dealing with complicated inputs. The notion behind them is loosely modeled on biological neural networks. Each artificial neuron is a node that takes a number of inputs. These are weighed and then summed as illustrated on the left hand side of Figure 4.12.

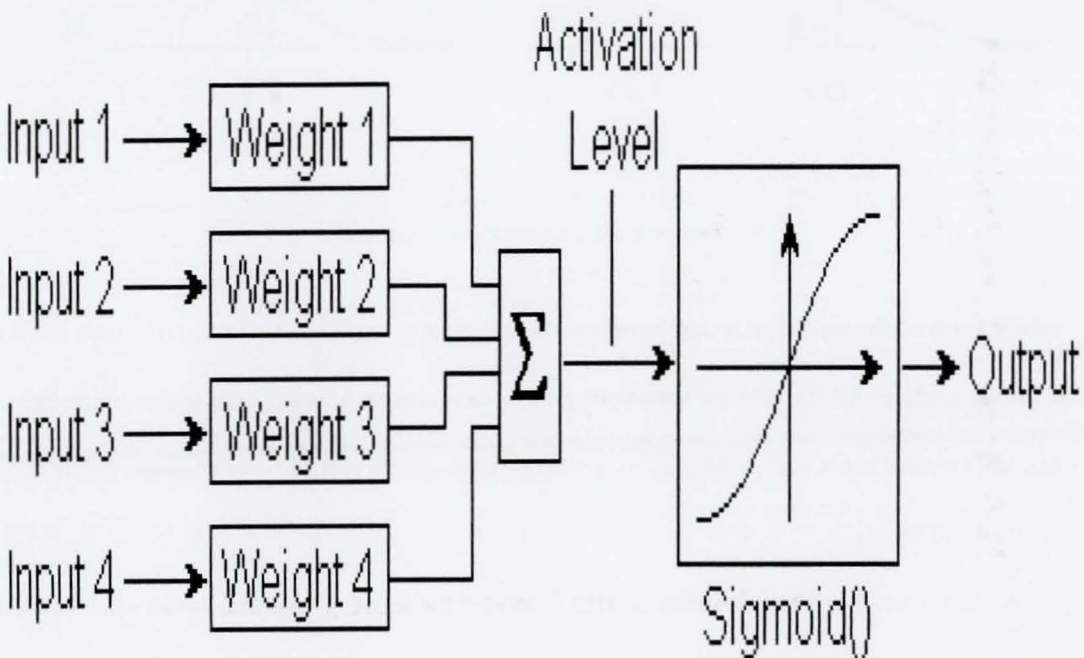


Figure 4.12: Schematic representation of an artificial neuron

The idea is to map inputs to outputs through a set of weights. This way, an input strongly affecting the output will have a relatively big weight associated with it. Thus, fluctuations in important inputs will result in significant changes to the weighted sum.

Finally, this weighed sum is passed through a transfer function to give the final output. There are various traditionally used transfer functions, some of which are shown in Figure 4.13.

The role of the transfer function is to "summarize" the inputs of the neuron into a value. The

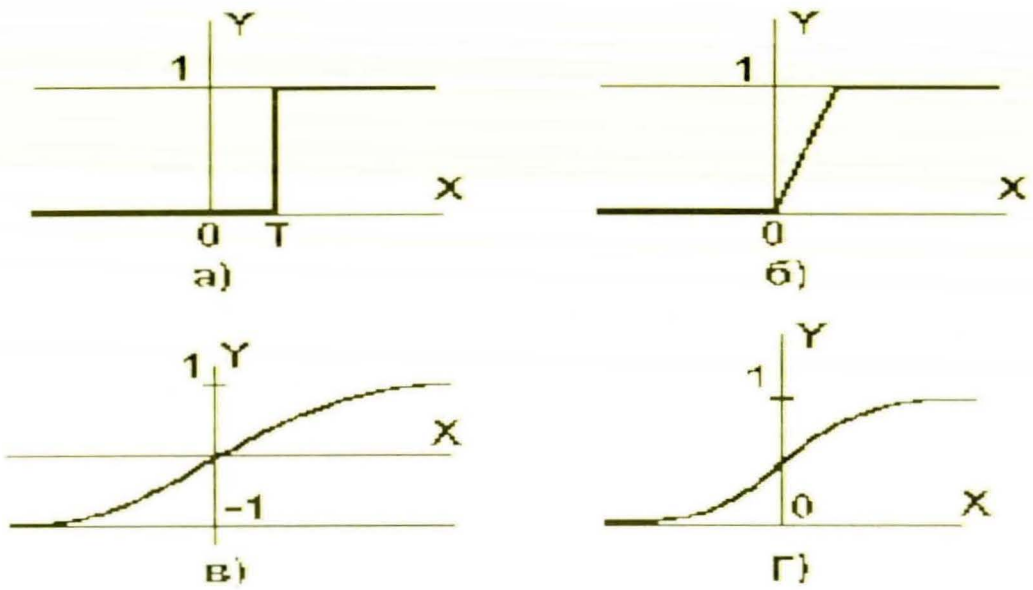


Figure 4.13: Sample transfer functions

simple form of the top left is a step function which basically translates to on and off states for the artificial neuron. All the rest are variations on the same theme, making a smoother transition so that information is not lost in the grey area where the weighted sum does not translate clearly into the on or off areas.

A collection of artificial neurons is what is termed the artificial neural network as illustrated in Figure 4.14. The inputs are taken in by the input layer of artificial neurons. These are then processed through successive layers until they reach the final “output” layer.

The main tasks when choosing an artificial neural network is to decide upon the architecture best suited for the task, e.g. number of layers and type of transfer functions and then tune its parameters, e.g. the various weights. There are many different types of training algorithms for this task. Very common are recursive algorithms where a network is presented with successive sets of inputs, small alterations are made each time according to its response compared to the desired values until at some point tuning is decided to be adequate for the task.

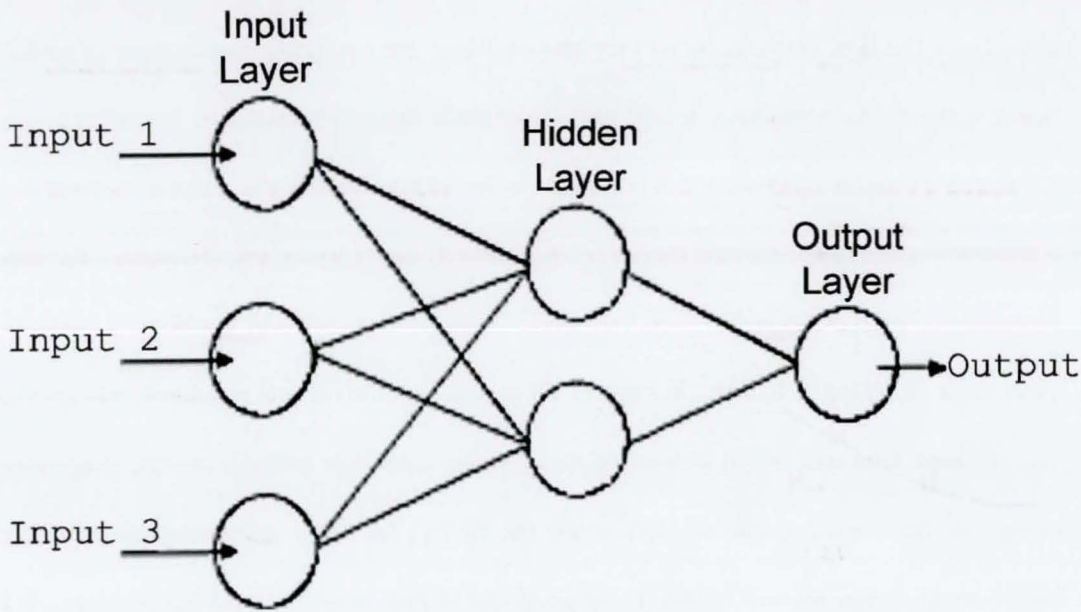


Figure 4.14: Sample transfer functions

In the case of this research, the following considerations have been taken into account:

First, the network has to be as uncomplicated as possible. If the model is to be usable on a cycle to cycle basis by an engine controller, all computations have to be completed fast enough to provide timely results for the next cycle for every cylinder. The simpler the network that does this, the less demand there is on the signal processing electronics that will carry out those computations.

Second, the network or some further algorithm behind it must produce continuous output. This is important as the measurants are numbers that cannot be represented by an on/off state. To code for such using step transfer functions requires a large amount of output artificial neurons for each output.

Third, the network must be easy to train with a reasonably small amount of data. In engineering applications, it is impractical to require a vast amount of data to train a neural network due to the cost and time needed to collect these. The goal was to use as low as 70 combustion events per engine operating condition.

There are several network families to choose from. Keeping the above points in mind, ADAP-tive LINear Element(s) (ADALINE(s)) were chosen. These are among the classic types of artificial neural network. An ADALINE(s) neuron takes a weighted sum of its inputs but, instead of passing it through a transfer function, sends it straight to its output. This is also helpful for producing continuous output since a single output artificial neuron can produce any real value. The main limitation of ADALINE(s) is that they will tackle linear relations but will not be very useful beyond these. Looking at the data in Figures 4.9 to 4.11, both linear and non linear relationships are indicated. However, the window of engine operating conditions tested is strongly exaggerated compared with normal operation. Despite this and the fact that linear approximations were used, the obtained results are well within the scope of closed loop engine control implementation. In addition, the range of operating conditions spanned by a production engine is such that the data produced would be in relations even more adequately modeled as linear.

Finally, for training purposes, ADALINE(s) can be trained using the Least Mean Square (LMS) algorithm. This is a very important consideration given the low data volume requirement. The strength of the LMS algorithm lies in that it competently handles this case where the data is limited. The way LMS trains the network is as follows: given a set of inputs and a set of desired outputs, the error is defined as the difference between the actual and the desired output. LMS minimizes the average of the sum of the square of these errors. Since this is a quadratic function, it will have one minimum. Thus, for a given set of inputs, LMS will *always* tune the network so that their averaged squared errors are minimized. This is in contrast to recursive training algorithms where no guarantee of “best” training is provided and the end of the training is usually signalled once the error drops below a predetermined level.

In this research, two sets of networks have been developed and tested. To test these, some data sets were set aside and used afterwards to assess performance under unknown inputs.

Measurant Predicting Network

The first network is the smallest one in terms of artificial neurons. It is a layer of four artificial neurons (ADALINE(s) are single layer networks), each one of which takes the thirteen ion current measurants as inputs and produces one of the predicted pressure measurants as an output. Each input is multiplied by a weight factor and all weighted inputs are then summed up into what becomes the output.

Figure 4.15 shows the network architecture. The 13 ion current measurants are the set of circles at top left. The set under them, labelled Conditions is a string of numbers (constant for each input file) that describes the operating conditions of the engine at the time. These conditions are: throttle position, engine speed, engine load, air to fuel ratio, ignition timing advance, and compression ratio.

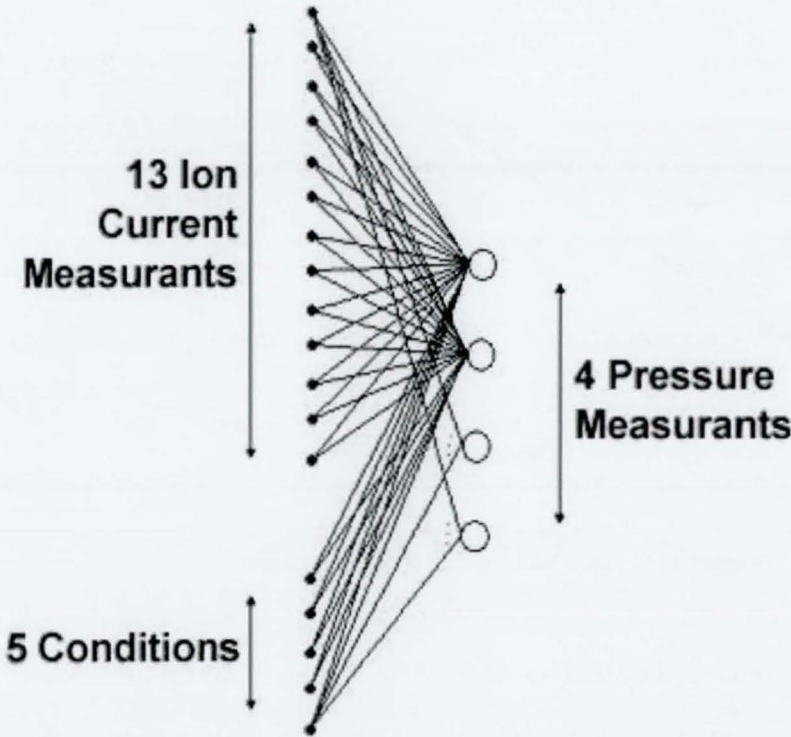


Figure 4.15: Schematic representation of the measurant predicting network

Training is done as follows. When data was logged, one of the aforementioned operating conditions was varied and a number of files logged for various values of that condition with everything else kept the same. This created “families” of files, e.g. the Compression Ratio family, the ignition timing family etc. Of these families, one member is selected to be the test set, the set of values to be shown to the network after training to test performance. The rest of the family is then used to train the network. Thus, when testing the network, it is given values not encountered during its training. By choosing the test set to be somewhere in the “middle” of the variable condition range, the network arrives at the correct results since these lie within its training window. The results of this process can be seen in Figures 4.16 to 4.19.

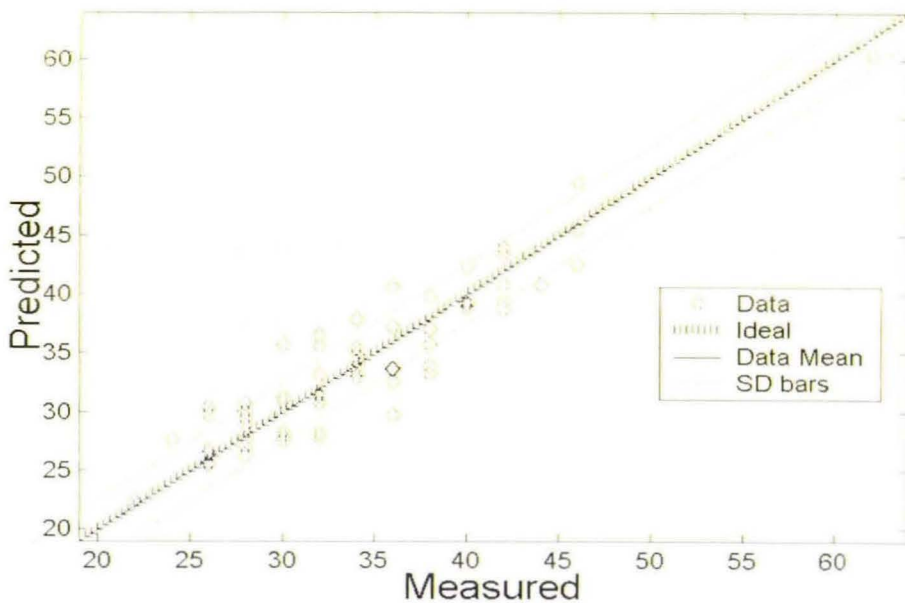


Figure 4.16: Predictions for Peak Pressure Position

The entries on the x-axis are the measured values of the measurant, and the entries on the y-axis are the predicted ones. Thus, a perfect prediction would plot a diagonal line. This is the ideal line mentioned in the legend and is used for reference. The solid line indicates the data mean. It often coincides to a great extent with the ideal line, which indicates a good match between

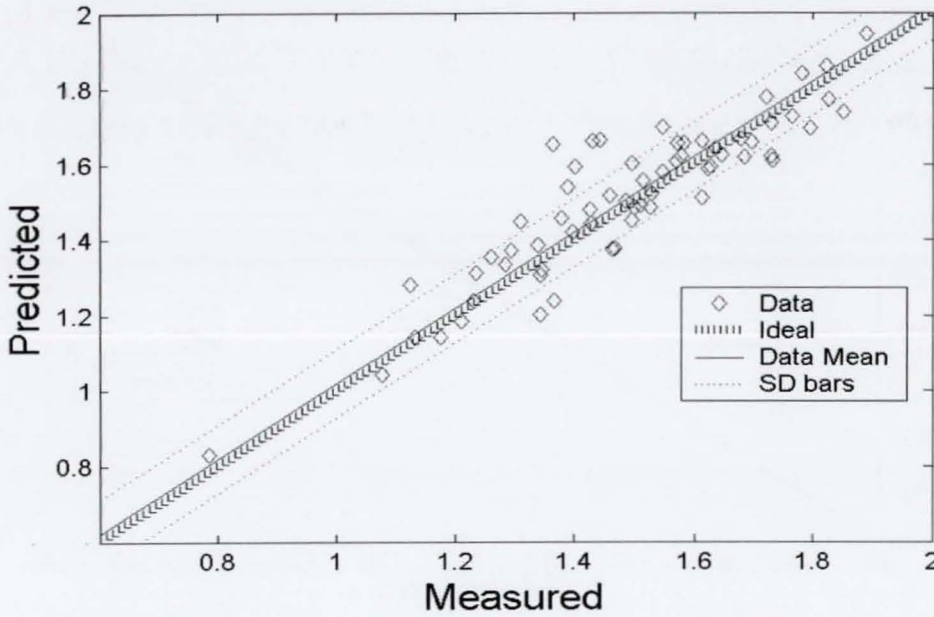


Figure 4.17: Predictions for Peak Pressure Magnitude

measurements and predictions. The two outer dotted lines indicate the standard deviation of the data. In these four figures, the network performs so well that the mean of the predictions and the diagonal are almost identical. The only figure in which they can be seen separately is figure 4.17.

Of the four outputs of the network, the most important are the Peak Pressure Position and Peak Pressure Magnitude which give the x and y coordinates respectively of the pressure curve's peak. Figure 4.16 shows the predictions for Peak Pressure Position. The mean of the predicted values is shifted by 0.062 CAD from the mean of the actual values and the standard deviation of the predictions is 2.55 CAD. A similar degree of accuracy was obtained for the rest of the in cylinder pressure measurant predictions. Given that the ion current signal is sampled every two CA degrees, this result is satisfactory.

The predictions in these figures are calculated from a mixed training set. The families used are the Compression Ratio family with varying compression ratios and the Speed and Load family with varying speed and load. The compression ratios for the first family were 11.2:1, 7.6:1, 6.2:1,

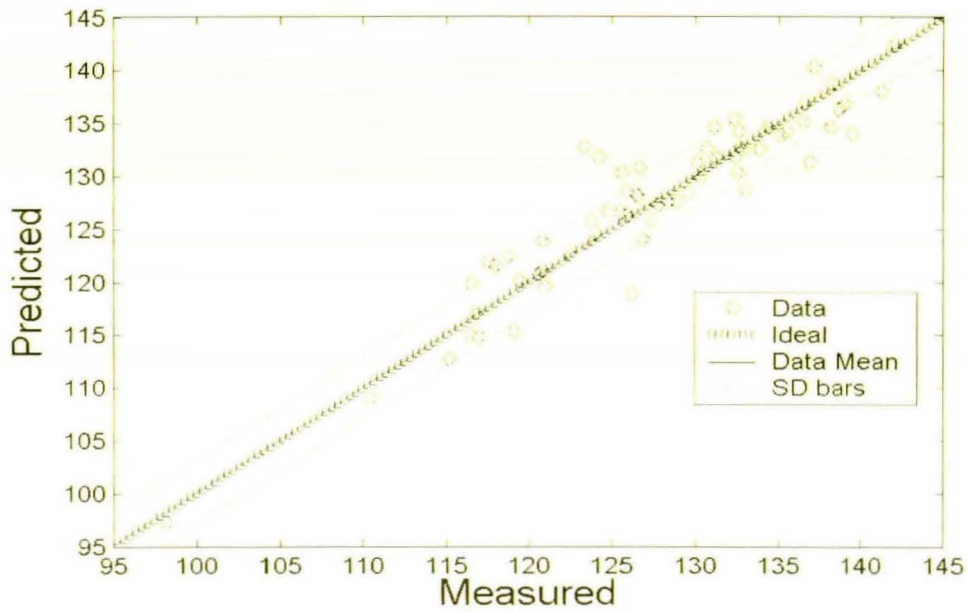


Figure 4.18: Predictions for Pressure Curve Area

5.2:1, 4.7:1 and 4.5:1. The speed/load settings for the second family are 33% at 1400rpm, 75% at 1400rpm, Wide Open Throttle at 1400rpm, 33% at 1750rpm and 75% at 1700 rpm. The test set is a member of the Compression ratio family with a compression ratio of 5.6:1. Ignition timing for these was kept constant at 30 CAD BTDC.

What is worth pointing out is that the network gives better results when the families are mixed together than when the training is done on each individual family. This is a satisfactory result, demonstrating how the network can interpolate and select the right predictions for the test set, the operating conditions for which it hasn't encountered at all during training.

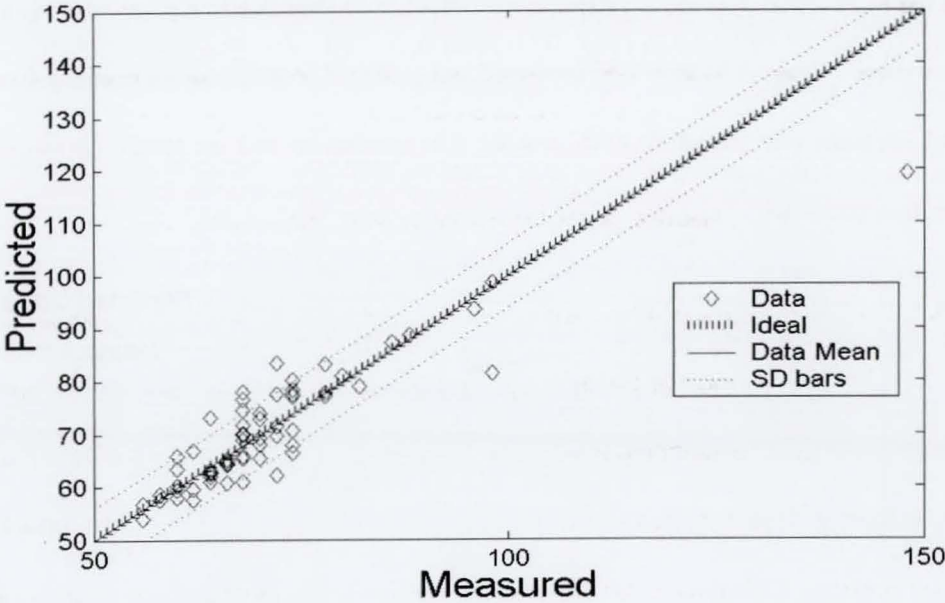


Figure 4.19: Predictions for Pressure Curve Width

Curve Predicting Network

Given the satisfactory performance of the simple ADALINE(s) in tackling the thirteen-input by four-output measurant predictions, a new network was tested predicting the whole pressure curve. Again an ADALINE(s) was used, but this time with the whole ion current signal as the input and the whole pressure signal as the output. More specifically, each cycle is examined between IVC and EVO. Given the sampling rate and the valve timing, this gives a data string of 117 elements for both ion current and pressure. Thus the network consists of 117 artificial neurons, each of which is connected to all inputs and which produces one output, corresponding to a point on the predicted pressure curve. Figure 4.20 shows the measured and predicted pressure curves resulting from this network averaged over the whole of the test set. The training set and test set are the same as for the previous network.

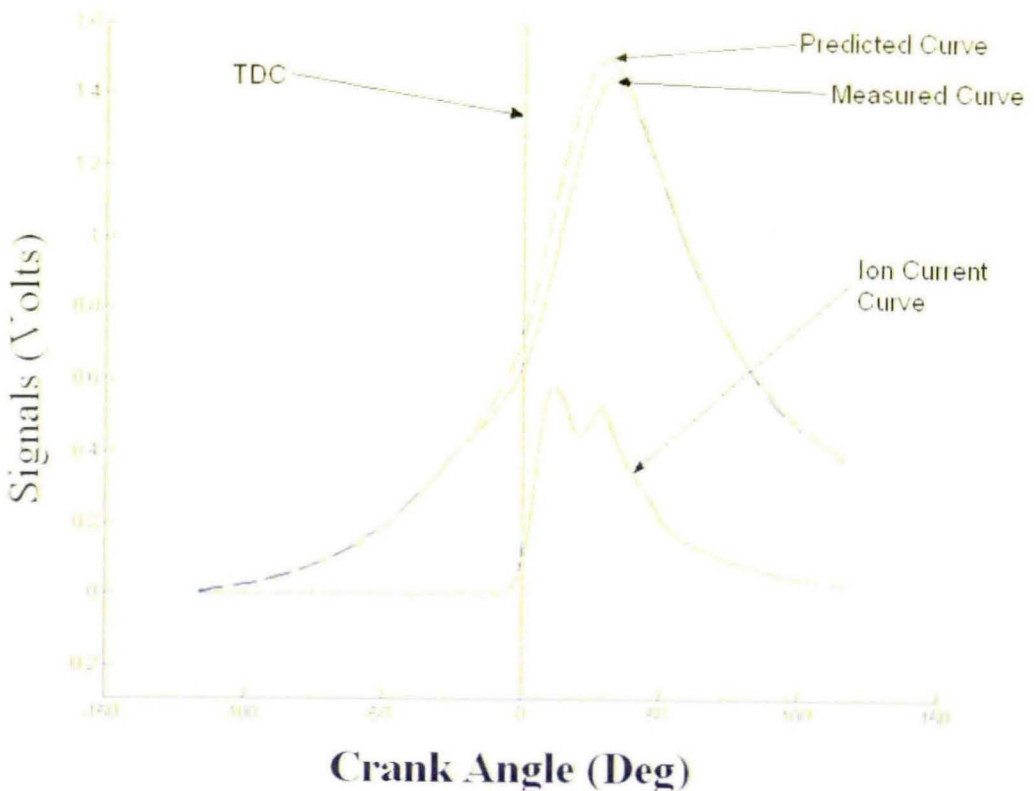


Figure 4.20: Averaged actual and predicted pressure curves

The averaged ADALINE(s) derived curve follows the target quite closely even though the compression ratio of the test data has never been encountered in its training. However, the measurants extracted from the predicted curves are not as good as for the previous network. Figure 4.21 shows the actual and predicted values for the Peak Pressure Position. The mean of the predicted values is shifted by 1.69 CAD (compared to 0.062 for the previous network) and the standard deviation is 5.45 CAD (compared to 2.55 for the previous network).

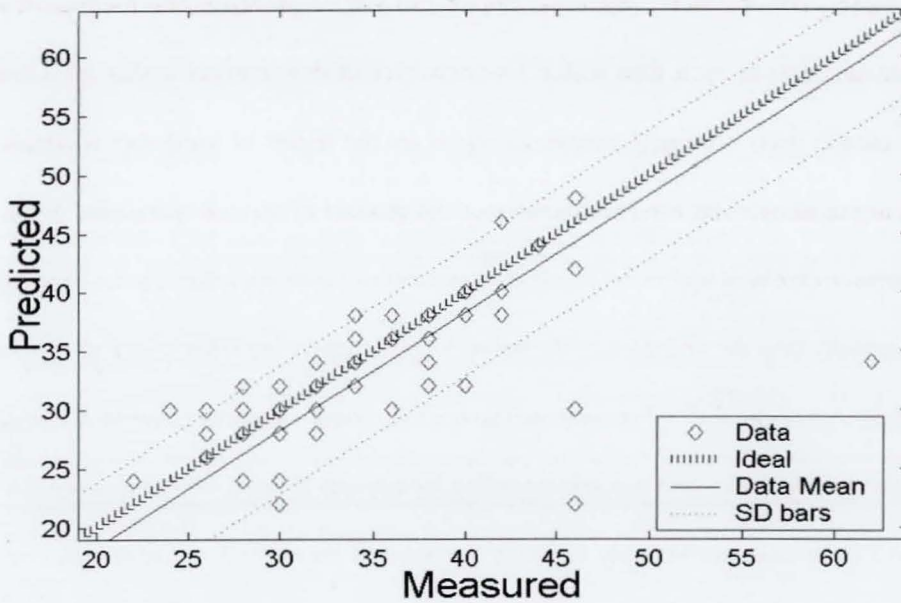


Figure 4.21: Predictions for Peak Pressure Position

Similar results are true for the rest of the measurants, with uncertainty increasing roughly twofold compared to the previous network.

This network is created with the task of matching the curve point to point. The objective of training the network is to minimise the average difference between the actual and predicted curves, which may result in that the error between the predicted and actual in-cylinder Pressure Peak Position is not minimum. Since, matching PPP, or any other pressure measurant, is not a prime priority, performance in this respect drops.

4.1.5 Summary of ion current use in SI combustion

The results presented here show how ion current data can be treated using simple techniques to predict various features of the in-cylinder pressure. Of two networks presented, the most likely to be suitable for the task of engine control is the one performing measurant prediction. This is by far the cheapest computationally and is specialised in predicting the most important aspect of the pressure curve, the location of its peak. This should be a welcome result for the further development of engine control systems striving to employ fast and simple algorithms for changing engine parameters on cycle-to-cycle time scales. One drawback of this approach is that, even though the network used is itself extremely simple, its inputs are the results of some data processing since the ion current measurants used are themselves the product of various operations. Even though these operations are well within the capabilities of modern electronics, they can be more expensive computationally than the operation of the network itself (depending what degree of sophistication is required), something that will have to be taken into account when designing such a system.

Another point to take into account regarding measurants is the y-axis data of the ion current signal. All the measurants strongly affecting the pressure curve results were the ones on the ion current signal x-axis, in other words related to the timing, not the magnitude, of the ion current events. Figure 4.5 shows an ion current signal. What has to be noticed is the sharp slopes leading up to the two peaks. In some cases, there could be 2-4 data points from bottom to top of the ion current spike. Therefore, the ion current signal might contain frequencies which are too high for the sampling rate employed in this part of the experiments. This might be an additional factor in that ion current magnitudes never showed any strong relation to any pressure measurants in the measurant to measurant plots.

The ADALINE(s) employed in this research manage their predictions based mostly on x-axis ion current measurants. It might be possible that higher sampling rates can improve the results further as the significance of y-axis ion current measurants will be taken into account. However,

other researchers [80] have pointed out that large cyclic fluctuations are a typical problem with ion current measurements anyway. Thus, by not relying on ion current magnitude but rather on ion current timing (made easy by measuring from the remote plugs) this problem can be avoided to some extent. This point gains significance when considering that fuel additives affect mainly the amplitude and not the shape of the ion signal curve [59]. Hence, relying upon x-axis measurants tackles this potential problem as well.

Apart from the most important position of the peak of the pressure curve an ADALINE(s) has been found to be able to tackle quite competently the task of predicting the pressure curve itself. Normally, such tasks are best left to more specialised (and more computationally expensive) ANN(s) tools like radial basis functions. An important point to consider in this second network is that the input is passed to it "raw" as it were, with no need for preprocessing to extract ion current measurants. There is a cost to pay at the output as pressure measurants are extracted from it couple with higher memory costs in order to parse the whole curve but the pressure measurant extraction is a much simpler task as there are only 4 measurants involved in the pressure curve as opposed to 13 in the ion current signal. However, this network is not as effective in locating the peak of the pressure curve.

It might seem to be a logical step to design an ADALINE(s) accepting a "raw" ion current signal and producing pressure curve measurants as output. Variations on this has been tried with poor results. Evidently, such a task is beyond the limits of the performance of the ADALINE(s).

Finally, not all data are necessarily in linear relations. Modified networks have been tried to see if performance can be improved by passing the inputs through a function, thus making the curve resemble a more linear form. The most important measurants, Peak Pressure Position and Magnitude, sometimes improved by as little as 2-3%. This is not a particularly strong case for adding computational cost to the system. It seems that, given the uncertainty in the data and the short segment of curve in question, a linear approximation is best suited for dealing with it.

4.2 Ion Current as a diagnostic tool in HCCI operation

The promising results obtained through use of ion current and ANN(s) during the SI experiments have led to implementing similar techniques during the HCCI experimentation. Again, on the hardware side, the design philosophy has been use of a dedicated remote sensor. The experimental setup for these experiments is described in Section 3.1.

The design criteria for the remaining issues have been the following:

On the software side, the algorithm must be implemented on a cycle to cycle basis with no averaging involved. The next consideration are the algorithms themselves. The use of the ADALINE(s) type of ANN(s) has been quite successful in SI operation, so it is a candidate as it is a very lightweight, robust ANN(s) despite it being uncomplicated.

It must be noted that a widely used ANN(s) for this kind of task is the Multi-Layer Perceptron (MLP) [57]. However, the MLP training rules do not have an unambiguous termination criterion, unlike the LMS algorithm employed in ADALINE(s). Hence, MLP design has been avoided and focus been given on the capabilities of ANN(s) employing unambiguous learning rules. Using ADALINE(s) as a starting point, the use of Generalised Regression Neural Network(s) (GRNN(s)) has also been explored. The advantages of both ADALINE(s) and GRNN(s) lies in the relative simplicity of their architecture, which offers little room for ambiguity over the optimum design. GRNN(s) are very similar to Radial Basis Function(s) (RBF(s)). For the data used in this research, GRNN(s) generally outperformed RBF(s) so were chosen instead.

The final consideration is the choice of preprocessing techniques. A classic approach is to use signal processing algorithms in order to extract the various characteristic measurants from the ion current signal to be used as input to the ANN(s). To this end, the possible use of wavelet algorithms has been evaluated. Wavelets are a signal processing tool that is being used in a variety of applications [83], ion current signal processing being an ideal candidate [59]. An interesting advantage of wavelets is that the treated signal can be reduced in size, thus making the use of the

wavelet output directly into the ANN(s) a possibility. This approach has also been investigated.

4.2.1 Ion Current Signal and Treatment in HCCI

The ion current signal in both SI and HCCI is usually in the form of a sharp spike, sometimes followed by a hump (figure 4.22). The spike is associated with flame in the vicinity of the sensor (chemical ionisation). It is the most obvious feature of the signal and is always present if combustion occurs in the chamber. The hump is associated with the increased temperatures and pressures following the combustion (thermal ionisation) and is hence a good indicator of PPP. However, because of the need for increased temperatures and pressures, it is most prominent in high load SI as discussed in 4.1. In the lower loads and temperatures associated with HCCI operation, this feature is greatly suppressed. Since this part of the experiments is concerned with HCCI combustion, where this feature is hardly noticeable as seen in the figure, only the initial spike needs to be considered. For this initial spike to be properly recorded under all conditions a dedicated circuit is needed for all the reasons discussed in 4.1.

The treatment of the signal requires certain operations to be performed upon it in order to extract certain characteristic measurants that will be used in order to quantify its features. This process is, in effect, a compression of the information contained in the signal into a small number of key variables. This has the advantage that, in the first instance, they can be directly investigated for correlation to corresponding measurants of the pressure trace (e.g. peak pressure position) and also that these can be used as a much reduced data source when using further algorithms, e.g. ANN(s).

4.2.2 Ion Current Measurant Extraction

Because of the single probe and lack of thermal phase, the HCCI ion current signal is much simpler than in the SI case previously described. The breakdown of the measurants extracted from the ion

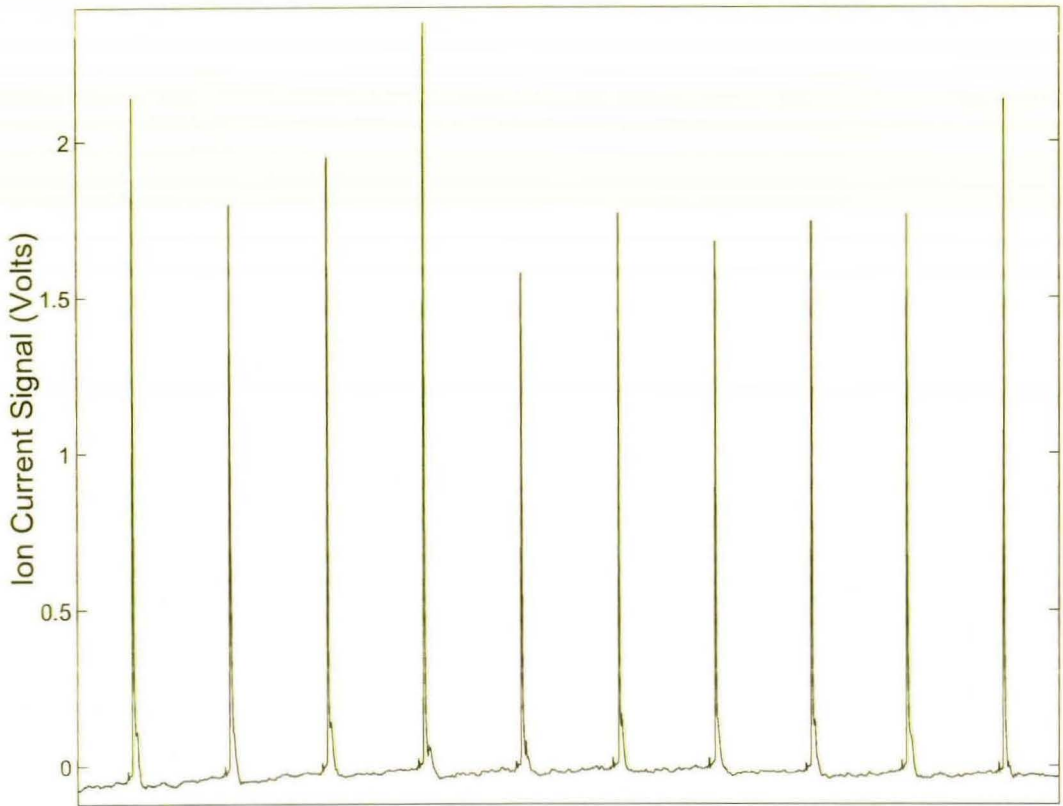


Figure 4.22: Typical HCCI ion current signal

current signal are shown in figure 4.23.

These are:

1. The start of the signal
2. The slope of the signal
3. The maximum of the signal
4. The position of the maximum of the signal

The easiest to extract and one of the most information rich is position and magnitude of the spike's peak, which is simply extracted by means of a maximum search. The SI case has shown that the timing of this is a good approximate indicator of combustion timing, having a strong relation with pressure measurants such as PPP.

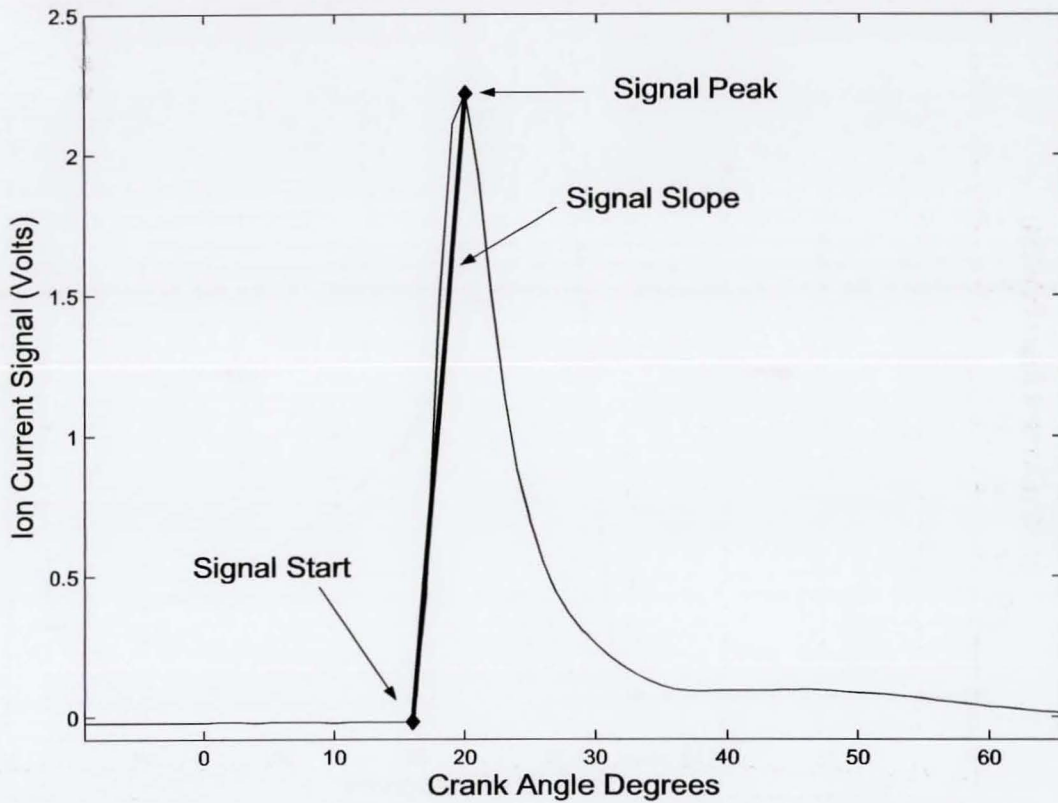


Figure 4.23: The ion current measurants

Another important ion current measurant is the position of the start of the signal. Coupled with the coordinates of the peak, it can lead to an estimation of the slope of the spike. Previous research on SI operation has established a correlation between this slope and AFR [43,45,54]. In HCCI, this effect is further complicated by the presence of TRG but still, slope information can be a valuable tool. Thus, in order to acquire it, an estimation of the start of the signal is required.

While the spike's peak is very straightforward to extract, its start can be more problematic. This is mainly because the base of the ion current signal can be a very noisy region. Added to that, is the fact that, because HCCI combustion is very sudden compared to SI, the spike can rise in a very short time, typical values can be as low as 3 data points (data is sampled every 1 degree CAD) as is demonstrated in figure 4.24. Hence, an uncertainty of even one or two degrees can have a big effect on the final value for the spike rise duration and hence the slope.

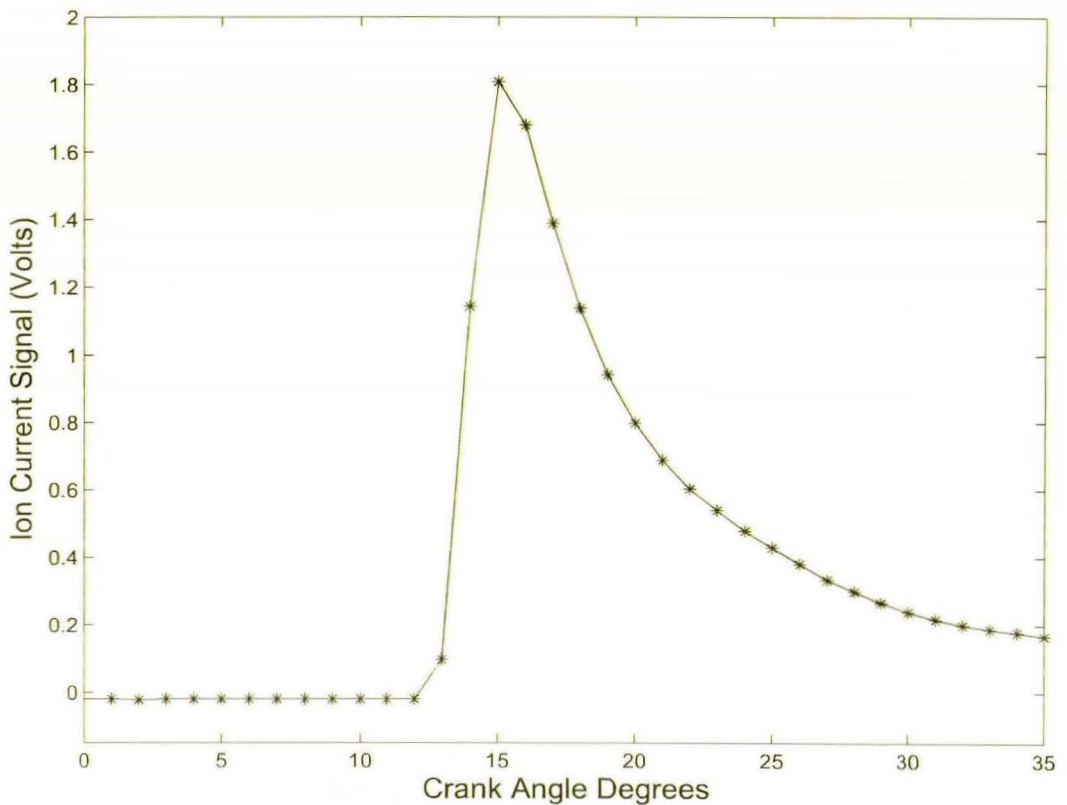


Figure 4.24: Example of sudden spike rise

Matters are complicated further by the fact that the start of the signal can be concealed by noise as is shown in figure 4.25. This should not normally be a problem as the spikes are usually high enough to easily rise above the noise. However, to guarantee a safe detection through a simple technique such as a static trigger level for example, compromises have to be made that will erroneously classify certain cycles.

Another problem is that the ion current signal can suffer from a noticeable base drift, an extreme example of which can be seen in figure 4.26. Coupled with the problem of noise and potentially weak spikes, this makes the use of a static trigger inappropriate.

To counter these problems, two different techniques have been tried out. One, designed for maximum speed, is based on classic concepts and employs a dynamic trigger to judge how to classify each candidate point. The other, designed as a more rigorous approach, is based on wavelet

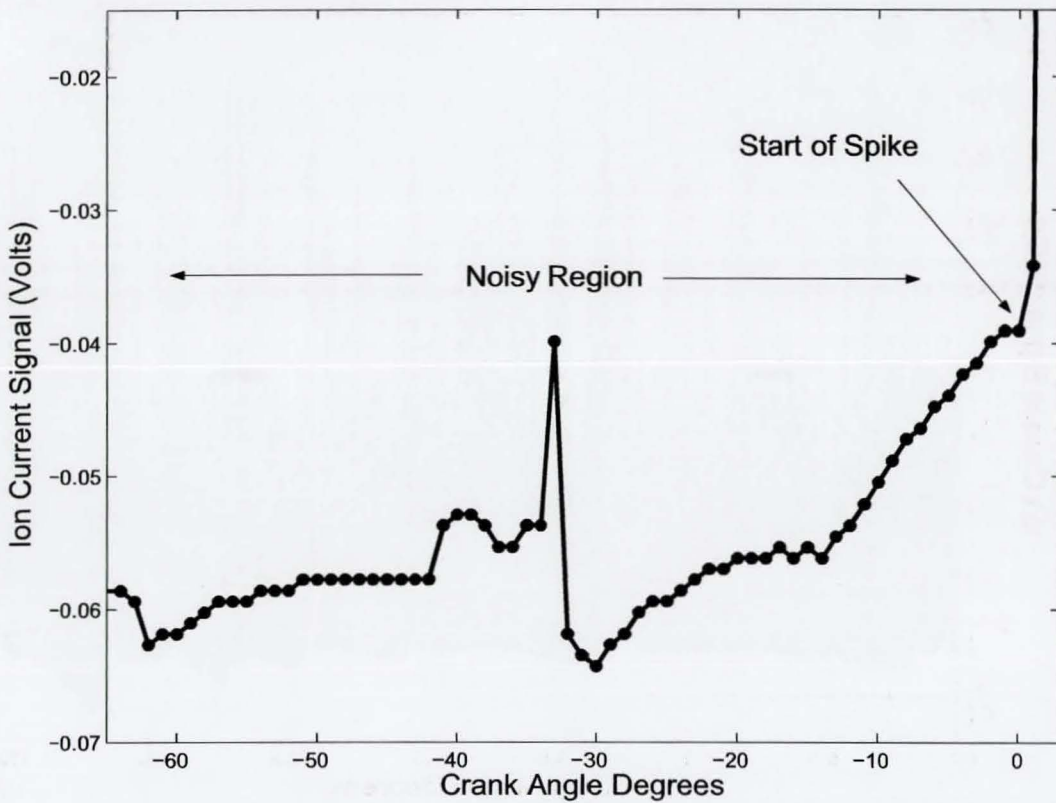


Figure 4.25: Detail of noisy region before spike

analysis and classifies points by processing the high frequency part of the ion current signal. Both these techniques are outlined below.

Classic Estimation of Signal Start

The classic approach is based upon certain assumptions which work well for the type of signal encountered during this research. These are that there is no combustion in the first 100 data points and that the base drift is not fast (high frequency) enough to affect the signal within a cycle. The algorithm employed uses the initial 100 data points of each cycle to work out the value for the base of the signal and to gauge its background noise by taking their standard deviation. A dynamic trigger level can then be established by setting a tolerance window around the base level (in this research and for this signal, set to 10 standard deviations).

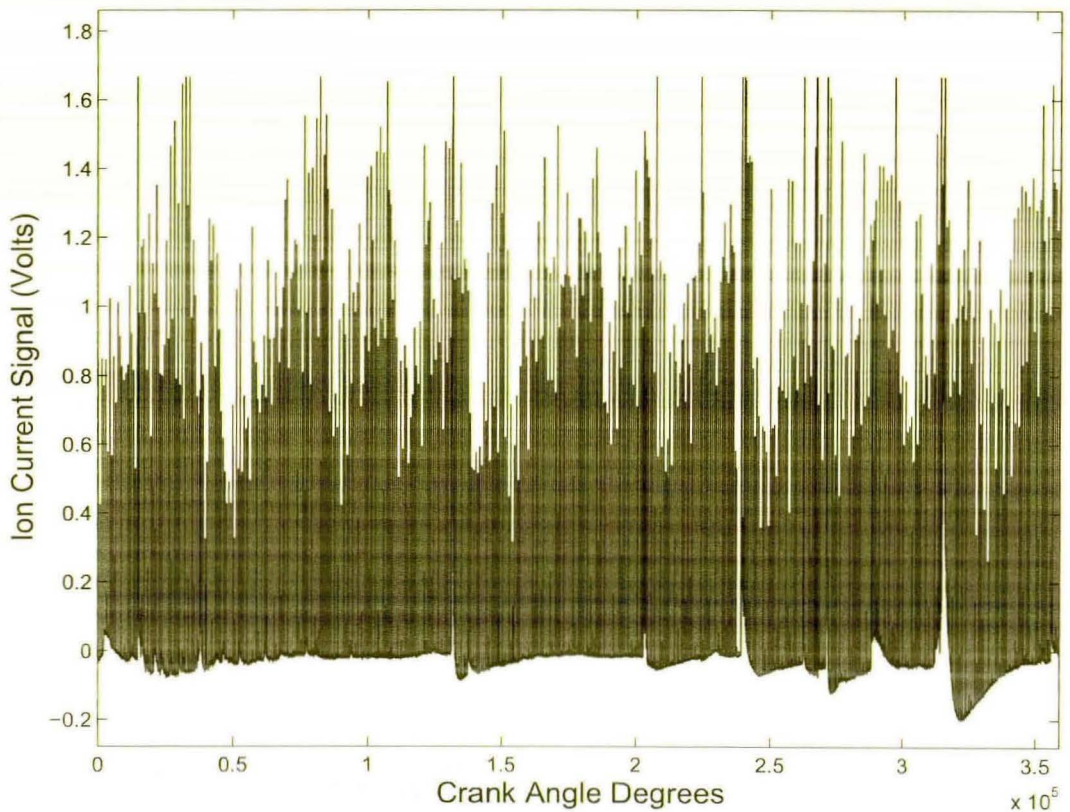


Figure 4.26: Example of base drift

The algorithm then starts from the position of the spike's peak and goes backwards towards the cycle's start. The criterion for classifying a point as the spike's start is for it to have dropped within the tolerance window. The value of ten standard deviations quoted might seem as unacceptably high. However, due to the sharpness of the spike, this value has been found to be appropriate.

Another variation of this technique can consider a rolling window instead of single points. This is essentially the same concept, looking at individual points backwards from the spike's maximum. In this scenario however, the average value and standard deviation of all the points previous to the point being considered is being estimated and used as a criterion. This variation also yields good results. However, since, both these variations can be tuned to yield almost identical results, only the first one will be discussed here as it is obviously the faster of the two.

The advantage of this technique is that, because the processing starts at the peak of the signal,

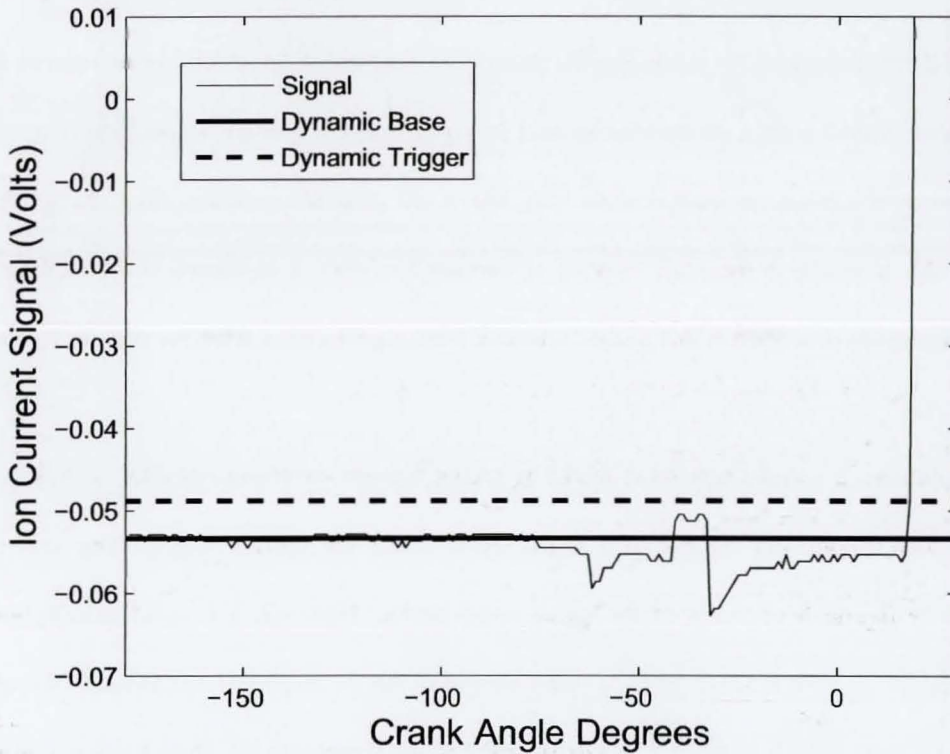


Figure 4.27: Ion current signal showing base and trigger level

it usually terminates after considering very few points, given that the start and peak are normally very close together. It can be further speeded up by considering fewer initial points in order to estimate the dynamic base and trigger level.

The disadvantage is that it needs to be presented with the whole signal since it needs to establish the position of the spike's peak first. This is a problem when considering real time, cycle to cycle implementation on a working engine. However, the magnitude of the spike for a non misfiring cycle is normally such that, even a simplistic static trigger approach should pick it out of the noisy signal (assuming the quality of the signal can remain similar to that encountered in this research, during real time implementation). If that is given, the processing for the estimation of the start of the spike can start immediately after the trigger level has been reached, even if the actual peak has not yet been recorded.

Wavelet Based Estimation of Signal Start

The second technique used for estimating the start of the ion current signal is based on wavelet decomposition. Wavelets are a very promising tool for signal analysis which have been implemented in the context of ion current interpretation [59]. Given this particular problem, their strength lies in being able to establish the exact location of various frequency components of a complicated signal. The results described in this research have all been implemented using the Wavelet toolbox in MATLAB.

Traditionally, a wavelet transform works by taking a given waveform (wavelet) scaling it to different wavelengths and comparing it to the signal across the signal's length. This analysis gives a very thorough overview of the signal composition. However, it is unrealistically time consuming for the task at hand. Thus, a faster algorithm can be employed, the Discrete Wavelet Transform (DWT), which in essence works by splitting the signal into a high and low frequency part, where the choice of wavelet acts as the kind of filter to be used. In wavelet analysis, these two low and high frequency components of the signal are often referred to as *approximation* and *details*. Through a process called downsampling, these are reduced to approximately half the length of the original signal.

Although, this process can be repeated to decompose the signal to deeper levels, in this case we are only interested in the high frequency, *details*, part and one level of decomposition is adequate.

Figure 4.28 shows the original signal zoomed in before the start of the spike, occurring around 20 CAD, along with its *details* after one decomposition. It is obvious how the *details* easily mark the start of the spike.

This behaviour lends itself to very easy identification of the spike start by simply working backwards from the maximum value of the *details* signal until reaching a "calm" region (implemented by checking that all members of a fixed size window are below a static trigger value) without need for a dynamic trigger. A major advantage, visible in figure 4.28 is that the *details* are

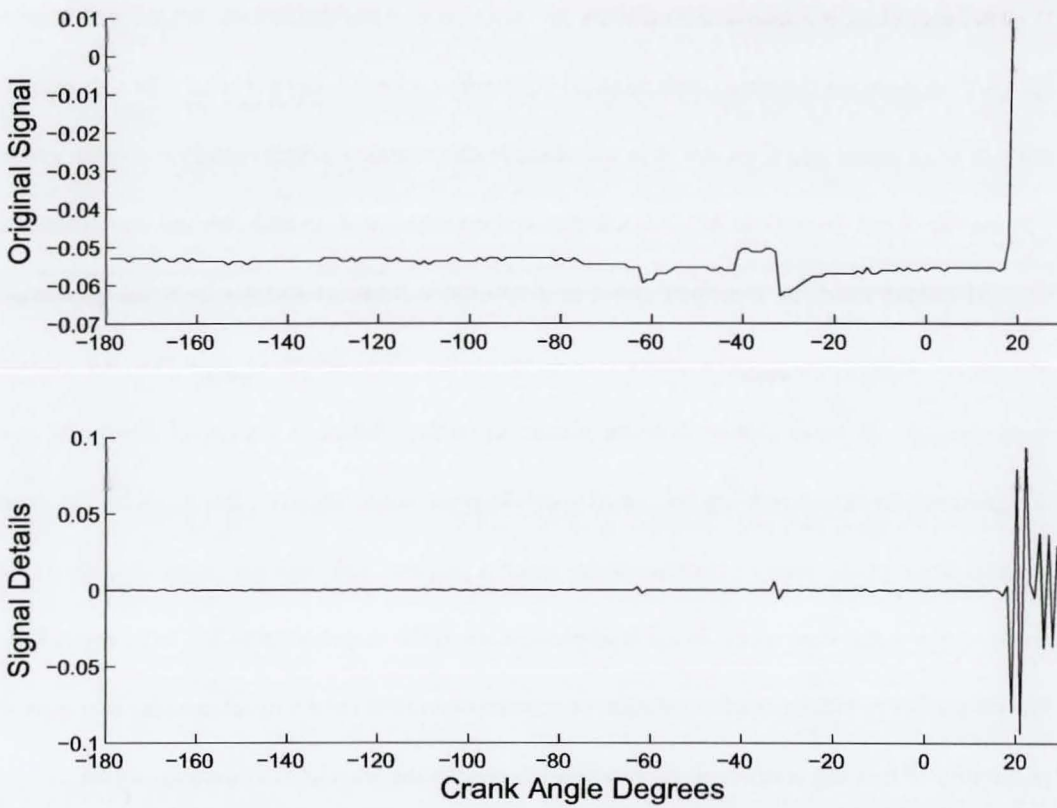


Figure 4.28: Original ion current signal and DWT generated details

not affected by the base drift, since the latter has very long wavelength. This is why a static trigger can be successfully implemented in the case of the algorithm employing wavelet decomposition.

Of the available wavelets, the *Daubechies* and *Symlet* families produce results that most readily resemble the results of the classic algorithm. In fact, the best agreement comes from the Daubechies 1 (also Haar) wavelet, where the average error between their results is less than 1 CAD. It has to be pointed out though that the results of the classic algorithm are not necessarily a “correct” target to be met. In most of the ambiguous cases, the precise start of the signal is open to interpretation, even by a human. Having been the first to be developed, the classic algorithm has been the one most closely tuned to return agreeable bulk results. Hence, agreement with it is a good indicator of performance but is by no means a definitive test since the algorithm can always be tuned to yield even “better” results for a particular wavelet.

This very elegant implementation hides the major processing that is done behind the scenes by the DWT. However, a real time implementation of such a technique can potentially be optimised for the task to an extent much greater than was done in this research, where readily available, general purpose functions from the MATLAB wavelet toolbox were used. In addition, the implementation can and indeed must, be narrowed down to a specific window of interest in a real time implementation. In this case, tested as proof of concept on the whole length of the signal, it performed approximately 20 times slower than the classic algorithm, which is a stripped down procedure designed strictly for identifying the signal start. As pointed out however, this is not by any means representative of the relative computational speed a purpose built wavelet based algorithm could achieve. For a real time, cycle to cycle implementation, the major concern has to be speed and at this point, this particular implementation of wavelets seems to be at a disadvantage. However, the possibility of treating additional information inherent in the wavelet decomposed signal, coupled with the ability to process the reduced size *approximation* and *details* signals make wavelets a promising tool for analysis of the ion current signal as is described below.

4.2.3 The Wavelet Decomposition of the Ion Current Signal Procedure

A major strength of the wavelet decomposition lies in the reduction in signal size. The measurant extraction method described previously, explicitly reduces the original signal to a few numbers describing geometrical characteristics. However, decomposing the signal through employing the DWT algorithm, reduces the signal while retaining significant information. Figure 4.29 shows an ion current signal and the subsequent two levels of decomposition. The figure highlights how varying levels of decomposition reduce the signal length while retaining the main features.

By reducing the signal size in this way, an ANN(s) can be designed whose input layer will be much shorter than would be needed if the whole signal was to be used as an input. Thus, the reduced size ANN(s) will be much faster. However, deeper levels of decomposition take more time

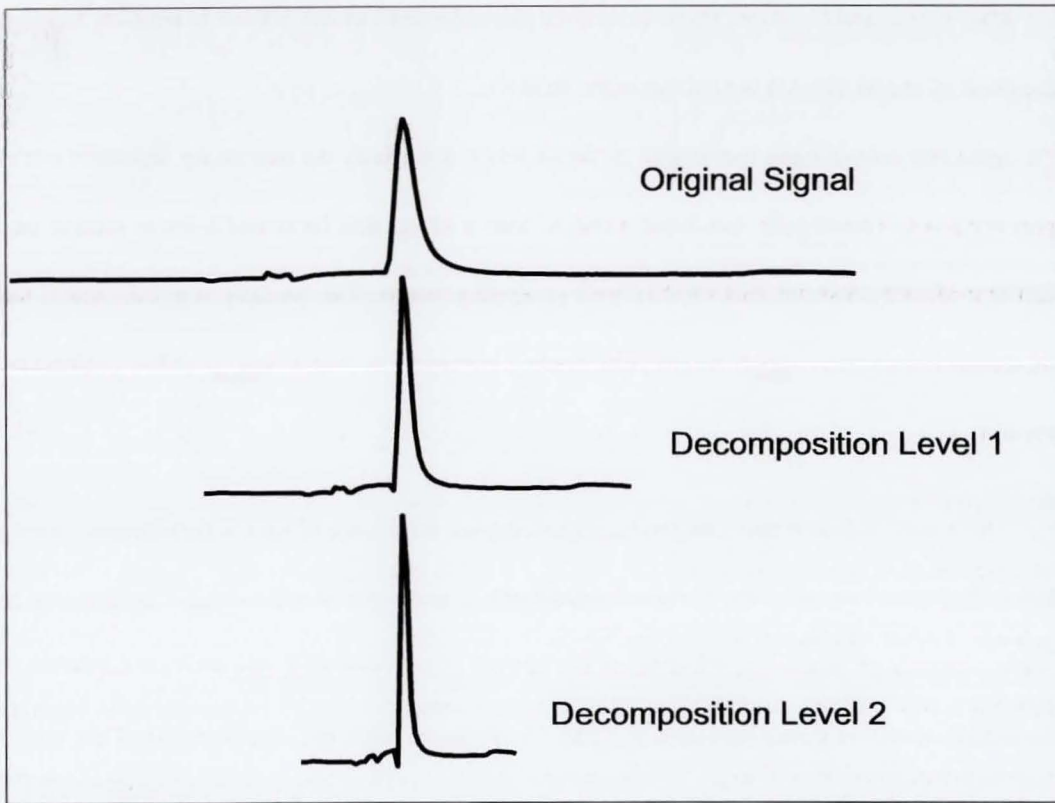


Figure 4.29: Example of two levels of wavelet decomposition of ion current signal

on the DWT. Also, deeper decomposition of the signal can potentially degrade the ANN(s) output.

Hence, there is a tradeoff between time spent on the DWT, time spent on the ANN(s) and the overall performance. All these issues need to be taken into account when designing a system that should, in principle, be able to process cycle to cycle information from the ion current signal.

4.2.4 Artificial Neural Network Based Predictions

Types of Input

In order to test the feasibility of a control system having ion current based information for the pressure measurants, the data extracted by the procedures described previously are presented to various different ANN(s). The aim is to get the best predictions possible from as uncomplicated an ANN(s) as possible for a wide range of operating conditions. The two types of ANN(s) investigated

are ADALINE(s), and GRNN(s). These have been implemented through the corresponding functions supplied by the MATLAB Neural Network Toolbox.

ADALINE(s) have been introduced in detail when describing the use of ion current in SI experiments 4.1. GRNN(s) are two layer ANN(s)s, with a RBF(s) first layer and a linear second layer. Initial trials demonstrated that GRNN(s) give promising results. The question is to establish if their increased complexity, which incurs performance penalties, is worth their possible performance benefits.

The ANN(s) fall into two categories, depending on what kind of inputs they accept. On one hand, the inputs consist of the extracted measurants as described in section 4.2.2. In this case, the ANN(s) input layer size is the 4 extracted ion current measurants plus any additional information on engine operating conditions such as RPM. On the other hand, the input consists of the wavelet decomposed signal, normally the *approximation*, plus any engine operating conditions. In this case, the input layer is variable depending on the decomposition level.

In the case of the extracted measurant data, certain additional tests have to be carried out. Before the data is presented to the ANN(s), it goes through a final selection process. The data is organised in matrices where a set of inputs and corresponding set of outputs take up a row. Certain rows may represent cycles where one of these numbers has not been established, most likely because of a misfire, in which case ion current information is unavailable. In that case, the whole cycle is removed by deleting the respective row in the matrix. The other part of the selection involves outliers. Again, cycles which are problematic for any reason can either fool the extraction algorithms into returning unrealistic values or the cycles themselves have uncharacteristic values. This is treated by doing a histogram of the data and identifying the left and right edges at which points a certain percentage of the total data is present (set to 1.5% in this research). Data outside the region specified by these edges are discarded.

It has to be noted that none of these techniques have to be employed in a real time implemen-

tation. Cycles that return no ion current signal up to a certain point can be quickly classified as misfires anyway. Similarly, predefined triggers based on the operational conditions for the allowable range of values can be employed on the extracted measurants to decide quickly if a cycle is to be considered as normal before proceeding with the processing of its data.

In the case of the ANN(s) using the whole decomposed signal as an input, no such processing is carried out. This can be considered as a token of added robustness, since there is no intermediary algorithm, other than the DWT itself, which might complicate the process.

The output of the ANN(s) is always PPP. In reality, there is a host of pressure related measurants that can be derived from a pressure trace such as described in the ion current in SI section, 4.1, not to mention combustion related measurants such as start of combustion, combustion duration etc, derived by combustion analysis, described in chapter 5. However, PPP is preferred because its extraction algorithm, which is simply maximum point search, is simple to the point of guaranteed perfect accuracy. This is important since there is uncertainty on the input side, especially where the measurant extraction algorithms are concerned. Adding uncertainty on the output side through using a harder to extract measurant, such as start of combustion for example, will yield results that are more unrepresentative. At this point however, the aim is to analyse the relative merits of different techniques, so the chosen output used as measure is PPP, though, of course, an ANN(s) can be designed to predict any pressure measurant.

ANN Testing within Different Speed Sites

The first kind of data to be treated consists of steady state data collected at different engine speeds. TRG sweeps are carried out at each speed. All are WOT, with $\lambda=1$. Spark advance varies among members of the same speed site. The Revolutions per minute (RPM) range covered is from 1500 to 3500.

To test performance of the algorithms described above, the initial test is done within the mem-

bers of each speed site. The reasoning is that, at the very least, a control system switching between ANN(s), each one trained for a certain RPM region, can be implemented for steady state operation¹.

Each training point corresponds to a cycle. The data points are randomly split into a training and a test group with the training group taking up 80% of the total sample. The ANN(s) is then tested on the test sample, which is made up of the remaining 20%. Because of the random nature of the selection of the test sample, no two consecutive tests will give the same result. For that reason, the numbers quoted throughout this section are averages of multiple tests. This scheme has been favoured over simpler ones, such as taking the first 20% of data from each data log for example. The reason for this is that, in logs which exhibit areas of localised behaviour, such as a series of unstable cycles, these might not be sampled, or not sampled at a representative fraction. By making the selection random, the test sample is spread evenly over the whole of the data.

The errors quoted throughout are RMS errors of the difference between the ANN(s) prediction and the actual value of the output. The units are always in CAD. The percentage errors quoted correspond to the percentage of the error as a fraction of the overall spread of the actual values of the output.

Performance of Measurant Based ANNs The results presented here correspond to the ANN(s) taking extracted ion current measurants as inputs. These initial trials do not supply the ANN(s) with information on any other operating conditions.

The performance of the ADALINE over the different speed sites is presented on table 4.2, which summarises the errors for PPP for each engine speed. The “Error Classic” and “Error Wavelet” refer to the CAD error for the speed group, depending on whether classic or wavelet

¹A question that might arise here is why classify the data according to RPM and not TRG. The reason is that, unlike RPM, TRG is not directly measurable. For a given valve setting, the engine will trap a different amount of TRG at different RPM. Note that, in this throttleless valve strategy, load is adjusted via TRG, hence the RPM - TRG space is equivalent to the speed and load space.

techniques are used to extract the ion current measurants. The number in square brackets is the respective percentage error.

Table 4.2: ADALINE performance for each speed site, only ion current measurant inputs

RPM	Error Classic (CAD) [%]	Error Wavelet (CAD) [%]
1500	2.34 [8]	2.35 [9]
2000	1.46 [6]	1.71 [8]
2500	2.19 [9]	2.23 [9]
3000	2.56 [10]	2.26 [10]
3500	3.08 [13]	3.53 [15]

The same trials, carried out on GRNN(s) are displayed on table 4.3.

Table 4.3: GRNN performance for each speed site, only ion current measurant inputs

RPM	Error Classic (CAD) [%]	Error Wavelet (CAD) [%]
1500	2.31 [9]	2.42 [9]
2000	1.46 [6]	1.40 [6]
2500	2.42 [5]	1.50 [6]
3000	2.14 [9]	1.86 [8]
3500	2.28 [10]	2.57 [11]

These trials demonstrate any differences between both the wavelet and classic ion current measurant extraction techniques as well as the relative performance of ADALINE(s) and GRNN(s). The differences between classic and wavelet measurant extraction methods generally appear small enough to be negligible. As far as the ANN(s) are concerned, the GRNN(s) seem to offer a slight advantage as well. However, it has to be noted that the present GRNN implementation takes approximately 7 times longer process the same input.

Table 4.4: Performance of conventional linear fit method for two different ion current measurants

RPM	Signal Max Pos. (CAD)	Signal Start Pos. (CAD)
1500	2.96	3.19
2000	2.21	2.64
2500	2.50	2.53
3000	3.70	3.62
3500	2.93	2.95

Table 4.4 is aimed at gauging the performance improvement of ANN(s) over conventional methods. The prediction method in this case is a simple linear fit of the data for an ion current measurant against PPP. The error quoted in the table prediction is based on either of two measurants which exhibit good correlation with PPP, the position of the signal's maximum or the position of the signal's start (see figure 4.23).

One point to note here is that all results seem to indicate a best performance at 2000 RPM. This is in agreement with the fact that engine operation was very been smooth at this speed, reflected by the lowest PPP variance of all speed sites.

Performance of Decomposed Signal Based ANNs To get a better understanding of the relative merits of the different ANN(s) designs, the same tests are carried out using the decomposed ion current signal. Using such a design does away with the whole measurant extraction algorithms. The idea behind it is that, measurant extraction is a procedure that has to be performed upon an ion current signal in order to produce certain numeric "handles". In effect, it compresses the information carried by the signal, thus allowing for a smaller sized input to the ANN(s). However, compression is also carried out by wavelet decomposition of the signal. Hence, it might be possible to retain a large part of the information content through the wavelet decomposition as opposed to

carrying out a measurant extraction. Table 4.5 displays the performance of these ANN(s).

Table 4.5: ANN performance for each speed site, decomposed ion current signal as input

RPM	ADALINE (%)	GRNN (%)
1500	4.04 (14)	4.02 (15)
2000	3.22 (13)	3.24 (15)
2500	3.62 (15)	3.5 (14)
3000	4.04 (16)	4.05 (16)
3500	3.30 (14)	3.33 (14)

These results were produced through ANN(s) at various decomposition levels. The ion current signal decomposition was carried out using the “db2” wavelet and the levels varied between 1 and 5. The errors quoted are the best results, however, the results did not vary for more than 7% across the decomposition levels in the case of these tests within RPM speed groups. The analysis of the relation between error, computational time and decomposition level is presented in detail in section 4.2.4.

The tests presented here are only carried out to investigate the capabilities of the ANN(s) on separated sets of data. The most important test, however, is to test performance of a single ANN(s) across the RPM range as well. The feasibility of such an ANN(s) can greatly enhance the performance of a cycle to cycle control system.

ANN Testing Across Different Speed Sites

Having tested that the performance of the ANN(s) seems promising within single RPM speed groups, the next step is to test it across the span of RPM. As in the previous section, the results are split between the measurant based and decomposed signal based ANN(s).

Performance of Measurant Based ANNs At this stage, the effect of adding operating condition information to the ANN(s) is assessed. In the first instance an ADALINE and a GRNN are trained and tested on the whole of the RPM range. In the second instance, apart from the ion current measurants, additional information is supplied to the ANN(s) in the form of the following:

1. RPM
2. Negative overlap
3. Ignition timing
4. Airflow

The negative overlap is one way of measuring amount of TRG. However, it is not directly representative of the actual mass of TRG, as this also depends on volumetric efficiency, a function of engine speed. It is however, an easy way of getting a handle of the TRG. Similarly, the airflow is a rough measure of each cycle's energy intake. Since for all these data $\lambda = 1$, logged at WOT, the power output is regulated by the TRG amount (which is in turn regulated by the negative overlap), which has a direct impact on the airflow.

Again, to account for statistical error arising from the random nature of the selection of the training and test sets, a series of tests have been performed for each case and the average results quoted. One point worth mentioning here is that care has to be taken when quoting the error across mixed speed groups. There are two factors that can contribute to unequal effects of each group's error on the final value. First, is the fact that not all groups have the same amount of logs in them. This will be reflected in the overall sample, making groups with larger populations dominate the result. Second, is the random selection process of the test points. Despite being superior, the disadvantage is that it adds fuzziness to the amount of cycles taken from each group. To address these concerns, the test points have been labelled according to the speed group they belong to and at the end, errors have been calculated for each individual group. The final error quoted is the

mean of these, thus each group contributes equally to it irrespective of how many of its members make it to the test sample.

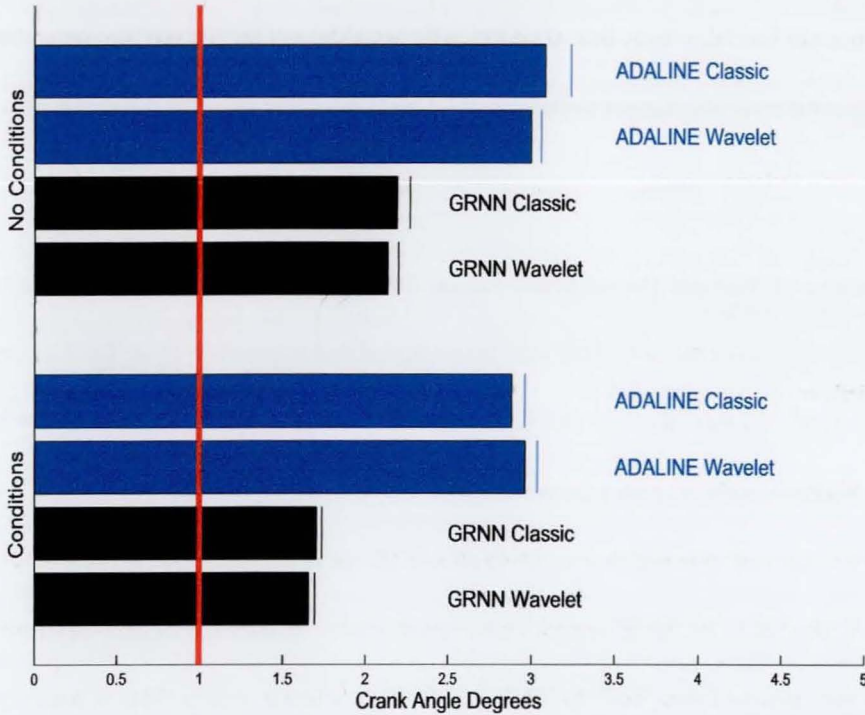


Figure 4.30: Comparative results of different measurant based ANN(s)

Figure 4.30 shows the various strategies tested and their associated outcomes. The horizontal bars show the errors for each ANN(s) design. The thin line at the edge of each bar shows the standard deviation encountered between the successive test performed on each design. The thick vertical line at $x=1$ marks the sampling rate.

The bars are split into two groups, depending on whether the ANN(s) have operating condition information among their inputs. Within these groups, they are further split into ADALINE(s) and GRNN(s). Finally, each type of ANN(s) is classified depending on whether the measurant extraction procedure employs classic or wavelet methods.

Hence, the top four bars show the cases where no operating condition information is presented to the ANN(s). GRNN(s) outperform ADALINE(s), while the type of measurant extraction technique (wavelet or classic) does not have any significant influence on the results.

The bottom four bars show that ADALINE(s) do not yield any significant improvement by adding operating condition information to their inputs. On the contrary, GRNN(s) respond with a noticeable improvement in performance.

Performance of Wavelet Decomposed Signal Based ANNs The second series of tests across speed groups involves the use of the ion current signal decomposed to some level through wavelet decomposition. In this case, certain additional factors need to be taken into account since the decomposition introduces new parameters.

The first parameter is which wavelet to choose for the decomposition. In the case of measurant extraction, the “db1” or “haar” wavelet gave good results. In the case of decomposing the signal, it seems that moving from “db1” to “db2” yields slightly better results. This is possibly due to the fact that the “db1” wavelet, being in essence a step function, generates a less faithful *approximation* signal than the “db2” which is a more sophisticated wavelet. When identifying measurants, the rough results of “db1” are probably best suited for the task. However, when using the decomposed signal as an input, “db2” outperforms “db1”.

The other parameter that has to be determined is the level of decomposition. As discussed in section 4.2.3, a deeper level will take more time spent on the decomposition itself but less time on the ANN(s) since the input layer is reduced in size. Clearly, a balance has to be struck. Figures 4.31 and 4.32 demonstrate these considerations.

The x-axis on these figures represents the decomposition level of the ion current signal. The lines represent the error, and the times spent on calculating the DWT and ANN(s) response to the test input. The y-axis represents these quantities normalised by dividing by their initial (i.e. at

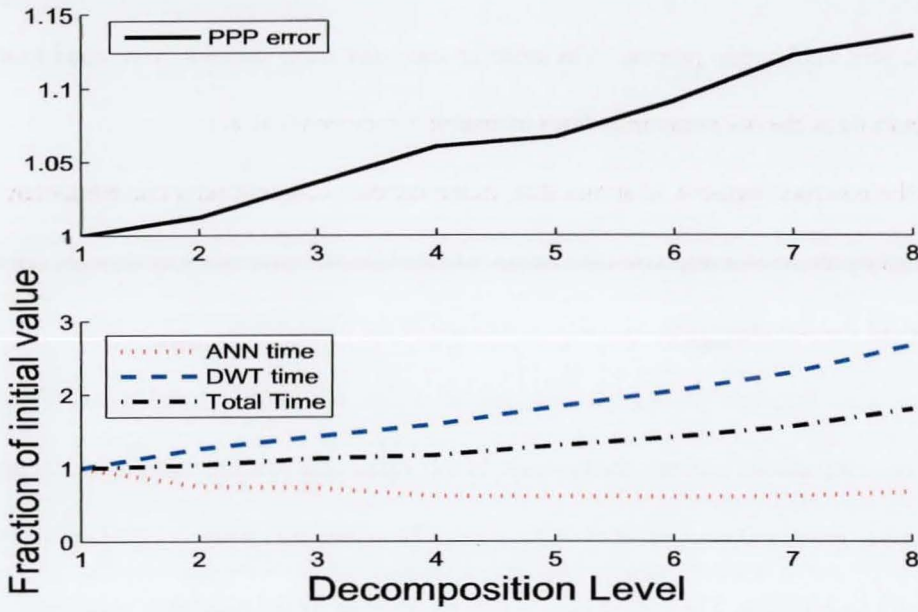


Figure 4.31: Breakdown of ADALINE design parameters

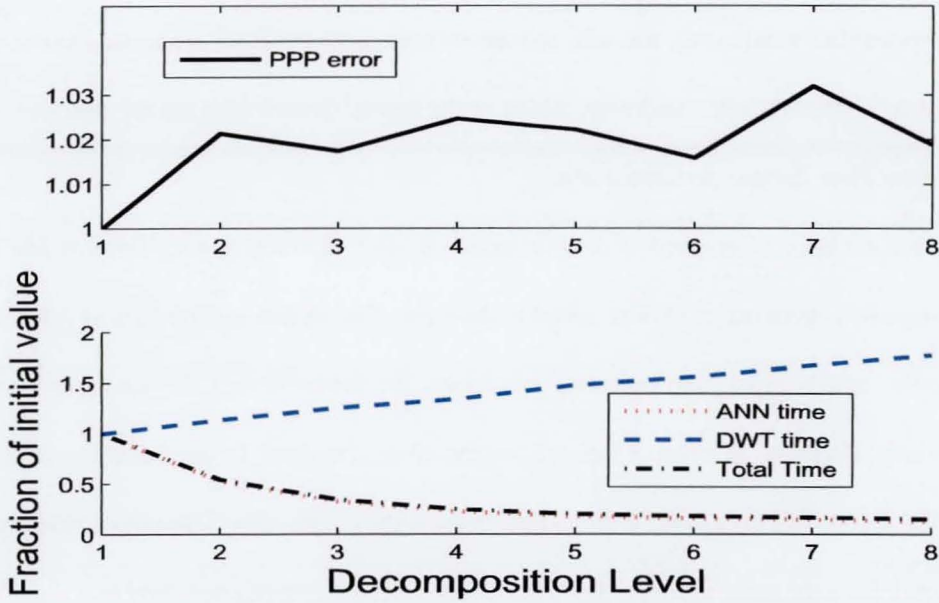


Figure 4.32: Breakdown of GRNN design parameters

decomposition level 1) values.

On figure 4.31, which corresponds to the ADALINE(s), the total time spent on both DWT and

ANN(s) is clearly dominated by the DWT time. This is because the ADALINE(s) response calculation is a very lightweight process. The error on the other hand shows a clear trend to increase monotonically as the decomposition level increases.

On the contrary, figure 4.32 shows that, in the GRNN(s) case, the total computational time is dominated by the ANN(s) response calculation. Meanwhile, the error is not as strongly affected by the depth of the decomposition as it was in the case of the ADALINE(s).

These tests highlight the relative concerns of design within the ANN(s) types. Figure 4.33 shows the comparisons between the designs. In this figure, the bars representing errors are black and their values are indicated on the bottom x-axis. The white bars represent total time (DWT plus ANN(s)) for each design. These have been scaled by dividing by the maximum value among them, hence showing their relative values. Their values are indicated on the top x-axis.

Starting from the top, the first three correspond to designs based on "db1" decomposition. They represent two ADALINE(s), one with and one without operating conditions added to the input, followed by a GRNN(s) with conditions added to the input. Quoted also are the decomposition levels where these designs performed best.

The second three correspond to designs based on "db2" decomposition. The first one is an ADALINE(s) with operating conditions added to the input. The second and third are an ADALINE(s) and GRNN(s) where, apart from operating conditions, the *details* part of the decomposition has been added to the input. In terms of size, this has the effect of making the input double, effectively taking the decomposition up one level. Thus, these ANN(s), both whose decomposition level is quoted as 4, have the same size input layers as ANN(s) whose decomposition level is 3.

The ANN(s) in this section are trained on all data available in the sample since normally there is no input measurant extraction process through which to classify outliers. To compare more objectively with the ANN(s) which accept extracted ion current measurants as input (and have outliers removed from the sample), a series of trials were performed where the same cycles were

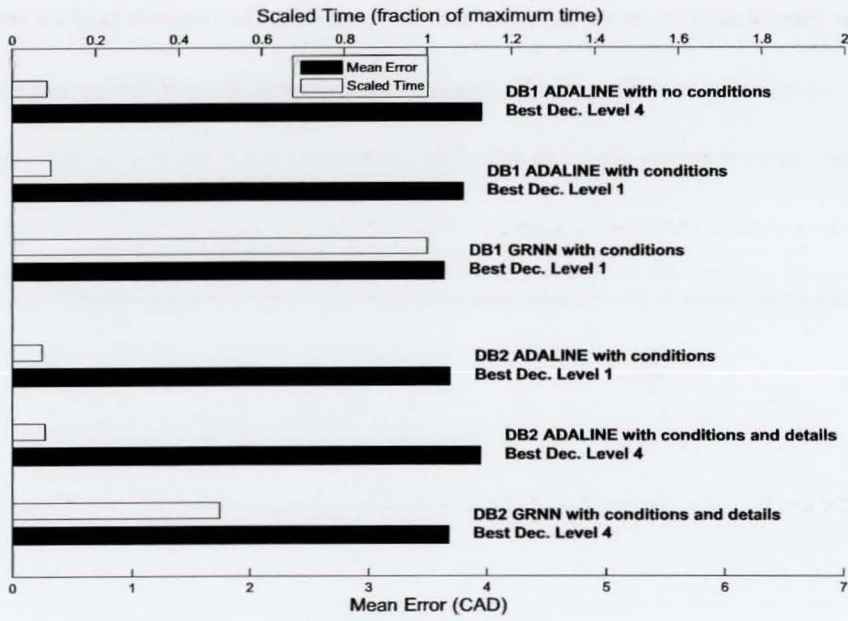


Figure 4.33: Comparative results of different decomposed ion current based ANNs

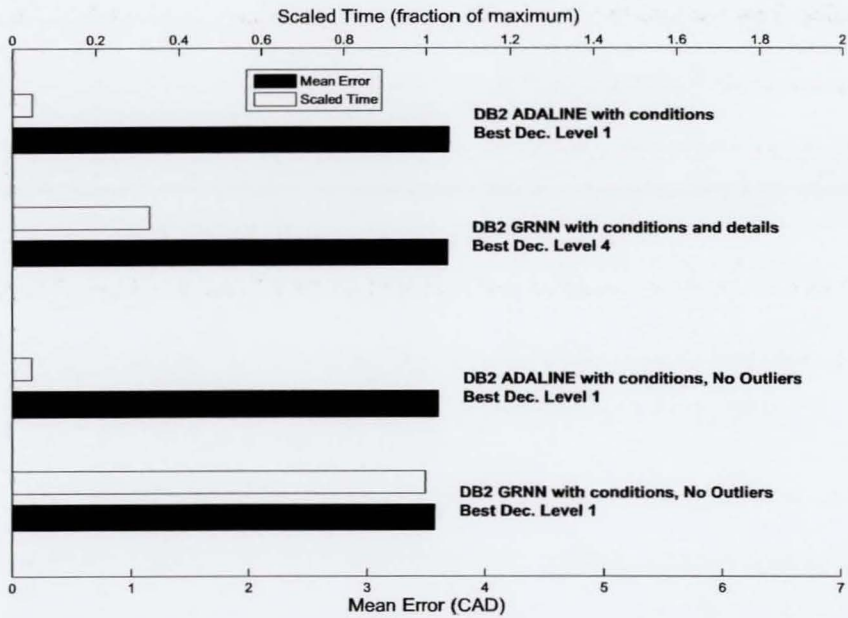


Figure 4.34: Comparative results of different decomposed ion current based ANNs with the same outliers removed as in the case of measurant based ANNs

removed from both. The results are presented in figure 4.34. The top two bars are the same as the 4th and 6th from figure 4.33, while the bottom two represent trials of similar design ANN(s) with the outlier cycles removed. The removal of the cycles does not result in a notable improvement.

4.2.5 Summary of ion current use in HCCI combustion

Two different approaches to ANN(s) design have been described and evaluated here. One is based upon extraction of relevant measurants from the ion current signal in order to present them to the ANN(s). The other relies upon the reduction in size which is achieved through wavelet decomposition in order to achieve a small and fast ANN(s).

The two approaches that have been tried were organised in two different ways. In the first instance, the data is presented in various groups and an ANN(s) is trained specifically for each case. In the second instance, data is not classified according to speed but is presented to the ANN(s) as a whole, with and without information on operating conditions as part of the input.

Two types of ANN(s) have been tested, ADALINE(s) and GRNN(s).

The results from the trials within the same speed groups are as follows:

Both types of ANN(s) achieve an RMS error between 1.5 and 3 CAD, depending on RPM, for the ANN(s) whose input is based upon measurants extracted from the ion current signal².

Both types of ANN(s) achieve an RMS error between 3 and 4 CAD when their input is the wavelet decomposed ion current signal itself³.

The results from the trials where testing is done across all data are as follows:

On ANN(s) whose input is based upon extracted ion current measurants, with no information on operating conditions as part of the input, GRNN(s) outperform ADALINE(s) by achieving an RMS error of around 2.2 CAD as opposed to around 3 CAD for ADALINE(s). When information on operating conditions is added to the inputs, the error drops to under 3 CAD for ADALINE(s) and to around 1.7 CAD for GRNN(s)⁴.

On ANN(s) whose input is the wavelet decomposed ion current signal, the error always remains

²Tables 4.2 and 4.3

³Table 4.5

⁴Figure 4.30

between 3.5 and 4 CAD, largely independent of the type of ANN(s), the presence of operating conditions in the input, choice of wavelet, or removal of potentially problematic cycles from the data⁵.

From the above, it follows that the ANN(s) whose inputs are based upon extracted ion current measurants outperform the ANN(s) whose input is the wavelet decomposed ion current signal⁶. Hence, for the particular task at hand, it is preferable to expend the computational resources required for the extraction of measurants from the signal if the ANN(s) of choice is the ADALINE(s) or the GRNN(s).

The performance of both these types of ANN(s) using extracted measurant inputs is all the more noteworthy, considering that no averaging takes place and the results at their best performance are only 50% above the sampling rate (best performance around 1.5 CAD with a sampling rate of 1 CAD). Thus, either of these ANN(s) could potentially be a strong candidate as part of a control system for the steady state operation of an HCCI engine.

⁵Figure 4.34

⁶Similar results have been demonstrated in the case of SI combustion, when the predicting ANN(s) has been designed to act upon the whole ion current signal.

Chapter 5

Combustion Analysis

The available experimental data offer the main bulk of information at the heart of this research. These have been logged at various different settings covering a broad range of both SI and HCCI operation. The information is either in the form of CAD resolved variables (e.g. the ion current and pressure traces) or variables which are fixed for a given log (e.g. speed and Indicated Mean Effective Pressure (IMEP)). Each log contains several hundred cycles, usually between 300 and 500.

While the study of the latter can offer significant insights into various aspects of combustion, the main goal has been to be able to investigate cycle to cycle effects. This is mainly because the performance of a HCCI cycle is heavily dependent upon the events taking place in the cycle preceding it. This interlinking is at the heart of certain phenomena of unstable combustion, understanding of the onset of which is desirable for control purposes.

The most valuable tool in this study is the pressure trace. However, it is by itself a poor indicator of the events taking place within a cycle. In order for meaningful characteristics of the cycle to be extracted, lengthy post processing has to be carried out. It is through the variables that form the outcome of this post processing that the events which occur during individual cycles can be understood.

Unfortunately, certain limitations come into play which complicate matters. On one hand, hardware limitations have to be identified and, where possible, accounted for. On the other hand, unstable combustion often results in very violent events, placing further strain upon the hardware's performance. One strategy is to identify these cycles and discard them, treating only the "well behaved" ones. Because, however, unstable combustion is a very interesting and important part of this research, the main goal has been to try and salvage as many of these cycles as possible while maintaining a high level of accuracy. In order to achieve this, the post processing method employed has been far from trivial and needs an in depth description in order to be understood and the choices made to be justified.

5.1 Averaged Pressure Trace Treatment

The "raw" pressure trace needs post processing before it can be used as an accurate measurement tool. In this research, two major areas that need correction have been identified: pegging and thermal shock related imbalances.

Due to the nature of the measurements, this processing has to be split into two categories: processing of averaged traces and processing of individual cycles. The former must be performed on a data log first before the latter is carried out.

To proceed linearly, the pressure trace would have to be pegged initially, before further post processing takes place. Unfortunately this is not possible because of the following interdependencies:

- Pegging via polytropic exponent, as used in this research, requires estimation of this exponent.
- Value of the exponent depends upon composition and temperature.
- Given that charge flow is directly recorded, total mixture composition and temperature de-

pend upon estimation of TRG.

- Value of TRG depends upon a correctly pegged pressure trace.

The method employed to overcome the cyclic nature of this problem is being examined in detail in the following sections.

5.1.1 Pegging

While the pressure transducer will respond to changes in pressure, the signal generally needs to be calibrated so that the trace is physically meaningful. This can be resolved by either using the reading of an extra sensor e.g. Manifold Air Pressure (MAP), or fitting a polytropic compression curve [84], [85].

Using an external MAP sensor has the advantage of trustworthy readings in the relatively small range of values it records. Assuming knowledge of the location at which the in-cylinder pressure transducer's trace and that of the MAP record equal pressure, the signal for a given cycle can be pegged very accurately.

The drawback of the method is that estimating the location of pressure equalisation is not trivial. Even assuming a thorough investigation, mapping the engine across the required speed and load range, HCCI combustion can suffer from violent cyclic oscillations [86] which can, in extreme cases, result in a heavy backflow from the cylinder into the inlet. Thus, an assumption of a specific location of pressure equalisation between cylinder and inlet for a given speed and load site will often be inaccurate if no further processing is carried out to determine the effects of individual cycles' performance.

On the other hand, trying to fit a polytropic curve has the disadvantage of requiring an accurate value for the polytropic exponent. These curve fitting methods rely upon the equation:

$$PV^\kappa = C \quad (5.1)$$

where P is the pressure, V is the volume and κ , C are constants, to fit a measured unpegged curve to a theoretical one. This is because the compression stroke is modeled well by Eq. 5.1. These methods are, however, sensitive to small variations of the value of κ (as shown in figure 5.3).

However, the big advantage is that the oscillations of unstable HCCI are less of an issue and thus, more cycles displaying extreme values can be salvaged. Because the characteristics of unstable combustion have been a topic of interest in this research, a polytropic fitting method has been used for pegging.

Implementation Issues

The idea behind using Eq. 5.1 is that an unpegged pressure signal will have a constant shift ΔP from the actual pressure value, thus transforming the equation into:

$$(P_m - \Delta P)V^\kappa = C \quad (5.2)$$

where P_m is the measured pressure value.

Thus, for a given value of κ , two points of known P_m and V will yield a system of two equations with two unknowns, ΔP and C .

Tunestal [84] points out that using only two points makes the method sensitive to noise in the measured signal. The proposed method solves Eq. 5.2 for P_m to yield:

$$P_m = CV^{-\kappa} + \Delta P \quad (5.3)$$

which can be written in matrix form as:

$$P_m = \begin{pmatrix} 1 & V^{-\kappa} \end{pmatrix} \begin{pmatrix} \Delta P \\ C \end{pmatrix} \quad (5.4)$$

For multiple P_m and V values, the equation is generalised as:

$$\begin{pmatrix} P_{m1} \\ \vdots \\ P_{mn} \end{pmatrix} = \begin{pmatrix} 1 & V_1^{-\kappa} \\ \vdots & \vdots \\ 1 & V_n^{-\kappa} \end{pmatrix} \begin{pmatrix} \Delta P \\ C \end{pmatrix} \quad (5.5)$$

Since the values of P_m and V are known, this form can be solved using matrix algebra to yield values for ΔP and C .

The main issue behind using this method is the choice of the polytropic exponent, κ . In an ideal case, $\kappa = \gamma = \frac{c_p}{c_v}$, where c_p and c_v denote specific heat at constant pressure and volume respectively. In practice, the values of γ and κ always deviate somewhat. However, given the composition and temperature of the in-cylinder gases, values for c_p and c_v can be worked out using the JANAF polynomials [87] as described in Heywood [88]. Hence, if a satisfactory relationship between γ and κ can be established, accurate pegging can be carried out for cycles of varying composition.

The values of γ and κ depend on composition and temperature of the in-cylinder gases. Examples of these changes for various gases and mixtures are given in Heywood [88]. In the case of the signal that needs to be pegged, matters are complicated by the presence of TRG. This is because, unlike normal SI operation, having a non negligible amount of TRG drastically changes the composition of the mixture.

As far as temperature is concerned, assuming an accurate pressure trace, the corresponding temperature trace will depend on the amount of in-cylinder gases through application of the ideal

gas equation of state¹:

$$PV = NRT \quad (5.6)$$

where N in this case represents the molar amount of the in-cylinder gases. However, this amount of gases depends on the pressure trace. This is because these gases are made up of fresh charge and TRG. The charge is directly measured, for the case of averaged traces, through flow sensors. However, the TRG is not directly measured, but calculated through application of this equation at EVC².

Hence, the final estimated value of the in-cylinder gases at IVC depends upon the value of the pressure at EVC, which depends upon a properly pegged signal, which depends upon the value of κ , which depends upon the composition and temperature of the in-cylinder gases.

This cyclical dependence forces an iterative method to be performed in order to accurately peg the pressure trace. The idea is to peg with a reasonable initial value of κ (say, 1.4) and then calculate the resulting amount of TRG and hence mixture and associated temperature at IVC. This will yield a new value of γ and hence κ and the cycle can then be repeated until the difference between iterations becomes vanishingly small.

When such approximation techniques are used it is useful to carry out a sensitivity analysis of the variables involved. Figure 5.1 demonstrates the γ variation of two drastically different mix-

¹Note that the gases and conditions present in the engine do not fulfil the criteria of "ideal gases". There are various alternative formulations of this law, each of which goes one step further in addressing the departure from the ideal. However, the corrections are very small in comparison to the overall uncertainty of the experimental data. Also, nitrogen, which is the most abundant gas in the cylinder follows the ideal very well. Finally, using an alternative formulation would add computational cost to calculations that need to be performed in bulk, thus slowing down an operation which is already considerably complex.

²The procedure for TRG estimation is presented in detail in section 5.1.2

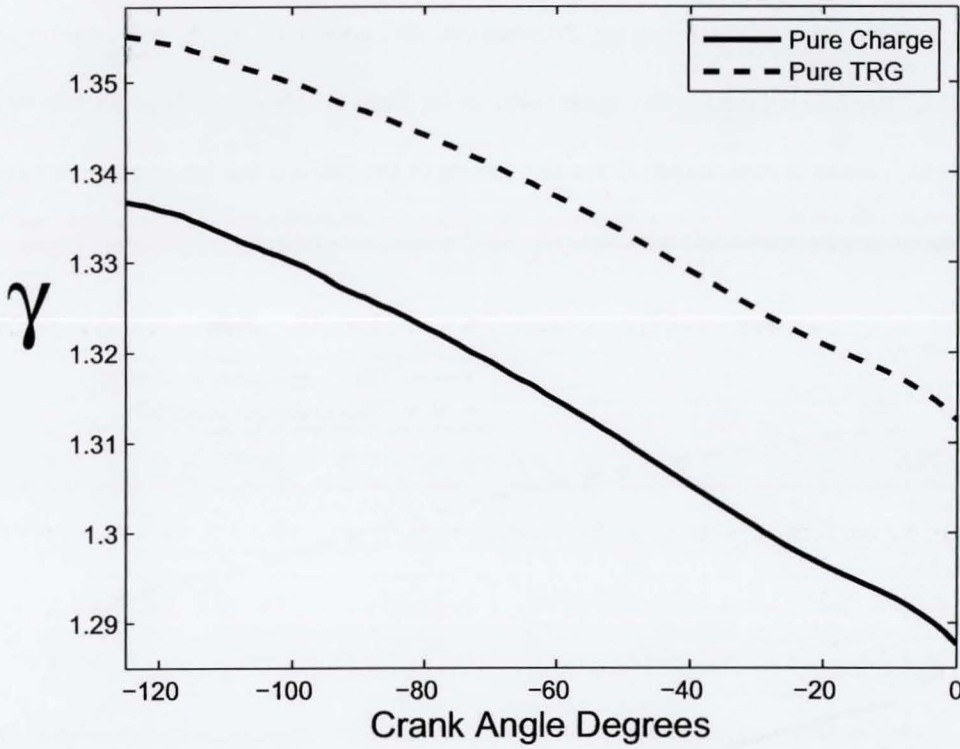


Figure 5.1: Gamma for the two possible extremes of mixture composition for a typical temperature trace of a compression stroke. 2000 RPM, 54% volumetric TRG, 2.9 bar IMEP

tures, one made up completely of fresh (stoichiometric) charge of the type used in this research³, the other made up entirely of burnt gas. The calculation has been based upon a typical temperature trace from a high TRG, HCCI data log. As can be seen in the figure, the value of γ remains largely unperturbed by the change in composition. The difference between the two traces is of the order of 1.6%.

Having examined the effect of composition upon γ , the temperature effect also needs to be investigated. Temperature cannot be directly measured and has to be derived from the pressure trace through use of the ideal gas equation of state (Eq. 5.6). Hence, the amount of TRG plays a role, not

³Commercial gasoline with H/C ratio of 1.78

only as a variable affecting the value of the mixture composition but also as a variable affecting the temperature trace. The effects of varying the estimated TRG amount by $\pm 50\%$ are demonstrated in figure 5.2. The data log used in this figure (same as for figure 5.1) has the maximum amount of TRG of a given series of experiments. Thus the varying of the TRG amount has maximum impact within experimentally reasonable numbers.

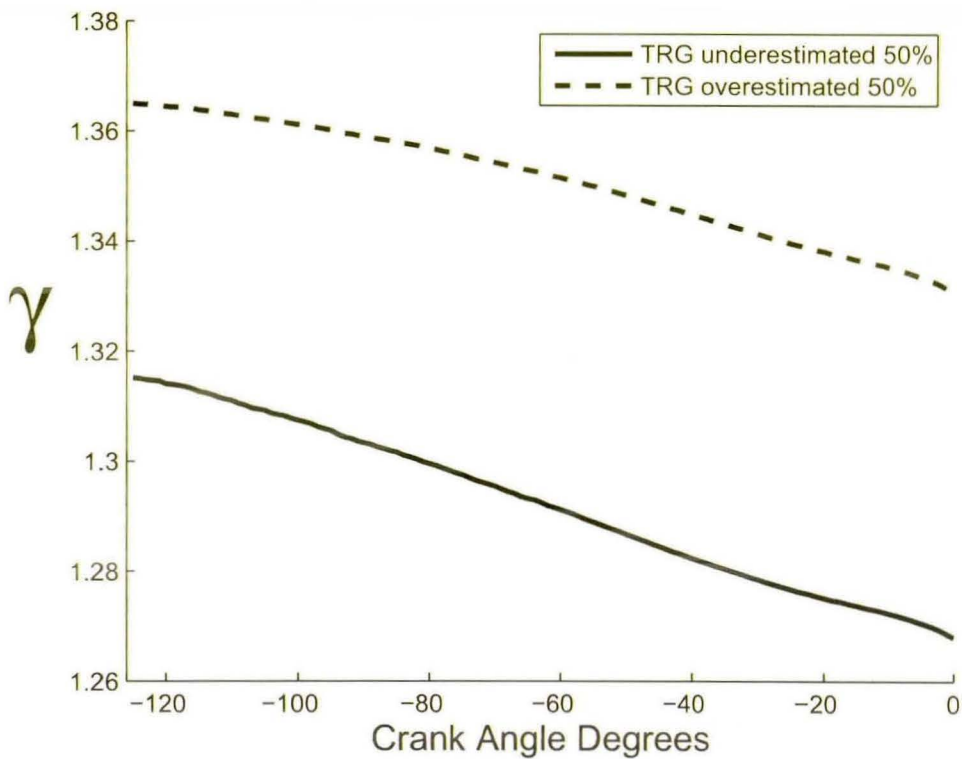


Figure 5.2: Gamma for a compression stroke where the temperature traces vary corresponding to varying the estimated TRG. 2000 RPM, 54%volumetric TRG, 2.9 bar IMEP

The effect shown here is calculated by taking a pegged pressure trace, changing the TRG amount and then calculating the new temperature trace and hence, the new γ trace. Thus, the changing TRG has a twofold impact upon on the final result. Note that, by looking at figure 5.1, increased amount of TRG in the mixture composition increases the value of γ . Also, since temperature increases from right to left as the compression stroke progresses towards TDC, it follows that

increasing temperature decreases γ . Now, because the temperature trace in figure 5.2 is affected by TRG amount according to Eq. 5.6, it follows that increased amount of TRG decreases the temperature, thus increasing γ . However, γ is further increased through the effect of increased TRG in the mixture composition. Still, despite the fact that the two effects add up, the overall effect on γ is of the order of 4.2%.

Having established the strength of the effect of mixture composition and temperature on γ , it follows that the next variable to be examined is the pegged pressure trace. In this case, κ has been varied by ± 0.05 , roughly the same magnitude as the variation presented in the extremes of figure 5.2. The result is demonstrated in figure 5.3. The pegging has been done following the matrix algebra technique of the polytropic method discussed above (page 91), with a fixed value for κ as quoted in the legend.

In order for the fixed κ assumption to yield accurate results, a suitable region has to be chosen to provide pressure/volume value pairs. The idea is to find a region that will yield some non trivial volume/pressure variation while keeping the value of γ and hence κ largely constant. The chosen region for the data throughout this research has been between -125 and -80 CAD.

As can be seen from figures 5.1 and 5.2, changes in γ are minuscule within this CAD region, hence making the constant κ assumption reasonable. It is also worth noting here that, because this region is early in the compression, temperature and pressure have not been increased significantly and hence any heat transfer between the gases and the walls is less pronounced than in the latter part of the compression.

Multiple data log method for estimation of the polytropic exponent

It is immediately obvious from figure 5.3, that high values of κ result in pegging the pressure trace lower. In the figure, the trace to the left of IVC is extrapolated using Eq. 5.1, while the

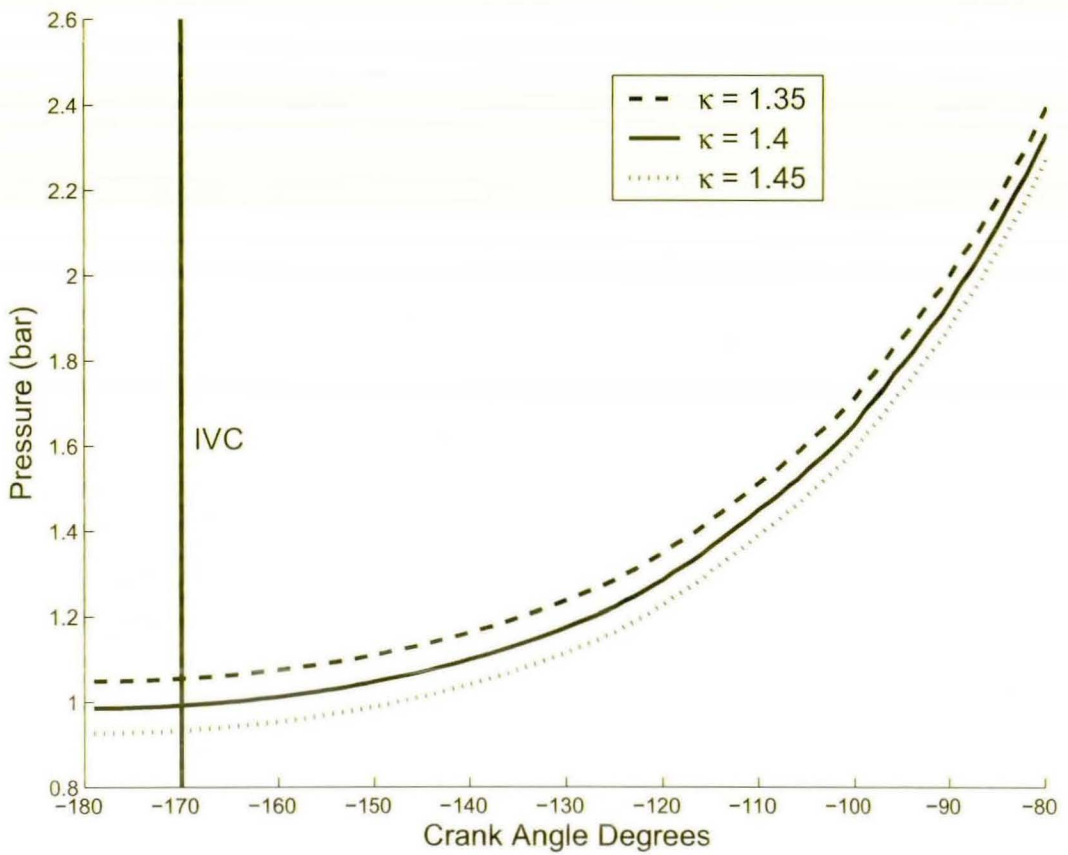


Figure 5.3: Pressure pegging at varying polytropic of expansion

trace to the right is the recorded experimental data. By extrapolating to the left of IVC the value of mixture pressure at Bottom Dead Centre (BDC) can be established. This is of course an ideal value, assuming that the mixture has been constant, i.e. discounting the effects of the valve flows. However, this value is important because there is an upper limit to it, that is, *it cannot exceed the value of MAP*. Hence, *this poses a lower limit on the value of κ* .

This result proves to be of great help when trying to establish the relationship between γ and κ . This is established by examining multiple data logs from different speed and load sites. The idea here is that, the extrapolated pressure value at BDC will vary according to these two settings. The simple assumption $\kappa = \gamma$ does not yield satisfactory results because certain data logs return pressure values at BDC above 1 bar. This is clearly an error, attributed to the fact that the κ deviation

from γ cannot be considered negligible.

To account for this, a linear relation $\kappa = \alpha \times \gamma$ is assumed. Because the pressure traces need to be pegged lower, α will have to be greater than 1.

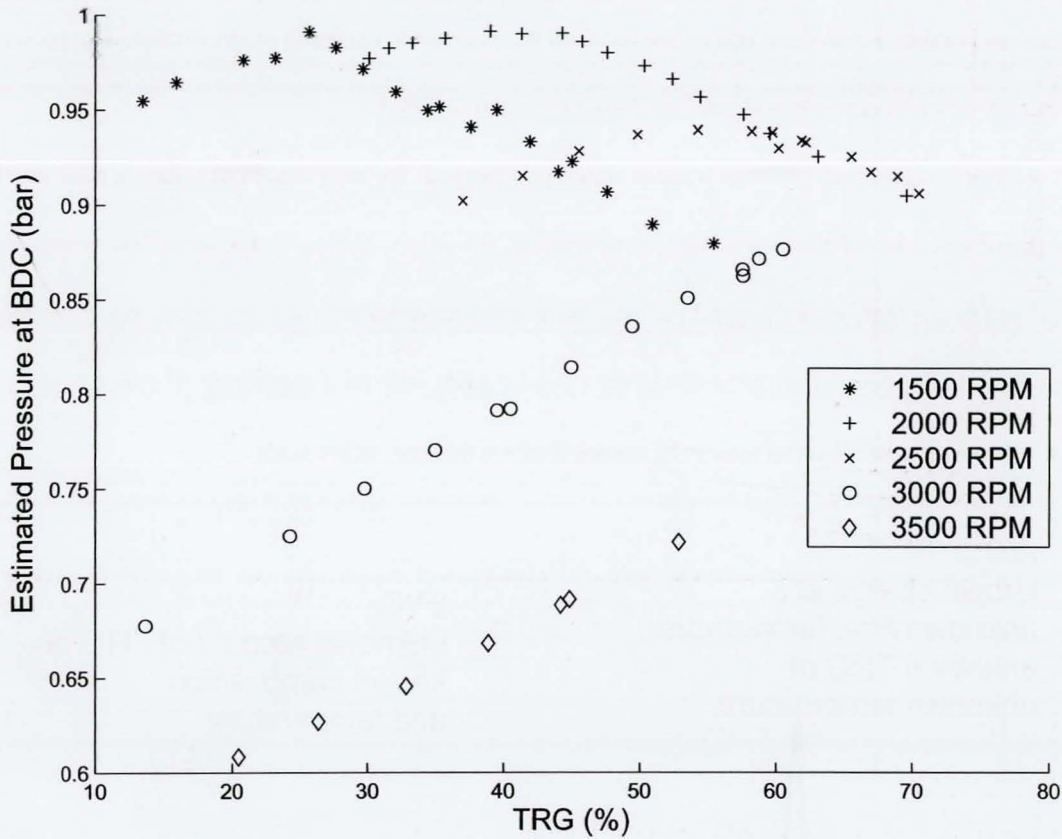


Figure 5.4: Estimated BDC pressure of averaged traces

Figure 5.4 demonstrates the resulting pressure values at BDC for data logs from multiple speed and load (TRG controlled) sites. For this research, setting the value of α to 1.05 yields the graph in figure 5.4. As can be seen, the points follow trends which correspond to what should be expected, offering the best overall fit that can be achieved with the data at hand. Thus, a very modest departure from the value of γ , calculated via the JANAF tables [87], corrects for κ - γ deviation.

5.1.2 TRG Estimation and Pressure Trace Imbalance

So far, no description has been offered concerning the TRG amount calculation. This is because of the cyclic interdependency nature of the variables involved. However, pegging and TRG estimation are inseparable due to the effect of the latter on the polytropic exponent of the former. The present section describes the method used for TRG estimation in detail.

Once an averaged pressure trace is accurately pegged, the next step is to estimate how much exhaust gas is being retained as TRG. Applying Eq. 5.6 to EVC will yield this value. The reasoning behind this is that, with a pegged pressure trace and known volume at every point, Eq. 5.6 effectively matches the number of moles of the cylinder gases with the temperature. If either is known at any point, then all variables can be established for that part of the trace.

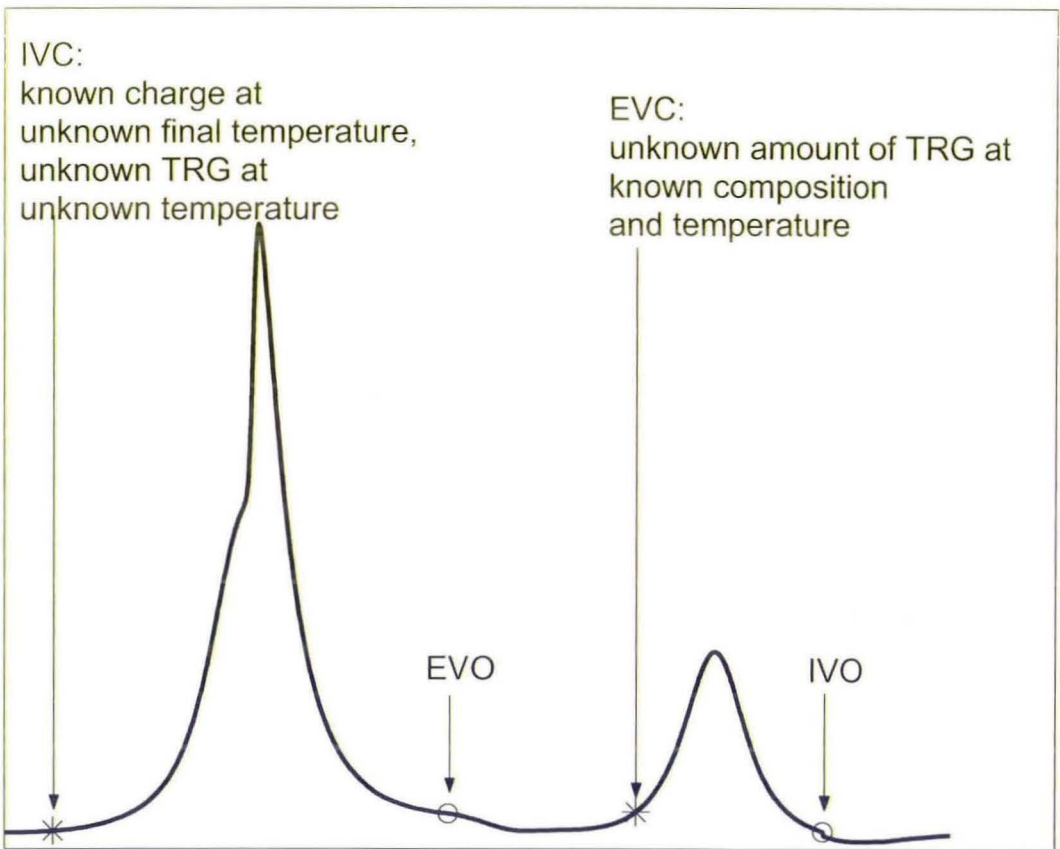


Figure 5.5: Comparison of IVC and EVC as starting points

The candidate points for such treatment are either IVC or EVC. Figure 5.5 summarizes the pros and cons of each of these as a starting point for further analysis. IVC boasts measured charge flows at measured temperature. However, these temperature measurements are taken outside the cylinder and are not representative of the final temperatures reached by the time the charge has been heated whilst entering the cylinder. Also, there is the very important factor of mixing with an unknown amount of TRG at an unknown temperature. Clearly, once these considerations are taken into account, IVC is not a good candidate for starting the analysis.

On the other hand, EVC offers a homogeneous mixture (completely made up of exhaust gas) and a temperature reading which is much more representative of the temperature inside the cylinder, the exhaust gas temperature. This measurement is taken very close to the exhaust valve and by the time the valve shuts, pressures and temperatures between the expanded gas inside and outside the cylinder should be identical. This might not hold for the whole length of the exhaust, due to non negligible thermal losses down the length of the pipe. However, in the close vicinity of the valve, bulk temperature and pressure inside and outside the cylinder are equalised soon after the exhaust valve opens.

The major drawback of assuming an equal temperature between TRG at EVC and the exhaust gas temperature reading is that exhaust gas temperature, is based upon an averaged thermocouple reading. Due to its slow response characteristics, this reading cannot be representative of the immediate temperature value at EVC. However, studies by fast response thermocouples [86] indicate a temperature variation under 80°C across the whole cycle for SI and HCCI combustion at 2 bar Brake Mean Effective Pressure (BMEP), 2000 RPM. This implies that, taking an averaged value, the corresponding error is an underestimation of temperature of the order of 40°C .

Simplified TRG Estimation

Given that pressure, volume and temperature are known, an application of Eq. 5.6 at EVC, yields a value for the moles of TRG.

However, the effects of the averaged thermocouple have to be accounted for at this stage. Because the temperature as used in Eq. 5.6 is measured in degrees Kelvin, the temperatures involved are large numbers (generally in the 600 to 900 range). Thus, a value shift of 40, as is the likely underestimation of the exhaust gas temperature, is a relatively small variation making the resulting overestimation of TRG equally small.

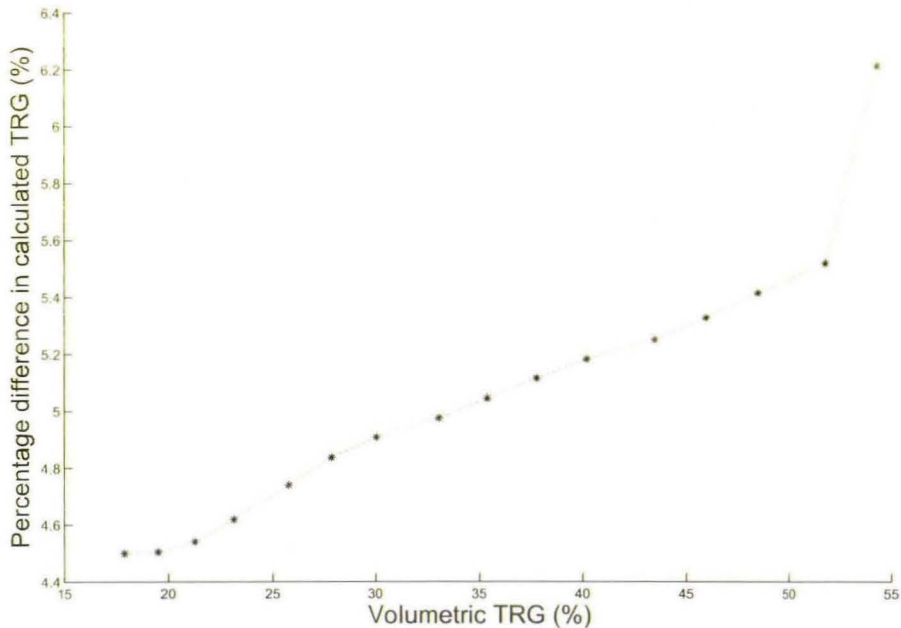


Figure 5.6: Percentage difference between TRG calculated by taking an averaged measurement and correcting by a temperature shift of 40°. 2000 RPM, WOT, TRG sweep.

Figure 5.6 demonstrates the percentage difference between TRG amount calculated by taking the averaged exhaust gas temperature and correcting by adding a 40°C shift. As can be seen from the figure, the resulting error in TRG is minimal, even in the case of data log with the maximum TRG amount. When considering figure 5.2, this TRG error will have an impact of the order of 0.002

on the value of γ .

Because of this negligible effect, the value of exhaust gas temperature has been used uncorrected throughout this research, rather than use a fixed temperature correction factor whose actual value might be influenced by unknown effects.

Assuming no significant blowby losses during the compression/expansion of TRG, the same amount of TRG present at EVC will be present in the following cycle's combustion stroke. Since, at this point, we are looking at an averaged trace for the whole data set, this cycle is one and the same. So, all that is needed is to add to it the amount of charge inducted in one cycle (calculated through knowledge of the intake flows and the RPM) and the total number of moles and composition of the mixture is then known. Applying Eq. 5.6 to IVC (with known pressure and volume), the temperature at IVC (and subsequent stroke) can then be calculated. The temperature trace of the TRG compression/expansion stroke can similarly be calculated, yielding the TRG temperature at IVO.

In practice, this number of moles for the mixture yields an unrealistic value for the temperature of the mixture at IVC. Certain data sets return a higher value for the temperature of the total mixture at IVC than the temperature of TRG at IVO, which is impossible since a hot gas (TRG) is being mixed with a colder gas (charge). This is illustrated in figure 5.7.

The problem might be simply erroneous pegging, resulting in a wrong value for TRG amount. The other suspicious value is the exhaust gas temperature which is assumed to equal the in-cylinder gases' temperature at EVC.

However, an analysis of the effects of these variables does not yield satisfactory results. In both cases, shifting the values to within a range wider than physically reasonable fails to resolve the issue.

Thus, a different source of error has to be identified in order for physically meaningful results

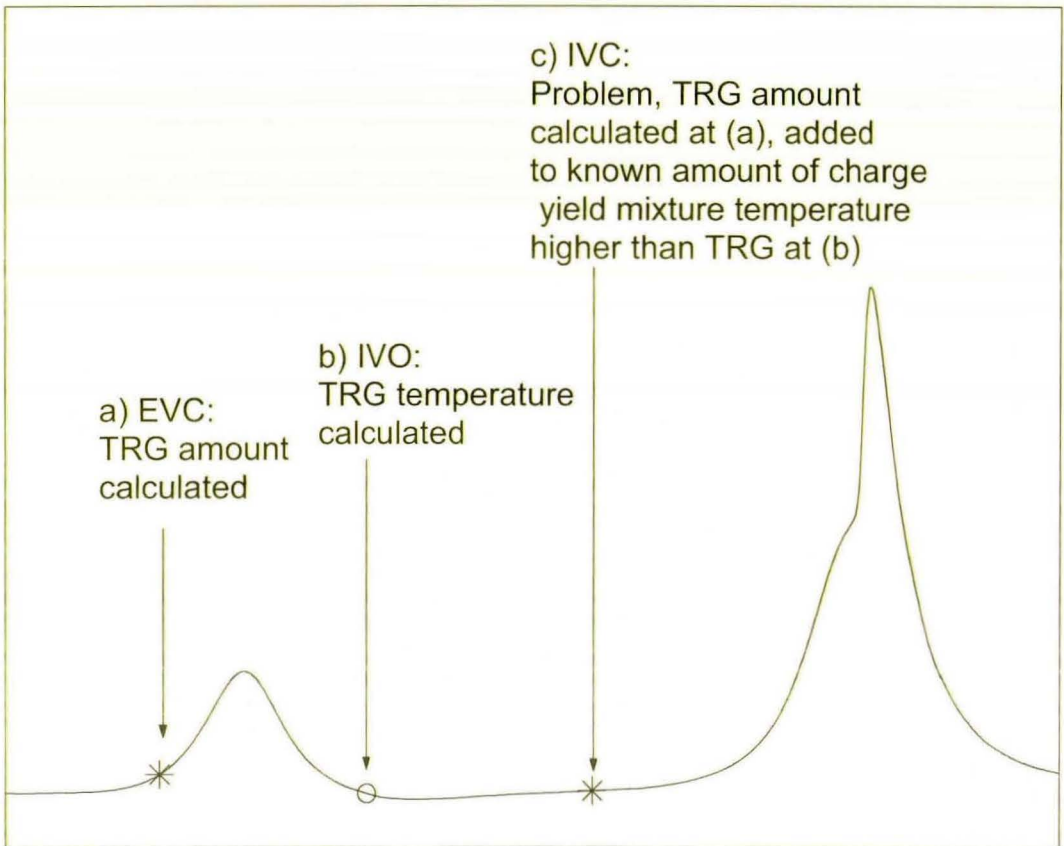


Figure 5.7: Temperature discrepancy between IVO and IVC

to be obtained.

Evidence of Pressure Trace Imbalance

The problem potentially lies with the response of the pressure transducer to thermal shock. The specifications of the non water cooled transducer used in this research allow for a possible 10% error in IMEP estimation on an SI engine. In this case, a water cooled transducer could not have been used due to limited space on the experimental engine cylinder head. Furthermore, HCCI combustion places a greater strain on the transducer due to the increased rate of pressure rise (typically, maximum rate of rise of HCCI 2.3 times greater than its SI equivalent).

This becomes apparent when investigating the characteristics of the HCCI cycle through P-V

diagrams. A data set has been considered, consisting of data where TRG was varied across its possible range (0% to 50% volumetric in that instance) while $IMEP_{gross}$ had been kept constant by throttling the inlet. By subtracting the losses of the gas exchange cycle, $IMEP_{net}$ can be worked out. Finally, through knowledge of BMEP, the value of Friction Mean Effective Pressure (FMEP) can be derived.

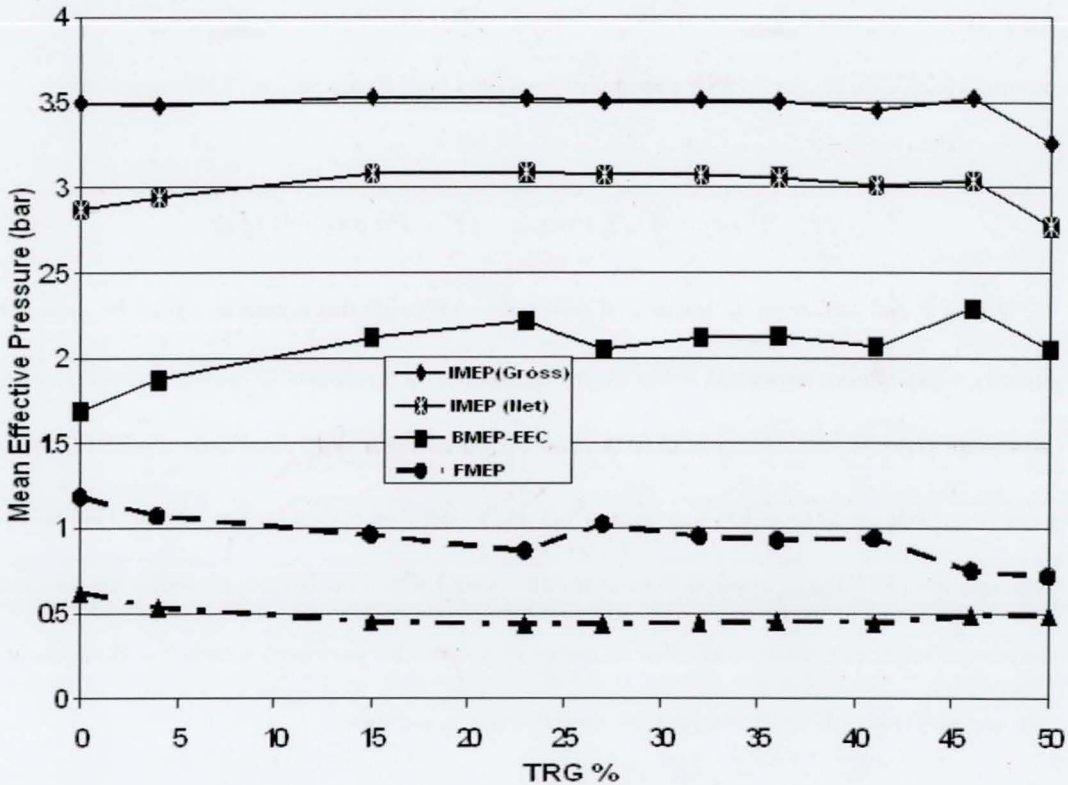


Figure 5.8: Suspicious IMEP, BMEP, FMEP trend

The observed trend was for measured BMEP to rise by approximately 0.5 bar across the TRG range, as seen in figure 5.8, leading the calculated FMEP to a drop of the same magnitude since $FMEP = IMEP_{net} - BMEP$ and the gas exchange work that is the difference between $IMEP_{gross}$ and $IMEP_{net}$ did not vary enough to affect the relation.

While BMEP measurement on a single cylinder engine can potentially be inaccurately related to IMEP, an observable 0.5 bar rise in BMEP (1.7 to 2.2 bar) is too big to be dismissed.

Rai et al [89] mention that cyclic exposure of a piezoelectric pressure transducer to combustion results in the expansion and contraction of its diaphragm due to large temperature variations throughout the cycle. This causes the force on the quartz to be different to that applied by the cylinder pressure alone. Thermal shock affects all parameters derived from pressure data, but the greatest is IMEP which can be affected by more than -10%. Thermal shock was found to be more significant at advanced ignition timings. Rai et al [89] derived an equation to compensate for thermal shock of a Kistler 6125A transducer used on a Ford Zetec engine. This equation is:

$$IMEP_{corr} = IMEP_{meas} + (F \times P_{max}) + Offset \quad (5.7)$$

Where F and $Offset$ are a function of RPM only. Although this equation cannot be used here directly, what is more important is that the compensation factor derived is only a factor of RPM and maximum pressure, increasing as they increase. It follows that HCCI combustion, with its greater peak in-cylinder pressures, has a greater effect on the IMEP measured by the sensor. That is why, although the $IMEP_{gross}$ appears to be constant, BMEP keeps increasing since BMEP has no errors introduced with increasing TRG. But as the peak in-cylinder pressures increase with increasing TRG and shift towards HCCI combustion, their difference increases.

Further evidence in support of this scenario surfaces when investigating unstable combustion. In these cases, a misfiring cycle will produce exhaust gases partly made up of its unburnt charge. When these are recompressed, during the TRG compression phase, they can sometimes ignite [86]. This ignition leads to an underestimation of the descending side of the curve. It is easier to appreciate this in the IVO region because the pressure values are expected to be in the region of 1 bar as is demonstrated in figure 5.9⁴.

In this figure, the second and fourth cycles misfire. Their respective TRG compression humps

⁴Also discussed on page 195

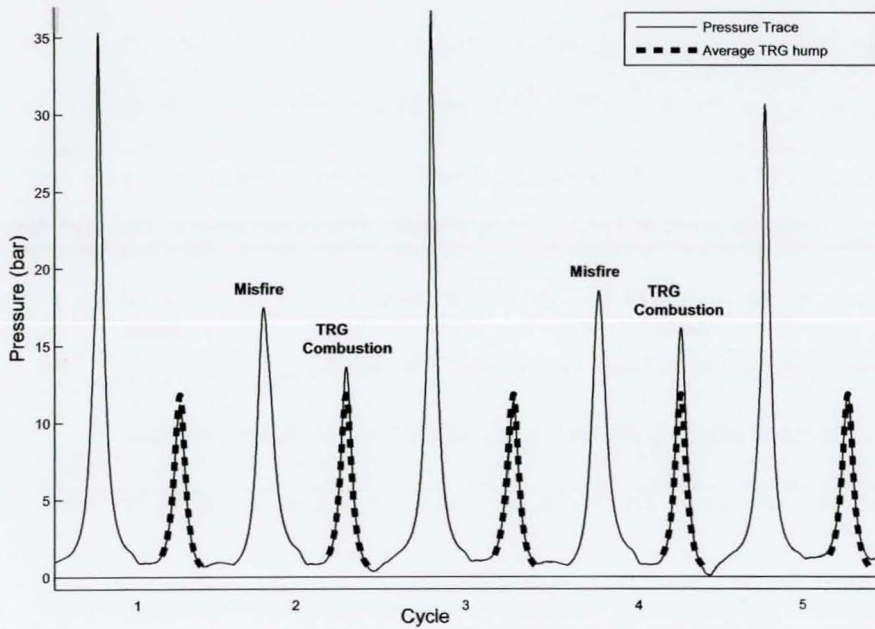


Figure 5.9: Thermal shock evidence following TRG combustion

are noticeably larger than the average (shown as a thick, dashed line). It is clearly visible that the lowest points of their IVO regions are unrealistically lower than their neighbours', in the case of the fourth cycle almost reaching a pressure of zero.

TRG Estimation via Corrected Pressure Trace

So far, the evidence in favour of a measuring imbalance between the 'hot' and 'cold' parts of a cycle seems plausible. In addition, preliminary tests done by shifting the EVC region, where TRG is calculated, relative to the IVC region, where the mixture starts the compression phase, yield very good results. The next step then becomes estimating how big this shift has to be.

In order to do this, some further equations have to be considered. What happens during the induction is that the hot exhaust gases in the TRG mix with the cold charge. Assuming negligible heat losses during this process, the sum of the energies of each must equal the energy of the total

mixture at IVC, i.e.:

$$(m_{trg} + m_{ch})c_{v_{mixt}(T_{mixt})}T_{mixt} = m_{trg}c_{v_{trg}(T_{trg})}T_{trg} + m_{ch}c_{v_{ch}(T_{ch})}T_{ch} \quad (5.8)$$

which is a conservation of internal energy equation between charge, TRG and their mixture. m_{trg} and m_{ch} are the masses of TRG and charge respectively. T_{mixt} , T_{trg} and T_{ch} are the temperatures of mixture, TRG and charge respectively. Finally, $c_{v_{mixt}(T_{mixt})}$, $c_{v_{trg}(T_{trg})}$ and $c_{v_{ch}(T_{ch})}$ are the specific heats of mixture, TRG and charge at their respective temperatures.

In addition to the above, Eq. 5.6 for the case of the total mixture at IVC becomes:

$$P_{ivc}V_{ivc} = (N_{trg} + N_{ch})RT_{mixt} \quad (5.9)$$

In both Eqs. (5.8) and (5.9), there are two unknowns, the amount of TRG, mentioned as mass in Eq. 5.8 and moles in Eq. 5.9 and the final temperature of the total mixture.

Also, 'unknown' is the specific heat of the total mixture (since it is at an unknown temperature). However, specific heat changes slightly with temperature and it can initially be taken as a constant until iterative methods yield a precise value.

The value of the TRG temperature is only dependent on the pressure values and not the moles of TRG as can be deduced from

$$T_{ivo} = T_{exh} \times \frac{P_{ivo}V_{ivo}}{P_{evc}V_{evc}} \quad (5.10)$$

Hence, by estimating specific heat values for the TRG, which has a known composition⁵, and the charge, an initial estimate for the specific heat of the mixture can be made by taking an average. Substituting these values into Eqs. (5.8) and (5.9) yields values for both the amount of TRG and

⁵the composition of the TRG is calculated through applying the equations for species' transformation found in [88] to the charge, whose composition is known through measurement of the fuel and air flows

the total mixture temperature. Recalculating the specific heat of the mixture based on the new temperature value yields more accurate values and so on until all terms in the equation balance.

What has been described above is in effect a statement that reads: calculate the amount of TRG at known temperature that, when mixed with a known amount of charge at a known temperature, will yield a mixture at an unknown temperature, occupying volume V_{ivc} at a pressure P_{ivc} .

However, there is also the initial method of estimation of TRG, based on applying Eq. 5.6 at EVC. These two methods should yield the same results. Unfortunately, they don't, which is where the pressure trace imbalance comes into play.

Hence, the first step in the analysis is one outer iteration whose aim it is to establish the shift of the 'hot' and 'cold' regions of the pressure trace. The shifted part has to be the 'hot' (in this research taken to be the region between 20 CAD after the combustion TDC and IVO) since the 'cold' region is where the whole trace has been pegged, via the polytropic curve fitting method, and is presumably correct. The aim of this iteration is to establish a positioning of the 'hot' region that yields a TRG amount and temperature at IVO that agrees with that predicted through the mixing method.

It has to be noted that the specific heats, used in Eq. 5.8 are composition and temperature dependent. Hence, with knowledge of the final mixture temperature arrived at through the mixing of charge and TRG, these specific heats can now be accurately established. However, changing their values will affect very slightly the mixing equation (5.8). Hence, an inner iteration deals with this temperature-specific heat dependency until successive calculations converge to a steady value.

Once both these iterative methods have been executed, the values for both TRG amount and hot-cold trace shift are established. The schematic in figure 5.10 sums up the procedure.

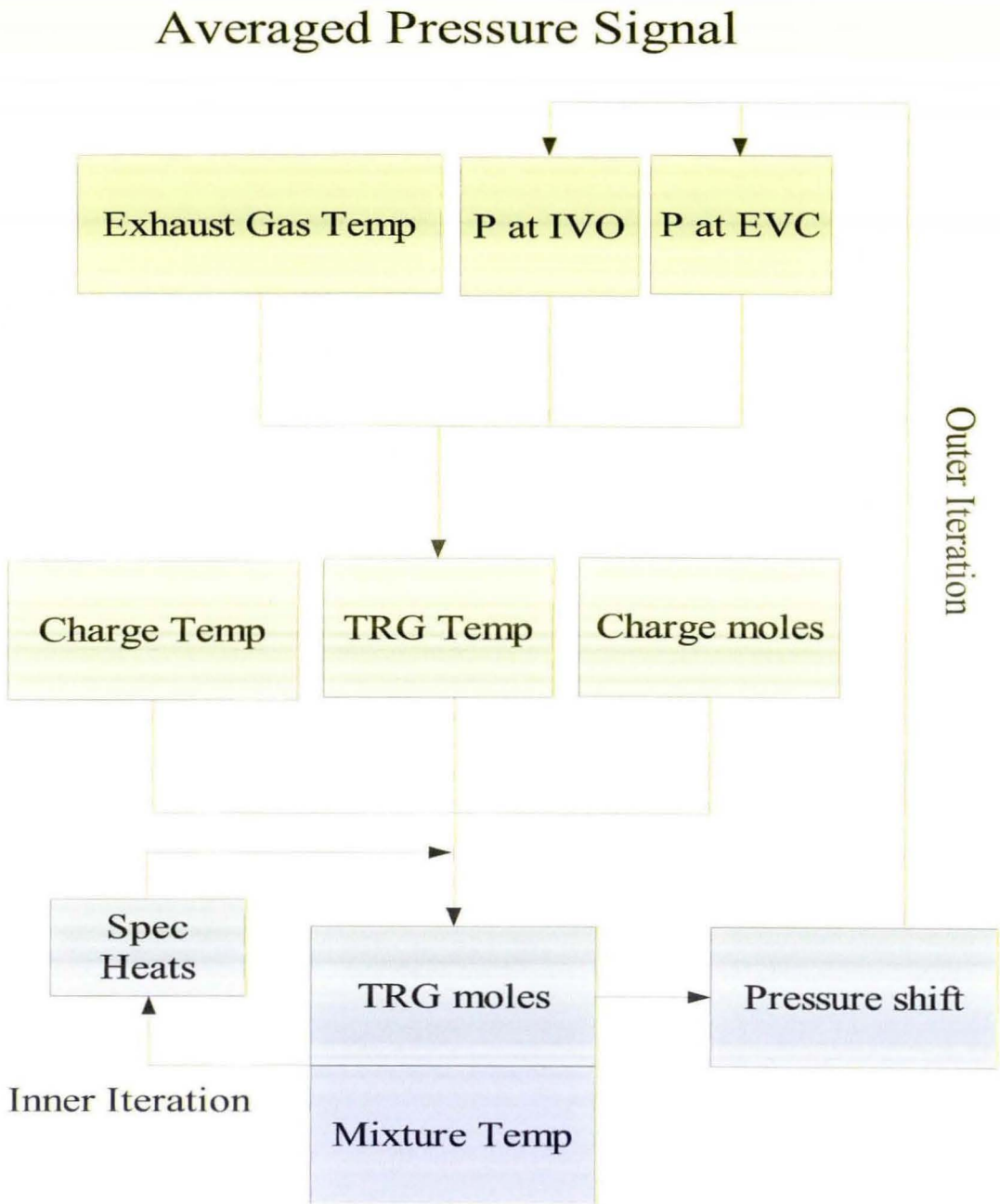


Figure 5.10: TRG, Mixture Temperature and Pressure Shift calculation process

5.1.3 Sensitivity Analysis of whole procedure to TRG temperature variation

As described so far, the proposed pegging and TRG estimation method depends upon various assumptions, the most debateable of which is the validity of the exhaust thermocouple reading as a gauge of bulk TRG temperature at EVC. The previous analyses of figures 5.1, 5.2, 5.3, 5.6 have dealt with single effects on certain variables at specific steps in the proposed method. However, it is not clear how the *overall* result is affected by errors in the actual value of bulk TRG temperature at EVC.

To test for this, a sensitivity analysis has been performed on a high TRG amount log at 2000 RPM. The reasoning behind is this, is that a) at higher RPM, the temperature variability should drop, since it is time dependent through cooling of the exhaust gases in the exhaust pipe. 2000 RPM being close to the low end of the experimental data available (data span 1500 to 3500 RPM), it is a perfect candidate and b) a high TRG log exhibits higher sensitivity to variables affecting TRG amount.

The affected variables are both TRG and the whole pressure trace, whose pegging depends upon the TRG amount through the temperature/composition dependent polytropic of compression. For varying TRG temperature at EVC, the resulting TRG amount is shown in figure 5.11. The thick vertical line marks the Exhaust Gas Temperature (EGT) as measured through the thermocouple, hence averaged. The dashed vertical line marks the $+40^{\circ}\text{C}$ point⁶. Thus, the marked region contains the likely actual values of EGT and hence TRG. It can be seen that the likely TRG error is of the order of 6%.

Similarly, figure 5.12 demonstrates the dependence of pegged pressure at IVC on TRG temperature at EVC. In this case, the result is even more insensitive, being under 1% for the whole 100°C region presented in the figure, let alone the 40°C plausible region.

⁶ 40°C is the likely underestimation of the actual value of EGT at EVC due to the averaging effect of the slow response thermocouple as discussed on page 100.

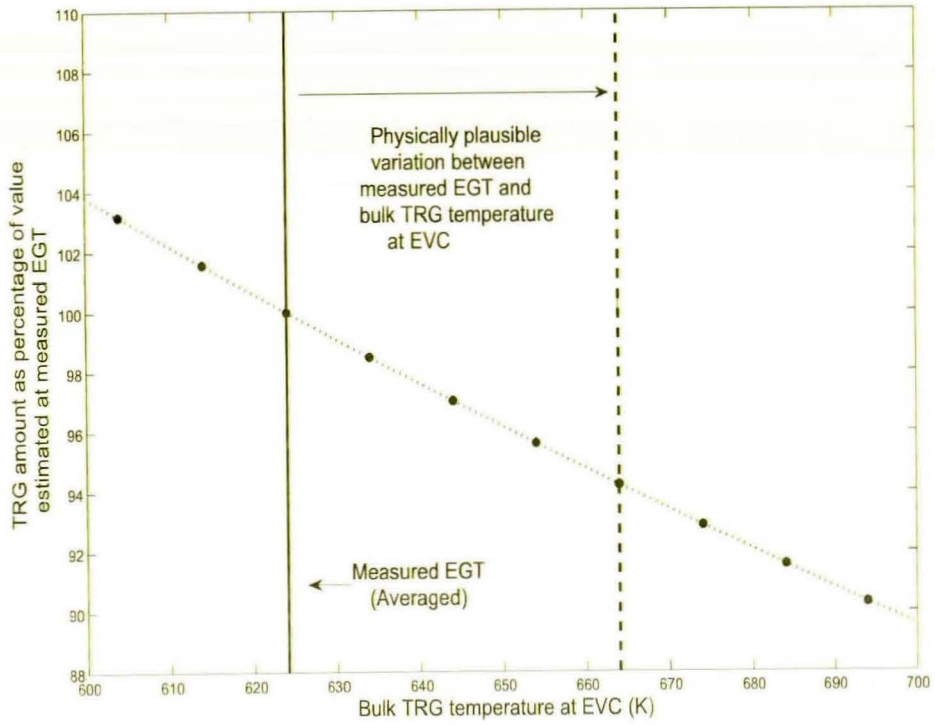


Figure 5.11: TRG amount dependence upon assumed bulk TRG temperature at EVC. 2000 RPM, WOT, 2.9 bar IMEP

From the above analysis, it follows that, within the expected inaccuracy due to the slow response nature of the thermocouple, the corresponding errors of pegging and TRG amount estimation are minimal once the whole procedure laid out in figure 5.10 has been carried out. Hence, the assumption that EGT can be used directly as a measurement of TRG temperature at EVC, as discussed on page 5.1.2, is justified.

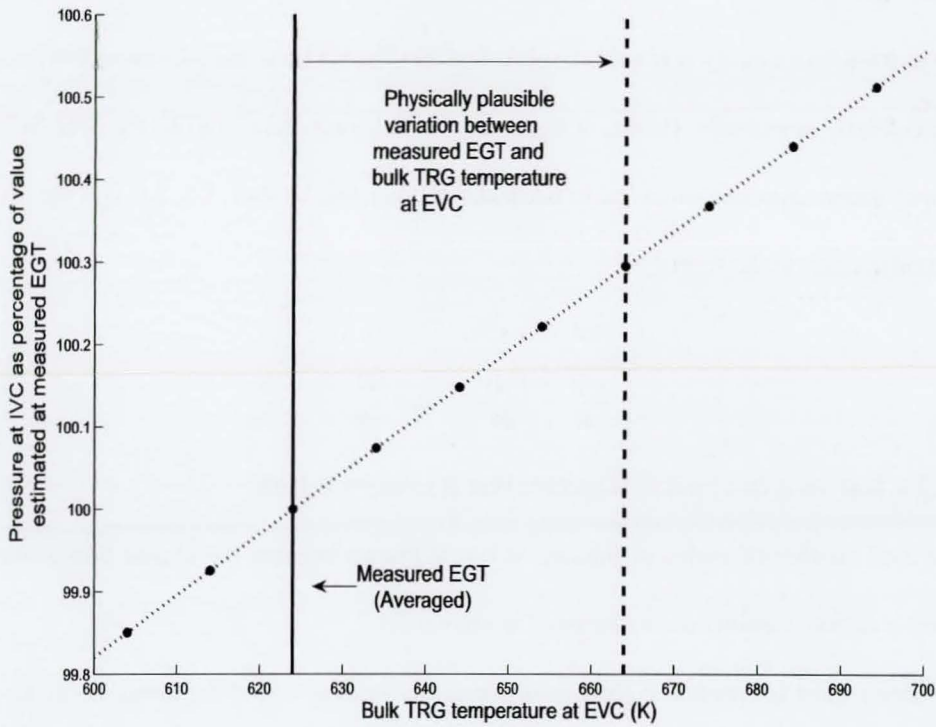


Figure 5.12: Pressure at IVC dependence upon assumed bulk TRG temperature at EVC. 2000 RPM, WOT, 2.92 bar IMEP

5.2 Heat Exchange

5.2.1 Theory of Heat Exchange Calculation

Once the pressure trace has been pegged and TRG estimated, combustion information can be extracted from the pressure trace. The main feature of interest is the heat release. This is often estimated through variants of the Rassweiler-Withrow method [90]. The main drawback of these, essentially geometric methods, is that although robust features like Location of 50% Mass Fraction Burnt (MFB50) are easily established, subtle features like start and end of combustion are much harder to identify objectively. Hence, in this research, the combustion analysis has been based directly upon thermodynamic variables, in particular the equation of state, Eq. 5.6, and the first law of thermodynamics in the form:

$$\frac{dQ}{d\theta} - \frac{PdV}{d\theta} = mc_v \frac{dT}{d\theta} \quad (5.11)$$

where Q is heat, m is mass and c_v is specific heat at constant volume.

The total number of moles of mixture at IVC is known because the charge flow is directly measured and TRG is estimated as discussed in section 5.1.2.

A volume trace is coupled to the pressure trace by making use of the crank slider with pin offset equation, which yields cylinder volume as a function of CAD:

$$V = V_c + \pi \frac{b^2}{4} \left\{ 1 + \frac{s}{2} - \frac{s}{2} \cos(\theta) - l \cos\left(\arcsin\left(\frac{\frac{s}{2} \sin(\theta) + PinOffset}{l}\right)\right) \right\} \quad (5.12)$$

where b is the bore, s the stroke, l the conrod length and $PinOffset$ is the piston pin offset.

Through knowledge of the number of moles, temperature traces can be calculated for both the mixture and the TRG compression-expansion strokes by means of Eq. 5.6. This temperature trace

can then be used to calculate the c_v values of the mixture through use of the JANAF tables [87]⁷.

Hence, through use of a measured pressure trace, a CAD dependent volume trace and a calculated mole dependent temperature trace, the $\frac{dQ}{d\theta}$ of Eq. 5.11 can be derived.

The evaluated expression, $\frac{dQ}{d\theta}$, represents a heat flow with respect to CAD. Since these correspond almost linearly to time within each engine cycle, they can be thought of as heat flow with respect to time, in effect Joules per second i.e. Watts.

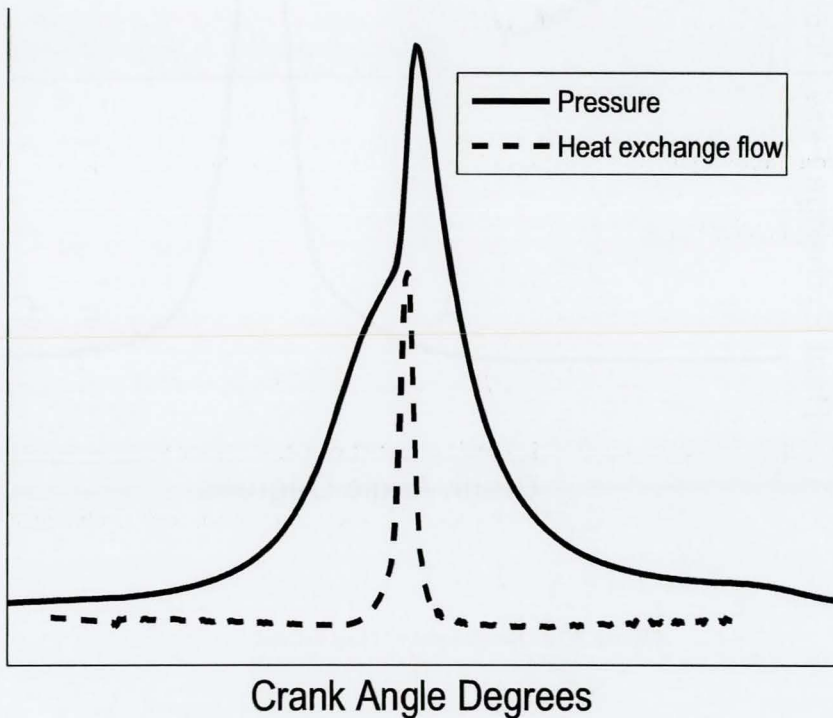


Figure 5.13: Typical Pressure and Heat Exchange Flow traces

Figure 5.13, shows a typical pressure trace, accompanied by the relevant heat flow trace. The energy term has been labelled *Heat Exchange Flow* because it represents the net heat flow between the gases and the environment, including heat generated chemically from within the gases. It does not represent the chemical heat release, even though it is mostly dominated by it. However, it is

⁷The effect of changing molar composition on this calculation is discussed in section 5.3.2

the sum of heat both transferred between the gases and the walls as well as generated within the gases through chemical transformations. Hence, some further manipulation is needed in order to identify the effects of the heat release.

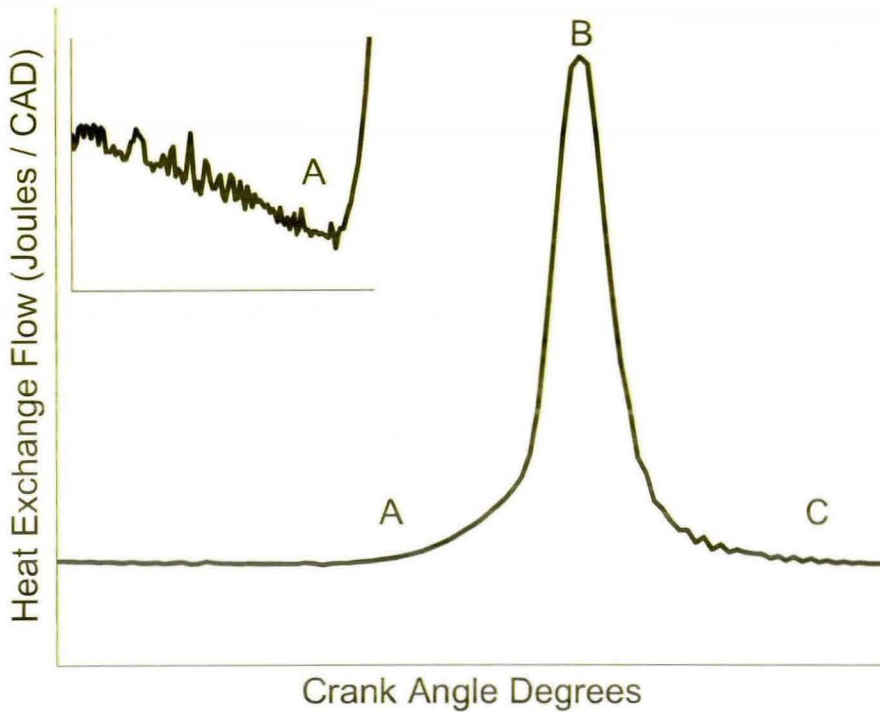


Figure 5.14: Breakdown of Heat Exchange Flow trace

The analysis of the heat exchange lies in identifying points A and C as shown in figure 5.14. A typical trace will strongly resemble a bell shaped curve. The important characteristics are the start and end of the bell, points A and C on the figure. These correspond to the start and end of the chemical heat release into the gases (and their subsequent chemical transformation), in other words, the limits of combustion. The curve to the left of A is not, in fact a straight line. A zoom of this area is shown in the inset of the figure. The reason the curve drops is because it indicates an increasing loss of energy to the cylinder walls as the gases' temperature increases due to compression by the moving piston. If no combustion occurs, this trend should continue as

long as the temperature rises, that is until TDC. However, any energy injection into the gases will reverse this trend. Thus, A is defined as the point where there is a turning point in this descending curve. By finding A, a very precise estimate of the start of combustion can be made [91]. Treating the curve similarly for C, the limits of the combustion can be derived.

Once the limits of the combustion have been established, further analysis is possible. The curve considered so far is $\frac{dQ}{dt}$, thus the area under it corresponds to energy. At any point, this new integrated curve gives the total of the heat exchanged between the gases and the environment since the start of the integration. This exchange is made up of the heat transfer between the gases and the cylinder walls and the heat injection by the chemical heat release. This is shown in figure 5.15.

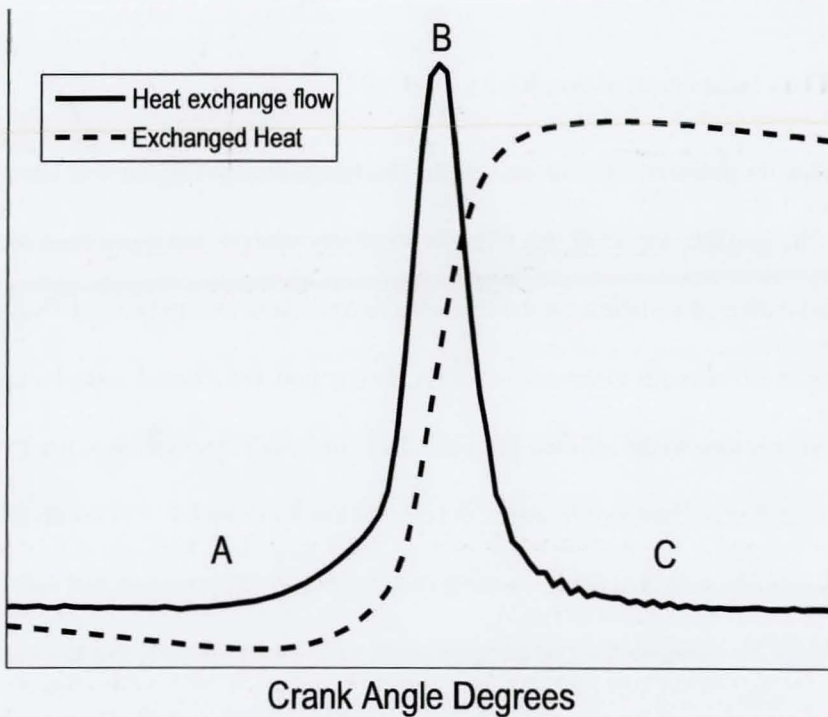


Figure 5.15: Heat Exchange Flow curve and its integral

This heat curve is the fingerprint of the combustion. If we assume that heat release and charge species' transformation are linearly related, then it follows that, scaled between 0 and 1 between

the A and C points, the curve corresponds to the Mass Fraction Burnt (MFB) trace.

Extraction of the MFB curve concludes the combustion analysis of a pressure trace. By using this curve as a reference, as well as the precalculated curves of P, V and T, a detailed investigation of the combustion event can be performed. However, the steps outlined in this section are by no means straightforward when it comes to implementation. What has been described so far has been applied to averaged pressure traces which are generally less noisy, do not exhibit great extremes and for which inducted charge values are directly measured. The main challenge is to be able to carry out this procedure on a cycle to cycle basis as accurately as possible, while maintaining a reasonably low computational load while sometimes having to treat cycles exhibiting extreme behaviour.

5.2.2 TRG temperature sensitivity analysis

At this point, the potential effect of the error in TRG temperature at EVC must be taken into account. To gauge the possible impact of this effect, a sensitivity analysis has again been carried out. The immediately affected variables are the temperature trace from EVC to IVO and TRG amount. From the mixing at IVO onwards to the rest of the IVC-EVO region, the affected variables are the total gas mixture amount (due to the affected TRG) and the corresponding temperature trace.

On the exchanged heat side however, the calculation, based on Eq. 5.11 depends on the $\frac{dQ}{d\theta}$, $\frac{dV}{d\theta}$ and $\frac{dT}{d\theta}$ derivatives with mc_v being a scaling factor of the $\frac{dT}{d\theta}$. The pressure and volume derivatives are unaffected by changing the TRG temperature at EVC. Hence the only variables affected are the mc_v product, m through the affected TRG amount and c_v through both the altered composition due to the former as well as due to the changed temperature. Finally, the temperature derivative term is also likely to be affected though not as much as the temperature trace itself.

The effect will be most strongly noticeable at high TRG levels. The numbers presented here are calculated from data at 2000 RPM, WOT, ITA=20, TRG set to 55% by volume, IMEP=2.9 bar.

The TRG temperature at EVC has been increased by $200^{\circ} K$ ⁸. This leads to a 24% decrease in the TRG amount and a subsequent 16% decrease in the total gas mixture. The gas mixture's IVC temperature increased by $92^{\circ} K$. The resulting heat exchange traces are seen in figure 5.16.

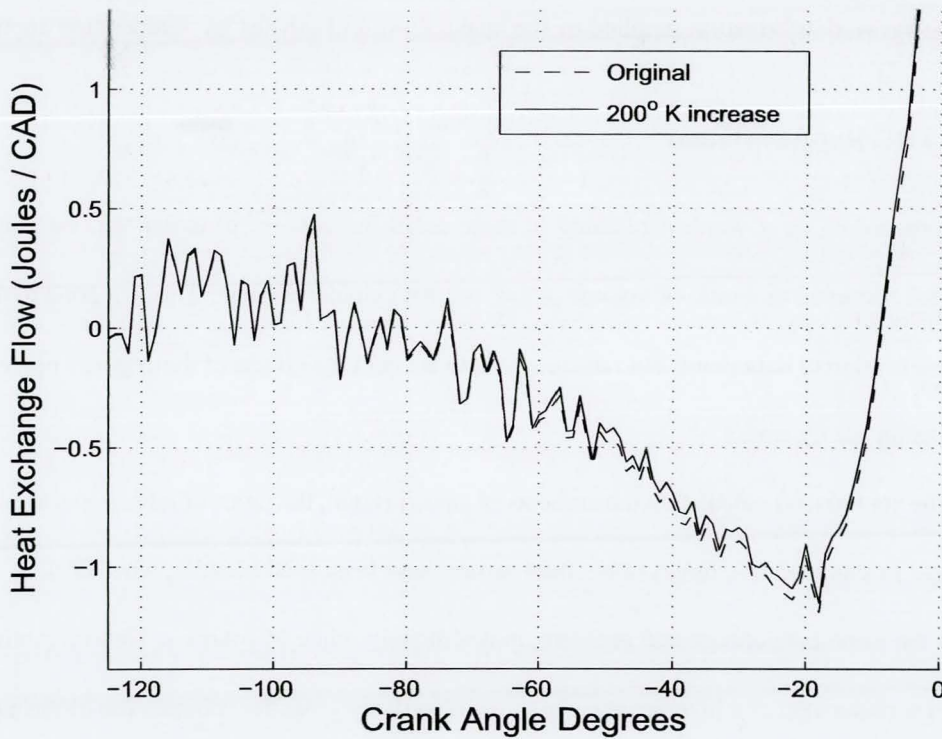


Figure 5.16: Heat Exchange Flow traces resulting from increasing TRG temperature at EVC by $200^{\circ} K$

The noticeable result is that, despite a very considerable change in the TRG temperature at EVC, the heat exchange trace is almost unperturbed. Hence, the choice in this research to use the exhaust gas temperature directly is again justified as far as the calculation of the heat exchange trace is concerned. Furthermore, because the main goal is to extract internally consistent values reflecting the dynamic behaviour between individual cycles, the accuracy provided so far appears

⁸Because the heat exchange trace is very insensitive to changes in TRG temperature at EVC, as seen in figure 5.16, a change much larger than in figures 5.11 and 5.12 has been required. This requirement further illustrates the point of the analysis.

more than adequate. However, if more advanced equipment or methodology is at hand, this can be readily employed in the present algorithm in order to produce even more accurate results.

All the procedures described so far only apply to averaged traces. This is because it is only for these that the vital information supplied by the intake flows and exhaust gas temperature apply.

5.2.3 TRG Representation

Before proceeding, it is worth explaining in more detail the concept of molar TRG estimation. Often, TRG is quoted as a ratio of volume at EVC to total cylinder volume. This is a good tool for easy classification of data points but fails to take into account the effects of the engine's operating conditions on gas dynamics.

On the contrary, by calculating the amounts of gases present, the ratios of moles or masses can be quoted. In this research, moles rather than masses have been used because, when dealing with gases at the same temperature and pressure, moles directly relate to volumes. Hence, quoting a number for molar TRG of a homogeneous mixture, effectively gives the volume ratio of the gases. This is comparable to the classic "volumetric" method mentioned above, with the added bonus that this number reflects a more accurate ratio of gases, implicitly taking the effects of gas dynamics into account. The obvious drawback is that, in order to calculate it, the procedures described in section 5.1.2 have to be carried out.

Figure 5.17 highlights the relation between the two TRG measuring conventions. It is noticeable that, in general, molar TRG is higher than volumetric. This is because the exhaust gases present at EVC are always at a pressure higher than that of the inlet (due to both exhaust back pressure being higher than inlet pressure and low valve lift of 2.5mm employed in the logging of these data). Hence, when the remaining volume fills up with fresh charge with the whole cylinder equating with the inlet pressure, the TRG takes up more volume than it did at EVC. The effect gets

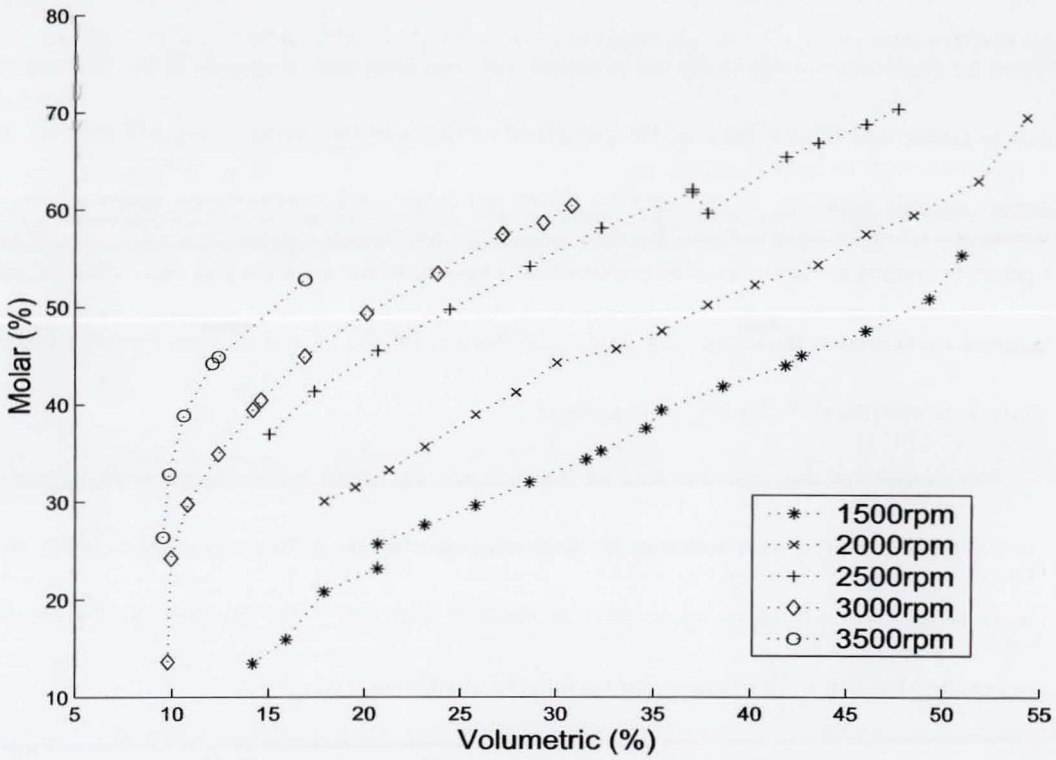


Figure 5.17: Comparison between TRG measuring methods

more noticeable with increasing RPM.

All the results demonstrated so far can be calculated from an averaged pressure trace with knowledge of inlet flows and exhaust gas temperature.

5.3 Individual Cycle Combustion Analysis

Once the combustion analysis for the averaged trace has been carried out, cycle to cycle analysis can be performed. This is because the calculated variables of the average trace will be close, but not necessarily identical, to the variables of the individual cycles within a log taken at a single operating condition. In the case of unstable combustion, where misfires and other extreme phenomena are common, these can vary greatly. In this section, the procedure used for extending the analysis to individual cycles will be explained.

The analysis in this case has to take into account the small variations between successive cycles. In the averaged trace scenario, the beginning and the end of the cycle could be assumed to touch. In this case, successive cycles pass information from one to the other through the TRG and temperature variables. This means that each cycle's variables, e.g.

- The pegging.
- The initial mixture composition.
- The thermal shock related pressure shift.
- The TRG.
- The exhaust temperature.

need to be established for each cycle. Also, due to the nature of this process, small errors can easily accumulate and damage the final result. This needs to be averted as explained in 5.3.1.

The first cycle "inherits" the data of the averaged cycle as a starting point. In the following text, we will consider the treatment of a random cycle, graphically represented in figure 5.18.

First, the cycle is pegged, using the value of κ estimated for the averaged cycle for the given data set (figure 5.18 (a)). Once the cycle is pegged, the pressure at IVC is known. This, in conjunction with the amount and temperature of TRG passed from the preceding cycle, the temperature and

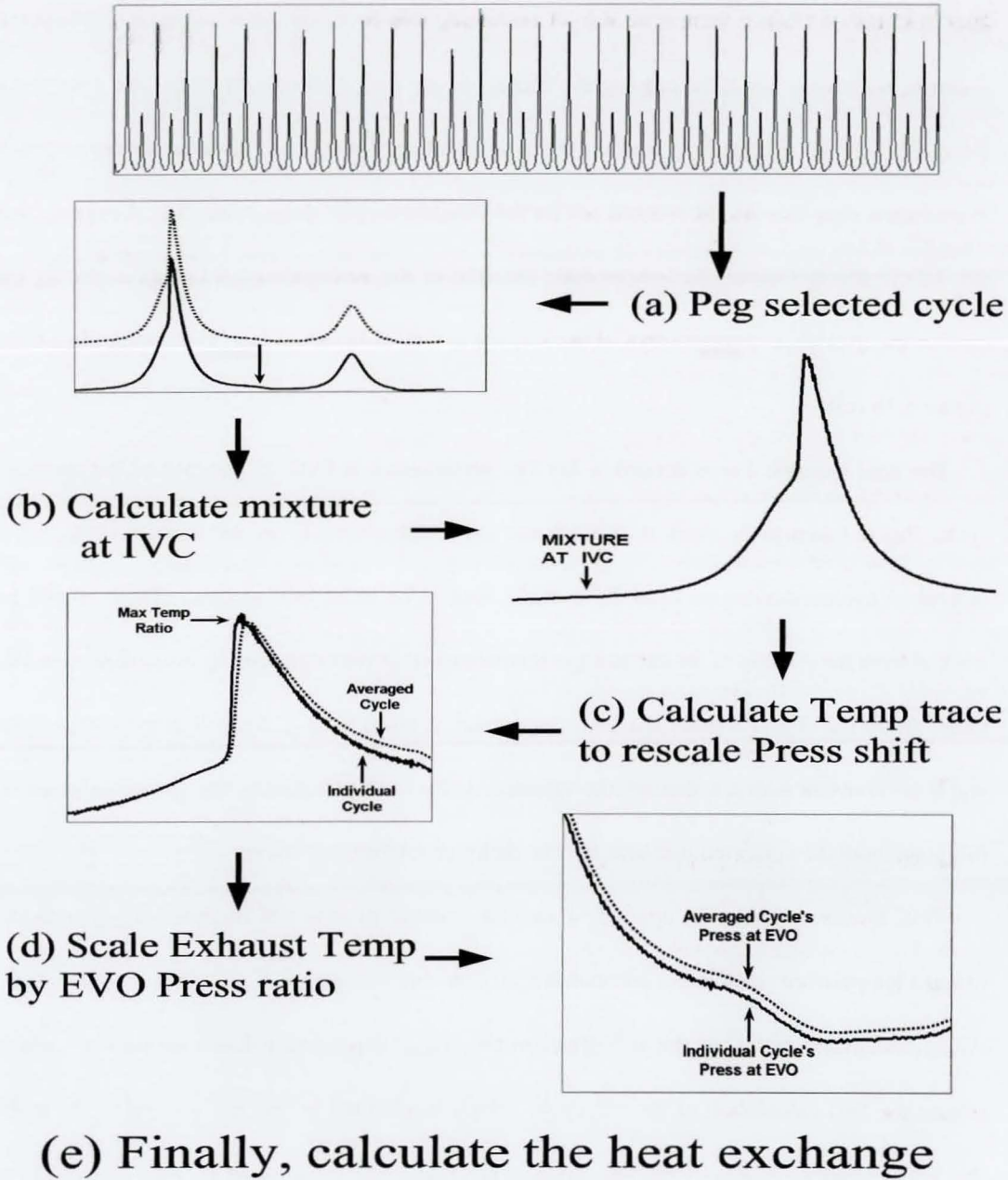


Figure 5.18: Treatment of individual cycles for cycle to cycle calculations

composition of the charge and the volume at IVC, yield the final amount of charge-TRG mixture at IVC through the use of Eqs. 5.8 and 5.9 (figure 5.18 (b)).

The pegged pressure trace is still not treated for the hot-cold shift. In this research, the shift calculated in the averaged case has been applied as a step change in the region between 20 CAD

after TDC and IVO. Since there is no way of estimating how much this shift varies between cycles, a simple technique has been employed. Since the pressure and volume traces are known for the individual and averaged cycles, and the total number of moles has been calculated at IVC, a temperature trace can also be worked out for the individual cycle through Eq. 5.6. Assuming that the shift is affected mostly by temperature, the shift of the averaged signal is then scaled by the ratio of the maximum temperatures of the two traces before being applied to the individual trace (figure 5.18 (c)).

The final variable that is needed is the TRG temperature at EVC. In the case of the averaged cycle, this is taken to be equal to the exhaust gas temperature. However, when looking at the individual cycles, deviations from the average need to be taken into account. These cannot be tracked from the reading of the exhaust gas temperature thermocouple since it is too slow to record them. From Eq. 5.6, it follows that this temperature is equal to $\frac{PV}{NR}$. Since V at the valve events and R are constant within a data set, the variation in this can be tracked by the $\frac{P}{N}$ fraction since by this stage both the corrected pressure and the moles of mixture are known.

This, however, cannot be applied. Using the number of moles of mixture, N_{mixt} , into the exhaust temperature calculation, introduces a variable that is inherited directly across cycles: from N_{mixt} , calculated at IVC of the n^{th} cycle, to the N_{mixt} dependent exhaust temperature which affects the TRG calculation of the n^{th} cycle, which is inherited by the $n^{th} + 1$ cycle. In trials, this led to runaway results. Thus, the variation in exhaust gas temperature is being scaled by the fraction of pressures only⁹ at EVC.

The operations described above yield all the variables needed to convert any given cycle to one treatable as per the average cycle treatment described in 5.1.2. Knowledge of the number of moles in the closed valve regions, IVC to EVO and EVC to IVO, also allows the calculation of the heat exchange as described in section 5.2.1.

⁹e.g. for the n^{th} cycle: $T_n = T_{average} \frac{P_n}{P_{average}}$

5.3.1 Safeguards against Erroneous Data

There are inherent safeguards in this procedure that guarantee results will be robust despite the unpredictability of the signal. The main problem of such an analysis is that certain cycles will yield wildly incorrect pressure values despite all corrective actions performed on the signal. These cycles most often occur after exceptionally violent combustion events and often exhibit unrealistically low pressure values that might persist after the pegging procedure. Since HCCI analysis is dependent on the fact that one cycle's TRG is used in the next cycle's mixture, such cycles will pass on highly inaccurate values.

The best safeguard for one incorrect cycle destroying the results of all subsequent cycles is that the amount of TRG is calculated by each cycle at EVC as a function of the directly measurable pressure trace only. To elaborate, consider that cycle n has a very inaccurate signal. Its TRG is calculated at its EVC and is wrong both as a mass and as a temperature, since the pressure at EVC is wrong and the temperature, scaled from the average signal's exhaust gas temperature via its pressure at EVO, is also wrong. The cycle following it, $n + 1$, inherits a wrong TRG estimation, leading to a wrong calculation of mixture moles at IVC and wrong results for the heat exchange terms. However, the damage stops here. The $n + 1$ cycle's exhaust gas temperature will be correct, assuming its pressure is correct, since it is scaled at its own EVO by pressure trace ratio only (averaged and individual). The TRG calculated for it will also be correct and hence the variables it passes on to cycle $n + 2$.

Of course, all this can be avoided if wrong cycles can be identified and treated separately. Such a safeguard has been put in place, stating that, if a cycle's pressure value at IVC deviates into improbable values even after pegging, it should be forcibly pegged to coincide with the averaged IVC pressure¹⁰. This will avoid getting too implausible values and potentially salvaging the following

¹⁰In this research a deviation of plus or minus 0.3 bar has been tolerated.

cycle. However, in some extreme cases, the pressure trace is visibly damaged along the whole length of the cycle, e.g. yielding extremely unrealistic pressure values in the EVO-EVC region even if forcibly pegged at IVC.

Given that such problems exist, having effectively a stop at the propagation of any information not dependent on the pressure trace at EVC, as described in the exhaust gas temperature scaling procedure above, makes for a robust analysis of all cycles.

5.3.2 Cycle to Cycle Heat Exchange Calculation Implementation

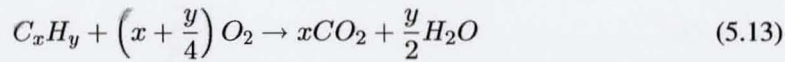
The procedures described in the previous sections, aim at supplying as accurate results as possible to the equations used for the calculation of the heat exchange flows. This theory has been laid out in 5.2.1. In this section, the implementation techniques used will be examined in more detail.

The most important result from the previous analysis is the composition of the mixture at IVC. In this research, 5 species are tracked: nitrogen, oxygen, fuel, carbon dioxide and water.

From the pressure and volume traces, their respective derivatives can be extracted. Given the number of moles present at any point, a temperature trace can also be calculated through Eq. 5.6. Since the specific heat is a function of composition and temperature, this can also be worked out through the JANAF polynomials [87]. Substituting these into Eq. 5.11 yields the gases' heat exchange.

The obvious question then to be asked is how to handle the transformation of the species in this scenario. The heat addition effect is traceable through its effect on pressure but this assumes correct estimation of the composition at every CAD.

Fortunately, the answer to that can be straightforward. If we examine the molar composition the molar change between reactants and products is actually very small. This follows from the chemical equation for combustion of a stoichiometric oxygen/hydrocarbon mixture:



In the case of this research, where commercial gasoline (which is a blend of various substances) has been used, the values for x and y are taken to be $x = 8.01$ and $y = 14.3$. Hence, the equation effectively reads that 1 mole of fuel reacts with 11.585 moles of O_2 . However, there are 3.773 moles of nitrogen per mole of oxygen in atmospheric air, hence the composition of a stoichiometric mixture for one mole of fuel is: 1 mole of fuel, 11.585 moles of O_2 and 43.71 moles of N_2 , a total of 56.3 moles. Of these, only the fuel and O_2 react. From an initial value of 12.585 moles ($1 + (x + \frac{y}{4})$), they produce 15.16 moles of products ($x + \frac{y}{2}$). When the 43.71 moles of N_2 are also accounted for, the total becomes 56.3 moles yielding 58.87 moles of products, an increase of around 4.5%¹¹.

Now, if we take into account that in HCCI combustion, the charge (fuel, O_2 and N_2) will be itself only a fraction of the cylinder gases, it is obvious that the *total* number of moles will be almost unchanged by the combustion. This means that the temperature trace, dependent only on the ideal gas law, Eq. 5.6, will be largely independent of the timing of the species transformation.

Although, the extracted temperature trace will be only slightly affected by the choice of combustion positioning, the effect on the composition and hence, to the specific heats, leading to a potential error in the final heat exchange is less easy to visualize.

To test for sensitivity in such a context, two heat exchange traces are presented in figure 5.19. These have been calculated by assuming the pressure traces are correct, composition is *fixed* to either pure charge (plus TRG) or pure exhaust gases throughout the stroke and the specific heats have been varied according to temperature at every point. Hence, equation 5.11 has been applied with c_v varying according to temperature only according to the JANAF Thermochemical tables [87] for both extreme cases.

¹¹ Also, see figure 6.6, page 155 and figure 6.13, page 164

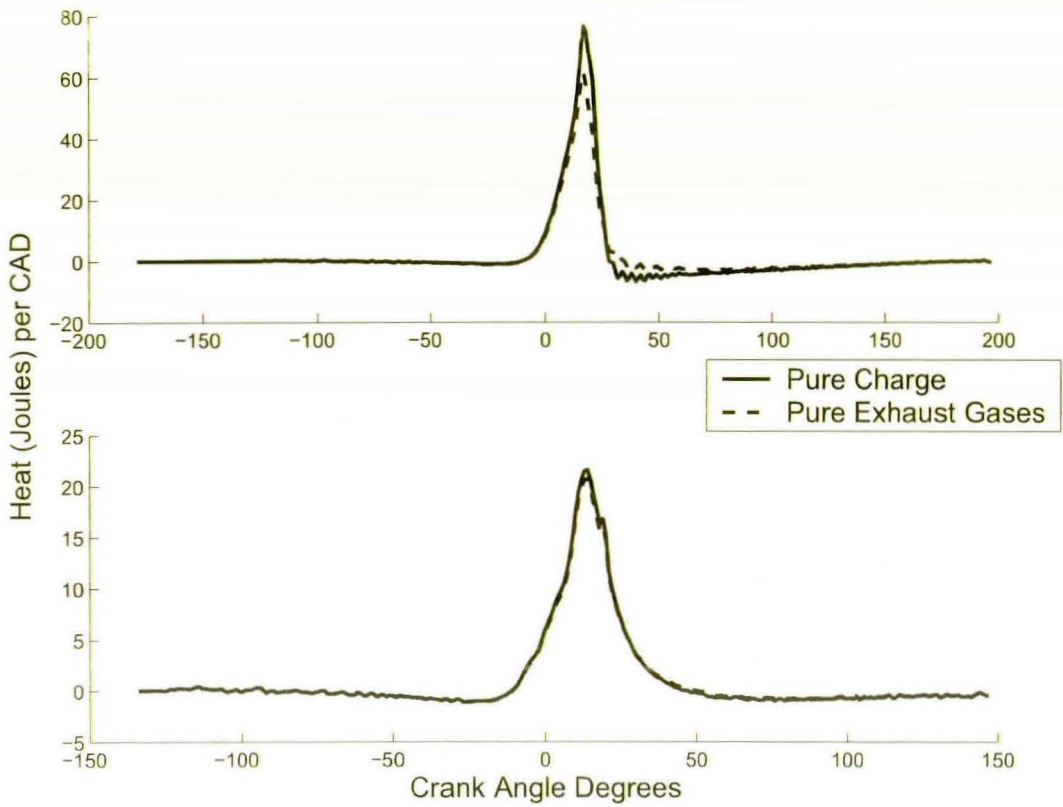


Figure 5.19: Comparison between $\frac{dQ}{d\theta}$ traces for minimum (top) and maximum (bottom) TRG

The top trace is from a data set with low TRG, 13% molar ratio, while the bottom has high TRG, 55% molar ratio. It is evident that, in the low TRG case, the dissimilarities are more obvious, since it contains a higher percentage of transformable species, while the high TRG case yields virtually identical plots.

In numeric terms, if we assume the charge does not undergo any transformation, the low TRG diagram (figure 5.19, top) yields 637 Joules of heat by integration over all data points since the trace represents Joules per CAD. At the other extreme of the spectrum, if we assume that the cylinder contents are made up entirely of exhaust gases, the resulting diagram yields 616 Joules of heat. The difference is less than 4%.

In the high TRG diagram (figure 5.19, bottom), the pure charge case yields 327 Joules, whereas the pure exhaust gases case yields 321 Joules, a difference less than 2%.

It is clear from the above that precise tracking of the species' transformation is not vital as far as calculation of the numeric value of the exchanged heat is concerned. However, great accuracy in this number, though welcome, is not of great importance in the scope of this research, since the main goal is the accurate extraction of the MFB trace. Since the MFB trace is normalised, the major consideration is the shape of the heat exchange curve, which, as has been demonstrated, does not vary significantly even among the extreme cases of TRG variation.

If maximum precision is the aim of research, then the following procedure can be carried out. The algorithm can be run initially to extract a "wrong" heat exchange trace, based upon a process with no species' transformation (or any another MFB extraction method such as the Rassweiler and Withrow method [90]). This will return a reasonably robust trace for the MFB. Then, the algorithm can be rerun, only this time tying the species' concentrations to the extracted MFB trace.

While this will, in principle, return the most accurate results available by this method, it has not been carried out in this research. The reason is that the slightly increased accuracy is not worth what is, in effect a doubling of the computational time¹². What has been used instead, is an instantaneous transformation of all reacting species at TDC.

5.3.3 Cycle to Cycle Investigation Example

The full power of the analysis comes into play when looking at cycle to cycle results. Figure 5.20 displays cycles from the same region as figure 5.9. The data is logged from an unstable combustion at 1500 RPM, Ignition Timing Advance (ITA)=34, Wide Open Throttle (WOT), volumetric TRG is set to 50%, resulting in an IMEP of 3.47 bar. In order to understand the flow of events, information on the following variables is very useful:

1. Moles of charge

¹²At the time of the publication, the MATLAB implemented algorithm ran for approximately half an hour in order to process a 500 cycle data set on a Windows 2000, 2.4 GHz Pentium 4 PC with 512 MB of RAM

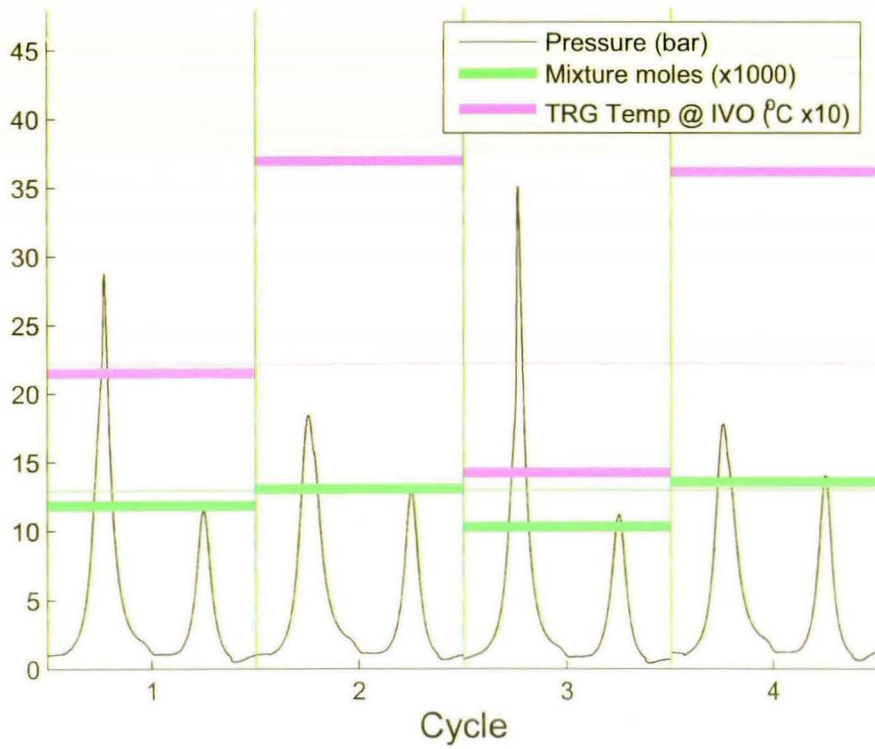


Figure 5.20: Cycle to cycle analysis of unstable combustion

2. Moles of TRG
3. Moles of total mixture
4. TRG temperature (at IVO)
5. Exhaust gas temperature (at EVO)
6. Start of Combustion
7. Duration of Combustion

In order not to overly clutter the figure, only parameters 3 and 4 are displayed. The values of the moles of total mixture and TRG temperature are displayed as thick bars of different colours over the regions of their respective pressure traces. The thinner bars in the same colour mark

their respective mean values for the whole data set and act as reference. The addition of standard deviation bars would lead to cluttering problems so these have been omitted. It should be noted that the temperature variation on the Y axis is larger than that expected on the basis of the moles of total mixture as can be seen by the scattering of the respective bars in the figure.

The leftmost cycle is slightly less energetic than average, having started with a slightly lower number of mixture moles (thick green bar) than average (thin green line). It is followed by a normal TRG compression hump, at the end of which, TRG has a temperature (thick red bar) very slightly lower than average (thin red line).

The slightly low TRG temperature of the first cycle, leads to a good intake at the start of the second cycle (as the fresh charge is not heated too much), ending up with total mixture just above average. The cycle then misfires, as can be seen by the low peak pressure of its first hump. The misfire leads to TRG rich in unburnt charge being recompressed during the second hump of the cycle. This second compression ignites the TRG [86], leading to a high peak pressure for the second hump and a TRG temperature far above average.

This very hot TRG now mixes with fresh charge at the start of the third cycle. Due to the high temperature heating up and expanding the incoming charge, the moles of total mixture end up very low. The cycle ignites relatively early, hence the high peak pressure. Then due to the early ignition leading to increased heat losses and to the low initial charge, bringing in less chemical energy, the final TRG temperature is very low.

This TRG at low temperature mixes with fresh charge in the final cycle, leading to the highest value of total mixture of these four cycles. The cycle then also misfires and ignites during the TRG compression as can be seen from the high peak pressure and TRG temperature.

This example illustrates both the interplay of consecutive cycles in HCCI combustion and the usefulness of carrying out the described combustion analysis in full in order to be able to investi-

gate the variations of all the representative variables.

5.4 Summary

This chapter has explained the technique employed in post processing the pressure data in order to gain a deeper understanding of events on a cycle to cycle basis. The focus has been on HCCI combustion, which poses certain demands not normally associated with SI operation. However, the same techniques in a simplified form (no need for TRG estimation, thermal shock not as important an issue) can be adapted for SI data analysis. This has been the case wherever results from SI data have been presented in this research.

The drive for devising such an analysis has been the nature of HCCI combustion. Because of the interlinking between cycles, a close look at the conditions dominating each individual cycle is a valuable tool in order to obtain an understanding of how and why certain behaviours are observed. This information cannot always be supplied directly by contemporary sensors and must thus be calculated in as computationally efficient a way as possible. By carrying out the presented analysis the following are derived:

1. polytropic of compression
2. pressure trace pegging
3. pressure trace shift between hot and cold region
4. TRG amount
5. mixture composition
6. temperature trace
7. heat exchange trace

8. MFB trace

While stable combustion does not usually exhibit great extremes of behaviour, it is unstable combustion that needs to be investigated in order to be understood and avoided to the greatest possible extent. However, it is exactly in the case of unstable combustion that the most violent extremes are recorded, leading to recording problems due to sensor limitations. Hence, the methods so far described have been tested and calibrated over a wide range of operating conditions and have proven to salvage most cases of unstable cycles without seriously compromising the accuracy of the results. Of course, more advanced hardware, mainly in the form of pressure transducers resistant to thermal shock and fast response thermocouples will enhance accuracy and do away with many of the assumptions which have been necessary in this research.

Chapter 6

Modeling

While post processing of the experimental data as described in chapter 5 is a vital consideration, it does not represent the whole picture. Though the extraction process yields the recorded values, it cannot present us with information on how things might be different under other circumstances. Thus, a modeling approach has also been performed, closely based upon the techniques described in Chapter 5. The aims of building such a model have been:

1. To create a versatile tool for future combustion research.
2. To be able to compare various theoretical cycles with existing ones.
3. To be able to predict a series of cycles purely from the model.

Since the main research aim has been HCCI, the model is focused on the closed valve segments (compression - combustion - expansion) of the cycle and also the TRG compression - expansion. However, the model has been expanded to include cycle to cycle coupling. This needs to be done to add extra functionality by making the model predict Start of Combustion (SoC), since achieving this goal can lead to a large extent to independence from time consuming and expensive experimental investigation.

Unfortunately, due to the difficulty in successfully predicting HCCI combustion phasing, only the first two goals have been adequately achieved. Given the current state of experimental data, it seems that the third goal is only achievable in very general terms but not in terms of cycle to cycle prediction to the extent of making experimentation redundant.

6.1 Software Design

What has been implemented is a zero dimensional thermodynamic model whose main design goal has been to be as versatile as possible through modular design. All the programming has been done in Mathworks' MATLAB environment using standard commands without recourse to any particular Toolbox. The general idea behind the software design has been to make the code largely independent of specialised functions, thus making it robust both in terms of possible changes in future MATLAB releases, as well as reasonably portable to other languages.

While a zero dimensional model is very limited compared to the many modeling approaches discussed in 2.3, building a highly advanced model had never been among the aims of the research. The main idea has been controlling HCCI, aided by experimental data as shown in Chapter 5. A complex model like for example, fine grid CFD, could not have been adequately validated anyway using the experimental setup at hand which only supplied a pressure and ion current reading and which would be unacceptably slow for control purposes. Hence, the design is focused instead on quantities that can be verified with the experimental setup at hand. The results demonstrate that insights can be gained regarding the behaviour of non measurable quantities (e.g. charge mixture). From a control point of view, a zero dimensional model is among the least computationally expensive, making it a potential candidate for hardware implemented engine control purposes.

6.1.1 Governing equations

There are two usual ways of implementing an internal combustion engine model: using a polytropic equation for the compression and expansion or implementing a conservation of energy equation based upon the first law of thermodynamics. In the case of the present model, the latter has been chosen as it allows for an easier visualisation of the variables involved.

In the present model, the first law of thermodynamics has been expressed in the form:

$$\frac{dQ}{d\theta} - \frac{PdV}{d\theta} = mc_v \frac{dT}{d\theta} \quad (6.1)$$

where Q is heat, m is mass and c_v is specific heat at constant volume. θ , used throughout these equations, corresponds to CAD.

The in-cylinder gas mixture is assumed to be adequately approximated as an ideal gas. The second equation that then has to be satisfied is the ideal gas equation of state¹:

$$PV = NRT \quad (6.2)$$

where N in this case represents the molar amount of the in-cylinder gases and R is the universal gas constant.

By inspection, Eqns 6.1 and 6.2 appear to have eight variables:

P, V, T, Q, m, c_v, N and θ

Of these variables, θ is the controlling variable everything else is a function of.

N is the total number of moles of in-cylinder species. When considering closed valve segments of the cycle, it remains constant when no combustion occurs. Thus it requires tracking only during the combustion segment of the cycle.

¹Regarding the use of the ideal gas equation see footnote on page 93

c_v is a function of composition and temperature only. Therefore, establishing these will also yield c_v .

m , which is exhaustively described by tracking the composition. It is constant during the closed valve segment of the cycle.

Q is the heat transferred to (e.g. as chemical heat release) and from (e.g. as heat loss through the cylinder walls) the gases. In other words, it is heat *exchanged*, as mentioned in Section 5.2.1.

V depends on θ only.

P and T are the remaining interlinked variables.

Extraction of Pressure, Temperature and Volume derivatives

If we consider the closed valve segment of the cycle, it is evident that composition changes occur only during the combustion. In contrast, volume changes occur continuously. Hence, we can separate two driving processes, on one hand continuously changing $V(\theta)$ and on the other hand, for θ within the limits of combustion, composition changes giving rise to $N(\theta)$ and $Q_{hr}(\theta)$, where Q_{hr} corresponds to the chemical heat release. The total heat exchanged, $Q = Q_{hr} - Q_{wall}$, where Q_{wall} corresponds to heat lost or gained through the cylinder wall.

The good thing about the changes occurring during the combustion is that they are dependent only upon the combustion profile. In other words, the only thing that needs to be determined is typically a sigmoid describing the shape and position of the MFB. Given this, the composition changes and chemical heat addition are exhaustively described. Because of this, the only θ variables that need to be determined are P , T and c_v . To track these it is best to change Eqn 6.2 to differential form and solve both Eqns 6.1 and 6.2 as a system of differential equations. Because c_v is only dependent upon composition (known via the combustion profile) and T , the problem ends up as two equations with two unknowns as is shown below.

To get Eqn 6.2 in differential form, take the logarithm of both sides and differentiate [92] to

yield:

$$\frac{1}{P} \frac{dP}{d\theta} + \frac{1}{V} \frac{dV}{d\theta} = \frac{1}{T} \frac{dT}{d\theta} \quad (6.3)$$

This form of the equation, along with Eqn 6.1 contain $\frac{d}{d\theta}$ derivatives for P, V, T, Q only². Furthermore, of these V depends solely upon θ .

Where Q is concerned, $Q = Q_{hr} - Q_{wall}$ and Q_{hr} depends solely upon the heat profile. Q_{wall} on the other hand, can be estimated via a heat transfer formula such as proposed for example by Annand [93] or Woschni [94]. The heat cylinder wall heat transfer formulation used in the present model is described on page 142, however, the important thing to note here is that these formulations (Eqns 6.14, 6.13) do not contain $\frac{d}{d\theta}$ derivatives for P or T .

Hence, by treating the $\frac{d}{d\theta}$ derivatives for P, V, T, Q as the variables of Eqns 6.1 and 6.2 and noting that in the case of V and Q , these can be cleanly separated, we can solve for the P and T derivatives.

The solution for $\frac{dT}{d\theta}$ is derived straight from 6.3:

$$\frac{dT}{d\theta} = T \left(\frac{1}{P} \frac{dP}{d\theta} + \frac{1}{V} \frac{dV}{d\theta} \right) \quad (6.4)$$

²It is worth mentioning here that for this form to hold, an assumption of constant N must be made, otherwise an extra term of $\frac{1}{N} \frac{dN}{d\theta}$ will also appear on the right hand side of the equation. The constant N holds everywhere in the closed valve region except for the combustion region.

However, while species transform during combustion, the *total* number of moles, N , remains mostly unperturbed. To illustrate this, consider that a purely stoichiometric mixture (where maximum species' transformation occurs) combusting changes its N by under 4.5% across the combustion. If inert TRG is present, this percentage drops even lower. Hence, to keep computation low, N has been assumed to be constant even in the combustion region as far as the equation 6.3 is concerned.

If, however, extra finesse is required, N and its derivative $\frac{dN}{d\theta}$ can be calculated through the species' transformation derivatives which are described in 6.10 and 6.11 on page 140.

By substituting 6.4 into 6.1, the solution for $\frac{dP}{d\theta}$ is derived:

$$\frac{dP}{d\theta} = \frac{P}{mc_v T} \left[\frac{dQ}{d\theta} - \left(P + \frac{mc_v T}{V} \right) \frac{dV}{d\theta} \right] \quad (6.5)$$

V is derived from the crank slider with pin offset equation:

$$V = V_c + \pi \frac{b^2}{4} \left\{ 1 + \frac{s}{2} - \frac{s}{2} \cos(\theta) - l \cos(\arcsin(\frac{\frac{s}{2} \sin(\theta) + PinOffset}{l})) \right\} \quad (6.6)$$

where V_c is the clearance volume, b is the bore, s the stroke and l the conrod length.

By differentiating with respect to θ we get the solution for $\frac{dV}{d\theta}$:

$$\frac{dV}{d\theta} = \pi \frac{b^2}{4} \left\{ \frac{s}{2} \sin(\theta) + \left(\frac{s}{2} \sin(\theta) + PinOffset \right) \left(\frac{1}{\sqrt{1 - \left(\frac{\frac{s}{2} \sin(\theta) + PinOffset}{l} \right)^2}} \right) \frac{s}{2l} \cos(\theta) \right\} \quad (6.7)$$

Thus, of the derivatives presented here, $\frac{dV}{d\theta}$ can be calculated as is given θ . For the rest, $\frac{dT}{d\theta}$ can be calculated once $\frac{dP}{d\theta}$ is established. This in turn, requires calculation of $\frac{dQ}{d\theta}$ whose derivation is explained below.

Species' Transformation and Extraction of the Heat derivative

So far, expressions for the derivatives of P , V , and T have been presented. In order to have a complete image of the $\frac{dP}{d\theta}$ expression (Eqn 6.5), the $\frac{dQ}{d\theta}$ needs to be known. Hence, some further assumptions must be clarified.

Because $Q = Q_{hr} - Q_{wall}$, it follows that both the chemical heat release and the heat loss through the cylinder walls must be established. The chemical heat release is dictated by the rate of species' transformation. By introducing a combustion profile, the changing species can be tracked during the combustion, along with the corresponding chemical heat release. This profile is typically in the shape of a sigmoid, in this instance implemented as a Wiebe function:

$$x(\theta) = 1 - e^{-\alpha \left(\frac{\theta - \theta_0}{d} \right)^n} \quad (6.8)$$

where θ_0 denotes the start of the sigmoid, d is the duration and α and n are parameters altering the shape of the curve as seen in figure 6.1.

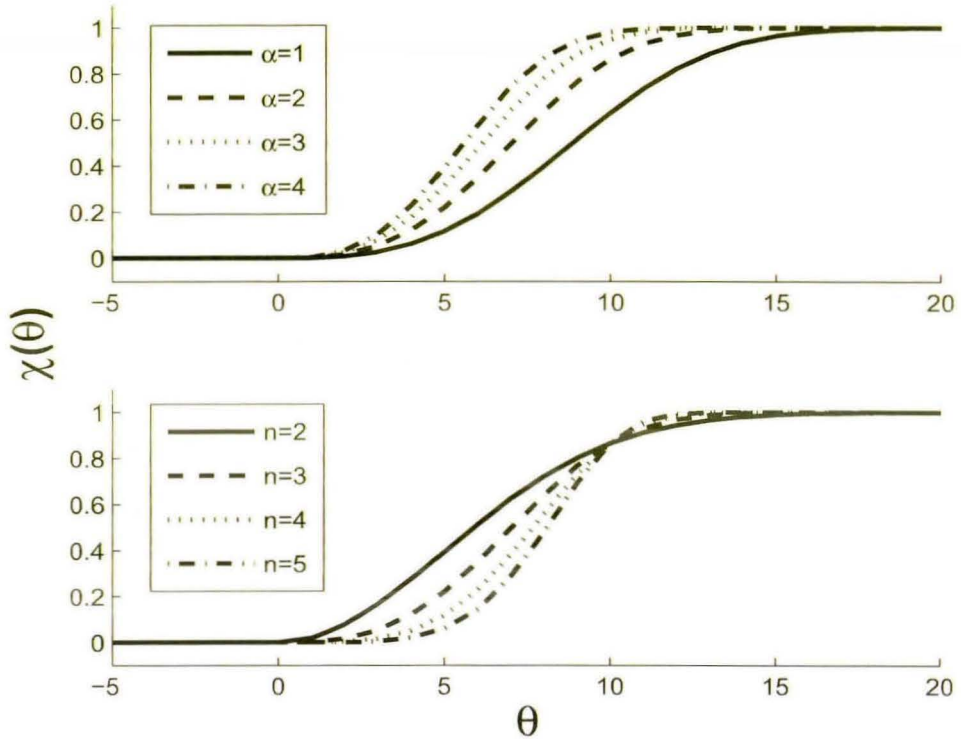
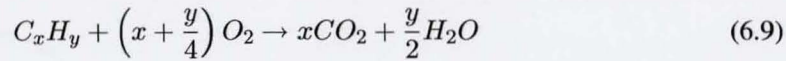


Figure 6.1: Effect of varying α (top) and n (bottom) on the shape of a Wiebe sigmoid

By relating the combustion to a Wiebe function, both the species' transformation and resulting heat release can be established. The former can be derived through the chemical equation describing combustion of a stoichiometric hydrocarbon. The latter is derived through knowledge of the calorific value of the hydrocarbon in question.

The chemical equation for combustion of a stoichiometric oxygen/hydrocarbon mixture is given by:



What is of interest however, is the changes to each individual species as the hydrocarbon fuel (C_xH_y) reacts with oxygen. The species tracked are Nitrogen, Oxygen, Carbon Dioxide, Water and the hydrocarbon fuel. The mole differentials of each of the non fuel species are related to the fuel differential through the following equations [84]:

$$\begin{aligned} \frac{dnO_2}{d\theta} &= \left(x + \frac{y}{4}\right) \frac{dnC_xH_y}{d\theta} \\ \frac{dnCO_2}{d\theta} &= -x \frac{dnC_xH_y}{d\theta} \\ \frac{dnH_2O}{d\theta} &= -\frac{y}{2} \frac{dnC_xH_y}{d\theta} \\ \frac{dnN_2}{d\theta} &= 0 \end{aligned} \quad (6.10)$$

By requiring that the Wiebe sigmoid represents the MFB, it follows that the hydrocarbon fuel's $\frac{d}{d\theta}$ derivative follows the negative³ derivative of the Wiebe function (Eqn 6.8).

Hence, by differentiating Eqn 6.8:

$$\frac{dx(\theta)}{d\theta} = -\frac{dnC_xH_y}{d\theta} = \frac{an}{d} \left(\frac{\theta - \theta_0}{d}\right)^{n-1} e^{-\alpha\left(\frac{\theta - \theta_0}{d}\right)^n} \quad (6.11)$$

The above expression relates the transformation of the hydrocarbon fuel and, as a consequence of Eqns 6.10, all in-cylinder species to the Wiebe sigmoid's derivative. This derivative is shown in figure 6.2. What must be noticed at this point is the relation between these two theoretical constructs and the relation between the exchanged heat and its integral as extracted from experimental data, shown in figure 5.15 on page 116.

The fuel's transformation, as dictated by the Wiebe derivative provides a measure of the chemical heat release through knowledge of the converted fuel's Lower Heating Value (LHV). For a LHV

³Negative because the Wiebe sigmoid represents MFB, whose rate of rise equals the rate of fuel depletion.

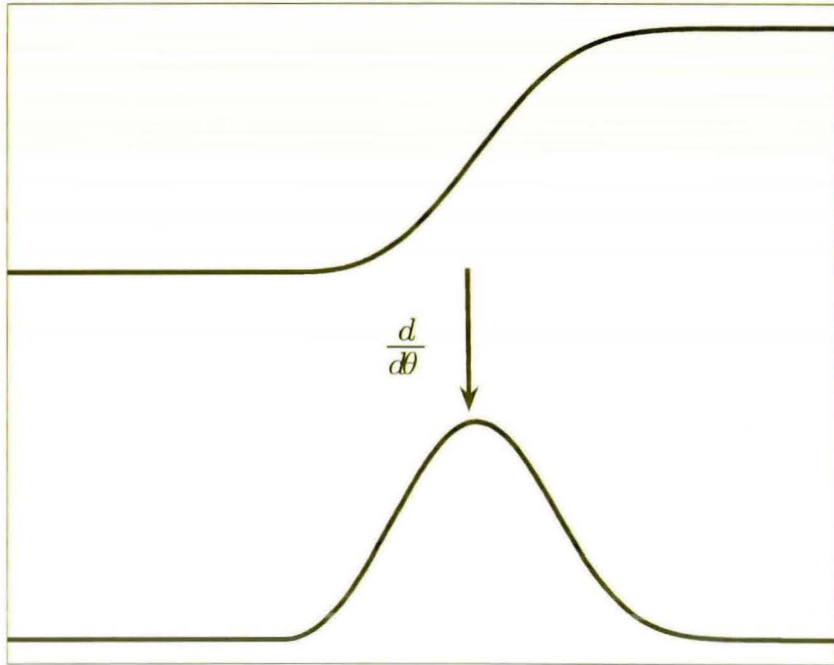


Figure 6.2: The Wiebe sigmoid and its $\frac{d}{d\theta}$ derivative

expressed in terms of energy per mass, the equation becomes:

$$\frac{dQ_{hr}}{d\theta} = \frac{dnC_xH_y}{d\theta} \times \text{MolecularWeight} \times \text{LHV} \quad (6.12)$$

Eqn 6.12 provides the chemical heat release component of the total $\frac{dQ}{d\theta}$ term but does not offer the complete value. The missing component corresponds to the heat transfer between the in-cylinder gases and the cylinder walls. To get a measure of this heat flow, the formula proposed by Woschni [94] has been incorporated into the model. This states that the heat exchanged between the walls and the in-cylinder gases will be proportional to the exposed surface area and temperature difference i.e.:

$$\frac{dQ_{wall}}{d\theta} = hA(T_{gas} - T_{wall}) \quad (6.13)$$

The Woschni formula suggests an empirical method for calculating the h coefficient. It can be written as:

$$h[W/(m^2K)] = \alpha b[m]^{-0.2} P[kPa]^{0.8} T[K]^{-0.55} (U \times Sp[m/s])^{0.8} \quad (6.14)$$

Apart from pressure and temperature, expressed in kPa and K respectively, variables α , Sp and U also appear. α is a constant, traditionally taken to equal 3.62. The $U \times Sp$ expression originally refers to the average cylinder gas velocity. Because this can be taken to be proportional to the mean piston speed [84], this last term includes a constant, U multiplying the mean piston speed Sp .

The Woschni formulation has been developed for SI engines and so is not necessarily applicable without modification to HCCI combustion. However, it is a good starting point for getting a reasonably accurate expression. Hence, the α and U parameters have been introduced in order to allow for a degree of tuning of the results. This tuning procedure is described in section 6.1.3.

By substituting the h coefficient of Eqn 6.14 into Eqn 6.13, the heat transfer component of $\frac{dQ}{d\theta}$ is established. Hence, by combining this with the chemical heat release component (Eq 6.12), the final expression for $\frac{dQ}{d\theta}$ is derived:

$$\frac{dQ}{d\theta} = \frac{dnC_xH_y}{d\theta} \times MolecularWeight \times LHV - hA(T_{gas} - T_{wall}) \quad (6.15)$$

By calculating a value for $\frac{dQ}{d\theta}$, the value of the $\frac{dP}{d\theta}$ and hence $\frac{dT}{d\theta}$ derivative can be established. The only missing value is that of the specific heat at constant volume, c_v . This final part of the derivative calculations is described below.

Specific Heat Tracking

The value of c_v does not appear as a $\frac{d}{d\theta}$ derivative in the differential equations for P (Eqn 6.5), V (Eqn 6.7), T (Eqn 6.4) and Q (Eqn 6.15). It has to be noted here that there are two different

ways of calculating its value at a given value of θ . One is to directly use the expressions used for deriving it as a function of composition and temperature. The other is to differentiate them with respect to θ and derive a $\frac{dc_v}{d\theta}$ expression. Both ways are similarly efficient from a computational point of view. In the case of this model, c_v has been tracked through its derivative purely for the sake of consistency since the other variables are tracked through a differential equation solver. The starting point for both of these algorithms is the specific heat equations described in Heywood [88].

The JANAF tables [87] provide a numerical method for calculating *molar* specific heat at constant pressure, c_p , through the use of polynomials. For gases, the polynomials take the form:

$$\frac{c_p}{R} = \alpha_1 + \alpha_2 T + \alpha_3 T^2 + \alpha_4 T^3 + \alpha_5 T^4 \quad (6.16)$$

where a set of α coefficients correspond to a given species.

For fuel, the polynomial becomes:

$$c_p = \beta_1 + \beta_2 \left(\frac{T}{1000} \right) + \beta_3 \left(\frac{T}{1000} \right)^2 + \beta_4 \left(\frac{T}{1000} \right)^3 + \beta_5 \left(\frac{T}{1000} \right)^{-2} \quad (6.17)$$

where the fuel's hydrogen to carbon ratio affects the β coefficients' values.

The above expressions can be differentiated with respect to temperature in order to link the c_p and T differentials:

$$\frac{dc_p}{dT} = R (\alpha_2 + 2\alpha_3 T + 3\alpha_4 T^2 + 4\alpha_5 T^3) \quad (6.18)$$

for nitrogen, oxygen, carbon dioxide and water and

$$\frac{dc_p}{dT} = \frac{1}{1000} \left(\beta_2 + 2\beta_3 \frac{T}{1000} + 3\beta_4 \left(\frac{T}{1000} \right)^2 - 2\beta_5 \left(\frac{T}{1000} \right)^{-3} \right) \quad (6.19)$$

for fuel.

For a mixture of different species, once the individual species' c_p values have been established, the whole mixture's mass based c_p value is calculated as follows:

$$c_{pmixt} = \frac{1}{M} \sum_i n_i c_{pi} \quad (6.20)$$

where n_i denotes the number of moles of the i^{th} species and M is the mass of the mixture.

By differentiating with respect to temperature, the mixture c_p differential can be linked to the temperature differential:

$$\frac{dc_{pmixt}}{dT} = \frac{1}{M} \sum_i n_i \frac{dc_{pi}}{dT} \quad (6.21)$$

where each $\frac{dc_{pi}}{dT}$ term is directly calculated from Eqns 6.18 or 6.19.

Since the $\frac{1}{M} \sum_i n_i \frac{dc_{pi}}{dT}$ term can be calculated, multiplying both sides of Eqn 6.21 with $\frac{dT}{d\theta}$ connects the derivative of the mixture's c_p with respect to θ to the corresponding temperature derivative (Eqn 6.4), i.e.:

$$\frac{dc_{pmixt}}{d\theta} = \left(\frac{1}{M} \sum_i n_i \frac{dc_{pi}}{dT} \right) \frac{dT}{d\theta} \quad (6.22)$$

Finally, the value of c_v can be calculated from the value of c_p through the use of:

$$c_p = c_v + R \quad (6.23)$$

in the case of molar based values. Some care must be taken when mixing molar based and mass based definitions of specific heat. In the case of the equations as they appear in Heywood [88], in the derivation of the mixture c_v value, R must be divided by the mixture's molecular weight e.g.

$$c_{pmixt} = c_{vmixt} + R \frac{N}{M}$$

With specific heat tracked, all variables taking part in the fundamental Eqns 6.1 and 6.2 are accounted for. The next step is then to implement all the equations into an integrated computer

algorithm.

6.1.2 Model Architecture

While the equations described so far are at the heart of the model, they do not represent the full picture. Software design considerations come into play which must be addressed at this stage.

The main variables have been presented in derivative form in order to allow the problem to be treated through a differential equation solver. In this particular case, MATLAB's **ode45** function has been used. The way the **ode45** works is by supplying it with a handle to a function which calculates derivatives for the tracked variables at given values of the controlling variable (in our case θ). Hence, a function must be created by the user which takes into account the equations presented in the previous section and supplies their outcome to **ode45**. This function will be called "**derivatives**" from here onwards. Because various parameters need to be taken into account, a number of other functions also supply the **derivatives** function with relevant data. The main idea at this point is to separate functionality in order to keep the overall model design modular, thus allowing for easy modifications.

In order to establish the control flow inside the function two considerations are made. One is that, because the **ode45** solver does not always proceed in a monotonic fashion (and as a portability consideration there is no reason to presume other ODE solvers will either), care has to be taken regarding information which has to be preserved between function invocations. The second consideration regards the types of in-cylinder conditions the function tackles. By and large, there are two main cases for the events happening inside the cylinder, combustion and lack of it.

Combustion Types

Things however are more complicated. If combustion occurs, it can happen either as spark initiated flame propagation or as auto ignition. There is a marked difference in the speed of propagation

between the two as is shown in figure 6.3 where varying MFB traces from a TRG sweep at 2000 RPM are presented.

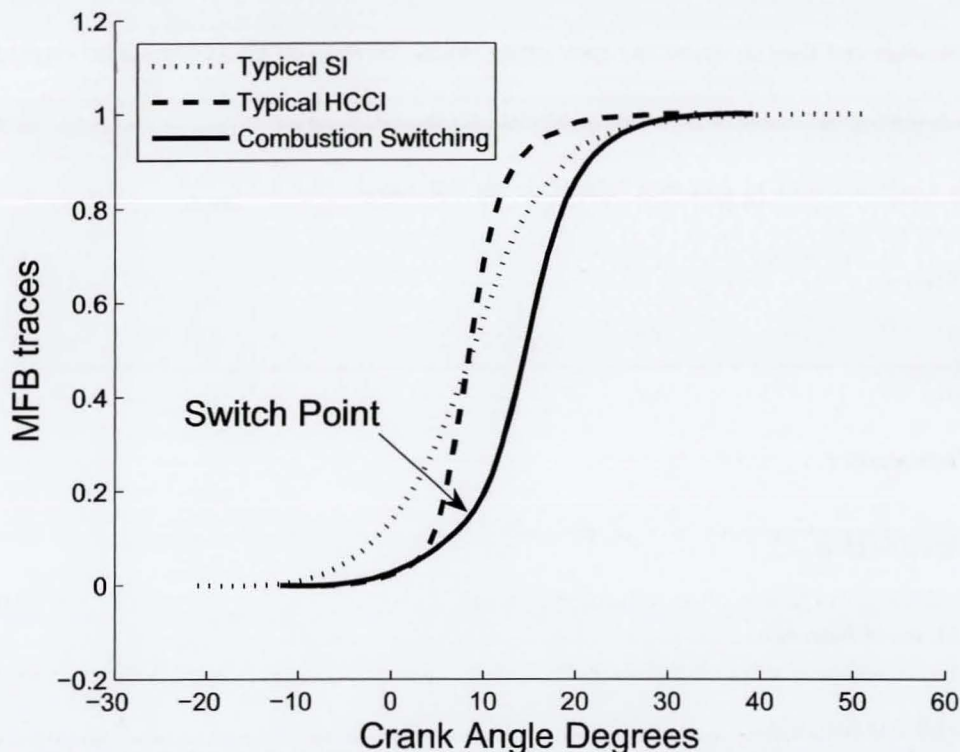


Figure 6.3: Comparison of typical combustion profiles for different combustion types

It is evident that a HCCI combustion is a much more sudden event. However, it can happen that auto ignition does not start until well into the development of the combustion. In those cases, a combustion can advance for part of its lifetime as a standard flame propagation combustion until, at some point, it switches to auto ignition as the remaining unburnt fuel autoignites. This is the case with the solid line in figure 6.3.

Control Flow for Combustion Type selection inside “derivatives” function

In order to accommodate the possible combustion cases, the control flow inside the function has to be accordingly constructed. As has been established so far, the main variable which is affected

by the combustion is the chemical heat release term. This is laid out in Eqn 6.12 where it has been connected to the rate of fuel conversion. This is in turn connected to the derivative of the Wiebe sigmoid as shown in Eqn 6.11. Hence, the **derivatives** function must differentiate between types of combustion and then associate the appropriate Wiebe curve to all tracked variables depending on which part of the combustion is under scrutiny by the ODE solver.

The function tracks 11 variables. These are the following:

1. Volume
2. Pressure
3. Temperature
4. Specific Heat
5. Moles of Nitrogen
6. Moles of Oxygen
7. Moles of Fuel
8. Moles of Carbon Dioxide
9. Moles of Water
10. Chemical heat release energy
11. Heat transferred through cylinder walls

In order to keep track of its state, the **derivatives** function makes use of persistent variables. In MATLAB, persistent variables are these which retain their value between function invocations. Thus, it is important for the calling functions of **derivatives** to clear it from memory before invoking the ODE solver or else variables from a previous invocation will confuse the outcome. These variables store all information that is specific to the region being calculated.

The ODE solves for the closed valve segments of a cycle. At initialisation of the **derivatives** function, persistent variables are initialised in order to store:

1. the initial and final values of the fuel
2. a data structure containing information about the auto ignition burn profile for the cycle
3. a data structure containing information about the flame propagation burn profile for the cycle
4. information about the conditions under which auto ignition will occur in the cycle

The initial and final values of the fuel are needed in order to anchor the ends of the sigmoid to them. The final value is defined as the value after a complete combustion, when all available oxygen has been consumed (and is hence 0 for a stoichiometric or lean mixture). The final result might be further modified by Completeness of Combustion (CoC) considerations as discussed further down.

Items 2 and 3 are needed in order to select the appropriate sigmoid to follow when the solver calculates the combustion region. Item 4 is used to determine when and if the auto ignition burn profile will be followed. The trigger mechanism can be set to some condition like a critical temperature or pressure or a more complex construct like an Arrhenius [95,96] integral⁴.

The persistent variables for the burn profiles are initialised but not filled until the appropriate moment. Because the ODE solver does not progress in a monotonic manner, there is no guarantee that once a certain point in CAD has been reached, the next invocation of the **derivatives** function will occur at a later (in CAD) stage. Hence, the use of persistent variables as flags to designate certain regions, e.g. if a combustion has occurred, is inappropriate. Instead, burn profiles are

⁴In the experimental part of this research no deciding factor for has been established for autoignition. At the time of writing, the trigger mechanism for the model has been set to a simple pressure or temperature condition. However, any mathematical construct can be used in its place.

calculated on the fly the first time they are needed. Once these have been calculated, they are stored in the (already initialised) data structure. At every invocation, the function checks if a non-empty burn profile exists and if it is applicable for the CAD point for which the ODE solver is requiring derivative values. This decision making chart is outlined in figure 6.4.

The top segment of the chart shows how possible autoignition is tackled. An existing autoignition burn profile implies that at some stage in the run, conditions favourable to autoignition have been encountered. This implies that past that point, the burn will follow the autoignition profile. However, just because an autoignition profile exists, does not imply that the present invocation of **derivatives** by the ODE solver occurs after the autoignition point. It is possible that the solver might backtrack and request information on some previous point. Hence, a check must be made to ensure that the present invocation occurs in the autoignition burn region.

If there is no non empty autoignition burn profile, a check must be made to ensure autoignition is not triggered by the conditions in the present invocation. If this is the case, a burn profile is calculated on the fly⁵ and the derivatives returned to the ODE solver follow this profile.

If none of the autoignition burn conditions are met, the bottom part of the chart is reached. In this case, the possibility of a spark firing must be considered. If no spark is fired there can be no burn at this CAD value (since the autoignition checks have been negative in order for this point to have been reached) so the **derivatives** function returns values corresponding to simple compression/expansion with no combustion.

If a spark is fired, the first thing to establish is if it has occurred before the present CAD value. If this is the case, a flame propagation burn *might* be established. The reason for the uncertainty is that a spark plug firing establishes a flame propagation burn with some delay. Hence, a CAD value after a spark is not guaranteed to be inside a flame propagation burn region. If the **derivatives**

⁵This will occur at most once for a cycle. After the profile variables have been filled, this branch of the chart will never be activated again.

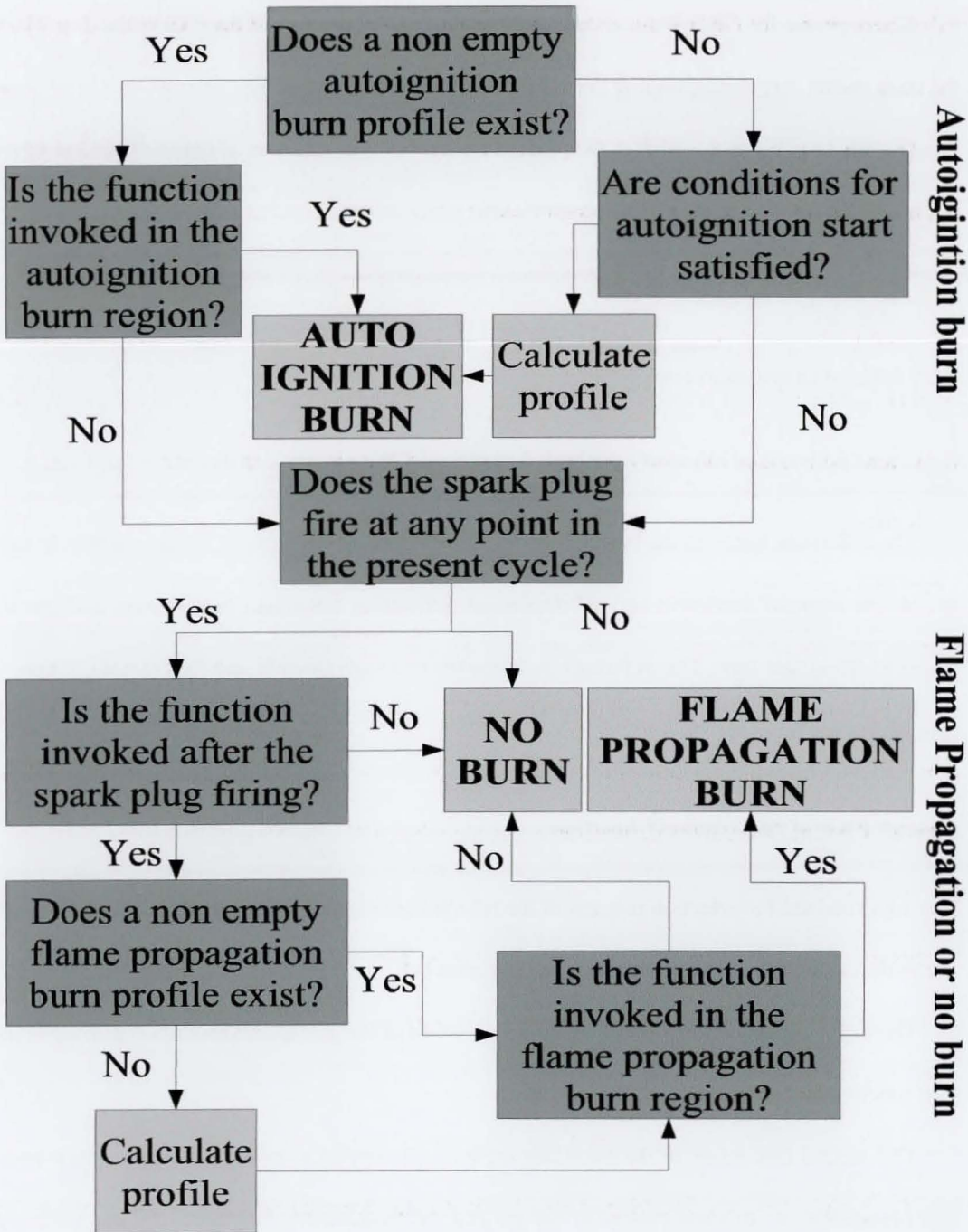


Figure 6.4: Combustion selection algorithm

function finds itself after a spark event it will calculate a flame propagation burn profile once, if such does not exist, then establish if its present position lies within the flame propagation burn region and take the corresponding action.

A burn profile for either flame propagation or autoignition consists of the CAD range over which the burn occurs, the corresponding Wiebe sigmoid and its derivative.

The whole point of the control flow inside the **derivatives** function as demonstrated in figure 6.4 is to establish one of three final possibilities:

1. an autoignition burn
2. a flame propagation burn
3. a no burn region (normally pre burn compression or post burn expansion)

The difference between the burn (cases 1 and 2) and the no burn (case 3) cases is that, in case the Wiebe sigmoid derivative and all dependent derivatives (chemical heat release and species transformation) are zero. The difference between the two burn cases (1 and 2) is that the SI burn is typically much more spread out⁶.

Overall Flow of “derivatives” function

Having explained the selection process of the relevant combustion type, the overall flow of events in the **derivatives** function is demonstrated in figure 6.5.

The top of the chart corresponds to the initialisation of the persistent variables occurring at the first function invocation.

The second box refers to the auxiliary expressions needed to be recalculated at each function invocation i.e. mixture molecular weight and the temperature derivative of each species as described in Eqns 6.18 and 6.19.

⁶Also, the Woschni based heat transfer coefficient has been set to different values in the present implementation depending on the combustion type. This reflects the different mechanisms of combustion prevalent in each case. This is explained further in Section 6.1.3

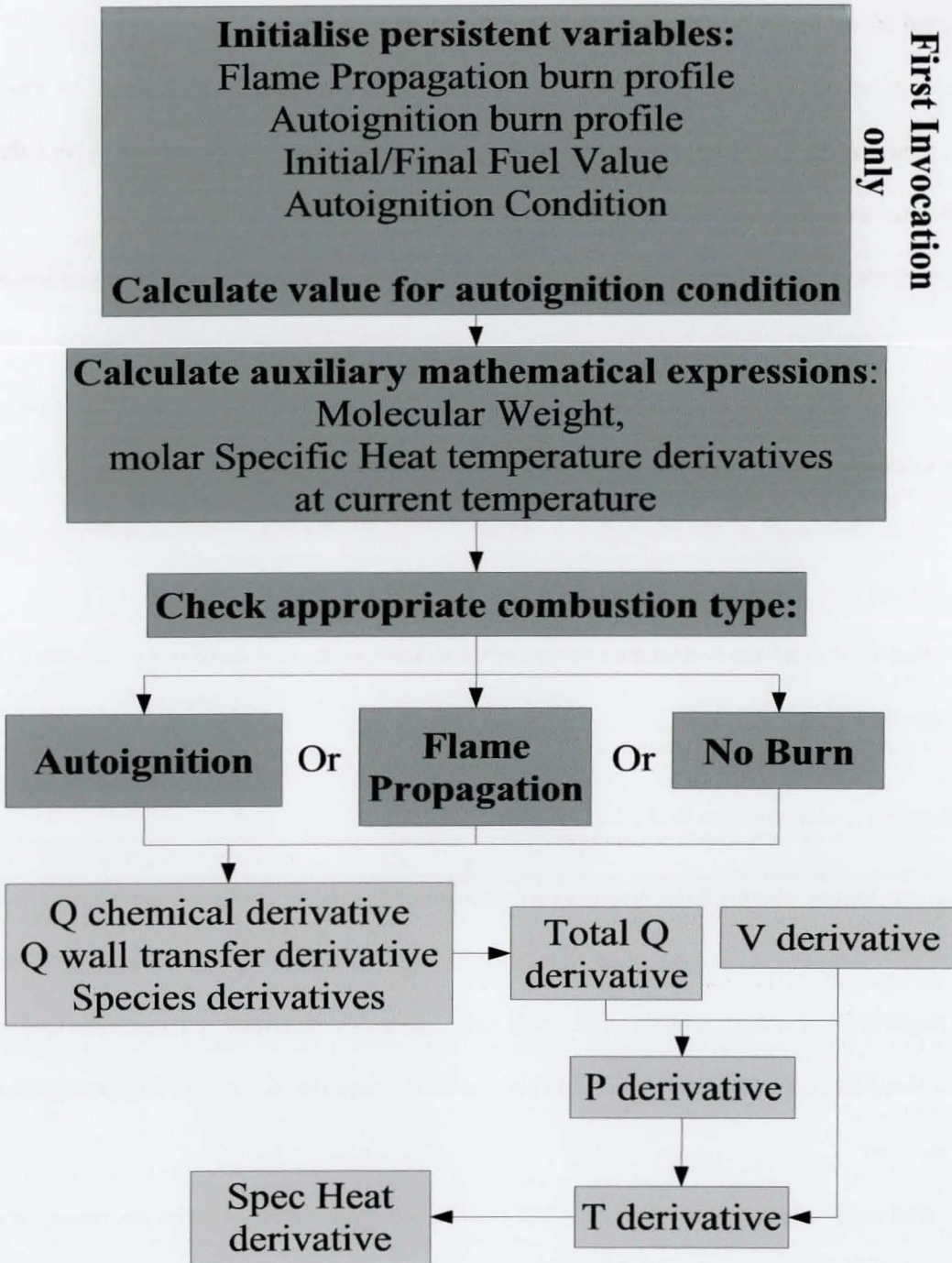


Figure 6.5: Overview of “derivatives” function

The meaning of the combustion types has been explained and is demonstrated in figure 6.4. The combustion selection is decisive for the shape of the Wiebe derivative to be used which in turn dictates the fuel conversion derivative as in Eqn 6.11, the species’ transformation derivatives as in

Eqns 6.10 and finally the chemical heat release derivative as in Eqn 6.12.

Furthermore, because the α and U parameters in the formula of the Woschni heat transfer coefficient (Eqn 6.14) have been implemented to be dependent upon the combustion type, this selection also affects the value of the wall heat transfer derivative (Eqn 6.13, 6.14).

Once both components of the heat derivative have been calculated, the total heat derivative is then calculated (Eqn 6.15). Now, the volume derivative (Eqn 6.7) is independent of everything but the CAD value, θ , hence can be calculated at any time. With both the heat and volume derivatives, the value of the pressure derivative is then established as in Eqn 6.5.

With knowledge of the pressure and volume derivatives, the temperature derivative is then calculated as in Eqn 6.4.

Finally, through the temperature derivative value, the specific heat derivative is calculated as in Eqn 6.21.

Chemical transformation in the burn region

The burn region, whether flame propagation or autoignition, is unique in that it is only within it that species transformation and subsequent chemical heat release occur. All other tracked variables' derivatives are non zero throughout the cycle independent of combustion. However, the species and chemical heat release only come into play inside the burn region which is why it requires a closer look.

The most important consideration when considering the combustion is its positioning and rate. The chemical path considered, hydrocarbon and oxygen forming carbon dioxide and water, ignores the complex intermediate steps which are the domain of more detailed chemical kinetic based models and concentrates on the physical quantity of heat associated with the hydrocarbon's combustion. Hence, one more consideration is to what extent the hydrocarbon is converted. This can be affected by either incomplete combustion or AFR considerations. If insufficient oxygen is

present (rich mixture), not all fuel is converted anyway.

To avoid runaway derivatives giving rise to negative values for oxygen or fuel in non stoichiometric cases, the initial and possible final values (the value assuming a complete burn of the given mixture until all fuel or all oxygen is depleted) of the fuel have been calculated at the first function invocation and stored as persistent variables. Hence, the Wiebe sigmoid value is tied to the Initial-Final rather than Initial-Zero range for fuel values.

Finally, the extent of possible conversion must also be taken into account since it is not necessary that all available fuel or oxygen is converted. Generally speaking, CoC is high for lean mixtures [88] so the default value is set to 0.98, when expressed as a 0-1 fraction.

Thus, the final expression for the fuel derivative, derives from Eqn 6.11 and becomes:

$$\frac{dnC_xH_y}{d\theta} = -(Fuel_{initial} - Fuel_{final}) \times CoC \times \frac{dx(\theta)}{d\theta} \quad (6.24)$$

and the dependent derivatives, Eqns 6.10, 6.12, follow suit. This process is shown in figure 6.6.

The top case of the figure corresponds to a rich mixture undergoing complete (CoC=1) burn. By looking at the right hand side of the graph, it is evident that it is the oxygen which reaches a value of zero while some fuel remains. The initial values of the mixture have been taken from measured data of a 50% molar TRG experiment, hence both CO_2 and H_2O start at high levels.

The middle graph shows a lean burn. In this case, it is evident that it is the fuel which reaches a zero value, while O_2 remains at high levels.

The bottom graph shows a stoichiometric mixture burning incompletely at CoC=0.8. In this case, both O_2 and fuel remain at the end of the combustion. Because of the much greater molar value of the O_2 in a stoichiometric mixture, the fuel trace cannot be shown to a scale which clearly demonstrates that it reaches a non zero value, as is the case here, while also keeping the other traces in the picture.

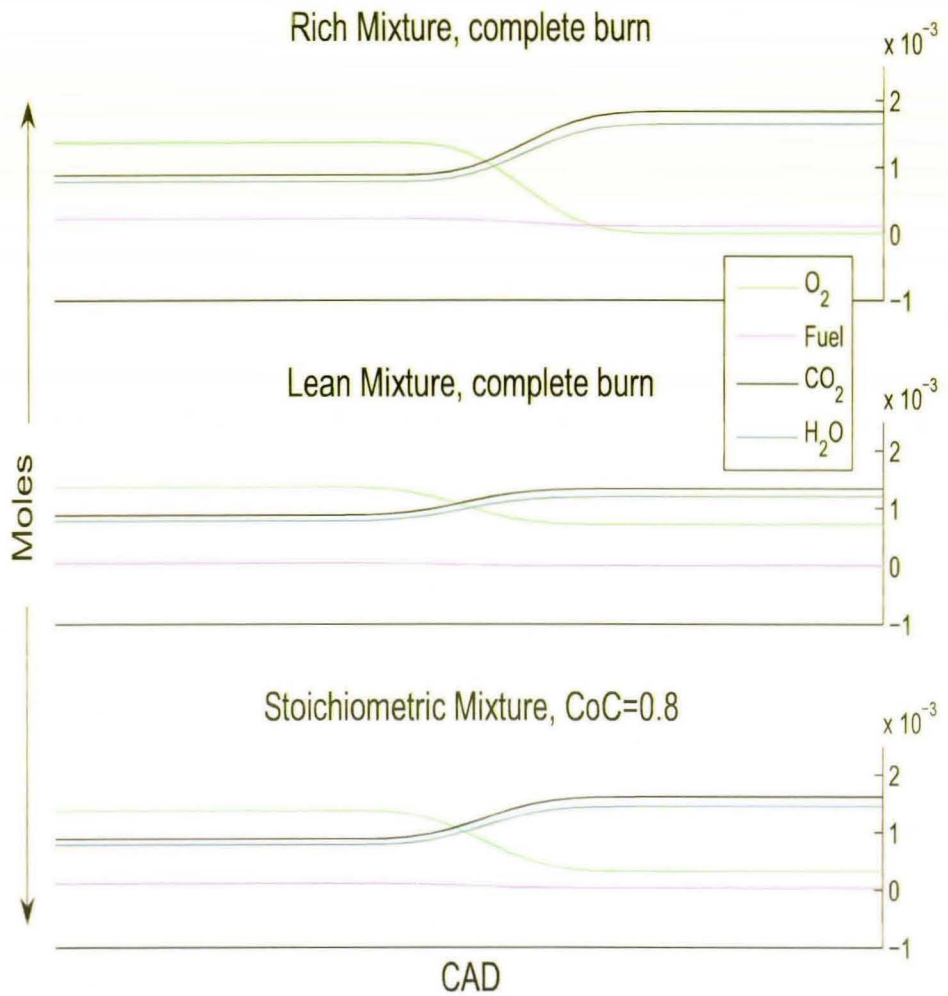


Figure 6.6: Species' transformations taking place during combustion

6.1.3 Wall Heat Transfer Tuning

The two components of the heat derivative have been introduced in Eqn 6.15. They are the chemical heat release (always as heat added to the in-cylinder gases) and the heat transferred between the gases and the walls (usually heat lost from the gases to the walls). The Woschni coefficient (Eqn 6.14), used in conjunction with Eqn 6.13 gives a value for this heat.

However, the Woschni formulation can be further tuned in order to account for specific cases. The coefficients originally proposed have been derived empirically on SI engines. In this case,

when a mixture of SI and HCCI is encountered, a slightly more elaborate scheme can be employed in order to account for the different mechanisms involved.

Experimental data fuel flow is measured directly. Hence, through knowledge of the engine speed for each set of data, the average fuel amount per cycle can be derived. This fuel introduces a known amount of energy. By carrying out a combustion analysis as outlined in Chapter 5, the exchanged heat trace can be derived. As explained in that chapter, this trace gives an accounting of the total energy flow of the in-cylinder gases, including both chemical and wall transfer components.

However, with the model developed so far, it is possible to predict a theoretical curve that will follow an ideal path with a heat release profile similar to the experimental one. The only thing that's required is an MFB curve. That curve can be either supplied by a tailor made Wiebe curve or simply taken from the experimentally established MFB derived from the exchanged heat curve as defined in figure 5.15 on page 116.

Figure 6.7 shows the pressure traces of such a trial. The ideal actual pressure trace is shown as a solid line. The theoretical curve (dashed line) in this case is created by setting the experimentally derived MFB curve and its derivative in the place normally taken by the Wiebe sigmoid. The wall heat transfer component has been set to zero, hence all heat exchange is due to the chemical heat release, making the theoretical trace an ideal trace. It is evident from the positioning of the abrupt increase in the pressure traces that the combustion profiles are indeed identical or at least very close. Whatever discrepancy remains between the two can be solely attributed to a difference in the amount of heat injection. Since both the total heat is known (through the amount of fuel per cycle) and the rate of its release (through the MFB), the discrepancy in heat can be solely attributed to heat transfer to the walls. This is demonstrated in figure 6.8.

Again, the actual experimentally derived exchanged heat trace is shown as a solid line, while the dashed line corresponds to the ideal case of no wall heat transfer. A point to consider is the

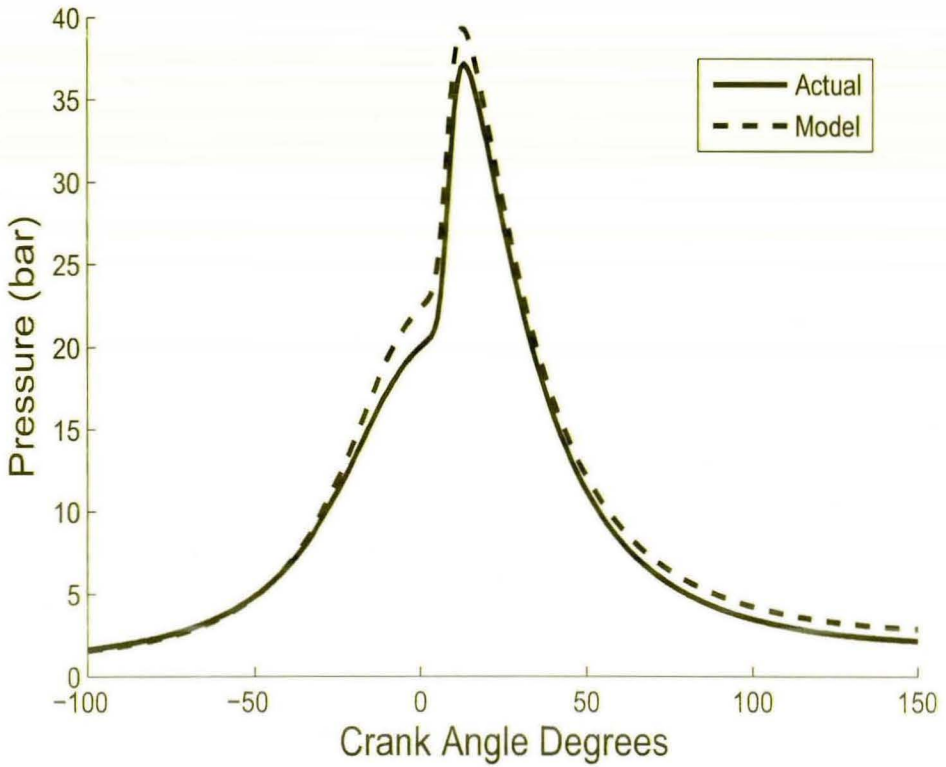


Figure 6.7: Pressure traces measured and modeled with no wall heat transfer

positive heat flow in the initial region of the experimental trace. This is due to the fact that, at the beginning of the compression, there can be a positive flow of heat from the walls to the in-cylinder gases, due to the fact that the latter are colder than the walls. The discrepancies between the two traces are due to this wall heat transfer, hence it is derived by simply subtracting the two. This is shown in the figure as the dotted line.

The final step is in tuning the Woschni coefficient. Since the formula of Eqn 6.14 gives an expression, the problem becomes a matter of curve fitting which can be tackled by a variety of methods. In MATLAB, the **fmin** family of functions, which perform a minimum search of multivariable functions can be employed. In this case, the variables are the degrees of freedom of the Woschni coefficient, parameters α and U , as described on page 142 and the function is some construct which scores the fit of the Woschni curve to the difference between the actual and ideal

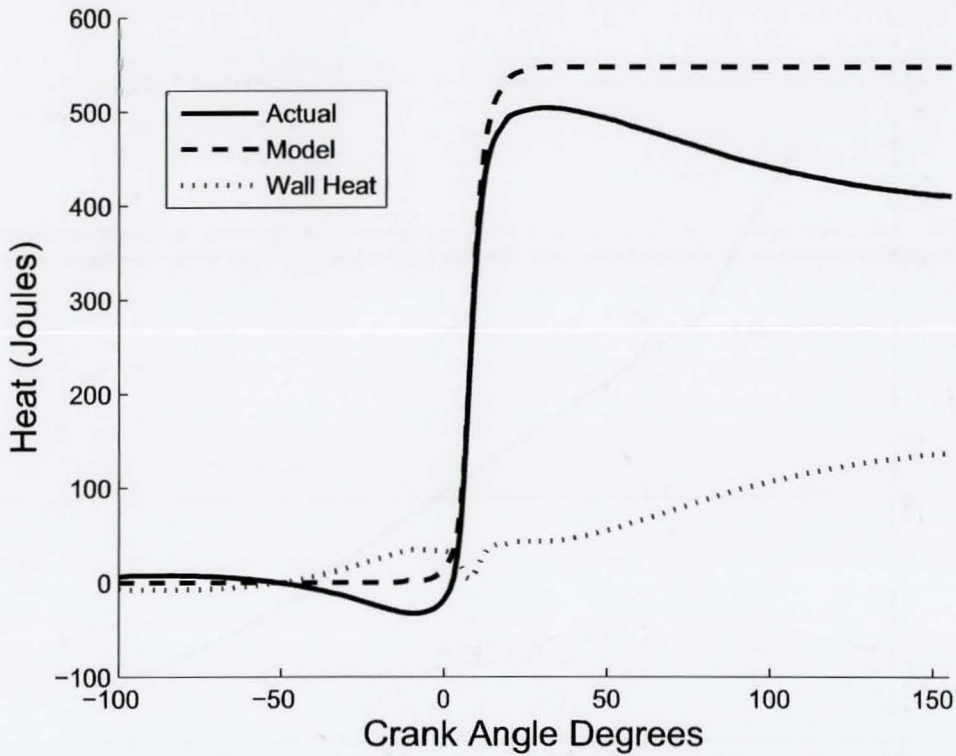


Figure 6.8: Heat exchange traces measured and modeled with no wall heat transfer

modeled exchanged heat traces.

What has been found is that it is very hard to get a single set of parameters which will fit all data. The tuning has been split into three parts, the non combustion part, the flame propagation combustion part and the autoignition combustion part. The parameters' values are shown for reference in table 6.1.

Table 6.1

	No Combustion	Flame Propagation	Autoignition
U	45	10	See fig 6.9
α	1	2	2

In the case of autoignition, the value of the U fits better as a TRG dependent value. An empiri-

cally derived U -TRG relation based on fitting experimental data is shown on figure 6.9.

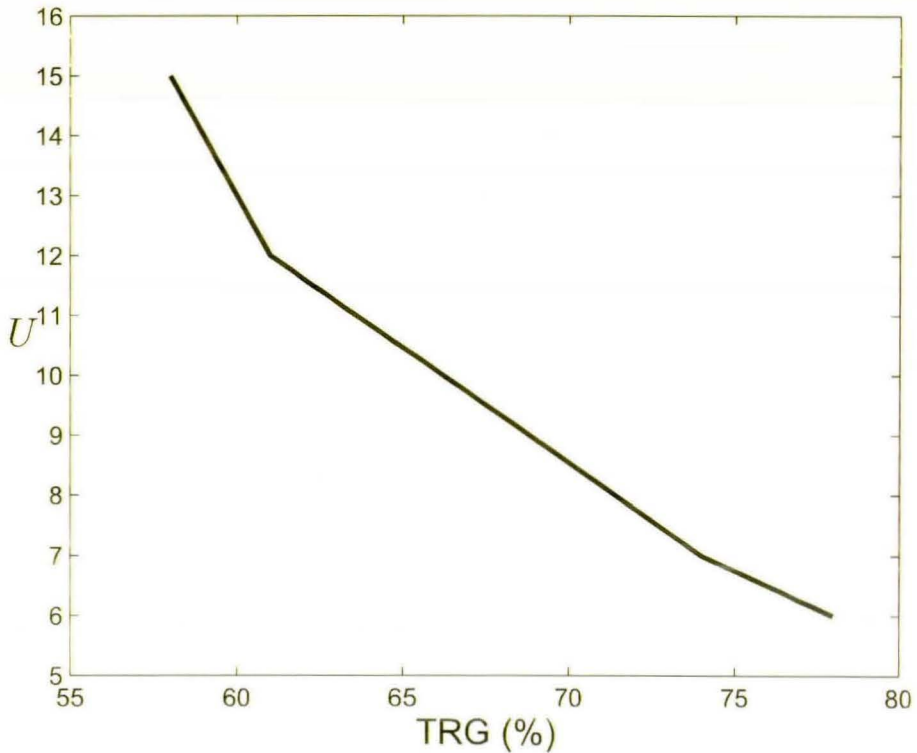


Figure 6.9: An example of empirically determined TRG dependent U parameter

It has to be noted that great care must be exercised when tuning the Woschni coefficient. Because it is an empirical SI formula, the selection and interpretation of tuning parameters is to an extent arbitrary. This has been made evident in the case of the data at hand as, for example, the set of numbers given here, tuned for a given series of experiments, does not fit the results of a different series of experiments on the same engine. This is why the numbers quoted here are purely an indication. It is important that tuning is performed individually on an experimental data set.

6.1.4 Combustion Profile Calculation

The model as described so far presents an accurate representation of the mechanisms involved when set to replicate a given user defined cycle. For example, given an existing pressure trace on which combustion analysis (Chapter 5) has been carried out, the model can yield the corresponding ideal traces as shown in figures 6.7 and 6.8. Alternatively, by shifting any parameter, such as combustion positioning, duration, heat transfer etc, very detailed results can be derived for theoretical configurations.

While all the above uses of the model are ideal and quite powerful descriptive tools, in order to have a truly predictive model, an automated algorithm for determination of the combustion profile is needed. As discussed on page 148, the model has been built to accommodate an autoignition condition, though the issue of combustion profile determination goes beyond the autoignition condition.

To make a truly versatile model, a combustion profile has to be calculated for both flame propagation and autoignition cases. As far as flame propagation is concerned, the matter is relatively simple since the combustion is regulated by the spark timing.

SI combustion profiles

The pure SI case has to take into consideration the delay between the spark timing and SoC. In this research, SI experimental data has been available from varying operating conditions. Figure 6.10 shows a surface of time delays at different pressures at spark timing⁷ and λ .

The results in the figure come from a set of data involving changing AFR, hence the reference to λ . However, AFR effects are not within the scope of this research so have been generally overlooked. Therefore, when considering the duration of SI combustion, the results are grouped

⁷Pressure at spark timing, rather than the CAD value of spark timing per se is more physically important when considering the flame propagation speed.

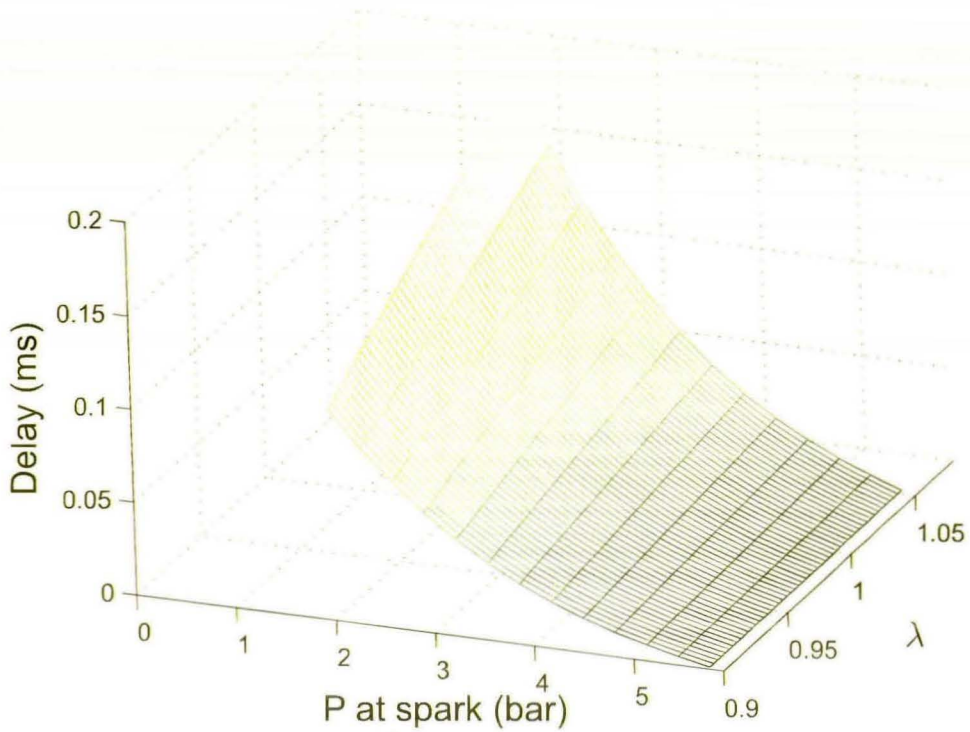


Figure 6.10: Example of SI combustion delays

by speed and load as shown in figure 6.11.

Each vertical line corresponds to the high and low IMEP and respective combustion duration of SI burns at speed sites of experimental data. The IMEP values are shown marked as text. The durations shown in the figure represent the load sites demarcating the HCCI envelope at each speed site. While this figure does not represent a full mapping of the SI speed and load space, it provides information which is relevant to the regions of interest, regarding possible transitions between SI and HCCI modes. Reasonable values for duration can be derived by extrapolation of these.

HCCI combustion profiles

While the SI cases are relatively straightforward, the HCCI combustion is a very complex case. This is because, it involves the full spectrum from flame propagation to full autoignition. While, at one

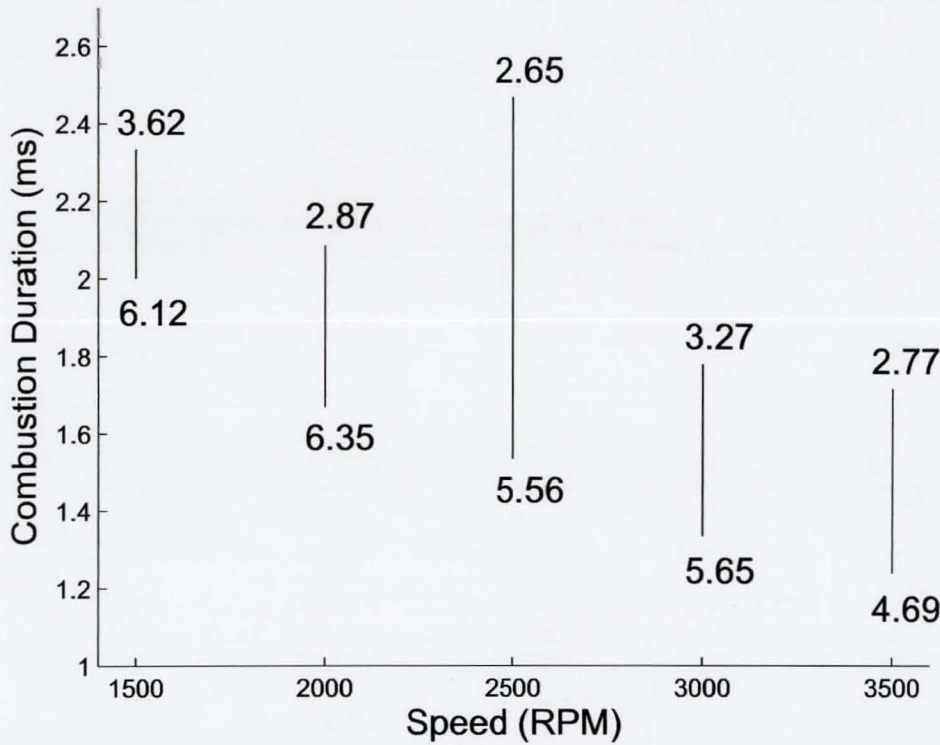


Figure 6.11: Combustion durations for stoichiometric SI files around the HCCI envelope

extreme, HCCI is synonymous with pure autoignition, this is not necessarily true of the whole spectrum of TRG values. At high IMEP, low amounts of TRG are present, making combustion initiation impossible without a spark. However, these are not pure flame propagation cases either, because the presence of TRG facilitates autoignition at some later stage in the combustion development as is shown in figure 6.3. As IMEP drops and TRG rises, it is possible to enter regions of pure autoignition, where the spark can be absent altogether. A fully predictive model should then be able to account for all of this spectrum and calculate the autoignition condition in each case.

Unfortunately, this has not been possible throughout this research. Though other researchers [95, 96] have proposed the use of Arrhenius type integrals as a simple mathematical construct of SoC estimation for simple fuels, no such construct has been able to accurately predict the behaviour of the experimental data. This matter is discussed in more depth in Chapter 7. What is relevant

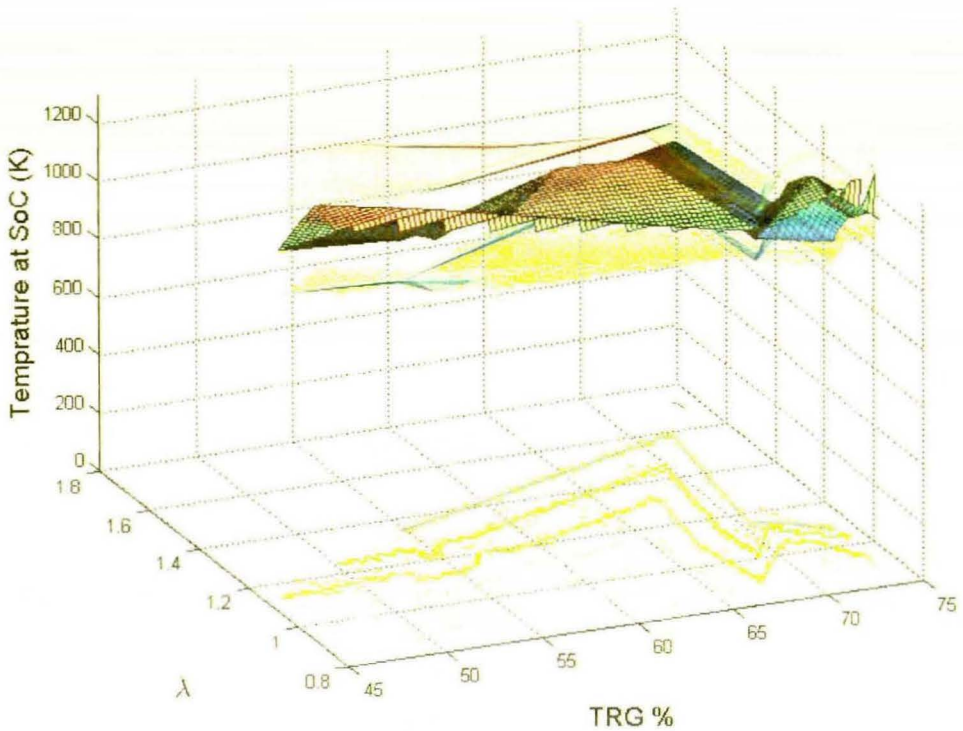


Figure 6.12: Example of large scale study of surface of SoC temperature

to the modeling side is that, *under stable conditions*, the HCCI engine is operating with little cyclic variation. Therefore, a simplistic approach is to require combustion to occur at a given CAD value. For a more sophisticated trigger mechanism, it is possible to require a certain pressure or temperature value to be reached before autoignition occurs as shown for example in figure 6.12.

The surface in the figure corresponds to a large scale study of autoignition temperature at SoC (including a λ component). The translucent top and bottom surfaces mark the standard deviation of the temperature values at every site. While such an approach does not offer a physical explanation as to why combustion occurs when it does, it can be used as a statistical based empirical way of giving physically plausible results.

6.1.5 Modeling of single SI and HCCI cycles

With the procedure described up to this point, it is possible to simulate the closed valve segments of both SI and HCCI cycles. Apart from a faster heat release and slightly different heat transfer, the two types obey the same equations. Typical traces from both can be seen in figure 6.13.

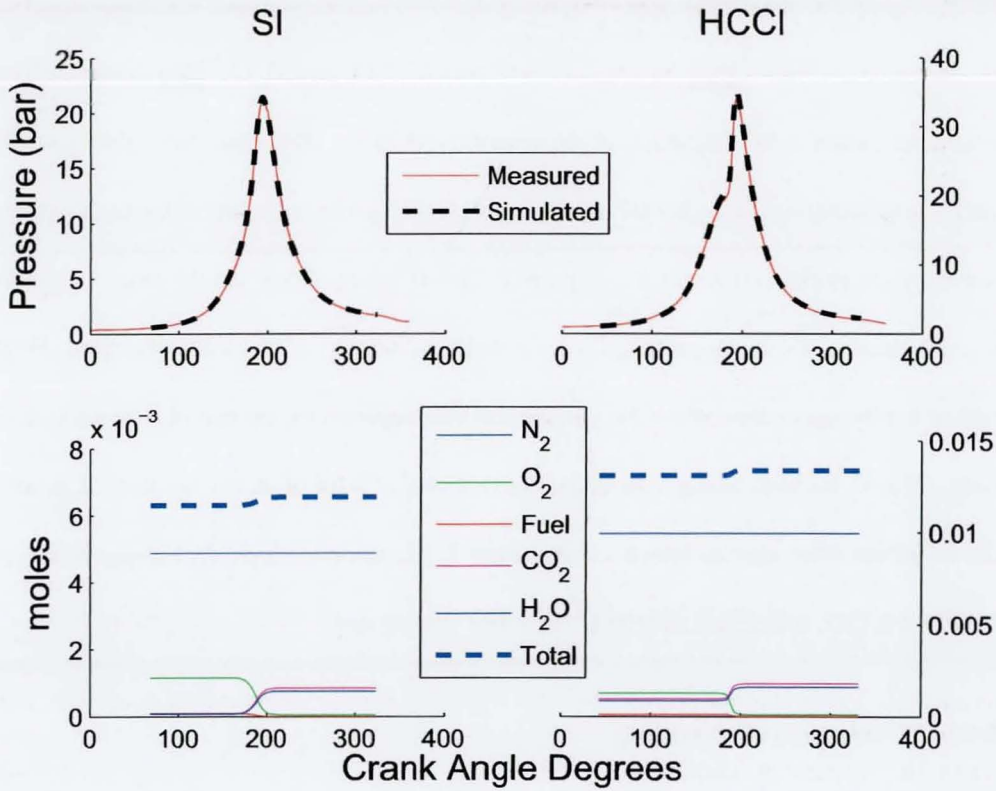


Figure 6.13: Actual pressure traces and simulated pressure and species output for typical SI and HCCI combustion

The SI trace has been taken from a stoichiometric log at 1500 RPM, 3.62 bar IMEP, ITA=32 CAD. The HCCI trace has been taken from a stoichiometric log at 2000 RPM, 3.96 bar IMEP, ITA=20 CAD, 43% volumetric TRG (54% molar TRG), fixed duration valve strategy.

The noticeable difference between the pressure traces is the sharper rise of the HCCI case, resulting from the shorter combustion duration. This, along with the species transformation traces can be seen in the bottom plots.

Looking at the total moles, the SI case, which operates throttled, has roughly half the total moles of the unthrottled HCCI. As can be seen in both cases, the combustion affects very little the total number of moles. The reason for this can be seen when examining the individual constituent species. In both cases, the mixture is dominated by N_2 , which remains unchanged all along the event. O_2 , on the other hand, gets completely depleted in a stoichiometric combustion. However, its decline is partially offset by a rise in two species, CO_2 and H_2O . These two start from non negligible values at the beginning of the compression in the HCCI case, since they constitute the TRG. On the contrary, in the SI case, they are almost zero at the beginning of the combustion (while ideally, an SI engine has zero exhaust gases at IVC, in reality this is not the case. To capture this, a small amount of exhaust gases has been included at the start of the SI compression). Finally, the fuel is hardly noticeable before the combustion and depleted by the end of it in a stoichiometric burn. This is because, being a large molecule it carries a lot of atoms (around 22 in this case), unlike all the other species which carry at most 3. Hence, one single fuel molecule can provide the C for 8 CO_2 molecules and the H for 7 H_2O molecules.

6.1.6 Cycle to cycle coupling

What has been described so far relates to the closed valve segments of the cycle, that is the compression - combustion - expansion (IVC to EVO) and the TRG compression - expansion (EVC to IVO) of an HCCI cycle. To expand the model to a series of cycles, a simple model has been added in order to string these together into a continuous flow.

A typical approach to such a problem is to use simple flow equations to model the valve effects as for example in [97]. However, at low engine speeds it is reasonable to expect straightforward pressure equalisation between the cylinder and the inlet/exhaust. The available experimental data cover a range of maximum 3500 RPM. Within this range, a generally well behaved pressure equalisation is observed.

Also, the employed TRG trapping strategy of early EVC simplifies matters since the exhaust gas is not forced into the exhaust and then rebreathed as is often the case. Thus, the simplification of assuming a pressure equalisation of the cylinder with the inlet and exhaust manifolds in the respective valve events seems justified.

Hence, in order to reserve the bulk of computation for the closed valve segments of the cycle⁸, the equations employed for the coupling have been kept very light.

Exhaust Valve Event

When considering the exhaust valve, there are two effects of interest, the venting of the exhaust gases and subsequent retention of some in the form of TRG. To account for these, the assumption is that venting is done until pressures between cylinder and exhaust manifold have been equalised. The fraction of gases retained is then given by the fraction of cylinder volume available at EVC related to the overall volume taken up by the expanded gas. No heat loss effects are taken into account, since these events are taking place at low pressure and over a short time. In terms of equations, the model is described as follows.

At EVO, the gas expands adiabatically with a polytropic coefficient κ_{exp} . This coefficient has been extracted from the low pressure (descending part, close to EVO) segment of various experimental curves and has exhibited a correlation to engine speed only (figure 6.14). Hence, in this implementation, it is interpolated between these values accordingly. So, given the coefficient value, the expansion occurring at EVO can be assumed to follow the adiabatic expansion equation, initially expressed in 5.1, in this case yielding:

$$P_{evo}V_{evo}^{\kappa_{exp}} = C_{exp} \quad (6.25)$$

⁸At the time of implementation, an IVC-EVO segment is calculated in a minimum of two minutes (more if high precision is required) on a Windows 2000, 2.4 GHz Pentium 4 PC with 512 MB of RAM

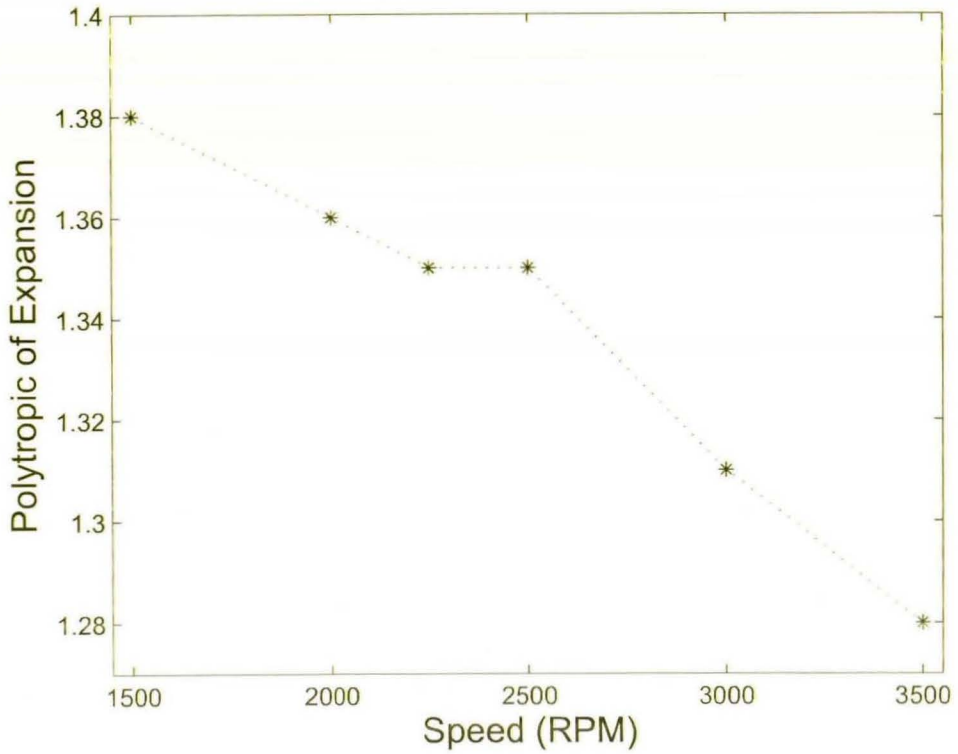


Figure 6.14: Speed dependent polytropic of expansion measured at the low pressure descending part of the experimental pressure trace

which gives a value for the constant C_{exp} . At this point, the pressure drops until it reaches the manifold pressure, P_{man} at which point the gases will be occupying an unknown volume. This new volume, V_{exp} , will be given by:

$$P_{man} V_{exp}^{\kappa_{exp}} = C_{exp} \iff V_{exp} = \left(\frac{C_{exp}}{P_{man}} \right)^{\frac{1}{\kappa_{exp}}} \quad (6.26)$$

The amount of gases retained as TRG will then be given by the ratio of the above and the EVC volume as $TRG = \frac{V_{EVC}}{V_{exp}}$ where TRG in this case is expressed as a 0-1 fraction.

Inlet Valve Event

The inlet valve event entails slightly more complicated calculations. This is because, a mixing of a known amount of TRG at known temperature is performed with an unknown amount of charge at known temperature. The ideas and equations are the same as the ones described in Section 5.1.2 but solved from another perspective.

The issue of mixing needs to be discussed at this point. The assumption is that mixing of charge and TRG is done completely, the gases reaching a uniform distribution and temperature during the open valve event. This is not necessarily the case. However, the only way to address this question is a CFD study which is out of the scope of this research. The reason why this is an issue is because of the way the induction is handled. The known amount and temperature of TRG is mixed with an amount of charge. The idea is that, for charge to flow into the cylinder, TRG by itself is insufficient to fill up the maximum volume at BDC while retaining a pressure at least as high as that of the inlet manifold. Hence, an amount of charge flows into the cylinder to make up for the discrepancy. A simplistic way of looking at this is to calculate the volume taken up by TRG at a pressure equal to that of the inlet while accounting for its final temperature and then calculate the amount of charge which, at inlet pressure will take up a volume equal to the remaining volume. Such a formulation will hold true for a two gases with a boundary which is completely impermeable by either mass or heat. On the other hand, if mixing occurs, the inducted charge will heat up and the TRG cool down, both of which effects have to be accounted for. To compound the problem, the specific heats involved will also be affected to some extent by the changing temperatures. Hence, the formulation of the problem has to be somewhat more complicated than the impermeable boundary example in order to address these issues. Since there is no way to quantify the effect of mixing without a CFD study, the gases are assumed to mix completely. The equations are then formulated as in Eqns 5.8 and 5.9 where this time the unknowns are the final mixture temperature and amount of charge e.g.:

$$(m_{trg} + m_{ch})c_{v_{mixt}(T_{mixt})}T_{mixt} = m_{trg}c_{v_{trg}(T_{trg})}T_{trg} + m_{ch}c_{v_{ch}(T_{ch})}T_{ch} \quad (6.27)$$

$$P_{BDC}V_{BDC} = (N_{trg} + N_{ch})RT_{mixt} \quad (6.28)$$

where $N_{ch} = \frac{m_{ch}}{w_{ch}}$, m_{ch} being the mass and w_{ch} being the molecular weight of the charge and similarly for TRG. Eliminating T_{mixt} through Eqn 6.28 and solving Eqn 6.27 for the mass of charge leads to a $\alpha x^2 + \beta x + \gamma$ quadratic with the values of α , β , γ given by:

$$\begin{aligned} \alpha &= \frac{Rc_{v_{ch}(T_{ch})}T_{ch}}{w_{ch}} \\ \beta &= R \left(\frac{m_{trg}c_{v_{trg}(T_{trg})}T_{trg}}{w_{ch}} + N_{trg}c_{v_{ch}(T_{ch})}T_{ch} \right) - c_{v_{mixt}(T_{mixt})}P_{BDC}V_{BDC} \\ \gamma &= RN_{trg}m_{trg}c_{v_{trg}(T_{trg})}T_{trg} - P_{BDC}V_{BDC}c_{v_{mixt}(T_{mixt})} \end{aligned} \quad (6.29)$$

The equations are solved by requiring that all specific heats are known. However, the mixture specific heat, $c_{v_{mixt}(T_{mixt})}$ is actually unknown until the equation for charge has been solved and hence a value derived for T_{mixt} . However, since specific heats are not too heavily dependent on temperature and the temperature does not alter much, a compromise can be made by requiring an initial value for the mixture specific heat to lie between $c_{v_{ch}(T_{ch})}$ and $c_{v_{trg}(T_{trg})}$. This leads to an initial solution for m_{ch} , T_{mixt} , yielding a more accurate value for $c_{v_{ch}(T_{ch})}$. This process can be carried on to get arbitrarily good precision as explained in Section 5.1.2.

Figure 6.15 demonstrates a series of modeled consecutive cycles (dashed line) where the coupling model has been implemented as described. The experimental trace from which initial conditions have been taken is shown as a solid line for reference.

6.2 Example Results

The example presented in figure 6.15 is convenient in highlighting how the model can demonstrate possible underlying mechanisms behind observed behaviour. The interaction between cycles is

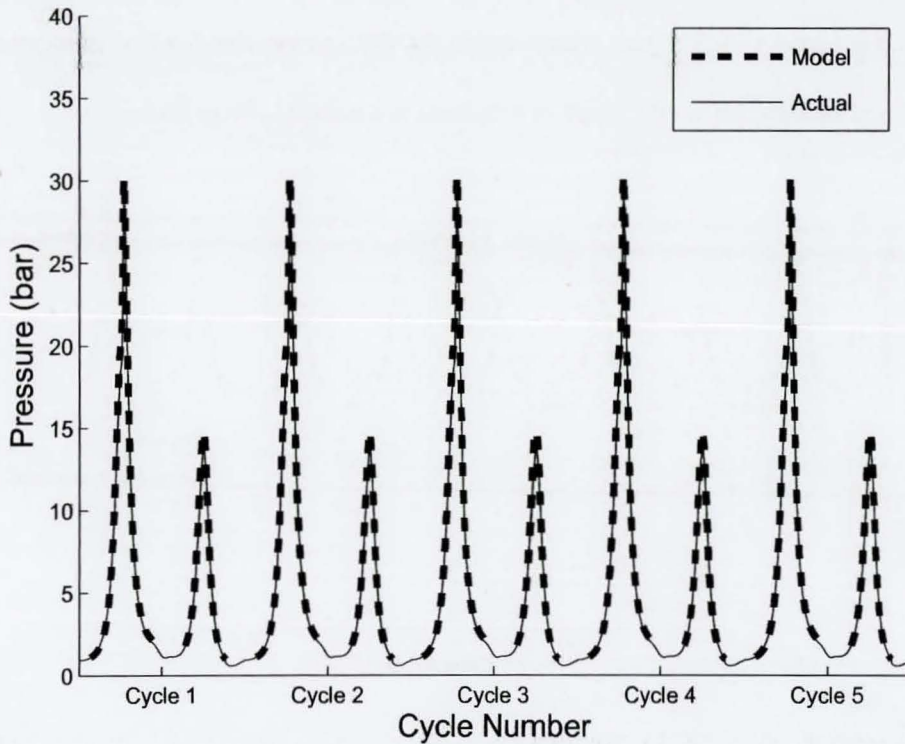


Figure 6.15: Example of coupled consecutive cycles

complicated to some extent by the fact that a number of factors come into play during the gas exchange processes. An extreme example of this behaviour, recorded experimentally under unstable combustion conditions, has been shown in Section 5.3.3. The modeling approach can be used to reproduce aspects of this behaviour and explore the underlying causes.

6.2.1 Simulated instability with fixed combustion phasing

An example of such a trial is shown in figure 6.16. In this case, the stable combustion of figure 6.15 has been artificially disturbed by a problematic cycle. While the model starts with a normal cycle, the 2nd cycle has had its combustion phasing delayed by 20 CAD and the CoC dropped to 0.5, thus simulating an incomplete late burn. In the corresponding TRG compression-expansion, a partial combustion also occurs, with a CoC of 0.4. This reflects the heat release of unburned charge during

the TRG compression, observed following incomplete burns in cases of unstable combustion [86] (discussed in Chapter 7). The heat release during the TRG compression leads to an increased TRG pressure and temperature at IVO, which in turn leads to a reduced charge intake.

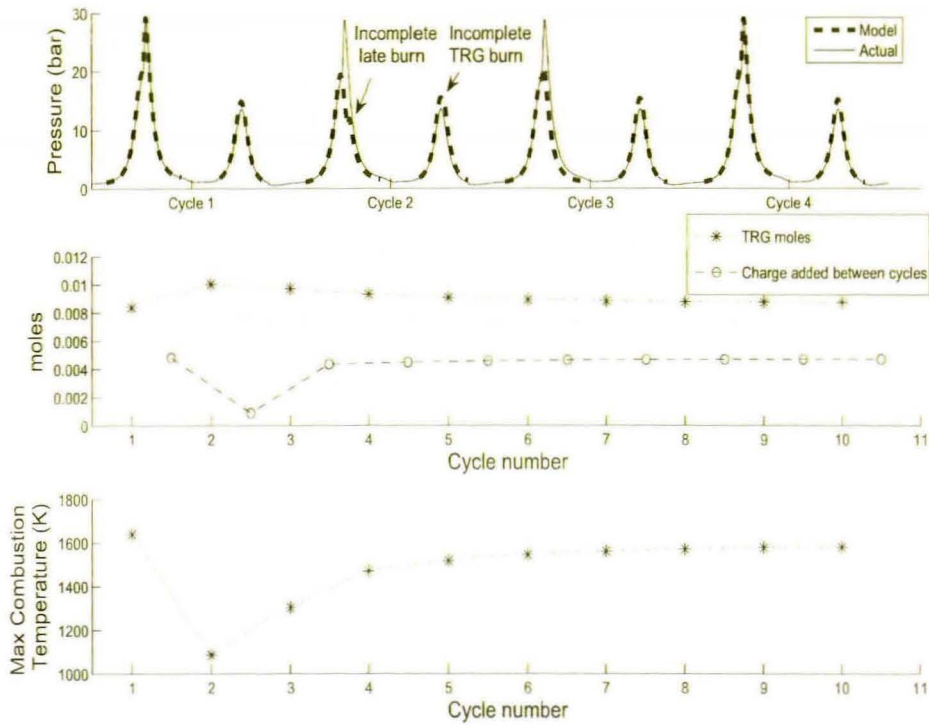


Figure 6.16: Example of simulated instability (artificially disturbed 2nd cycle) with an otherwise fixed combustion phasing

The top of the figure shows the modeled pressures of the first 4 cycles as thick dashed lines. The experimental pressure is also included as a reference against which to gauge the departure from “normal” combustion. The pressure trace of the 2nd and 3rd cycles are visibly altered.

The 2nd cycle has an earlier PPP compared to normal, due to the fact that, in the absence of noticeable heat release, the PPP is centred at 180 CAD. Its maximum pressure is very low, resulting simply from the compression of the gases. The delayed incomplete combustion can be seen as a small bump on the descending part of the pressure trace. In the TRG compression-expansion of the

2^{nd} cycle a heat release for 40% (CoC of 0.4) of the remaining unburnt gas takes place, raising the maximum pressure to 15.6 bar as opposed to a "normal" 14 bar.

The effect of this raised pressure and temperature is noticeable in the middle subplot which shows the molar amount of TRG and added charge for the cycles. The convention is that, a cycle number's "TRG moles" refer to the moles trapped in the EVC - IVO region of this cycle and *not* to the TRG in the IVC - EVO region. The added charge moles on the other hand are positioned so that they occupy positions in between integers on the x-axis, these being the cycles between which the charge addition is taking place. Hence, the first point of the TRG moles data corresponds to the first cycle's TRG compression - expansion region, while the first point of the added charge data corresponds to the charge added between cycles 1 and 2. Thus, looking at the middle subplot, the charge addition between cycles 2 and 3 is greatly reduced compared to the "normal" level represented by the charge addition between cycles 1 and 2. Also, it is worth noticing that the late incomplete burn of cycle 2, leads to a higher than normal TRG amount, since the end gas at EVO needs less venting to equalise its pressure with that of the exhaust manifold.

The reduced charge intake between cycles 2 and 3 leads to a much lesser available amount of chemical energy for the 3^{rd} cycle. Thus, despite the fact that combustion phasing after the problematic 2^{nd} cycle has been returned to normal in all subsequent cycles in this modeling run, the 3^{rd} cycle reaches a very low maximum pressure. Also, because the combustion occurs earlier than in the case of the incomplete but late burn of the 2^{nd} cycle, more of this energy is given as work to the piston or lost to the walls, so the final pressure around EVO is noticeably lower.

The lower heat release of cycle 3 is also noticeable in the lower subplot which shows maximum temperatures achieved during the combustion. The first point corresponds to the "normal" temperature, the point corresponding to cycle 2 is by far the lowest, being the incomplete late burn which is hampered both by the incomplete conversion but also by the fact that releasing the energy at a higher volume and lower pressure, it reaches much reduced temperature. Cycle 3, starting the

combustion at “normal” phasing (low volume and higher pressure) reaches higher temperatures than cycle 2 but is still hampered by the fact that it carries a very low charge amount as has been established by the middle subplot.

After the 3rd cycle, the engine slowly returns to normal. This is seen in the middle and bottom subplots (the top subplot only contains 4 cycles so as to reduce cluttering), where all values seem to be converging to the initial values.

6.2.2 Simulated instability with temperature triggered combustion phasing

The example above gives an insight into mechanisms of the cycle to cycle coupling. However, true unstable combustion suffers from one more factor which cannot be addressed by the previous example, that is, combustion dependence on chemical kinetics. A simplistic mechanism is employed in the next example: instead of forcing a fixed phasing, SoC is triggered by temperature threshold (in this case set to 850^o K). Thus, phasing is affected as well after the artificial destabilising cycle. The destabilising 2nd cycle is identical as in the previous example but this time the recovery is altered. The results are shown in figure 6.17.

The top subplot in this figure shows the SoC timings for each cycle. In this case, the “normal” SoC occurs around -10 CAD, while the artificially late combustion is clearly visible in the 2nd cycle. The recovery however exhibits oscillations which are a very usual phenomenon in unstable combustion (see Chapter 7). The basic underlying mechanism is that a cycle starting hot will acquire less charge and will end up igniting early, producing cold TRG and the following cycle will acquire more charge, starting at colder temperature, igniting late, producing hotter TRG and so on and so forth. These oscillations usually die out as has been observed in experimental data. However, in extreme cases, a violent SoC oscillation will result in cascading misfires which will stall the engine in the absence of spark.

Despite the simple trigger mechanism involved, the modeling run presented in this case is

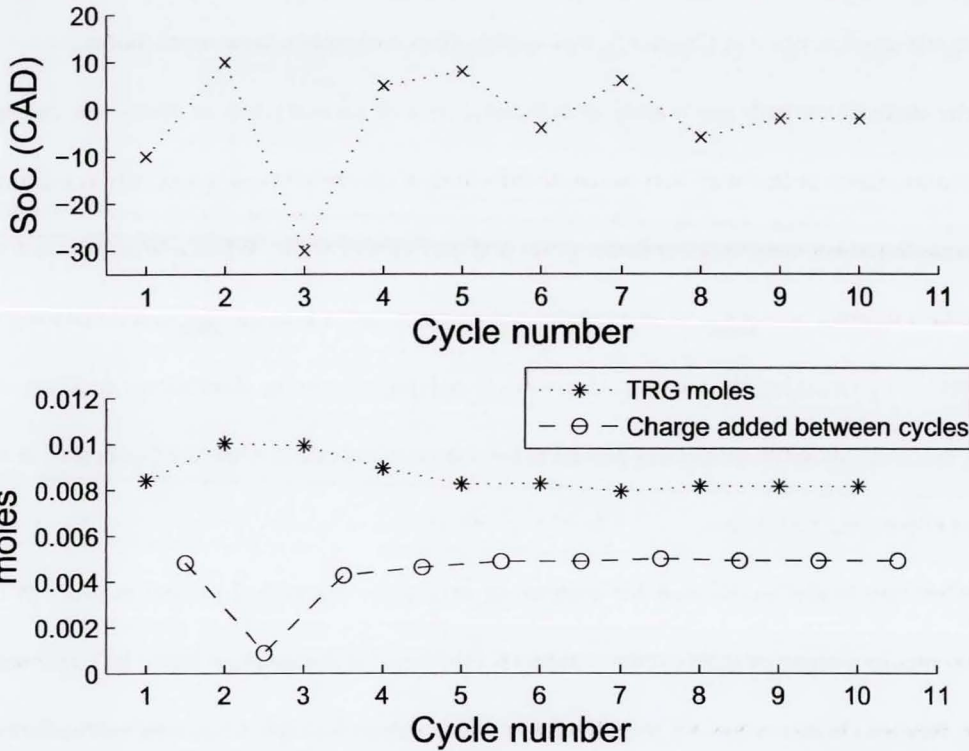


Figure 6.17: Example of simulated instability with a temperature triggered combustion phasing

characteristic of the types of instability encountered experimentally. The SoC oscillation is set up in cycle 2, has the maximum effect on cycle 3 and is then gradually damped as the cycles progress. Similarly, the moles graphs are exhibiting the overall behaviour encountered in figure 6.16 but with an added oscillation component which is not easily evident at a zoom level which keeps the whole data into view.

6.3 Summary

A zero dimensional modeling approach based on the first law of thermodynamics and the ideal gas equation of state has been implemented as a research tool. The driving idea behind this implementation is to solve the same equations presented in Chapter 5 from a different point of view, where, instead of interrogating a pressure trace about the underlying combustion profile, a com-

bustion profile is assumed and the resulting pressure trace is examined. Thus, in conjunction with the algorithms described in Chapter 5, this model offers a complete view of the issue.

The model's strength lies mainly in comparing it with known pressure traces and noting the differences, since in this way very accurate information can be derived, especially regarding the heat transferred between the in-cylinder gases and the cylinder walls. While a Woschni coefficient based heat transfer model has been implemented, more complex heat transfer models can be easily substituted by tweaking the auxiliary functions supplying data to the **derivatives** function, especially since the Woschni model has proved to be relatively inflexible when used over a wide range of HCCI operating conditions.

While the model works well for comparing existing to theoretical cycles, in order to completely predict a series of HCCI cycles, a model for the onset of autoignition has to be implemented. Since detailed chemistry has not been the focus of this research simple triggering mechanisms like temperature or Arrhenius rate styled equations have been investigated. However, none of these has been successful in predicting the observed experimental data. This appears to be generally the case for gasoline autoignition as discussed by Ogink [98] (Chapter 5.2). A fully predictive gasoline HCCI model will remain elusive as long as no mathematical formulation exists which can accurately predict autoignition under all operating conditions. Furthermore, this formulation must be computationally efficient if it is to be of any use for control purposes.

Still, the existence of a versatile model against which to check various aspects of HCCI combustion has been helpful and will probably continue to be so as future researchers keep expanding its functionality.

Chapter 7

Autoignition Study of Experimental Data

The algorithms developed for treatment of the experimental data have been analysed in Chapters 5 and 6. Using these as research tools, a long term study has focused on the mechanisms behind HCCI. The drive behind the study has been to understand how HCCI combustion, especially autoignition, occurs in order to model and hence, control it. However, after research into the measurable data from the experimental results, no satisfactory autoignition condition has been established. This has been mentioned in Chapter 6, since such a condition would have enhanced the functionality of a gasoline HCCI model.

Still, research into various experimental data have yielded insights into aspects of HCCI operation. All data presented in this chapter are experimental involving both valve strategies (as explained in 3.2) and both “pure” HCCI as well as spark assisted SACAI.

7.1 Search for an autoignition criterion

Gasoline combustion can be generally thought of as an oxidation of the hydrocarbon fuel yielding water and carbon dioxide as described in Eqn 6.9. While this will serve as a generalisation of start and end states, it is by no means a comprehensive description of the chemical paths of combustion. Commercial gasoline is a mixture of different compounds, all of which follow their respective oxidation paths. A rigorous treatment involving chemical kinetics even where possible is a very computationally demanding process. Thus, the research has been focused instead in enquiring whether a particular empirical lightweight criterion might be derived to account for autoignition prediction.

The obvious candidates for such an investigation are temperature and pressure. From manual investigation of cycle to cycle behaviour, such as described in section 5.3.3, it is evident that combustion is affected by such measurable parameters. Unfortunately, extensive large scale analysis of autoigniting cycles fails to provide an adequate trigger mechanism for autoignition.

Hence, a more complex model has to be developed to account for autoignition prediction. To such an end, various formulations of Arrhenius integral [99] have been tried. The Arrhenius integral is a relatively simple model thus making it an ideal candidate for adoption as a lightweight trigger condition. It is based upon the requirement that a continuously integrated expression will reach a threshold value when autoignition occurs. Various formulations have been employed by HCCI researchers [96–98, 100] reporting various degrees of success for different setups. In the case of the present data however, all Arrhenius-styled formulations have often failed to even produce a prediction that yields results more precise than simply taking the mean value of SoC at a given operating point.

Although, some researchers [97, 100] have pointed out certain limitations that relate to Arrhenius rate fitting, the discrepancies between experiment and best fit are difficult to account for. The experimental data in this research exhibit a puzzling behaviour. That is, for operating conditions

where the combustion mechanism is pure autoignition, combustion occurs within a very small CAD window regardless of a multitude of changing operating conditions. The results are as follows.

- For the valve strategy employing constant IVC and EVO, where the highest amount of autoigniting operating conditions exist, combustion occurs within a window of 6 CAD, centred on 4 CAD BTDC, with a standard deviation of 1.5 CAD. This behaviour is generally maintained across an RPM span of 2000-4000, a TRG span of 37%-76% (by volume) and a lambda span of 0.8 to 1.7. (Only cases where Location of 5% Mass Fraction Burnt (MFB5) is located before spark timing are considered as pure autoignition).

The corresponding temperatures are centred on 1000 K, with a window of 250 K and a standard deviation of 65 K.

- For the constant duration valve strategy, the pure HCCI operational region is much reduced due to the effect of reduced effective compression ratio as TRG increases. However, the observed behaviour hints at similar values of autoignition occurring within a window of 4 CAD, centred at 2 CAD after Top Dead Centre (ATDC) with a standard deviation of 2 CAD. The RPM span is 2000-2500, TRG span is 28% to 38% (by volume) and all tests are stoichiometric.

The corresponding temperatures are centred at 890 K with a window of 25 K and standard deviation of 12 K. Of course, the scarcity of the data points in this case makes such statistical metrics unreliable.

In both strategies, temperature based and integrated Arrhenius rate based predictions yield results whose scattering is far larger than the clustering observed by the data. The best predictions based on variants of integrated Arrhenius rate formulation give results within a CAD window at least double the size of that observed in practice.

The conspicuous failure of the Arrhenius rate models and data clustering seem to indicate that different mechanisms might be at work in initiating the combustion of the mixture. Hence, a

more detailed analysis has to be performed in order to investigate the possible explanation for the satisfactory behaviour of the engine over so diverse operating conditions.

7.1.1 Data Analysis

To get an understanding of the mechanisms at work, various traces of exchanged heat across the spectrum of operating points have been examined, generated as described in figure 5.18 on page 122. The traces normally exhibit a Gaussian-like curve of the short duration typically associated with the sudden nature of HCCI combustion. What is of interest however, is when a trace of normal combustion is compared with that of a misfiring cycle as shown in figure 7.1.

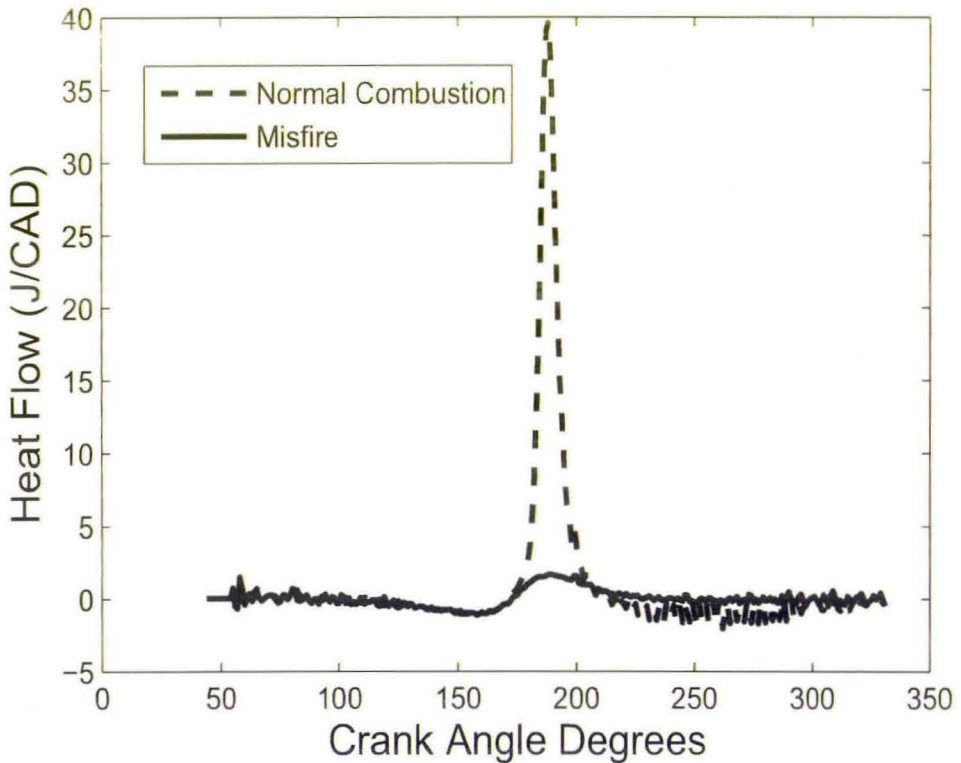


Figure 7.1: Exchanged Heat traces for a normal and a misfiring cycle

This figure shows the average of firing and misfiring cycles across a wide band of RPM / TRG values. The dip at the start of both traces is due to increasing heat losses as the gases are warmed

up through compression. Similarly, the discrepancy between the two traces in the region after the combustion can be attributed to the increased heat losses of the non misfiring case.

What is less easy to explain is the apparent small magnitude heat addition in the misfiring case. It can be argued that the cycles used to create it were not complete misfires. However, *all* individual misfiring cycles observed exhibit a similar heat profile.

To get a clearer understanding of the mechanisms involved, the NVO region of each cycle needs to be investigated. This is done in order to gauge the effect of compression and expansion on a theoretically completely inert mass of gasses, as is the case of TRG during NVO.

Heat profiles across the TRG range are sampled and the results shown in figure 7.2.

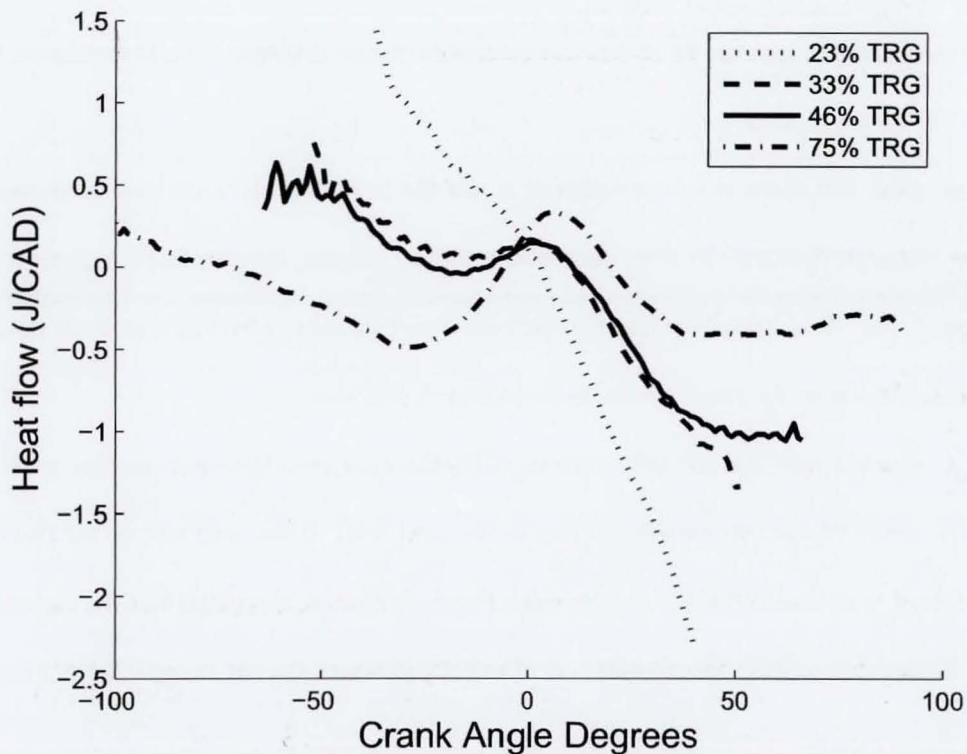


Figure 7.2: Exchanged Heat traces for the TRG compression-expansion region over a TRG sweep

Because the higher amounts of TRG imply an earlier EVC and subsequently, later IVO, the CAD range (x-axis) of each trace differs. The highest TRG trace (75% by volume) is also the longest

on the x-axis, while the lowest TRG (23%) is the shortest. The implication is that a source of heat is present in the case of high amounts of TRG which does not come into play when TRG is reduced. Other effects like differing blowby are hard to quantify and the difference they would make between the two cases is unclear, however, it is unlikely to be the cause for such a big discrepancy in the overall shape of the curves involved. The curves presented in the figure indicate very clearly the connection between the amount of TRG and the different profiles of heat addition.

One more piece of information is derived through the comparison of the relative magnitudes of different traces as shown in figure 7.3¹. This gives an appreciation of the scale of heat profiles encountered in a typical misfire from unthrottled HCCI, a typical trace at NVO of a high TRG HCCI test and finally a misfire from throttled SI (normally, the two misfires are located around the TDC of the power stroke, whereas the NVO is located around the gas exchange TDC. In this figure, both these TDCs occupy point 0).

One point that needs to be stressed here is that the SI tests in this case have zero overlap. Hence, although their TRG level is theoretically 0% by volume, they do retain a certain, low, amount of TRG. This might be relevant to the behaviour exhibited in the figure as small amounts of TRG might potentially play a role in the development of a trace.

It is apparent here that the HCCI misfire yields the most prominent heat profile, while the throttled SI and TRG at NVO are more or less on the same level. It has to be pointed out that both the throttled SI and the TRG at NVO cycles reach lower pressures at every CAD than the unthrottled HCCI, though their starting temperatures are drastically different, the TRG being much hotter than

¹One point that might need clarification here is why the misfire of throttled SI trace exhibits so much noise. The reason is that these traces are averaged over a series of cycles to eliminate noise. Compression of TRG at NVO yields hundreds of candidate cycles, HCCI misfires are also more numerous because more HCCI data were available during these experiments. SI data were not as abundant so there were less cycles to average and hence iron out the effects of noise.

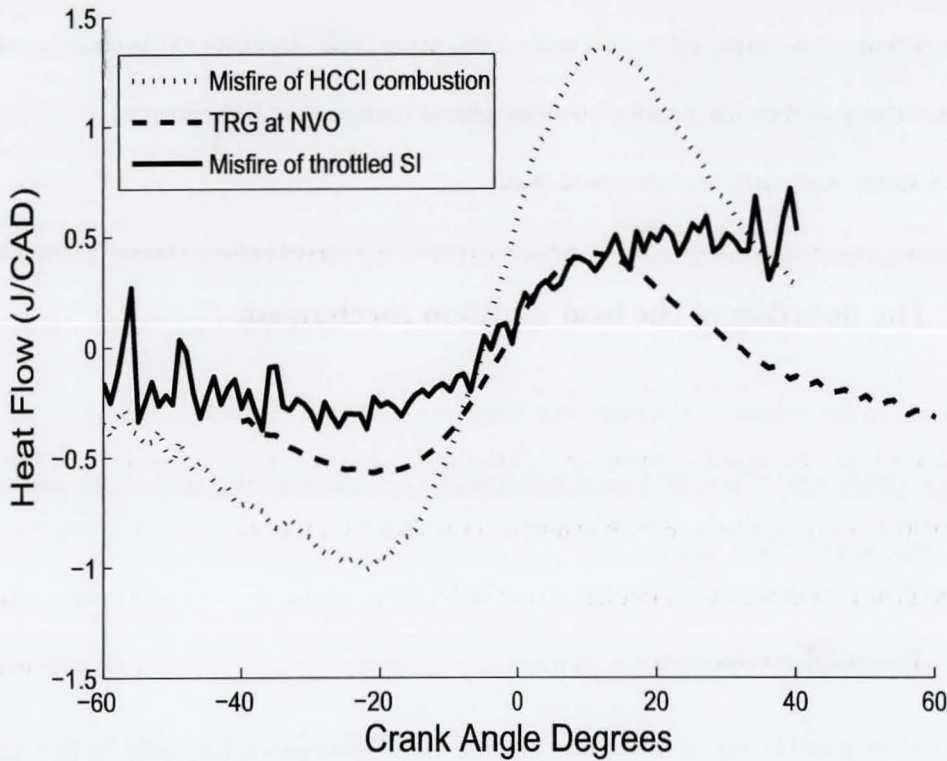


Figure 7.3: Heat profiles of HCCI and SI misfires and TRG compression-expansion

the relatively cool gases of the SI case.

Thus, the evidence presented so far seems to indicate the following:

1. Every misfiring combustion cycle (including SI) yields some amount of heat. This heat appears to be more prominent with increasing pressure.
2. Every TRG cycle above a certain level of TRG also yields some heat, the profile of which becomes more prominent with increasing TRG amounts.
3. TRG cycles below a certain level of TRG exhibit a different heat profile, giving a monotonically decreasing trace at the lower extreme of TRG.
4. These heat profiles, when prominent, are always well developed by TDC, peaking a short time afterwards.

In all of the above cases, the heat profiles are extremely low magnitude when compared to values of heat release expected at a normally combusting cycle. However, the persistence of their shapes, rather than their magnitudes which are almost negligible, indicates that there is a physical process, rather than random noise behind them.

7.2 The question of the heat addition mechanism

According to this evidence, it appears that some process of heat addition comes into play in all cases of compression. Thus, the logical next question is to establish the nature of the mechanism behind this observed heat addition.

7.2.1 Potential mechanisms

There are two possible ways in which heat could be added to the gases, externally, by heat transfer, or internally, by chemical reactions (or a combination of the two). Both these mechanisms offer some advantages and disadvantages as far as explaining the observed data is concerned.

If chemical heat addition is assumed to be the mechanism, a number of questions arise:

1. Why autoignition onset appears insensitive to both time (RPM, valve timing) and composition (AFR, TRG) and
2. Why does heat addition, which appears in every single case, not always develop into a proper combustion (figure 7.1).

The evidence points to the fact that autoignition is more affected by CAD than by temperature, pressure or time. These are not normally characteristics of a chemically driven process.

On the other hand, if an external heat transfer mechanism is assumed, similar questions arise:

1. Heat transfer, which is dependent upon the geometrical shape of the cylinder, as well as the gases' pressure and temperature, should be symmetrical around TDC. This is not the case.

2. The gases reach temperatures in the proximity of 900 K by compression. Similar temperatures are not to be found on the surrounding material. Hence, conduction is ruled out, especially close to TDC, where the heat profiles are very prominent.

7.2.2 Noteworthy engine characteristics

With both internal and external heat sources being unlikely to account alone for the observed heat profiles, a combination of the two might be able to help. Before proceeding, certain characteristics of the engine used in the experiments have to be pointed out which might prove relevant.

The engine is equipped with hydraulically activated valves. In particular the cylinder head is not lubricated, reaching higher temperatures than conventional cylinder heads where oil circulation helps carry off excess heat.

The valve stems are longer than those of conventional valves, helping the exhaust valves in particular to retain higher temperatures than normal.

The cylinder head exhibits a squish zone as seen in figure 3.5 (page 30). As the piston nears TDC, this zone can be expected to violently expel a volume of gas towards the centre of the combustion chamber, increasing turbulence at certain CAD dependent phase during the compression.

7.2.3 Proposed mechanism

Based on the facts presented so far, it is plausible that what is exhibited is a combination of both internal and external heat sources.

The main evidence for the chemical nature of the heat addition profile is the asymmetry around TDC. The main evidence for a strong effect by external heat transfer is the locality of the traces, which seems largely unaffected by changing RPM.

Hence, what has to be appreciated is that, although temperature and pressure increase as the piston moves up, the ratio of the area of gases exposed to the cold cylinder wall to the area of

gases exposed to the relatively hotter cylinder head and exhaust valves decreases. Hence, although a positive heat flow, from the surroundings to the gases is impossible, it might be possible that the heat losses are not as high as would otherwise be expected close to TDC, despite the gases at TDC presenting their greatest area to volume ratio. The reduced heat losses, coupled with increased pressure, might have quite a significant effect on a slow, low magnitude chemical reaction that is always present but not easily noticeable.

The squish zone might also play a role. The gases in close contact with the walls generally incur higher heat losses. The temperature dependent reactions taking place will, therefore be more prominent at the regions where fresh charge is in better contact with hot TRG and preferentially away from the cold walls. As the piston gets closer to TDC, the gases in the squish zone are expelled quite suddenly towards the centre of the cylinder, increasing turbulence just as peak compression approaches. Since this effect will always happen close to TDC irrespective of RPM, it is possible that it also plays a role in the observed clustering of the autoignition events.

One more thing to notice in the case of combustion cycles is the dependency of the heat profile upon the pressure. Highly throttled SI, exhibits a lower magnitude profile than HCCI, which operates unthrottled (figure 7.3). This dependency on pressure is a possible explanation for the observed delay in the combustion timing of the constant duration valve strategy, where, due to late inlet valve closing, lower pressures dominate.

Moving to the TRG at NVO region, similar conclusions can be drawn. The very strong dependence of the heat profile on TRG has already been demonstrated on figure 7.2. The different heat profiles of the low and high TRG cases indicate a very marked difference between the two, most likely to be chemically related.

It is generally the case that reactions are still occurring after the exhaust gases have been expelled from the cylinder. What is probably happening is this: in HCCI combustion, still reacting TRG is trapped within the cylinder. The main source of heat is this reaction. In the low TRG cases,

EVC is very close to the NVO TDC, leading to a low pressure rise due to compression. This pressure rise is insufficient to reverse the natural trend of the reaction to die out, which is what is being recorded (e.g. the 23% TRG trace in figure 7.2). As TRG is increased, EVC occurs further away from TDC, leading to a higher pressure rise. This pressure rise gradually becomes sufficient to keep the reaction going.

It has to be pointed out that all these phenomena are very low magnitude and are unlikely to be obvious purely by inspection of the pressure trace. However, evidence of this imbalance can be derived by looking at the TDC region of averaged $\log(P)$ - $\log(V)$ diagram of TRG at NVO as in figure 7.4.

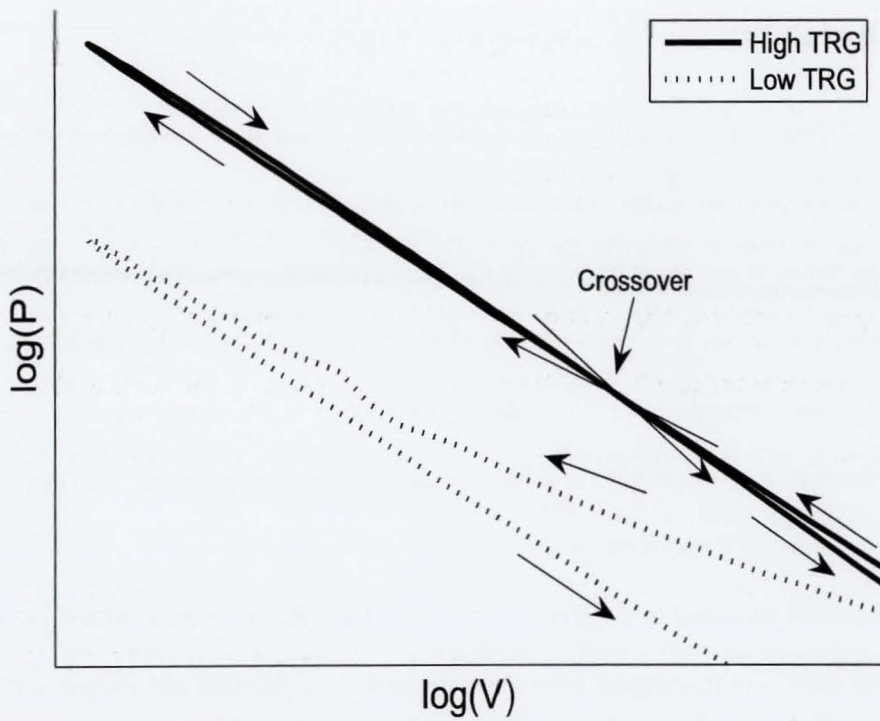


Figure 7.4: Evidence of crossovers in $\log(P)$ - $\log(V)$ at high TRG levels

In this case, there is an obvious difference between the two traces. The lower one, with low TRG (4% by volume) is a conventional trace of TRG compression and expansion, with associated

losses making the trace lower on the expansion side. On the contrary, the top one, with high TRG (76% by volume), exhibits almost identical traces in both compression and expansion. Closer examination reveals that there is in fact a crossover point before TDC, leading the end of the expansion segment to be above the compression segment. This relatively easy to perform test is a first crude indication of heat release in the TRG at NVO region. This is because, given no heat exchange during the NVO, the going and returning segment should exactly coincide. In reality, the returning trace must be lower. This is due to heat losses from the in-cylinder gases to the cylinder walls (as well as mass losses to blowby). So, a trace that actually returns at the *same* level, not to mention *higher* is highly suspect and must be considered as a clear indication of heat release.

7.3 Instability

Having a degree of understanding of the mechanisms involved in the autoignition of the charge, a question that then arises is that of unstable combustion. While HCCI combustion can exhibit very low cyclic variation this is not necessarily true at all operating points. Near the upper TRG boundary, combustion can become increasingly unstable for one of the two valve strategies tested. The linking of cycles through use of TRG is the key mechanism in this situation and an understanding of the effects at play is desirable in order to avoid unstable regions which can have detrimental effects on the engine's operation.

As has been described in the previous section, in general, combustion timing is a largely self regulating process in this engine, most likely dependent on chemical and geometric characteristics. However, this does not imply that it does not have certain limitations. As hinted by the shift in mean autoignition location between the two valve strategies (effectively switching compression ratios) as well as by the different heat profiles of throttled SI as opposed to unthrottled HCCI misfires, the initial reaction leading the way to autoignition is dependent on at least pressure (which, in turn, implies a certain temperature regime as well. The relevance of temperature is unclear

seeing how SI, with greatly different temperatures to HCCI, exhibits similar heat profiles to TRG at the NVO region of HCCI).

Hence, the upper limits of HCCI in the valve strategy of fixed IVC and EVO seem not to be prone to instability due to the non varying compression and the fact that high TRG operates throttleless, ensuring a roughly similar pressure rise in all cases. Maximum recorded TRG at 76%, yields a remarkably stable combustion with no misfires as seen in figure 7.5, top.

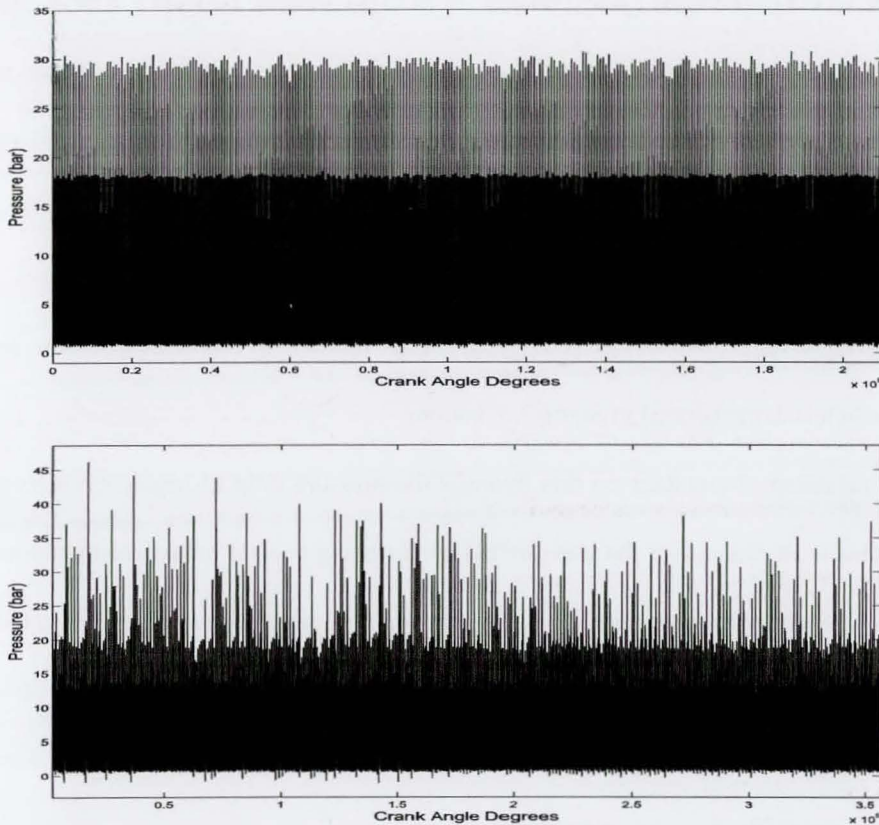


Figure 7.5: Example pressure traces of:

TOP: Very stable combustion at high TRG (76% by volume), fixed IVC/EVO valve strategy, 2000rpm, 1.73 bar IMEP.

BOTTOM: Extreme unstable combustion at 50% TRG by volume, fixed duration valve strategy, 2000rpm, 1.47 bar IMEP

In the valve strategy with constant duration and shifting IVC and EVO, the maximum attainable

TRG level is decreased to around 55% by volume, since the added effect of reduced compression at high TRG comes into play. The high TRG operating points in this valve strategy are greatly prone to instability, resulting from pushing the autoignition point too late. Hence, random variations (potentially in non recordable physical quantities like for example homogeneity) among cycles can influence certain cycles while leaving others unaffected. This can have a cascading effect often leading to misfires.

At the level of individual cycles, misfires in HCCI are usually associated with certain characteristic signs. Unstable HCCI combustion often exhibits great variations in maximum pressures, yielding some cycles with uncharacteristically large values. Although the onset of instability is by and large unpredictable, a closer look at individual cycles reveals certain patterns that generally characterise unstable combustion.

The first and most obvious sign is the great overall variation in maximum pressure, an extreme case of which is demonstrated in figure 7.5, bottom.

An interesting observation on this figure is the pressure drop to *negative* values in certain places. This is an example of the pressure transducer being heavily influenced by thermal shock, occurring after strongly knocking cycles. The short duration of HCCI combustion, coupled with the violent pressure rises of preignition, present in unstable regions, cause tremendous stress on the sensor (not to mention the engine) which greatly undershoots the subsequent low pressure regions of the trace (typically the valve opening events).

The methodology for correcting this kind of measurement error has been discussed in Chapter 5, section 5.1.2. However, the extremes of behaviour exhibited in unstable combustion cannot be accounted for without a host of extra sensor inputs correcting the major deviations of the in cylinder transducer, leading mainly to uncertainty in individual cycle estimation of TRG amount and temperature.

The instability demonstrated in figure 7.5, bottom, was deliberately caused in order to in-

investigate this kind of behaviour. In practice, this kind of operation should never be encountered. Instead, instability will most likely arise through what initially appears as a normal, stable HCCI, gradually deteriorating until the engine stalls. This is illustrated in the pressure trace of figure 7.6 which is based on an experiment designed to test this gradual deterioration.

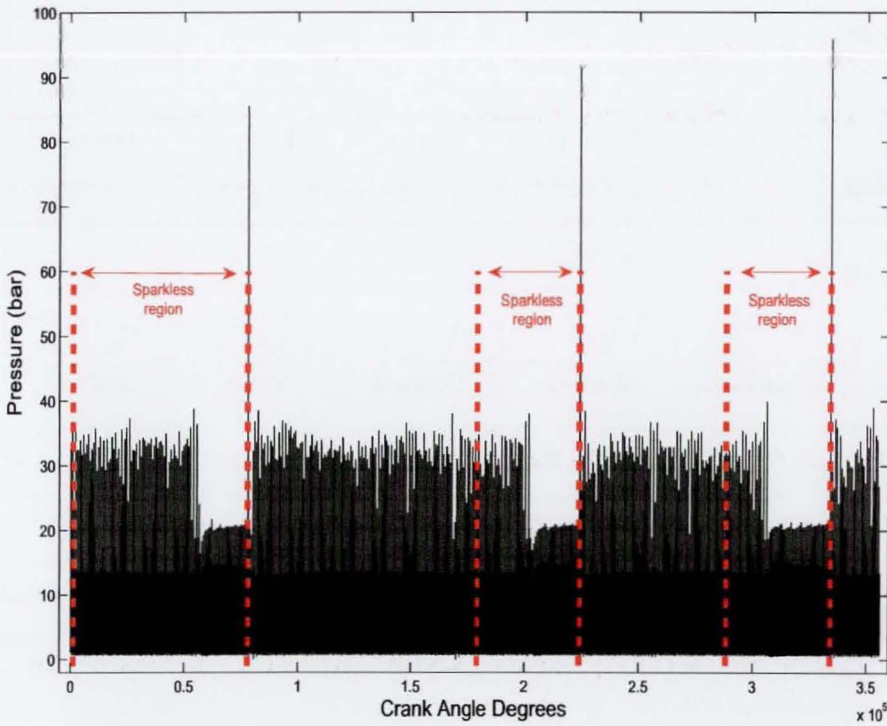


Figure 7.6: Example pressure trace of repeated instability at 38% TRG by volume, fixed duration valve strategy, 2400rpm, 3.5 bar IMEP (when not stalled)

In this experiment, the spark is switched off three times. Each time, the engine runs in normal HCCI mode, at 38% TRG by volume, 2500 RPM, until it stalls. Having stalled, the spark is reintroduced at 30 degrees BTDC, then switched off again and so on.

A few things are noticeable initially just by looking at the overall pressure trace. The three regions where the engine has stalled are clearly visible. Also visible are three very high magnitude pressure peaks at the end of each stalled period. These correspond to the first cycle that ignites on

reintroduction of the spark after the stalled period. These cycles have expelled all exhaust gases and are charged with fresh charge at WOT inlet pressures. Given a spark (at 30 degrees BTDC), they reach much higher pressures than the subsequent cycles, where the charge is diluted with TRG.

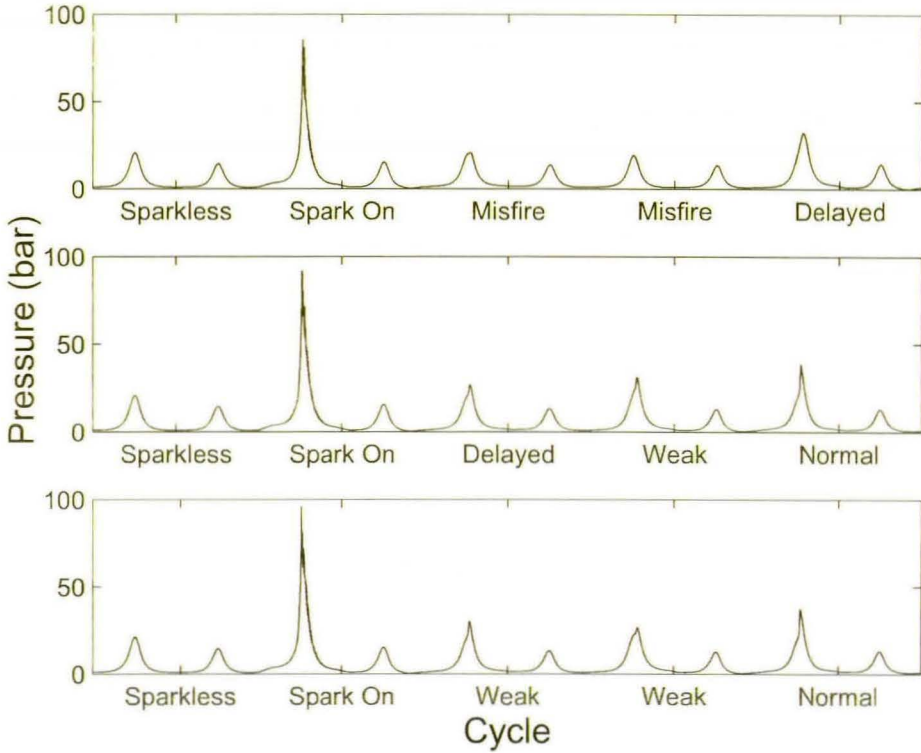


Figure 7.7: Zoom of the events around the reintroduction of spark

Looking closer, the first piece of information on misfires is given by these cycles, the three high magnitude combustions on reintroduction of spark (Figure 7.7). They have very early combustion timings, with MFB 5% values at 11, 13 and 14 degrees BTDC, when the average for the non stalled part of the log is around 2 degrees ATDC. However, what is more interesting is that all of them are followed either by misfires (in the case of the first one), or by delayed, weak combustions (in the case of the second two).

This is the first piece of relevant information on the instability exhibited by this engine. The next step, is to plot the MFB5 values for the cycles in the three regions. These are shown in figure

7.8.

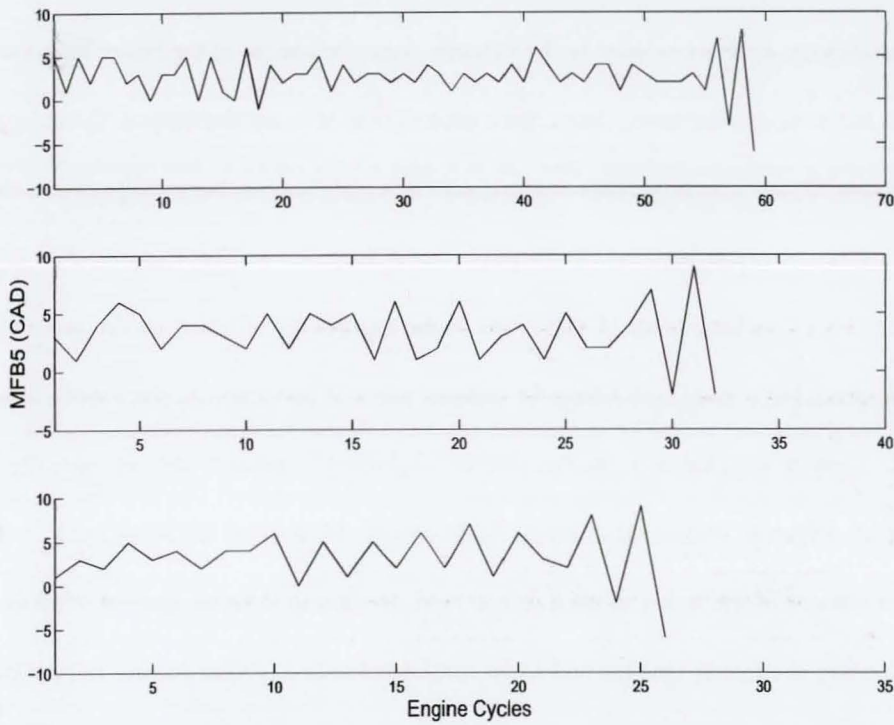


Figure 7.8: MFB5 traces near the 3 unstable regions

On all three of these, the blank region on the right is where misfires start. An important thing to notice is that in all cases, before the misfires, a large oscillation has been established, the last firing cycle of which exhibits a very early MFB5 value.

The oscillations established in the above examples are visible, in general, across experiments of the second valve strategy (constant duration, shifting IVC and EVO) at the upper limits of TRG. The explanation proposed for them is the following.

At the limit of HCCI, the autoignition is constantly at the threshold of failure (in the experiment presented here, mean MFB5 for non misfiring cycles is 2 degrees ATDC). When, for any reason, autoignition almost fails, a very late combustion occurs. If that is the case, the exhaust gas temperature rises, both because combustion occurring later incurs fewer heat losses, or, in extreme

cases, because combustion is still strongly occurring at EVO. Part of these hotter than average exhaust gases are then passed as TRG to the next cycle. Thus, at the intake stroke of that cycle, less than average air is introduced to the cylinder since the energy of the hotter than average TRG expands the incoming air more. Since the injector pulse remains unchanged, the charge ends up slightly rich. This cycle now starts compression at higher than average temperature, richer than average. Because of the increased temperature, it combusts early. This early ignition is not problematic from a knocking point of view (due to the cushioning afforded by the presence of high TRG amounts), but it ends up robbing the exhaust gases of temperature, since more time for heat losses is allowed, coupled with the fact that the slightly rich mixture does not have the sufficient amount of oxygen to release all of its available energy. Hence, the following cycle, will acquire a higher amount of air, will end up lean and cold, leading to delayed ignition, leading to hotter gases, leading to an early ignition and so on, until eventually a misfire occurs. In pure HCCI mode with the spark off, a misfire is non recoverable, since it produces no TRG to ignite the subsequent cycles, hence the cascading misfires witnessed in this experiment.

Having this framework in mind, further evidence surfaces when considering the TRG compression and expansion cycles occurring at NVO. The engine used in these tests has been equipped with a dedicated ion current probe as described in 3.1. Thus, the ion current trace can be interrogated for possible hints of activity during the supposedly inert TRG compression and expansion cycles. The results are displayed in figure 7.9.

This figure is the same as 7.8, displaying the three regions leading to the misfires, but it has the cycles where ion current activity has been recorded at NVO marked with circles. Unfortunately, the results are not conclusive, the main reason being that the probe used in the collection of this data has been designed for collecting a significant ion current signal during the combustion cycles but not for the requirements of the much lower magnitude events of the TRG cycles. Still, it is evident that all three instability oscillations leading to the cascading misfires (the rightmost parts of all

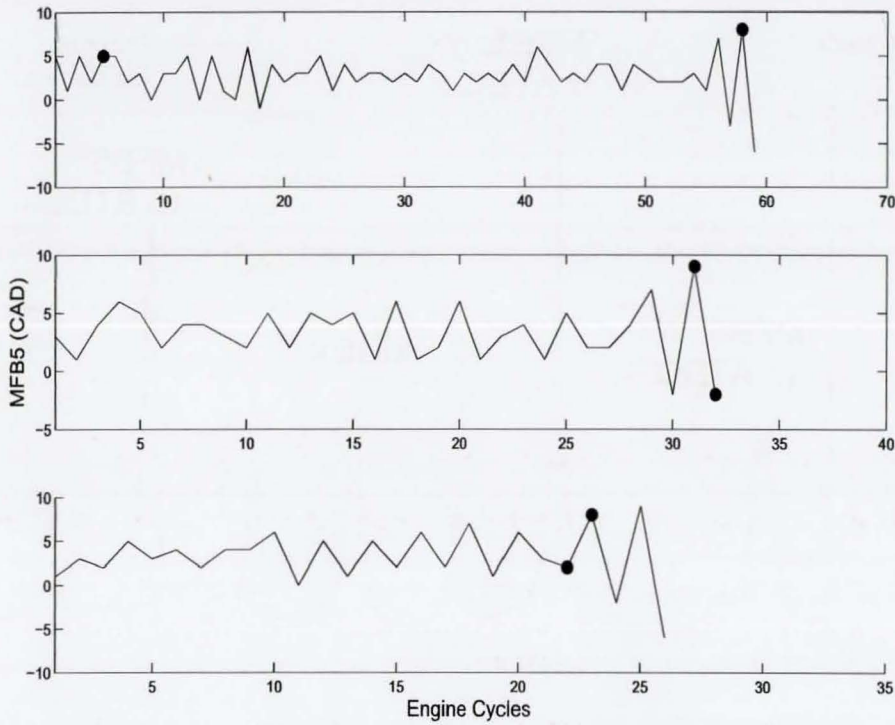


Figure 7.9: MFB5 traces near the 3 unstable regions with marked ion current activity at NVO

three traces) have exhibited ion current activity in their TRG at NVO. It is also evident that activity has been recorded at least once in other regions even if these did not lead to misfires (top trace of figure 7.9).

The behaviour described above is clearly demonstrated in figure 7.10 taken from a log of a similar unstable experiment at 30% TRG by volume, 2200 RPM (again spark switched off until cascading misfires recorded).

In this instance, the text above each cycle is the cycle's MFB5 value. Starting from the left, a very delayed ignition at 13 degrees ATDC results in the following cycle combusting relatively early at 1 degree ATDC, when the average value for non misfiring cycles for this experiment is 6 degrees ATDC.

The early combusting cycle is followed by a complete misfire. Looking at the ion current trace

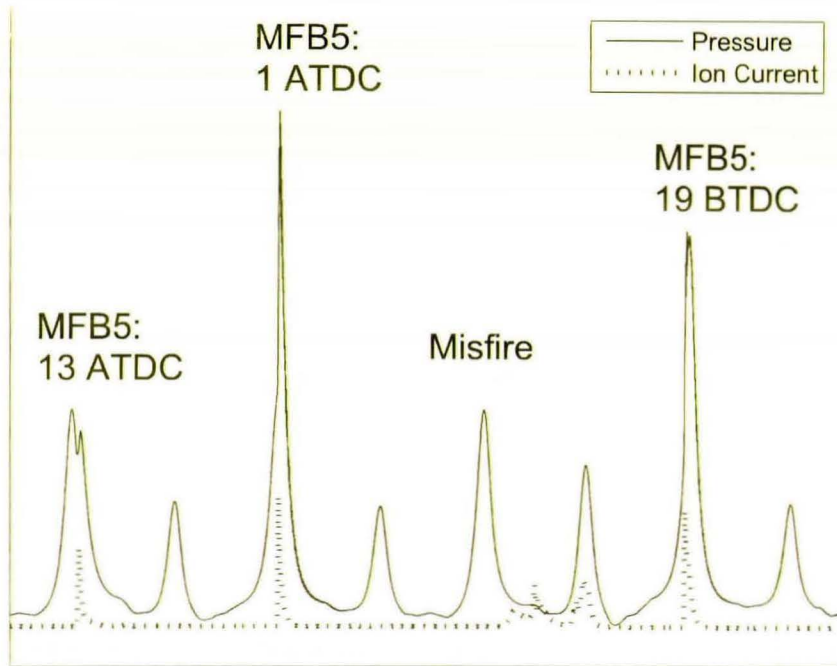


Figure 7.10: Example of TRG combustion

however, it is evident that the charge ignites at EVO, most possibly through contact with the exhaust gases. This combustion is carried into the NVO region where a highly prominent ion current signal is given throughout. The effects of the TRG combustion in the NVO region are obvious from the pressure trace by comparing its peak magnitude to that of the same feature of the neighbouring cycles.

The increased temperature of this region is being evident by the noticeable dip in the induction region just before the compression of the final cycle. Namely, notice how the start of pressure at the start of that final cycle touches the base level of the ion current signal (in fact, it goes slightly negative at 0.006 bar). This is again evidence of thermal shock making the pressure trace undershoot following heat release. In the pressure values usually encountered it is hardly noticeable, however, in the low pressure region of the induction, it can lead to suspiciously low

values. In this case, the heat release in the NVO region has left no time for the transducer to recover, leading to this pronounced effect.

Hence, the final cycle in the figure gets mixed with very hot TRG, resulting in a lower amount of air in the fresh charge and an extremely early ignition with an MFB5 value of 19 degrees BTDC. The reduced amount of oxygen in the charge is most likely the reason why the combustion fails to yield very high maximum pressure. It has to be noted here that these cycles are at the end of an unstable region. After the final cycle in the graph, continuous misfires occur until the spark is reintroduced.

7.3.1 Potential use of low tension coil as alternative in-cylinder sensor

The test presented in figure 7.10 illuminates a few more things not covered by tests of figures 7.8 and 7.9. Unlike those, where the high TRG limit had been pushed too far, 38% by volume, which is a lot for this valve strategy, this test operated in a more sedate region of 30% by volume. Thus, running times between switching off the spark and eventual misfires are much longer, allowing for a better study of the unstable pure HCCI region. The picture that emerges from a study of this test adds some more information concerning the use of in-cylinder diagnostics.

The relation between combustion timing and ion current has been explored in Chapter 4. In the context of this experiment, the location of the ion current trace in the combustion region of a cycle would be the most obvious candidate, had MFB5 (whose estimation requires a pressure transducer) not been available. Figure 7.11 highlights their strong interrelation (correlation coefficient of 0.93).

The secondary use of ion current, as a diagnostic for TRG heat release combustion in the NVO region has been proposed above. However, there is yet another signal lending itself to the same task, a simple processing of the trace of the (inactive in pure HCCI) spark plug's low tension coil voltage.

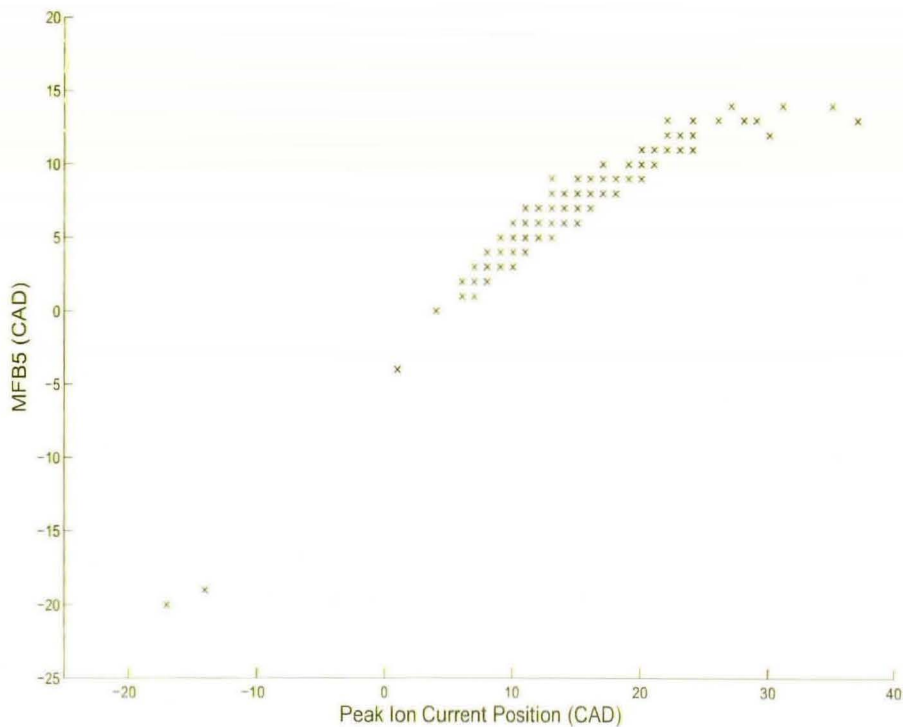


Figure 7.11: Relationship between MFB5 and Peak Ion Current Position

Under normal operation, this signal describes the voltage in the primary ignition coil. In pure HCCI, the inactive spark plug acts as a sensor, returning an information poor signal that by and large shows a weak response to the combustion. Figure 7.12 shows average traces from pressure and coil for comparison.

Normally, the coil trace seems to initially respond to compression by deflecting upwards. After TDC, there is a drop, followed by another drop, presumably related to the effects of combustion.

In late combustion, the second drop is less accentuated, making the first drop the most dominant as seen in figure 7.13. While the mechanism behind this behaviour is unknown, it is clearly a potentially useful diagnostic for detection of instability during HCCI combustion and a promising candidate for further investigation using advanced signal processing techniques.

The potential use of this signal becomes apparent when comparing the location of its minimum

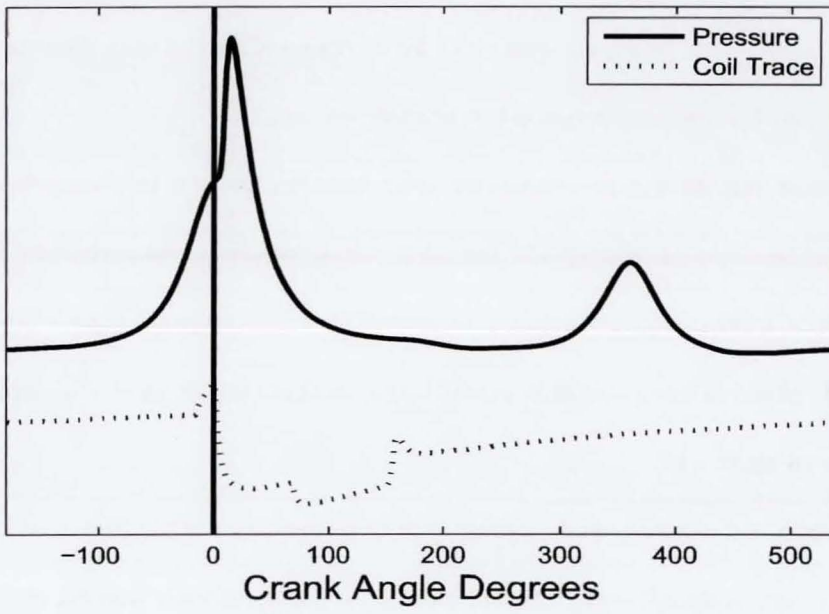


Figure 7.12: Typical trace taken from the low tension coil, shown alongside the corresponding pressure trace

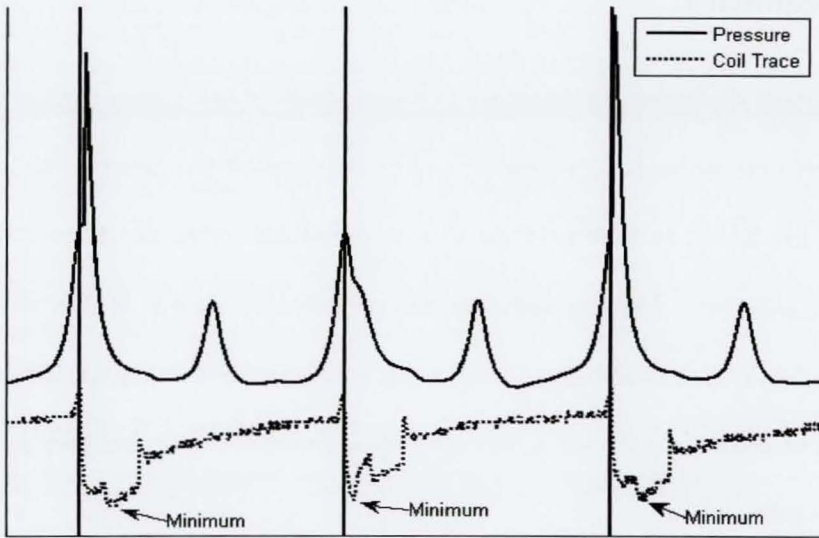


Figure 7.13: Close up of pressure and coil traces for three cycles including one late combustion

value within each cycle against the corresponding MFB5 values. The results are shown in figure 7.14. As shown in the figure, the location of the minimum of the coil trace presents a tendency to respond to the late combustions present at unstable regions.

The most intuitive way to visualise the effect described above is by considering the signal to be made of two descending segments. Instead of relying on how the location of the minimum will be shifted, it is straightforward to derive the ratio of the minimum points of these segments. When the results cross 1, a late combustion can be flagged and possibly the onset of unstable combustion as shown on figure 7.15.

The ratio of the two segments appears to respond to delayed MFB5. Hence, it is potentially a cheap and very computationally efficient method for getting an early warning of the onset of an unstable region, even in the absence of pressure or ion current sensors.

7.4 Summary

A hypothetical mechanism for the strong CAD dependency of autoignition of gasoline HCCI in the experimental engine has been proposed, based on experimental data gathered over a wide range of operating conditions. In the process, the effect on autoignition of the two different valve strategies have been evaluated. The proposed autoignition mechanism aims to explain why “pure” HCCI operation for this particular engine seems largely insensitive to operating conditions. To that end, a two effect process, combining a geometric and a chemical process has been put forward as a possible explanation.

Further investigation has revealed possible mechanisms leading to instability in the case of high TRG for one of the two valve strategies. A linking of successive cycles through TRG at varying temperatures is used to explain the oscillatory behaviour often seen leading to instability and, eventually, to misfires. Evidence of vigorous combustion in the TRG cycles is backed up by ion current measurements as well as investigation of P-V diagrams.

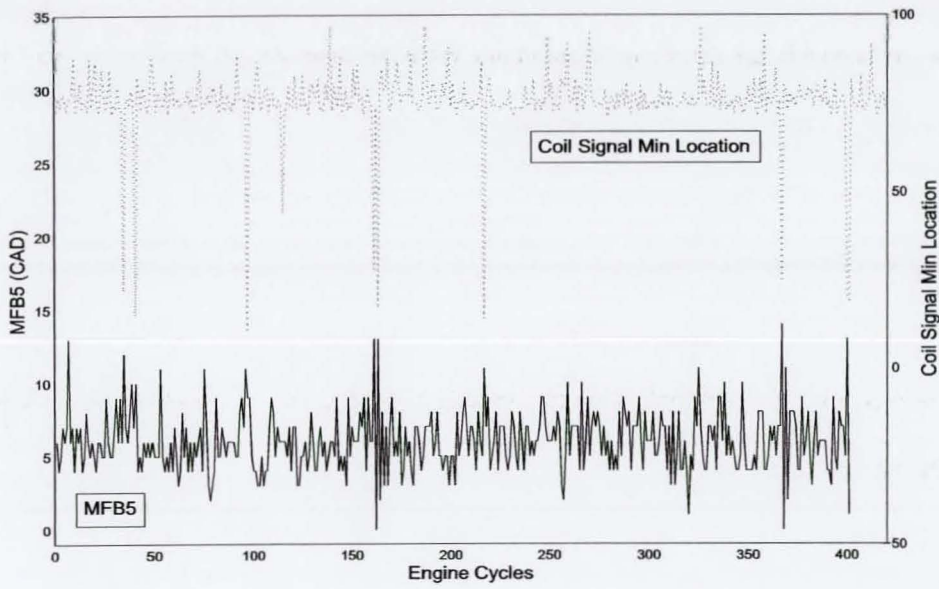


Figure 7.14: Location of minimum of coil signal and MFB5 for successive engine cycles

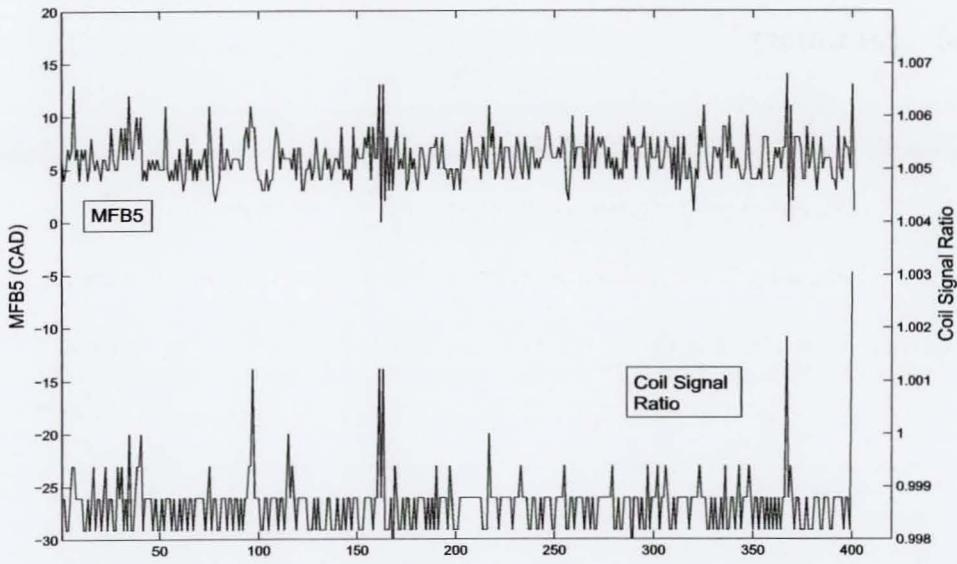


Figure 7.15: Coil signal ratio and MFB5 for successive engine cycles

In this type of engine, autoignition has been witnessed to be less responsive to AFR, TRG, and RPM than to effective compression ratio. In conclusion, it is plausible that an engine with the

geometry presented here could operate reliably in HCCI as long as the effective compression ratio is not reduced through throttling or unsuitable valve strategies.

Chapter 8

Conclusion

The goal of the work has been to investigate control options for gasoline HCCI combustion based upon experimental data. The main problem with HCCI control is that initiation of the combustion, though to some extent managed by the spark in SACAI, is by and large dictated by hard to manage (and establish on a fast basis) factors like TRG amount. The use of feedback signals from in-cylinder sensors has been investigated as a means of achieving control strategies.

8.1 In-cylinder Feedback Signals

While a host of sensors monitor the operation of contemporary engines, the important candidates for this research have been the pressure transducer and ion current sensor. The pressure transducer is a traditional tool for engine research, however its high cost makes it unattractive for production purposes. Furthermore, the signal produced needs to be post processed to some extent in order to extract information that is useable regarding the combustion, an issue that is worth bearing in mind when considering control applications.

On the other hand, ion current is less costly alternative which can provide more direct information on combustion. Also, features traditionally associated with the pressure signal, like PPP, can be extracted from the ion current trace. The accuracy of these can be improved by introducing

more complex techniques like ANN(s). Finally, ion current can provide information on abnormal cases of combustion, like the mixture igniting at EVO or during NVO, which would be undetectable or at least very hard to extract using the pressure trace alone.

Although the ion current signal is an invaluable tool for combustion detection, it cannot by itself offer a whole view of engine operation. This is achieved better when both signals are used together, completing or backing up each other. The area where use of the pressure sensor remains invaluable is in extracting the heat trace of a cycle. This process is particularly complicated in HCCI, due to cycle coupling through TRG, thus making TRG estimation an integral part of the process.

8.2 Control

The signals and extracted information described above serve very well as diagnostics and hence as simple tools of control. However, high accuracy controllers will need to predict to some extent the possible reaction of the system to changes in its operation. To account for this, a modeling approach has been attempted, based upon physical principles. The model has been found to respond as expected to simulated changes, although the uncertainty in the experimental data themselves makes absolute numerical verification impossible.

In order for totally reliable predictive control to be achieved, a fast and accurate algorithm must be incorporated in the engine model to estimate the onset of autoignition. Efforts to do so have been tried, based on Arrhenius styled formulations as well as purely mathematical approaches such as ANN(s). These however, seem incapable of explaining the autoignition behaviour exhibited by gasoline given the data at hand. Still, the experiments indicate that stable steady state SACAI and sometimes pure HCCI operation exhibit exceptionally constant behaviour. This good behaviour has been observed to be linked to cylinder pressure being kept high (throttleless operation with no delayed IVC).

Although the autoignition behaviour has not been explained, the onset of instability (which leads to misfires) can be detected to some extent by monitoring the ion current trace¹. This gives clues as to when abnormal behaviour takes place (e.g. combustion at NVO) which information can easily be incorporated into a controller.

8.3 Future Work

8.3.1 Experimental

Due to the great promise of ion current, there is a lot of experimental work that could be performed. The most interesting areas to be investigated are use of multiple collectors, possibly on the gasket and/or multiple sites on the cylinder head, and use of collectors designed to give a better signal in the case of the low magnitude ionisation sometimes exhibited during NVO.

8.3.2 Theoretical

The quest for a lightweight (so it can be implemented fast on an engine controller) autoignition criterion remains a very important goal. While detailed chemistry models might prove useful from an academic point of view, a fast algorithm is what is needed if total control of HCCI is desired.

ANN(s) both for ion current interpretation and for control are still an important area where big improvements can be made. While ADALINE(s) and GRNN(s) have been tried in this work, there is a large number of possible architectures which might prove advantageous. It is possible that an autoignition criterion might be arrived at through using a suitable ANN(s) as opposed to trying to model the extremely complicated and time consuming chemistry involved.

¹For a cheaper/backup alternative, the spark plug's low tension coil has also been shown to be of use when operating in pure HCCI mode.

Bibliography

- [1] Michael Guenther, Werner Sauter, Frank Schwarz, Amin Velji, and Ulrich Spicher. A study of the ignition and combustion process in a gasoline HCCI engine using port and direct fuel injection. Institute of Reciprocating Engines, University of Karlsruhe, Germany.
- [2] Shigeru Onishi, Souk Hong Jo, Katsuji Shoda, Pan Do Jo, and Satoshi Kato. Active thermo-atmosphere combustion (ATAC) – a new combustion process for internal combustion engines. *SAE*, 790501, 1979.
- [3] Yoichi Ishibashi and Masahiko Asai. Improving the exhaust emissions of two-stroke engines by applying the activated radical combustion. *SAE*, 960742, 1996.
- [4] M. Noguchi, Y. Tanaka, T. Tanaka, and Y. Takeuchi. A study on gasoline engine combustion by observation of intermediate reactive products during combustion. *SAE*, 790840, 1979.
- [5] Craig D. Marriott and Rolf D. Reitz. Experimental Investigation of Direct Injection-Gasoline for Premixed Compression Ignited Combustion Phasing Control. *SAE*, 2002-01-0418, 2002.
- [6] M. Alperstein, W. B. Swim, and P. H. Schweitzer. Fumigation kills smoke improves diesel performance. *SAE Transactions*, 66:574–588, 1958.
- [7] Paul M. Najt and David E. Foster. Compression-ignited homogeneous charge combustion. *SAE*, 830264, 1983.

- [8] R. H. Thring. Homogeneous-charge compression ignition (HCCI) engines. *SAE*, 892068, 1989.
- [9] R.M. Green, N.P. Gernansky, W.J. Pitz, and C.K. Westbrook. The role of low temperature chemistry in the autoignition of n-butane. *SAE*, 872109, 1987.
- [10] R.M. Green, N.P. Gernansky, W.J. Pitz, and C.K. Westbrook. Chemistry of oxidation preceding end-gas autoignition. *Combustion science and technology*, 50(1-3):3-25, 1986.
- [11] T.J. Held, A.J. Marchese, and F.L. Dryer. A semi-empirical reaction mechanism for n-heptane oxidation and pyrolysis. *Combustion science and technology*, 123(1-6):107-146, 1997.
- [12] H.J. Curran, P. Gaffuri, W.J. Pitz, and C.K. Westbrook. A comprehensive modeling study of n-heptane oxidation. *Combustion and Flame*, 114:149-177, 1998.
- [13] W.L. Easley, A. Agarwal, and G.A. Lavoie. Modeling of HCCI combustion and emissions using detailed chemistry. *SAE*, 2001-01-1029, 2001.
- [14] Johney Green Jr. Novel combustion regimes for higher efficiency and lower emissions. National Transportation Research Centre, Oak Ridge National Laboratory, 2002.
- [15] E. Murase, K. Hanada, T. Miyaura, J. Ikeda, and N. Konishi. Experimental studies of hcci combustion. Kyushu University, Nobby Tech. Ltd., Japan.
- [16] R. Reitz. The Use of CFV Technology for Internal Combustion Engine Applications. University of Wisconsin-Madison, 2004.
- [17] I. Glassman. *Combustion*. Academic Press, Inc., 1987.
- [18] L. Koopmans. HCCI for Gasoline Engines Retaining Residuals An Experimental Study. Licentiate Thesis, Chalmers University of Technology, Gothenburg, Sweden, 2002.

- [19] Magnus Christensen, Anders Hultqvist, and Bengt Johansson. Demonstrating the multi fuel capability of a homogeneous charge compression ignition engine with variable compression ratio. *SAE*, 1999-01-3679, 1999.
- [20] Magnus Christensen, Bengt Johansson, Per J. H. Amneus, and Fabian Mauss. Supercharged homogeneous charge compression ignition. *SAE*, 980787, 1998.
- [21] T. Urushihara, K. Hiraya, A. Kakuhou, and T. Itoh. Parametric Study of Gasoline HCCI with Various Compression Ratios, Intake Pressures and Temperatures. In *Proceedings of the IFP International Congress*, pages 77–84, 2001.
- [22] P. Wolters, W. Salber, and J. Dilthey. Radical Activates Combustion a New Approach for Gasoline Engines. In *Proceedings of the IFP International Congress*, pages 153–162, 2001.
- [23] Z. Chen, M. Konno, and S. Goto. Study on homogenous premixed charge CI engine fuelled with LPG. *JSAE Review*, 22:265–270, 2001.
- [24] R.H. Stanglmaier, T.W. Ryan, and J.S. Souder. HCCI Operation of a Dual-Fuel Natural gas Engine for Improved Fuel Efficiency and Ultra-Low NO_x Emissions at Low to Moderate Engine Loads. *SAE*, 2001-01-1897, 2001.
- [25] J.O. Olsson, P. Tunestal, G. Haraldsson, and B. Johansson. A Turbo Charged Dual Fuel HCCI Engine. *SAE*, 2001-01-1896, 2001.
- [26] J.O. Olsson, P. Tunestal, and B. Johansson. Closed-Loop Control of an HCCI Engine. *SAE*, 2001-01-1031, 2001.
- [27] Axel Zur Loye, Omowoleia Akinyemi, Russ P. Durrett, Patrick F. Flynn, Gary L. Hunter, Greg A. Moore, Jackie M. Mudd, George G. Muntean, Julie A. Wagner, and John F. Wright. Premixed Charge Compression Ignition Engine with Optimal Combustion Control. International Patent WO/1998/007973, World Intellectual Property Organization.

- [28] J.O. Olsson, P. Tunestal, B. Johansson, S. Fiveland, R. Agama, and D. Assanis. Compression Ratio Influence on Maximum Load of a Natural Gas Fuelled HCCI Engine. *SAE*, 2002-01-0111, 2002.
- [29] J. Zheng, D. Miller, and N. Cernasky. The Effect of Active Species in Internal EGR on Preignition Reactivity and on Reducing UHC and CO Emissions in Homogeneous Charge Engines. *SAE*, 2003-01-1831, 2003.
- [30] D. Law, D. Kemp, J. Allen, G. Kirkpatrick, and T. Copland. Controlled Combustion in an IC-Engine with a Fully Variable Valve Train. *SAE*, 2000-01-0251, 2000.
- [31] I. Denbratt. Method of controlling the process of combustion in an internal combustion engine with means for controlling the engine valves. Volvo Car Corporation, Patent application No. WO0028197, 1998.
- [32] G. Kontarakis, N. Collings, and T. Ma. Demonstration of HCCI Using a Single Cylinder Four-stroke SI Engine with Modified Valve Timing. *SAE*, 2000-01-2870, 2000.
- [33] L. Koopmans and I. Denbratt. A four stroke camless engine, operated in homogeneous charge compression ignition mode with commercial gasoline. *SAE*, 2001-01-3610, 2001.
- [34] J. Willand, R.G. Nieberding, G. Vent, and C. Enderle. The knocking syndrome: its cure and potential. *Automotive Engineering International*, pages 64–68, 1999.
- [35] N. Milovanovic, R. Chen, R. Dowden, and J. Turner. An investigation of using various diesel-type fuels in homogenous charge compression ignition engines and their effects on operational and controlling issues. *International Journal of Engine Research*, 5(4), 2004.
- [36] K. Schnauffer. Engine-cylinder flame-propagation studied by new methods. *SAE*, 340074, 1934.

- [37] S. Yoshiyama, E. Tomita, and Y. Hamamoto. Fundamental Study on Combustion Diagnostics Using a Spark Plug as Ion Probe. *SAE*, 2000.
- [38] J. Forster, A. Gunther, M. Ketterer, and K. Wald. Ion Current Sensing for Spark Ignition Engines. *SAE*, 1999-01-0204, 1999.
- [39] E. A. VanDyne, C. L. Burckmyer, and A. M. Wahl. Misfire Detection from Ionization Feedback Utilizing The Smartfire Plasma Ignition Technology. *SAE*, 2000-01-1377, 2000.
- [40] D. Lundsstrom and S. Schagerberg. Misfire Detection for Prechamber SI Engines Using Ion-Sensing and Rotational Speed Measurements. *SAE*, 2001-01-0993, 2001.
- [41] R. Raymond, S. Andre, and M. Fabian. Local Air-Fuel Ratio Measurements Using the Spark Plug as an Ionization Sensor. *SAE*, 970856, 1997.
- [42] U. Devesh and R. Giorgio. AFR Control on a single Cylinder Engine Using the Ionization Current. *SAE*, 980203, 1998.
- [43] Ming Chia Lai, K. Ratton, Eric N. Balles, Ed Vandyne, Alex Wahl, Bradley J. Darin, and Gary C. Hirschlieb. In-Cylinder Air-Fuel Ratio Approximation Using Spark Gap Ionization Sensing. *SAE*, 980166, 1998.
- [44] Thorsteinn S. Rognvaldsson, Ian J. Carpenter, Stan E. Golunski, C. Carlsson, M. Hellring, Jessica Reinkingh, M. Larsson, T. Munther, and N. Wickstrom. Robust AFR Estimation Using the Ion Current and Neural Networks. *SAE*, 1999-01-1161, 1999.
- [45] D. Schneider and M. D. Lai. Real-Time Air/Fuel Ratio Control in a Small SI Engine Using the Ionic Current Signal. *SAE*, (1999-01-3323), 1999.
- [46] H. Klovmark, P. Rask, and U. Forssell. Estimating the Air/Fuel Ratio from Gaussian Parametrizations of the Ionization Currents in Internal Combustion SI Engines. *SAE*, 2000-01-1245, 2000.

- [47] Y. Ohashi, W. Fukui, F. Tanabe, and A. Ueda. The Application of Ionic Current Detection System for the Combustion Limit Control. *SAE*, 980171, 1998.
- [48] T. Bie, M. Ericsson, and P. Rask. A Novel Start Algorithm for CNG Engines Using Ion Sense Technology. *SAE*, 2000-01-2800, 2000.
- [49] Lars E. Eriksson, Lars Nielsen, and Mikael Glavenius. Closed Loop Ignition Control by Ionization Current Interpretation. *SAE*, (970854), 1997.
- [50] M. Asano, T. Kuma, M. Kajitani, and M. Takeuchi. Development of New Ion Current Combustion Control System. *SAE*, 980162, 1998.
- [51] Morito Asano, Tetsuo Kuma, Atsushi Ito, Mitsunobu Kajitani, Manabu Takeuchi, Yoshiyuki Fukumura, and Mitsuhiro Izumi. Further Development of an Ion Current Combustion Control System. *SAE*, 2001-01-0266, 2001.
- [52] A. Franke, P. Einewall, B. Johansson, and R. Reinmann. Employing an Ionization Sensor for Combustion Diagnostics in a Lean Burn Natural Gas Engine. *SAE*, 2001-01-0992, 2001.
- [53] Thorsteinn S. Rognvaldsson, C. Carlsson, M. Hellring, M. Larsson, T. Munther, and N. Wickstrom. Spark Advance Control Using the Ion Current and Neural Soft Sensors. *SAE*, (1999-01-1162), 1999.
- [54] N. Wickstrom, M. Taveniku, A. Linde, M. Larsson, and B. Svensson. Estimating peak pressure position and air-fuel ratio using the ionization current and artificial neural networks. In *Proceedings of IEEE Conference on Intelligent Transportation Systems*, 1997.
- [55] A. Saitzkoff, R. Reinmann, and F. Mauss. In-Cylinder Pressure Measurements Using the Spark Plug as an Ionization Sensor. *SAE*, 970857, 1997.

- [56] C. Daniels. The comparison of mass fraction burned obtained from the cylinder pressure signal and spark plug ion signal. *SAE*, (980140), 1998.
- [57] M. Hellring and U. Holmberg. An ion-current based peak-finding algorithm for pressure peak position estimation. *SAE Technical Paper Series*, 2000-01-2829, 2000.
- [58] M. Hellring, T. Rgnvaldsson, N. Wickstrm, and M. Larsson. Ion current based Pressure Peak Detection Under Different Air Humidity Conditions. *Advanced Microsystems for Automotive Applications (AMAA)*, Technical Paper, 2000.
- [59] G. W. Malaczynski and M. E. Baker. Real-Time Digital Signal Processing of Ionization Current for Engine Diagnostic and Control. *SAE*, 2003-01-1119, 2003.
- [60] P. Amnus, D. Nilsson, F. Mauss, M. Christensen, and B. Johansson. Homogeneous Charge Compression Ignition Engine: Experiments and Detailed Kinetic Calculations. *4th International Symposium COMODIA 98*, 1998.
- [61] Nakano M., Mandokoro Y., Kubo S., and Yamazaki S. Effects of Exhaust Gas Recirculation in Homogeneous Charge Compression Ignition Engines. *Int. J. Engine Research*, 1(3), 2000.
- [62] Nicholas Cernansky, Jincai Zheng, Weiyang Yang, and David L. Miller. A Skeletal Chemical Kinetic Model for the HCCI Combustion Process. *SAE*, 2002-01-0423, 2002.
- [63] Song-Chang Kong, Craig Marriott, Rolf D. Reitz, and Magnus Christensen. Modeling and Experiments of HCCI Engine Combustion Using Detailed Chemical Kinetics with Multidimensional CFD. *SAE*, 2001-01-1026, 2001.
- [64] Song-Chang Kong, Rolf D. Reitz, Magnus Christensen, and Bengt Johansson. Modeling the Effects of Geometry Generated Turbulence on HCCI Engine Combustion. *SAE*, 2003-01-1088, 2003.

- [65] Gang Li, Tao Bo, Changyou Chen, and Richard J. R. Johns. CFD Simulation of HCCI Combustion in a 2-Stroke DI Gasoline Engine. *SAE*, 2003-01-1855, 2003.
- [66] S. Iida, J. Kusaka, and Y. Daisho. Numerical Study on Iso-Octane Homogeneous Charge Compression Ignition. *SAE*, 2003-01-1820, 2003.
- [67] J. Kusaka and Y. Daisho. Multi-Dimensional Modeling Combined with a Detailed Kinetics (Application for HCCI of Natural Gas). *5th Inter. Symp., COMODIA*, 2001.
- [68] S. B. Fiveland and D. N. Assanis. Development and validation of a quasi-dimensional model for HCCI engine performance and emissions studies under turbocharged conditions. *SAE*, 2002-01-1757, 2002.
- [69] S. Fiveland and D. Assanis. Development of a Two-Zone HCCI Combustion Model Accounting for Boundary Layer Effects. *SAE*, 2001-01-1028, 2001.
- [70] R. Ogink and V. Golovitchev. Gasoline HCCI Modeling: An Engine Cycle Simulation Code with a Multi-Zone Combustion Model. *SAE*, 2002-01-1745, 2002.
- [71] Salvador M. Aceves, Daniel L. Flowers, Charles K. Westbrook, J. Ray Smith, Robert W. Dibble, Magnus Christensen, William J. Pitz, and Bengt Johansson. A Multi-Zone Model for Prediction of HCCI Combustion and Emissions. *SAE*, 2000-01-0327, 2000.
- [72] A. Babajimopoulos, D. Assanis, and S. Fiveland. An Approach for Modeling the Effects of Gas Exchange Processes on HCCI Combustion and Its Application in Evaluating Variable Valve Timing Control Strategies. *SAE*, 2002-01-2829, 2002.
- [73] P. Maigaard, F. Mauss M., and Kraft. Homogeneous Charge Compression Ignition Engine: A Simulation Study on the Effects of Inhomogeneities. *Spring Technical Conference, ASME*, 34-2. No. 2000-ICE-275, 2000.

- [74] Markus Kraft, Peter Maigaard, Fabian Mauss, Magnus Christensen, and Bengt Johansson. Investigation of Combustion Emissions in a Homogeneous Charge Compression Injection Engine: Measurements and a New Computational Model. In *Proc. Of the Combustion Institute*, volume 28, pages 1195–1201, 2000.
- [75] Amit N. Bhave, Markus Kraft, Fabian Mauss, and Luca Montorsi. Modelling a Dual-Fuelled Multi-Cylinder HCCI Engine Using a PDF Based Engine Cycle Simulator. *SAE*, 2004-01-0561, 2004.
- [76] U. Kiencke and L. Nielsen. *Automotive Control Systems*. Springer-Verlag.
- [77] M. Hellring and U. Holmberg. A Comparison of Ion-current Based Algorithms for Peak Pressure Position Control. *SAE*, 2001-01-1920, 2001.
- [78] L. Nielsen and L. Ericsson. An ion-sense engine-fine-tuner. *Vehicular Systems, Department of Electrical Engineering, IEEE Control Systems Magazine*, 18(8), October 1998.
- [79] J. Auzins, H. Johansson, and J. Nytomt. Ion - gap sense in misfire detection, knock and engine control. *SAE*, 950004, 1995.
- [80] Ludovic Peron, Alain Charlet, Pascal Higelin, B. Moreau, and Jean-Francois Burq. Limitations of ionization current sensors and comparison with cylinder pressure sensors. *SAE*, 2000-01-2830, 2000.
- [81] S. Russ, G. Peet, and W. Stockhausen. Measurements of the effect of in-cylinder motion on flame development and cycle-to-cycle variations using an ionization probe head gasket. *SAE*, 970507, 1997.
- [82] SMETEC GmbH. email:info@smetec.de, Webpage:<http://www.smetec.de>.
- [83] A. L. Graps. An introduction to wavelets. *IEEE Computational Sciences and Engineering*, 2(2):50–61, 1995.

- [84] P. A. Tunestal. *The Use of Cylinder Pressure for Estimation of the In-Cylinder Air/Fuel Ratio of an Internal Combustion Engine*. PhD thesis, Lund University, 1993.
- [85] A. L. Randolph. Methods of processing cylinder pressure transducer signals to maximize data accuracy. *SAE*, 900170, 1990.
- [86] Lucien Koopmans, Ove Backlund, and Ingemar Denbratt. Cycle to cycle variations: Their influence on cycle resolved gas temperature and unburned hydrocarbons from a camless gasoline compression ignition engine. *SAE*, 2002-01-0110, 2002.
- [87] U.S. National Bureau of Standards. *JANAF Thermochemical Tables*, 1971.
- [88] J. B. Heywood. *Internal Combustion Engine Fundamentals*. McGraw-Hill Book Company, 1988.
- [89] Harjit S. Rai, Michael F. J. Brunt, and Colin P. Loader. Quantification and Reduction of IMEP Errors Resulting from Pressure Transducer Thermal Shock in an S.I. Engine. *SAE*, 1999-01-1329, 1999.
- [90] G. M. Rassweiler and L. Withrow. Motion pictures of engine flames correlated with pressure cards. *SAE Transactions*, 42(5):185-204, 1938.
- [91] Richard Stone. *Introduction to Internal Combustion Engines*. Macmillan, 1999.
- [92] G. H. Abd Alla. Computer simulation of a four-stroke spark ignition engine. *SAE*, 2001-01-0578, 2001.
- [93] W. D. Annand. Heat transfer in the cylinder of reciprocating internal combustion engines. In *Proc. I MechE*, volume 177, 1963.

- [94] G. Woschni. Universally applicable equation for the instantaneous heat transfer coefficient in the internal combustion engine. *SAE Transactions*, 76(SAE Technical paper 670931), 1967.
- [95] Gregory M. Shaver, Matthew Roelle, and J. Christian Gerdes. Modeling Cycle-to-Cycle Coupling in HCCI Engines Utilizing Variable Valve Actuation. In *Proceedings of the 1st IFAC Symposium on Advances in Automotive Control*, pages 244–249, Salerno, Italy, 2004.
- [96] D. J. Rausen, A. G. Stefanopoulou, J-M. Kang, J. A. Eng, and T-W. Kuo. A mean-value model for control of homogeneous charge compression ignition (HCCI) engines. In *IEEE Proceedings of 2004 American Control Conference*, 2004.
- [97] Gregory M. Shaver, J. Christian Gerdes, Parag Jain, P.A. Caton, and C.F. Edwards. Modeling for Control of HCCI Engines. In *Proceedings of the American Control Conference*, pages 749–754, Denver, Colorado, 2003.
- [98] Roy Ogink. *Computer Modeling of HCCI Combustion*. PhD thesis, Chalmers University of Technology, 2004. ISBN: 91-7291-458-0.
- [99] S. R. Turns. *An introduction to combustion*. McGraw-Hill, 1996.
- [100] J. Bengtsson, M. Gäfvert, and Petter Strandh. Modeling of HCCI Engine Combustion for Control Analysis. *Conference in Decision and Control (CDC 2004)*, 2004.

List of Tables

4.1	Specification for engine used on SI ion current research	36
4.2	ADALINE performance for each speed site, only ion current measurant inputs . .	76
4.3	GRNN performance for each speed site, only ion current measurant inputs	76
4.4	Performance of conventional linear fit method for two different ion current measurants	77
4.5	ANN performance for each speed site, decomposed ion current signal as input . .	78

List of Figures

1.1	Comparison of SI (top) and HCCI (bottom) combustion duration, 1500rpm, 2.5 bar IMEP	5
1.2	Comparison of NO_x emissions for different engines) combustion duration, 1500rpm, 2.5 bar IMEP	6
1.3	Schlieren photography of SI (top three rows) and HCCI (bottom three rows), and close ups. Taken from [2].	8
2.1	Rotating Ark Spark Plug (RASP) (top [14]) and Pulsed Flame Jet (PFJ) initiated HCCI combustion(bottom [15])	16
3.1	Research Engine with AVT system	25
3.2	Details of the AVT design	26
3.3	Valve lift traces in the constant EVO/IVC strategy	27
3.4	Valve lift traces in the constant duration strategy	28
3.5	Cylinder head, showing the location of ionization probe	30
3.6	Voltage source circuit diagram	31
4.1	Typical ion-current signal (and pressure signal) recorded by a central plug [57]	33
4.2	Cylinder head fitted with 1 spark plug and two remote ion sensors	37
4.3	Circuit Diagram of DC Source	37

4.4	Pressure and ion current traces from single and twin sensor configurations	39
4.5	Typical pressure and ion current signals	40
4.6	Typical pressure curve and associated measurants	41
4.7	Single sensor trace	42
4.8	Typical Ion Current Signal and associated measurants	43
4.9	Relationship between 1st ion current peak position and peak cylinder pressure position	45
4.10	Relationship between 2nd ion current peak position and peak cylinder pressure position	46
4.11	Relationship between 2nd ion current peak position and peak cylinder pressure .	47
4.12	Schematic representation of an artificial neuron	48
4.13	Sample transfer functions	49
4.14	Sample transfer functions	50
4.15	Schematic representation of the measurant predicting network	52
4.16	Predictions for Peak Pressure Position	53
4.17	Predictions for Peak Pressure Magnitude	54
4.18	Predictions for Pressure Curve Area	55
4.19	Predictions for Pressure Curve Width	56
4.20	Averaged actual and predicted pressure curves	57
4.21	Predictions for Peak Pressure Position	58
4.22	Typical HCCI ion current signal	63
4.23	The ion current measurants	64
4.24	Example of sudden spike rise	65
4.25	Detail of noisy region before spike	66
4.26	Example of base drift	67

4.27 Ion current signal showing base and trigger level	68
4.28 Original ion current signal and DWT generated details	70
4.29 Example of two levels of wavelet decomposition of ion current signal	72
4.30 Comparative results of different measurant based ANN(s)	80
4.31 Breakdown of ADALINE design parameters	82
4.32 Breakdown of GRNN design parameters	82
4.33 Comparative results of different decomposed ion current based ANNs	84
4.34 Comparative results of different decomposed ion current based ANNs with the same outliers removed as in the case of measurant based ANNs	84
5.1 Gamma for the two possible extremes of mixture composition for a typical tem- perature trace of a compression stroke. 2000 RPM, 54%volumetric TRG, 2.9 bar IMEP	94
5.2 Gamma for a compression stroke where the temperature traces vary corresponding to varying the estimated TRG. 2000 RPM, 54%volumetric TRG, 2.9 bar IMEP . . .	95
5.3 Pressure pegging at varying polytropic of expansion	97
5.4 Estimated BDC pressure of averaged traces	98
5.5 Comparison of IVC and EVC as starting points	99
5.6 Percentage difference between TRG calculated by taking an averaged measure- ment and correcting by a temperature shift of 40°. 2000 RPM, WOT, TRG sweep.	101
5.7 Temperature discrepancy between IVO and IVC	103
5.8 Suspicious IMEP, BMEP, FMEP trend	104
5.9 Thermal shock evidence following TRG combustion	106
5.10 TRG, Mixture Temperature and Pressure Shift calculation process	109
5.11 TRG amount dependence upon assumed bulk TRG temperature at EVC. 2000 RPM, WOT, 2.9 bar IMEP	111

5.12	Pressure at IVC dependence upon assumed bulk TRG temperature at EVC. 2000 RPM, WOT, 2.92 bar IMEP	112
5.13	Typical Pressure and Heat Exchange Flow traces	114
5.14	Breakdown of Heat Exchange Flow trace	115
5.15	Heat Exchange Flow curve and its integral	116
5.16	Heat Exchange Flow traces resulting from increasing TRG temperature at EVC by $200^{\circ}K$	118
5.17	Comparison between TRG measuring methods	120
5.18	Treatment of individual cycles for cycle to cycle calculations	122
5.19	Comparison between $\frac{dQ}{d\theta}$ traces for minimum (top) and maximum (bottom) TRG	127
5.20	Cycle to cycle analysis of unstable combustion	129
6.1	Effect of varying α (top) and n (bottom) on the shape of a Wiebe sigmoid	139
6.2	The Wiebe sigmoid and its $\frac{d}{d\theta}$ derivative	141
6.3	Comparison of typical combustion profiles for different combustion types	146
6.4	Combustion selection algorithm	150
6.5	Overview of “derivatives” function	152
6.6	Species’ transformations taking place during combustion	155
6.7	Pressure traces measured and modeled with no wall heat transfer	157
6.8	Heat exchange traces measured and modeled with no wall heat transfer	158
6.9	An example of empirically determined TRG dependent U parameter	159
6.10	Example of SI combustion delays	161
6.11	Combustion durations for stoichiometric SI fires around the HCCI envelope	162
6.12	Example of large scale study of surface of SoC temperature	163
6.13	Actual pressure traces and simulated pressure and species output for typical SI and HCCI combustion	164

6.14	Speed dependent polytropic of expansion measured at the low pressure descending part of the experimental pressure trace	167
6.15	Example of coupled consecutive cycles	170
6.16	Example of simulated instability (artificially disturbed 2 nd cycle) with an otherwise fixed combustion phasing	171
6.17	Example of simulated instability with a temperature triggered combustion phasing	174
7.1	Exchanged Heat traces for a normal and a misfiring cycle	179
7.2	Exchanged Heat traces for the TRG compression-expansion region over a TRG sweep	180
7.3	Heat profiles of HCCI and SI misfires and TRG compression-expansion	182
7.4	Evidence of crossovers in log(P)-log(V) at high TRG levels	186
7.5	Example pressure traces of: TOP: Very stable combustion at high TRG (76% by volume), fixed IVC/EVO valve strategy, 2000rpm, 1.73 bar IMEP. BOTTOM: Extreme unstable combustion at 50% TRG by volume, fixed duration valve strategy, 2000rpm, 1.47 bar IMEP	188
7.6	Example pressure trace of repeated instability at 38% TRG by volume, fixed duration valve strategy, 2400rpm, 3.5 bar IMEP (when not stalled)	190
7.7	Zoom of the events around the reintroduction of spark	191
7.8	MFB5 traces near the 3 unstable regions	192
7.9	MFB5 traces near the 3 unstable regions with marked ion current activity at NVO	194
7.10	Example of TRG combustion	195
7.11	Relationship between MFB5 and Peak Ion Current Position	197
7.12	Typical trace taken from the low tension coil, shown alongside the corresponding pressure trace	198

7.13	Close up of pressure and coil traces for three cycles including one late combustion	198
7.14	Location of minimum of coil signal and MFB5 for successive engine cycles . . .	200
7.15	Coil signal ratio and MFB5 for successive engine cycles	200
A.1	Specifications of the Horiba Mexa 7100 gas analyzer. Source: Horiba Corporation at URL http://www.emd.horiba.com/engmeas/mexa7000/#SPECIFICATIONS . .	223
A.2	Data sheet for the Kistler 6123 piezoelectric pressure transducer. Source: Kistler Instrument Corporation at URL http://www.kistler.co.kr/Ver1/File/000-024/\$File/DB03.6123m-07.97.pdf	224
A.3	Specifications of the Froude Hofmann AG30 eddy current dynamometer. Source: Froude Hofmann at URL http://www.froudehofmann.com/product_family_2.htm .	224

Appendix A

Hardware Specifications

Standard MEXA-7000 Specifications		
MEXA Model	7100, 7100H, 7100D 7200, 7200H, 7200D,	7400, 7400H, 7400D 7500, 7500H, 7500D
Sample Gas	Direct: 7100 Dilute: 7200	Direct and dilute: 7400 Two lines direct: 7500
Sample Flow Rate	Approx. 9 L/min for cold systems Approx. 11 L/min for heated systems Approx. 2 L/min for Tracer Approx. 4 L/min for EGR	
Sample Inlet Pressure	0 to 30 kPa for normal lines, -66.7 to 0 kPa for EGR line	
Sample Delay Time	Main sample: Td = 2.5 s with 5-m (16-ft) hose (3.0 s for MPA and CLA(NO _x)) CO ₂ EGR: Td = 3.0 s with 5-m (16-ft) hose	
Purging	External shop air	
Ambient Conditions	5-40°C, less than 80% as relative humidity	
Dimensions and Weight	Height and weight depend on configuration. Standard sizes include the following. Others available upon request. W x D x H 570 x 850 x 1190 / 1500 / 1562 / 1785 / 1970 mm 22.4 x 33.5 x 46.9 / 59.1 / 61.5 / 70.3 / 77.6 in Max. 350 kg / 772 lb	
Power	100/120/200/220/230/240 V AC (± 10% Max.250V), 50/60 Hz (± 1 Hz), single phase (to be specified) 1.5 kVA to 9.0 kVA (depending on configuration)	

Figure A.1: Specifications of the Horiba Mexa 7100 gas analyzer. Source: Horiba Corporation at URL.

<http://www.emd.horiba.com/engmeas/mexa7000/#SPECIFICATIONS>

Technische Daten	Données techniques	Technical Data*		
Bereich	Gamme	Range	bar	0 ... 250
Kalibrierter Teilbereich	Gamme partielle étalonnée	Calibrated partial range	bar	0 ... 50
Überlast	Surcharge	Overload	bar	300
Empfindlichkeit	Sensibilité	Sensitivity	pC/bar	=-16
Eigenfrequenz	Fréquence propre	Natural frequency	KHz	=100
Linearität, alle Bereiche	Linéarité, toutes les gammes	Linearity, all ranges	%FSO	±0,5
Beschleunigungsempfindlichkeit	Sensibilité aux accélérations	Acceleration sensitivity	bar/g	<0,0015
Betriebstemperaturbereich	Température d'utilisation	Operating temperature range	°C	-50 ... 350
Empfindlichkeitsänderung 200± 150°C	Décalage de la sensibilité 200± 150°C	Sensitivity shift 200± 150°C	%	<±3
200± 50°C	200± 50°C	200± 50°C	%	=±1
Thermoschock	Choc thermique	Thermal shock		
Abweichung von der Referenz 7061B bei 1500 r/min, p _{ref} = 9 bar	Différence par rapport à la référence 7061B à 1500 r/min, p _{ref} = 9 bar	Difference from reference 7061B at 1500 r/min, IMEP = 9 bar		
Δp (kurzzeitdrift)	Δp (dérive due au court temps)	Δp (short-time drift)	bar	<-1,5
Δp _{mi} bis zu	Δp _{mi} jusqu'à	ΔIMEP up to	%	<-10
Δp _{max} bis zu	Δp _{max} jusqu'à	Δp _{max} up to	%	<-3
Isolationswiderstand bei 20°C	Résistance d'isolement à 20°C	Insulation resistance at 20°C	TΩ	≥10
Anzugsmoment	Couple de serrage	Tightening sensitivity	Nm	10
Kapazität	Capacité	Capacitance	pF	8
Gewicht	Poids	Weight	g	10
Stecker, Keramik-Isolator	Connecteur, isolateur céramique	Connector, ceramic insulator	Type	10-32 UNF

1 bar = 10⁵ Pa = 10⁵ N · m⁻² = 1,0197... at = 14,503... psi; 1 psi = 0,06894... bar; 1 g = 9,80665 m · s⁻²; 1 Nm = 0,73756... lbf·ft; 1 g = 0,03527... oz
 * In all Kistler documents, the decimal sign is a comma on the line (ISO 31-0:1992).
 Kistler Instrumente AG Winterthur, CH-8408 Winterthur, Switzerland, Tel. (052) 224 11 11. Kistler Instrument Corp., Amherst, NY 14226-2171, USA, Phone (716) 691-5100

Figure A.2: Data sheet for the Kistler 6123 piezoelectric pressure transducer. Source: Kistler Instrument Corporation at URL [http://www.kistler.co.kr/Ver1/File/000-024/\\$File/DB03.6123m-07.97.pdf](http://www.kistler.co.kr/Ver1/File/000-024/$File/DB03.6123m-07.97.pdf)

Product	Power kW (BHP)	Torque Nm (lb.ft)	Max Speed RPM	Curve Ref
AG30	30 (40)	95 (70)	12,000	003606

Figure A.3: Specifications of the Froude Hofmann AG30 eddy current dynamometer. Source: Froude Hofmann at URL http://www.froudehofmann.com/product_family_2.htm

Appendix B

Publications

Analysis of SI Combustion Diagnostics Methods Using Ion-Current Sensing Techniques

Dimitris Panousakis, Andreas Gazis, Jill Patterson and Rui Chen
Loughborough University

Copyright © 2006 SAE International

ABSTRACT

Closed-loop electronic control is a proven and efficient way to optimize spark ignition engine performance and to control pollutant emissions. In-cylinder pressure sensors provide accurate information on the quality of combustion. The conductivity of combustion flames can alternatively be used as a measure of combustion quality through ion-current measurements. In this paper, combustion diagnostics through ion-current sensing are studied. A single cylinder research engine was used to investigate the effects of misfire, ignition timing, air to fuel ratio, compression ratio, speed and load on the ion-current signal. The ion-current signal was obtained via one, or both, of two additional, remote in-cylinder ion sensors (rather than by via the firing spark plug, as is usually the case). The ion-current signals obtained from a single remote sensor, and then the two remote sensors are compared.

Ion-current signal interpretation was then conducted using an artificial neural network strategy (using adaptive linear networks) to interpret the measured signals, and also to predict the associated cylinder pressures. The combination of remote sensors with a linear neural network gives a more accurate and 'noise' free signal that can be processed at greater speed through computationally inexpensive methods.

The computed results agree well with measured cylinder pressures under all analyzed conditions. It will be shown that ion-current signals can be used to directly diagnose combustion abnormalities (and as such could suitable as part of a closed loop control strategy), even though the effects of ignition timing, air to fuel ratio, and compression ratio on ion-current were more complex.

INTRODUCTION

Electronic control with closed-loop feedback is a proven and efficient way to optimize the spark ignition (SI) engine performance and to control pollutant emissions [1]. In-cylinder pressure sensors provide accurate information on the quality of combustion, but alternatively, so called 'ion-

current' signals can be used to monitor in-cylinder combustion performance. The prevailing conditions inside the engine during combustion causes ionization of the gases in the cylinder. By applying a voltage (of the order of a hundred volts), a current will be produced since the ionized gasses are conductive.

The most obvious way to apply a voltage inside the cylinder is to use two existing electrodes; the spark plug tips [2], and a typical trace of data acquired by this method is shown in Figure 1, where the signal has been averaged over a number of engine cycles that were acquired with the firing plug. It is unlikely that such a well behaved trace would be encountered without averaging over several cycles with this method.

It can be seen in Figure 1 that the ion-current signal can be generally divided into three phases: the first phase consists of two sharp spikes located at 30 and 15 degree of crank angle (degCA) before top dead centre (BTDC). These are due to ignition and the measuring circuit rigging where the ion-current is measured most commonly from the low voltage side of the coil, and the emf interference causes some spikes to appear in the ion-current signal. This problem also occurs even when the less common practice of measuring from the high voltage side of the coil is employed.

After the first two spikes, the second phase of the ion-current signal appears as a first hump at around 10 degCA BTDC. This is a result of the flame kernel development around the tips of the spark plug. The level of the ion-current within this region is generally high due to intense chemical reactivity in the vicinity of the tips.

After the establishment of the combustion kernel, flame propagation towards the rest of the mixture starts. The intensified heat energy release from the burning "flame ball" growing in the cylinder warms the burned gasses inside it and further increases their temperature. As a result, the internal energy of the burned gasses increases and the ion formation rate becomes strong in comparison to the ion recombination rate [2]. Overall, after a short period of decline due to the flame front moving away from the sensor, the ion signal starts to rise again due to energy

addition from the surrounding burning mixture. This gives the second hump in the signal, and the third phase of the ion-current signal. As the piston moves away further from TDC, the volume of the combustion chamber increases and in-cylinder pressure and temperature of the burned gasses decline. The ion recombination rate increases, and the measured ion-current signal starts to decline. This third phase of the ion-current signal is a post-flame or thermal ionization induced signal [5,6,7,8,9,10], and it is proportional to the cylinder pressure produced by combustion.

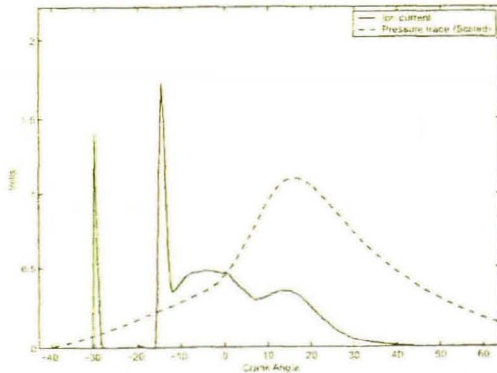


Figure 1 Typical ion-current signal (and pressure signal) recorded by a central plug [2]

There are some problems associated with using the spark plug as the ion-current sensor. Firstly, because the spark generating voltage is substantially higher than the typical voltages used in an ion-current measuring circuit, the latter has to be protected somehow, and no meaningful information can be gathered until the ignition circuit has dumped down thus the initial phase of combustion cannot be recorded. The best signal therefore derived from the thermal phase of the signal, but this second hump is not always very well pronounced thus making it a less than perfect feedback signal for engine diagnostic and control purposes. Moreover, cylinder pressures decrease as the engine load reduces, further reducing the signal strength of this second hump. Consequently, the diagnosable region of the engine loads are limited to a minimum of 75% of full load.

In this research, two ion-current sensors were used in addition to a single spark plug in order to avoid the weak signal experienced by using a combined spark plug and ion signal sensor. Here, the spark plug was used only as a combustion initiator, and the ion-current sensors were located on the opposite side of the combustion chamber. This configuration allows for the measurement of flame propagation speeds, since the timing of flame arrival at the sensors is possible.

EXPERIMENTAL INVESTIGATION

A single cylinder 4-stroke research engine was used, and full details are presented in Table 1. The engine featured variable compression ratio, variable ignition timing, variable air to fuel ratio and four access points in the cylinder head.

Bore	80 mm
Stroke	100 mm
Inlet Valve Opening	12degCA BTDC
Inlet Valve Closing	64degCA ABDC
Exhaust Valve Opening	64degCA BBDC
Exhaust Valve Closing	12degCA ATDC
Compression Ratio	4.5:1 - 13:1
Ignition Timing	55degCA BTDC - 20degCA ATDC

Table 1. Engine Specification



Figure 2 Cylinder head fitted with 1 spark plug and two remote ion sensors

Figure 2 shows the arrangement of the cylinder head and the spark plug locations. The firing plug, which is located next to the inlet valve was used as the ignition source while one, or both, of the two remote sensing plugs were used as the ion-current sensing units. One was fitted on the other side of the inlet valve opposite to the firing plug (sensing plug (1) in the diagram) whilst the other, (sensing plug (2)), was fitted next to the engine exhaust valve. The distance between sensing plug (1) and the firing plug was 42mm, and the distance between the sensing plug (2) and the firing plug was 55mm.

Since the mass of positive ions, such as H_3O^+ , is approximately 30,000 times larger than that of an electron (negative), the light electrons can be accelerated much more easily towards the positive electrode than the heavy ions when driven by an applied electromagnetic field [1]. The voltage polarity at the gap of sensing spark plugs was therefore selected so that the small area electrode, the centre electrode, was positive, and the large area electrode and the rest of the combustion chamber were negative. This coincides conveniently with the spark plug's

original polarity as it is used in most engines where the engine block is negative.

A purpose built DC voltage source, (shown in figure 3), was used to power the measuring plugs. The output of the voltage divider was passed to a data acquisition (DAQ) board as the ion-current signal. The voltage divider would produce a voltage that was inversely proportional to the sensed ion-current (i.e. 5V for zero ion-current and 0V for infinite) to avoid the possibility of damage caused due to excessive voltage. The signal was inverted during the post processing phase. The DAQ sampling rate was one sample per 2 degCA. Data were acquired using either a single sensing plug (1) or both. When using both sensing plugs, these were connected in parallel, as shown in Figure 3, which essentially results in the addition of the two ion-current signals.

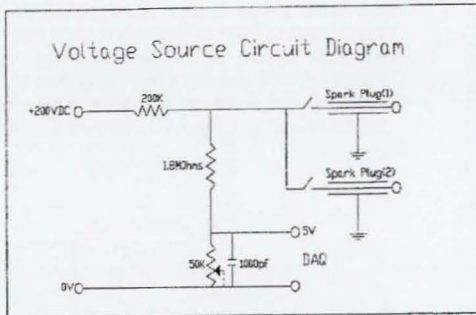


Figure 3 Circuit Diagram of DC Source

All experiments were conducted first using the single remote ion-current sensor, and then repeated with both remote sensors to assess the extent by which additional sensors improve the quality of ion-current data.

When the flame front passes the sensing plug, the gas around the plug is burned. The balance between the ionization and recombination of the burned gas constituents is then a function of temperature and pressure. This leads to a post-flame hump similar to that recorded when the firing plug is also used for measurement.

EXPERIMENTAL RESULTS WITH REMOTE ION SENSING PLUG(S)

The ion-current signal was initially measured using a single remote sensor, namely sensing plug (1). Figure 4 shows a typical measured cylinder pressure and a correlated ion-current, taken from a selected single cycle, rather than from an average of cycles, so that the phase transitions are clearly shown. By comparing Figure 4 with the results obtained from the firing spark plug shown in Figure 1, it can be seen that there is a significant difference between the

two ion-current signals. One sharp spike instead of two is recorded during the first phase when a remote sensor is used, because there is no interference from the ignition circuit. The remote sensing plug detects the flame front as ion-current, caused by ionization within the gap of its electrodes, yielding this single sharp spike. Additionally, as the flame needs a certain time to propagate through the distance between the two plugs, the use of a separate sensor allows for this time to be measured as the delay between spark timing and the ion-current spike.

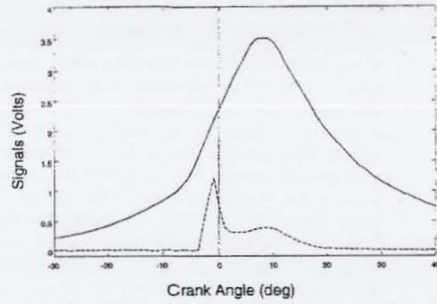


Figure 4 Single Plug Ion-current and Pressure Signals

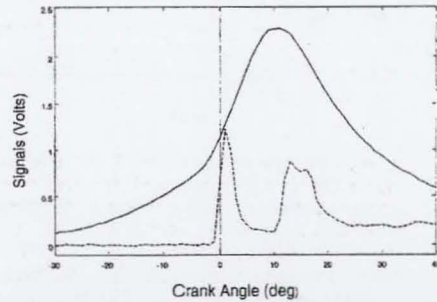


Figure 5 Twin Plug Ion-current and Pressure Signals

The output from the twin remote sensors is combined, to give one signal, and it can be seen in Figure 5 that this results in additional information in the form of an additional spike between the original spike and hump. This is the result of the chemi-ionization ion-current signal produced as the flame front hits the second sensor's electrodes. The post flame hump here is the result of the pressure rise after the flame has passed both sensors and thus contains less information.

Comparison of figures 4 and 5 show that whilst most of the combustion information can be obtained from the spikes, the use of two sensors gives a greater insight into the combustion process, and provides a wider diagnostic window because the signal strength of second hump is increased. The drawback is that the use of the two additional sensors does not leave a time window for the

post-flame information to be collected. The use of a single additional sensor provides a great improvement over using the spark plug as the only sensor where the weaker signals and lower slopes lead to unstable and inconsistent data, however the use of an ion-current sensor separate to the spark plug can potentially represent a significant increase in cost and complexity, and additionally difficulty to manufacturers.

The results also show that the location of the additional sensor is important. Assuming that a flame ball is generated by ignition, if the ion-current sensor is located symmetrically with the spark plug, the same result will be recorded. Alternatively, ion-current sensors can be embedded in the cylinder head gasket, to overcome sealing and manufacturing problems, and represent the lowest cost approach to installation of ion current sensors. However, in terms of location, the use of remote ion-current sensors also represent an improvement cylinder head gasket sensors [26], because they cannot be used to analyze the first ion-current spike and provide no post flame data. Thus, in order to achieve the widest possible diagnostic window, it is better to locate a sensor between the ignition site and the flame out site. These effects are described further in the following section.

RESULTS AND ANALYSIS

MISFIRE

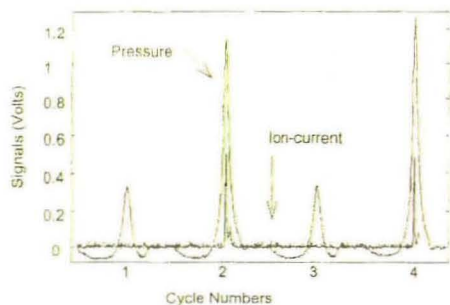


Figure 6 The misfire effect on ion-current recorded by a single remote sensing plug

Misfire detection is a major subject of on board diagnostics (OBD). Conventional crankshaft speed fluctuation sensing does not guarantee misfire detection at high engine speeds and low load conditions. This method is particularly poor for multi-cylinder engines where the effect of misfire of a single cylinder on crank shaft speed is masked by the frequent and successful combustion events of the other cylinders. The potential of ion-current sensing for misfire detection has already been reported [11,12,13,14], and this study confirms that when misfire occurs the ion-current signal and its integral are zero, while under any other combustion condition they are non-zero.

This is demonstrated in Figure 6 where cycles 1 and 3 are misfired. Although, the signal shown here was obtained using one remote sensing plug, identical behavior was evident with two remote sensing plugs.

IGNITION TIMING

The effect of the ignition-timing on both pressure and ion-current can be seen in Figure 7. Advanced timing results in higher in-cylinder pressures and earlier first spikes of the ion-current signals since the flame propagates earlier. The flame starts earlier but also travels faster due to the increased pressure buildup. Again the number of sensors used is not critical in this application, since most information is given by the location of the starting point of the signal. The only advantage of recording of the location of two spikes from both sensors is increased signal strength. It is worth noting that the results in figure 7 are taken from a single cycle as opposed to an average of cycles, and the position of peak ion-current signal, and indeed peak cylinder pressure are not solely functions of ignition timing, but also of ignition delay. As such the spacing between pressure and ion-current peaks are not necessarily the same as the spark advance, but if this correlation is sought it can be improved by using averaged data.

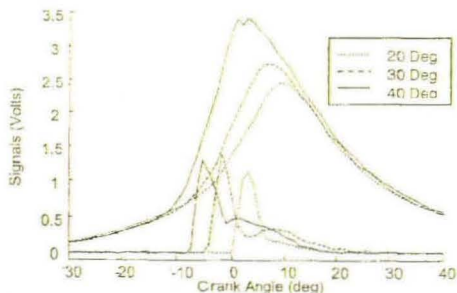


Figure 7 Ignition Timing Advance Effect on ion-current at 1500 rpm, 50% throttle, 50% load and $\lambda=0.9$ from single cycles

AIR TO FUEL RATIO

In the plots shown in Figures 8 and 9, a comparison between the pressure and the ion-current signal under different AFR values is shown using data that was averaged over ten cycles using a single sensing plug. It can be seen that there is a very good correlation between pressure and ion-current at each air-fuel ratio, and the ion-current signal remained measurable at all AFR conditions.

In Figure 8, the AFR was swept from a value of $\lambda=0.65$ to 1 at half load while the engine speed was held constant at 1600 rpm and the ITA was 30 deg. In Figure 9, the AFR was swept from $\lambda=1$ to 1.26 under the same engine conditions.

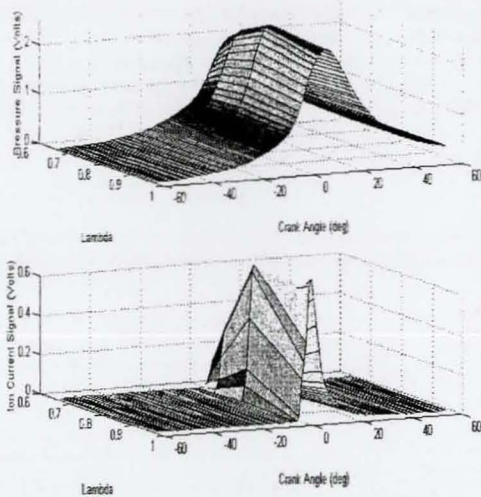


Figure 8 AFR swept from rich to stoichiometric at half load and 1600 rpm

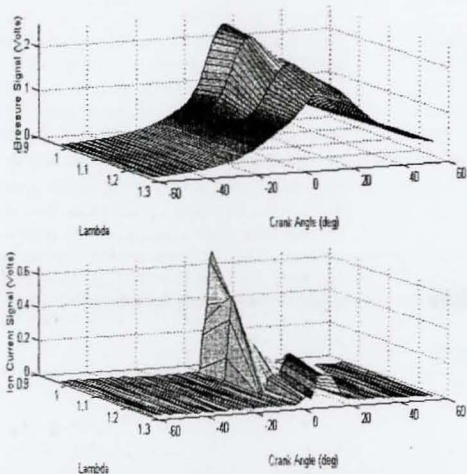


Figure 9 AFR swept from stoichiometric to lean at half load and 1600 rpm

The location of start of ion-current signal and peak ion-current position are interdependent with the pressure signal slope and location of peak pressure, and all of these parameters are a function of flame propagation speed. Where mixtures burn fast (at AFR's that are slightly lean of

stoichiometric), the positions of the start and peak ion-current occur earlier, but very lean (and hence slow burning) mixtures have the greatest delays.

The magnitudes of the ion-current signals also correlate with the magnitudes of pressure signals. The mildly rich mixtures produce the highest values for ion-current and pressure signals. The signal strength decreases at both richer and leaner AFR's. For very lean mixtures, as with any low in-cylinder pressure condition, the post-flame phase disappears. What looks like a second hump on the signal from the leanest mixtures is in fact very late combustion.

Previous research has identified that the behavior of the first slope of the ion-current signal is an indicator of mixture strength [14], and this is confirmed by the results in Figure 10 where the AFR is plotted against the first ion-current slope. Each of the seven slope values is an average over sixty cycles under the same AFR conditions. The trend is for the ion-current signal to peak near to a stoichiometric AFR and decrease for richer or leaner mixtures. Further research is required to establish whether the ion-current sensor could replace an oxygen sensor, but it is clear that the ion-current signal can provide feedback for individual cylinder fuel trims in order to equalize cylinder air/fuel imbalances. The impact that such a strategy will have on the efficiency and emissions of production vehicles is considerable.

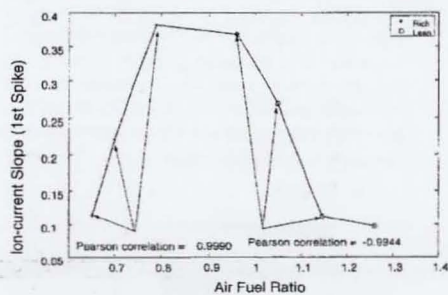


Figure 10 Relationship between the slope of the first ion-current spike and Air-Fuel Ratio

COMPRESSION RATIO

Two sensors were used to acquire the data shown in Figure 11. The engine was run at half load and 1650 rpm, with the ITA at 30 deg BTDC and an air fuel ratio of $\lambda=0.95$. Figure 11 shows plots of the in-cylinder pressure and ion-current signal for different compression ratios. As the compression ratio drops reducing the flame propagation speed, the start of the ion-current signal is delayed, and the peak pressure is also reduced and retarded.

It is important to note that the engine was rebuilt between each test in order to vary the compression ratio. The reduced compression ratio would have affected the engine's thermodynamic efficiency, but this was not compensated for in the experiments.

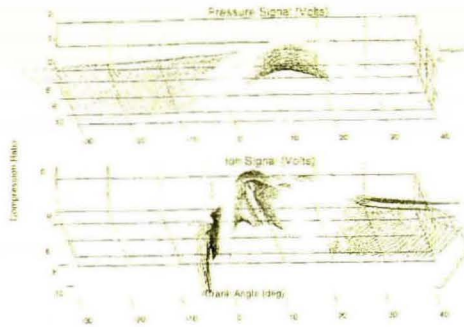


Figure 11 – Compression Ratio Effect

LOAD / SPEED

For the load/speed data collection the load was swept from 0% to 100% and the speed from 1000 to 3000 rpm. The air to fuel ratio was held at 0.9 lambda, and figure 12 shows the results recorded by using both ion-current sensors. Figure 12 shows that as the load increases the pressure increases and the peak cylinder pressure occurs earlier. The ion-current signal also increases and the maximum point appears earlier, but only up to about 75% load. After this point the ion-current signal continues to occur earlier but starts to fall in magnitude.

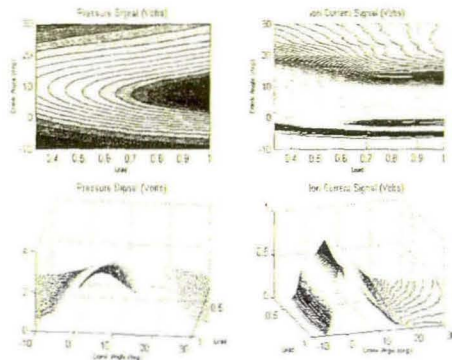


Figure 12 Load contour graphs

This effect was also observed with a single ion-current sensor, and no easy explanation for this phenomenon is available since the ion formation process is not yet fully understood.

TRANSIENT OPERATION PERFORMANCE

The pressure and ion-current signals recorded during acceleration are shown in Figure 13, where the engine was accelerated from 1000 rpm to 4000 rpm at full load. A log obtained during deceleration is shown in Figure 15. The engine was decelerated from 4000 rpm to idle speed at three quarters load.

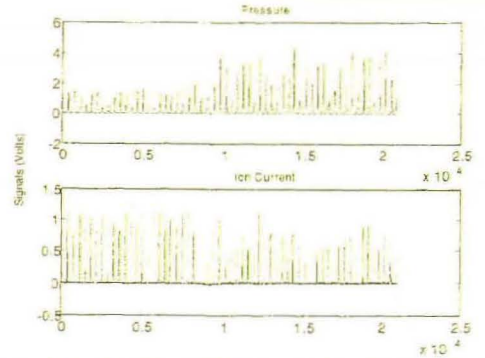


Figure 13 – Pressure and ion-current signals recorded as the engine was accelerated from 1000 rpm to 4000 rpm at full load.

In the data logs of Figure 13, the engine was kept at idle until the 0.8×10^4 data point, and then the throttle was suddenly fully opened. It is particularly interesting to note here that although the pressure increases after that point, the ion-current drops. This is largely due to the mixture leaning out momentarily at the sudden opening of the throttle, but it may also partly be due to the effect noted in the load/speed section where the magnitude of the ion-current signal drops above three quarters load. It can also be seen that misfire occurs at the point where the throttle is opened. This is due to fuel condensation in the inlet manifold and to inability of the carburetor to sustain stoichiometry during transients.

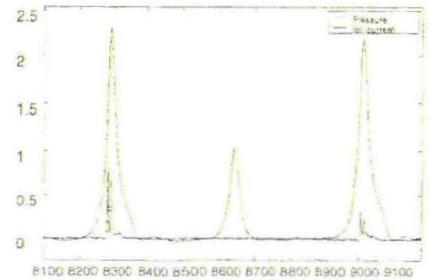


Figure 14 – Acceleration Misfire Detail from Figure 13.

Figure 14 is an enlargement of data taken from Figure 13 over the cycles where misfire occurs. It can be seen that the ion-current signal is absent on the misfired cycle and weak on the cycle occurring directly after the misfire:

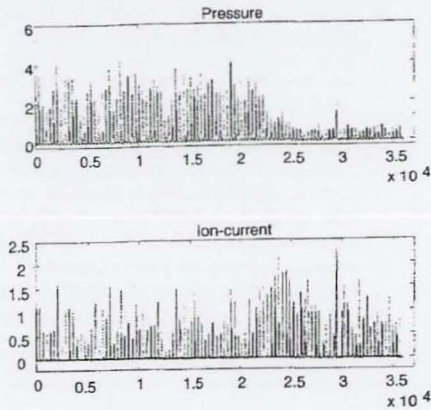


Figure 15 – Pressure and ion-current signals recorded as the engine was decelerated from 4000 rpm to 1000 rpm at three quarters load.

The behavior of the ion-current signal is exactly the opposite of the behavior shown during acceleration. Again, misfired cycles occur as the throttle is shut off due to momentarily over-rich air-fuel mixtures. Figure 15 also illustrates that the correlation between ion-current and cylinder pressure is very close in the x direction, but is much more complex in the y direction as during transient performance, as the cylinder pressure decreases, ion-current actually increases. This may be partially understood by examining Figure 16, where it can be seen that the mixture actually ignites after the exhaust valve is opened.

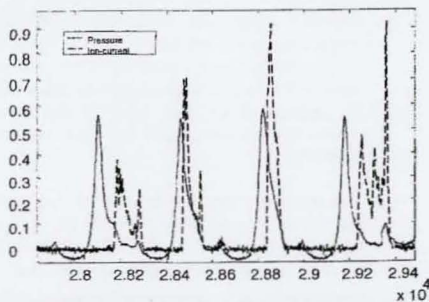


Figure 16 – A detail of the deceleration log showing misfired cycles where the mixture ignited at EVO.

STATISTICAL ANALYSIS

Preliminary understanding of the combustion attributes can be achieved by examining the signal characteristics as described above. In order to be able to extract more detailed information, some post-processing of the signal is needed. In this section a brief description of how the signals were analyzed and the portions of the signals that were used to extract useful information is given.

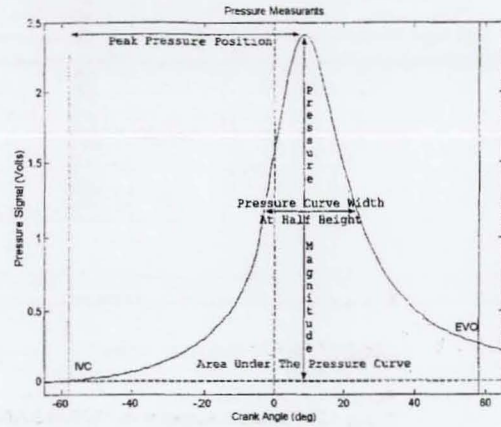


Figure 17. – Diagram of relevant pressure signal measurants.

For the curve integration, the start and endpoints are taken at the point where the inlet valve closes (IVC) and the exhaust valve opens (EVO) respectively for the given engine, IVC was 116 degrees before the combustion TDC and EVO 116 degrees after it. Hence, the areas of the pressure curves quoted in this report are all between these two points.

The pressure measurants, as shown in Figure 17, with their names and their units are:

1. The position of the signal peak – measured in CA degrees after IVC
2. The magnitude of the signal peak – measured in signal Volts
3. The width of the curve at half its height – measured in CA degrees
4. The area under the curve – measured in CA degrees by signal Volts

For the ion-current signal curve integration, the start point is taken as the point where the signal rises above noise levels, while the end point is taken as the point where the signal drops to noise levels. If the ion-current signal is still

strong at EVO, then this is taken as the end point since any combustion after EVO will not have a considerable effect on the pressure.

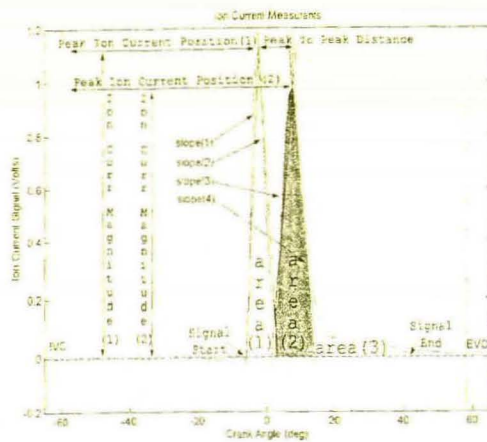


Figure 18 – Diagram displaying ion-current signal measurants

The most useful ion-current signal measurants (shown in Figure 18) are:

- 1 The position of the first point of a signal – measured in CA degrees after IVC, and the difference between the two peaks
- 2 The positions of the first and second spike peaks – CA degrees after IVC
- 3 The magnitude of both spikes – Volts
- 4 The three areas under the different regions of the signal – CA degrees x Volts
- 5 The four slopes of the spikes – Volts / CA degrees

DATA MANIPULATION

In order to further analyze the ion-current data via artificial neural networks, the pressure measurants must be related to those of the ion-current, and so graphs of all possible combinations of the 4 pressure measurants were plotted against the 13 ion-current measurants described above.

The important trends, in terms of pressure ion-current correlation are common under all engine parameter changes. The results shown here, obtained by varying the ignition timing, are representative of all tested conditions. Results obtained by varying the compression ratio, load/rpm, air-fuel ratio and generally parameters that affect

flame propagation speed, exhibit the same behavior, and thus the results from the other tests are omitted.

To find the best matches, a Pearson correlation test was carried out on the data. This is a statistical method that measures how well a linear equation describes the relation between two variables that are measured on the same object. It is defined as the sum of the products of the standard scores of the two measures, divided by the degrees of freedom. A score of 1 or -1 shows that the data lies on a line, whereas a score of zero shows there is no linear relationship between the variables.

The data that were subject to this analysis were not averaged and the following graphs present the results on a cycle to cycle basis. The engine was run at 1600 rpm, half load, an air fuel ratio of 0.9 and the ignition timing advance for was swept from 55 to 50 to 40 to 20 and finally to 0 deg. Figure 19 shows correlation between the position of the first peak of the ion-current signal against the area under the pressure curve, and the Pearson correlation coefficient was -0.96588 showing an inversely proportional and almost linear relationship exists.

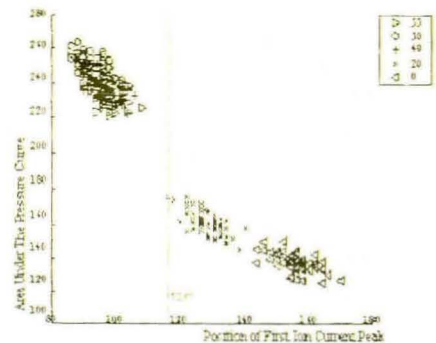


Figure 19 – Area under the pressure curve against the position of first peak of ion-current signal

The area under the pressure curve is linked to peak pressure magnitude, (the higher pressure results in a larger area under the curve). Both of these measurants are closely related to the position of the first peak of the ion-current. The same inversely proportional relationship exists for position of the first peak of the ion-current against pressure magnitude, and the Pearson correlation was -0.98016.

The position of peak pressure is plotted against the peak of the first ion-current spike in Figure 20, and gives a Pearson correlation coefficient of 0.97866. Again, this demonstrates a near linear relationship except this time the two measurants are directly proportional. This very good correlation was expected as the earlier the peak position occurs the earlier the flame reaches our sensor.

Similar correlations were found between the position of the start of the ion signal and peak pressure position, yielding a Pearson coefficient of 0.97540. The early start of the ion-current signal means early flame propagation, which equates to early peak pressure position.

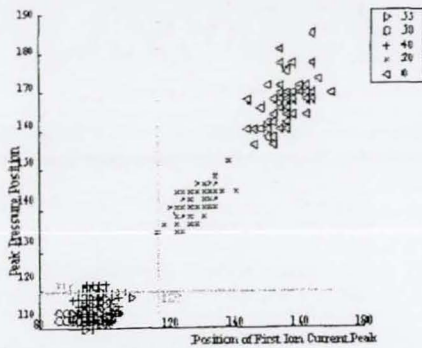


Figure 20 – Peak Pressure Position against the position of peak of the first ion-current spike

If the mixture was trimmed to higher dilution levels, a delay in the start and the peak of the spike of the ion signal would be noted. However, the slower flame speed would also affect the slope of the signal thus increasing the delay in-between these two points. So, since most of the characteristics are interrelated, it is not surprising that similar, although less striking trends were found when comparing most of signals' measurants.

ARTIFICIAL NEURAL NETWORK MODEL

The correlations mentioned above do not lend themselves to an analytic solution. No single correlation is strong enough to provide direct and robust pressure estimation while simplistic prediction algorithms will probably not meet the requirements if more than one parameters change simultaneously.

However, Artificial Neural Networks (ANNs), (which are known to be efficient in dealing with noisy and incomplete data) are a good candidate for tackling this kind of problem. These are fast computational constructs loosely modeled on real neural networks where each artificial neuron is a node that takes a number of inputs which are weighted and summed. Then the weighted sum is passed through a transfer function to give the final output. Their role is to summarize the inputs of the neuron into a value.

There are several network families to choose from when designing an ANN, but in the present study ADALINES (ADaptive Linear NEtworks) [23] were used. In the past, perceptrons have been used for position of peak pressure estimation through ion-current sensing [17, 18, 19]. Like the perceptrons, ADALINES are among the classic

networks used extensively in various industrial functions are pure lines ($y=x$). One advantage of using them is that their inputs and outputs do not need any scaling in order to be used. Another advantage is that, if the input/output sets are used. A further advantage is that, an ADALINE can always be designed with minimized error for these sets without need of iterative training techniques.

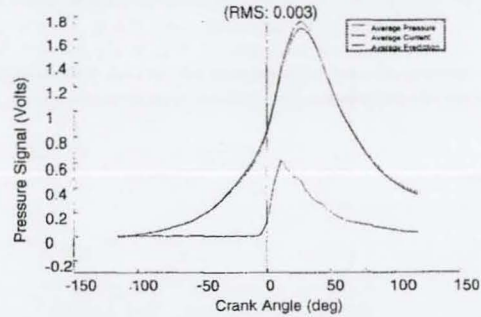


Figure 21 – The average actual pressure and ion-current signals, with the predicted pressure in dotted line

The nets were fed the signals of the logged files, the ion-current signal as an input set and the pressure signal as an output set. In addition, the engine conditions (throttle position, lambda value, rpm, ignition timing advance, compression ratio) were also provided in log files. The ADALINE was trained on a small number of these (5 to 15 logs) and was then tested on a hold out data set, that had not been previously supplied to the network, and that had different parameter setting than had been used before. On the following plots, the performance of the ADALINE is demonstrated. All results shown are cycle-to-cycle predictions, apart from the average pressure curve in Figure 21.

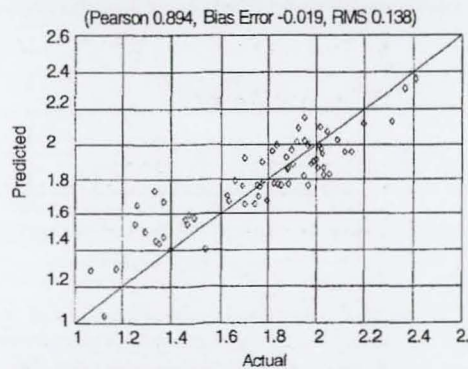


Figure 22– Pressure Magnitude

For the data presented here, the ADALINE was trained using logs under, mainly, varying compression ratio, while

logs with varying load and speed were also used. The test file has a speed, load and compression ratio combination that the net has never seen before. As can be seen from the average pressure prediction over the 70 cycles is in good agreement with the actual average pressure shown, with a point-to-point RMS error of just 0.003 Volts.

The pressure magnitude prediction shown in Figure 22, exhibits an RMS error of 0.138 and a Bias error of -0.019 Volts, or 8% and -1%, respectively. The position of peak pressure prediction of Figure 23 has an RMS error of around 3 CA degrees and a Bias error of around -0.5 CA degrees.

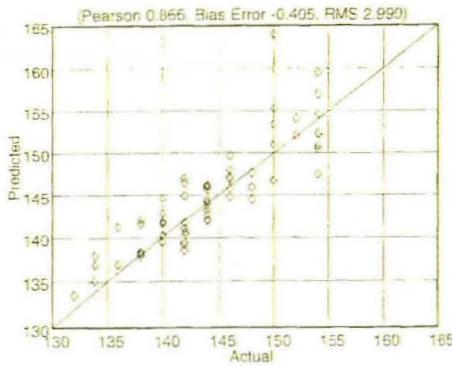


Figure 23 – Peak Pressure Position

Again, the area under the pressure curve, is a good estimation with less than 3.5% RMS and less than -0.2% Bias errors, as shown in Figure 24.

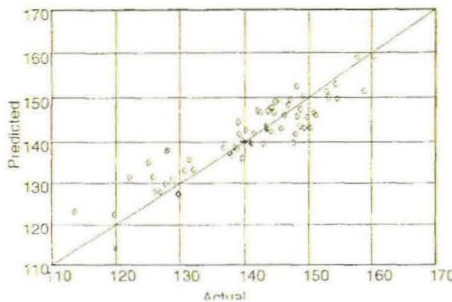


Figure 24 – Area Under the Pressure Curve

Figure 25 demonstrates the effect of using less training cycles on the quality of the reconstructed pressure trace. Here, only 7 of the previous design files (less than 500 design cycles) were supplied, and information about the engine operating conditions were not supplied to the ADALINE. The hold out data set used for testing was the same as for the previous tests.

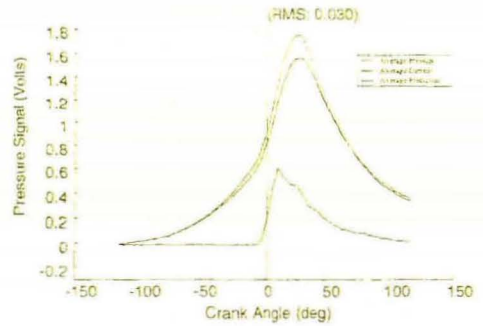


Figure 25 – The average predicted and actual pressures, along with the average ion-current

In this case, the pressure magnitude estimation RMS error rose to 8.2%, an increase of about 4% over the previous results. The Bias error changed sign, but is still under 2%. The position of peak pressure estimation was within 4 CA, an increase of around 0.6 degrees uncertainty, while the bias error remained under -0.5% CA degrees.

Compared to the previous results, the area under the curve prediction accuracy fell to a worst case scenario of less than 5% RMS and less than 1.5% Bias errors. Reasonable results were obtained for all predictions, in spite of the fact that the only information supplied to the ADALINE was the ion-current signal. In addition, the net only "saw" 500 combustion events that were logged under different operating conditions to the test file. Similar prediction accuracies were noted under all engine operating condition sweeps, including ignition timing, air fuel ratio, and load/rpm, as long as the design files are selected so that the test file lies within the sweep's boundaries, thus demonstrating the suitability of using the ion-current signal when combined with a computationally inexpensive ANN for gathering in cylinder pressure data.

DISCUSSION

Misfire detection through ion-current measurement is a robust and reliable method under all operating conditions, even on a multi cylinder engine because under misfire conditions there is no ion-current signal. If the ion-current signal were to be incorporated into a closed loop control system, misfire judgment could be made by the time the piston is at TDC allowing the spark to be re-fired and some of the chemical energy in the charge could be recovered, and more importantly, burning the mixture before it reaches the catalyst, (although this strategy is unfeasible on standard ignition systems as the coil cannot be recharged in time). When an ion-current sensor that is separate to the spark plug is used, misfire caused due to electrode tip deposits can also be detected.

Pre-ignition detection is also possible, if an ion-current signal is sensed earlier than it is expected, for example

because the mixture ignited due to hot surfaces in the chamber. Under some conditions, a very mild pre-ignition may occur that may not be detected due to the time taken for the flame to travel to the remote sensor. For this to be confused with normal combustion, it would have to occur very shortly before normal combustion, so this is not a serious drawback to the use of remote sensors.

The results indicate that there are some linear relationships between the pressure and ion signals characteristics. An analytical approach might not yield enough accuracy to resolve the feedback problem, but with the help of ANNs the precision of the predicted values, as indicated by the error's RMS and the Pearson coefficient, becomes impressive. In real world terms, if the engine parameters are known a PPP prediction should fall within 3.5° C.A. Also, the pressure magnitude prediction should be within 10%. All OBDII vehicles are equipped with the sensors needed to inform the neural network about the engine operating conditions, but even if these are not known, the PPP prediction uncertainty only increases to 4° C.A. and the pressure magnitude to 11% total errors. These results were attained on a cycle-to-cycle prediction, with a sampling frequency of 1sample/2° C.A., and without averaging nor information about important engine parameters such as coolant temperature, mass air flow, manifold absolute pressure etc and with relatively few "design" cycles. (Upwards of 50,000 cycles are normally used) [7,20,21]. Keeping in mind, that with a linear speed versus load table interpolation model, like the ones generally used in production vehicles today, the RMS error for PPP estimation is 3.3 C.A. degrees and the Bias error 1 C.A. degrees [8] the ANN performed adequately.

A further advantage is that table interpolation model performance drops considerably with ageing, whereas the ion-current in-cylinder sensor will contain ageing information. This is because the ion-current signal will decrease as the engine ages and cylinder compression decreases. Although no ageing test was performed, this effect was simulated by varying compression ratio and the results obtained promise good ageing behavior.

Similar issues like fuel additive effects and carbon contamination of the sensor were not examined. However, other studies [24] have shown that fuel additives affect mainly the amplitude and not the shape of the ion signal curve. As such, it was reported that they can be overcome through data normalization. Soot contamination, although not a major problem in gasoline engines, could be resolved through techniques like auto-calibration by measuring the resistance of the ion sensor prior to combustion [25].

Good estimation capabilities under varying compression ratio were also shown. Altering the compression influences the flame propagation speed. This can be measured with a remote spark plug ion sensor. The main use of this type of information is likely to be for correction of load table interpolation models as the engine ages. However, further

research is required to establish why the ion-current signal decreased above 75% load.

The effect of changing air-fuel ratio was also investigated. It was shown, that in agreement with other researchers observations, the slope of the first spike of the ion-current is indicative of mixture strength. Although the possibility of completely substituting the oxygen sensor is arguable, it is clear that ion-current signals can be used for cylinder balancing. It is known that cylinders on a multi cylinder engine can have an AFR difference of 7% between them, with the oxygen sensor registering a stoichiometric value. If the ion-current signal can be used to balance cylinder AFR, the overall emissions will drop, the temperature variance between cylinders will also drop and the output torque of each cylinder will equalize improving engine refinement.

The most commonly used technique for rapid catalyst warm-up is to retard the ignition at start-up. Manufacturing tolerances, equate to differences of AFR, dwell time and airflow between the cylinders and dictate a conservative maximum retard that will not sacrifice drivability, for the worst-case scenario. Ion-current sensing will enable the maximum retard to be used, under all conditions.

With regards to the use of the additional ion-current sensors, it is noteworthy that since the measuring plug(s) was some distance away from the firing plug, a direct and firm relationship under all conditions of flame propagation speed and the start of the ion-current measurements was recorded. This is a unique characteristic of this investigation that proved worthwhile. When measuring from the firing plug, since the first peak is a result of the flame kernel created by the plug, it does not carry any valuable information. Only the second peak is dependent on the pressure and temperature. The problem with this is that under low load conditions this second peak disappears, since there is not enough pressure in the cylinder to cause post-flame ionization. This was, also, observed in our investigation, but had no effect on the results.

The difference in results between one and two sensor usage is small, but more measuring points result in higher accuracy. Sensors are mostly affected by local events, and an averaging strategy through the use of multiple sensors improves the quality of the data.

CONCLUSIONS

In this research, the potential of the ion-current measurement as feedback for engine control has been assessed. Data was collected using a single, and the two remote ion-current sensors, and it was found that whilst the use of a remote sensor provides better insight than a single spark plug sensor, the is little benefit in using two remote sensors other than increased signal strength leading to a slightly wider diagnostic window.

The single and double remote sensors were tested under different engine operating conditions to obtain an insight into the behavior of the ion-current signal when misfire occurs, air-fuel ratio changes, ignition timing is advanced, and compression ratio is changed. The ion-current signal was measurable under all tested conditions. Even in cycles where data was noisy or incomplete, the ANN method was still able to predict pressure measurants with adequate accuracy.

Detection of misfire has been shown to be possible through trivial methods. The ANN has also allowed for more complicated analysis adequate accuracy, such as AFR.

Also the predictive abilities of adaptive linear network designs that take the ion sensor's output as input and calculate PPP, pressure magnitudes, the area under the pressure curve, the width of the curve and also reconstruct the whole pressure signal were compared. The results prove that there is great potential for the use of ANN with ion-current signals in closed loop control.

The practical implementation in production vehicles still poses a few challenges. The provision of superior computational power in engine management systems being one of them, and the additional cost and complexity of using even a single remote sensor is also an issue.

REFERENCES

1. Kiencke U, Nielsen L, Automotive Control Systems, 2000, SAE International
2. Hellring M, Holmberg U, An Ion-current Based Peak-Finding Algorithm for Pressure Peak Position Estimation, 2000-01-2829, SAE Technical Paper Series
3. Daniels C F, The Comparison of Mass Fraction Burned Obtained from the Cylinder Pressure Signal and Spark Plug Ion Signal, 980140, SAE Technical Paper Series
4. Saitzkoff A, Reinmann R, Mauss F, Glavmo M, In-Cylinder Pressure Measurements Using the Spark Plug as an Ionization Sensor, 970857, SAE Technical Paper Series
5. Hellring M, Holmberg U, A Comparison of Ion-current Based Algorithms for Peak Pressure Position Control, 2001-01-1920, SAE Technical Paper Series
6. Hellring M, Munther T, Rognvaldsson T, Wickstrom N, Carlsson C, Larsson M, Nytomt J, Spark Advance Control Using the Ion-current and Neural Soft Sensors, 1999-01-1162, SAE Technical Paper Series
7. Hellring M, Rognvaldsson, Wickstrom N, Larsson M, Ion-current based Pressure Peak Detection Under Different Air Humidity Conditions, 2000, Technical Paper, Advanced Microsystems for Automotive Applications (AMAA)
8. Nielsen L, Ericsson L, An Ion-Sense Engine-Fine-Tuner, Vehicular Systems, Department of Electrical Engineering, IEEE Control Systems Magazine, Vol. 18, no.8, Oct 1998.
9. Eriksson L, Nielsen L, Glavenius M, Closed Loop Ignition Control by Ionization-current Interpretation, 970854, SAE Technical Paper Series
10. J. Auzins, H. Johansson and J. Nytomt "Ion - Gap Sense in misfire detection, knock and engine control" 1995, SAE 950004
11. J. Forster, A. Gunther, M. Ketterer and K.J. Wald "Ion-current sensing for spark ignition engines" 1999, SAE 1999-01-2004
12. Y. Ohashi, M. Koiwa, K. Okamura and A. Ueda, "The application of ionic current detection system for the combustion control" 1999 SAE 1999-01-0550
13. L. Peron, A. Charlet, P. Higelin, B. Moreau, and J.F. Burq "Limitations of Ionization-current Sensors and Comparison with Cylinder Pressure Sensors" 2000 SAE 2000-01-283.
14. Hellring M, Munther T, Rognvaldsson T, Wickstrom N, Carlsson C, Larsson M, Nytomt J, 'Robust AFR Estimation Using the Ion-current and Neural Networks, 1999, SAE 1999- 01-1161
15. Heywood J B, Internal Combustion Engine Fundamentals, 1988, McGraw Hill International
16. Hellring, M., Rognvaldsson, T. and Wickstrom N. (2000). Ion-current Based Pressure Peak Detection Under Different Air Humidity Conditions. Advanced Microsystems for Automotive Applications 2000, pp.125-138
17. Hellring, M., Munther, Rognvaldsson, T. and Wickstrom N. (1999). Spark Advance Control using the Ion-current and Neural Soft Sensors. SAE Technical Paper 991162. Society of Automotive Engineers.
18. Hellring, M., Holmberg, U., An Ion-current Based Peak-Finding Algorithm for Pressure Peak Position Estimation. (1998) Society of Automotive Engineers.
19. Byttner S, Rognvaldsson T, Wickstrom N, Strategies for Handling the Fuel Additive Problem in Neural Network Based Ion-current Interpretation, 2001-01-0560, SAE Technical Paper Series
20. Hellring M, Munther T, Rognvaldsson T, Wickstrom N, Carlsson C, Larsson m, Nytomt J, Robust AFR Estimation Using the Ion-current and Neural Networks, 1999-01-1161, SAE Technical Paper Series

21. Daniels C F, The Comparison of Mass Fraction Burned Obtained from the Cylinder Pressure Signal and Spark Plug Ion Signal, 980140, SAE Technical Paper Series

□ MIL – Malfunction Indicator Light

22. Nakajima Y, Onoda M, Nagai T, Yoneda K, Consideration for Evaluating Knock Intensity, JSAE Rev, Vol.9, 1982

23. Gazis A, Panosakis D, Chen R, Chen W-H, Computationally inexpensive Methods of Ion-current Signal Manipulation for Predicting the Characteristics of Engine In-Cylinder Pressure

24. Malaczynski, G.W. and M.E. Baker, Real-Time Digital Signal Processing of Ionization-Current for Engine Diagnostics and Control, SAE Technical Paper Series. 2003-01-1119:(2003).

25. Glavmo, M., P. Spadafora, and R. Bosch, Closed Loop Start of Combustion Control Utilizing Ionization Sensing in a Diesel Engine, SAE Technical Paper Series. 1999-01-0549:(1999)

26. Russ S., Peet G., Stockhausen W., Measurements of the Effect of In-Cylinder Motion on Flame Development and Cycle-to-Cycle Variations Using an Ionization Probe Head Gasket, SAE Technical Paper Series, (970507), 1997

ABBREVIATIONS

□ TDC – Top Dead Center

□ IVC – Inlet Valve Close

□ EVO – Exhaust Valve Open

□ CR – Compression Ratio

□ ITA – Ignition Timing Advance

□ AFR – Air Fuel Ratio

□ DAQ – Data Acquisition

□ MBT – Maximum Brake Torque

□ PPP – Peak Pressure Position

□ CA – Crank Angle

□ RMS – root mean square

□ OBD – On-board Diagnostics

Computationally inexpensive methods of ion current signal manipulation for predicting the characteristics of engine in-cylinder pressure

A Gazis*, D Panousakis, R Chen, and W-H Chen

Department of Aeronautical and Automotive Engineering, Loughborough University, Loughborough, UK

The manuscript was accepted after revision for publication on 5 September 2005.

DOI: 10.1243/14680874JER04005

Abstract: Recent research on the use of ion current has focused on matching the characteristics of the in-cylinder pressure, thus avoiding the use of a pressure transducer. This paper explores techniques of calculating these pressure characteristics through the use of simple and computationally inexpensive artificial neural networks. Two neural networks are presented to deduce the in-cylinder pressure from ion current measurements, where one is used to predict the characteristics directly and the other is used to calculate the in-cylinder pressure curve. Experimental results show that both networks give satisfactory results for different purposes. Some engineering implementation issues and the further improvement of the developed techniques are discussed.

Keywords: ion current, in-cylinder pressure, artificial neural networks

1 INTRODUCTION

In the race for more efficient engines, conventional means of control have to evolve in order to provide the finesse required. A modern engine is a greatly computerized entity with a host of sensors checking a variety of aspects of its operation. However, largely owing to the extreme conditions that it contains, the cylinder itself is usually not equipped with any sensors monitoring it directly. Still, knowledge of what happens inside the cylinder is highly desirable for a modern control system. Most manufacturers try to deduce relevant information indirectly through knock sensors, lambda sensors, airflow sensors, etc., and conditions inside the cylinder are predicted from models based on these sensors' outputs, rather than on direct measured evidence. Thus these are not as suitable for the task as an in-cylinder sensor.

Cylinder pressure is one of the most important variables in monitoring engine performance. The most obvious solution is to install a pressure sensor in each cylinder. This, however, is impractical because of the prohibitively high cost and question-

able long-term performance of such a device. Thus pressure sensors are used for research purposes, a target to be met rather than a solution in themselves.

Ion current has long been investigated as a combustion diagnostic tool [1–5]. It works as follows. The prevailing conditions during the combustion causes ionization of the gases inside the cylinder. This ionization occurs mainly in two phases. The first phase occurs during combustion as fuel reacts with oxygen. It is defined as the chemical phase. The second phase occurs as the already burnt gases are compressed by rising pressure created by the fuel farther away from the spark plug combusting. It can therefore be defined as the thermal phase. By applying a voltage through these gases, a current will be observed. It is up to the engine controller then to decide what kind of information can be deduced from this ion current signal [6–7].

The potential of ion current has been researched and used in production as a means of misfire detection (a task that it is well suited for as a misfire produces no ion current) and knock detection [8–10]. More research has focused on the estimation of air-fuel ratio (AFR) from manipulation of ion current signals [11–16] and how to incorporate it into a closed-loop control system [17–22].

Recent research has gone further, trying to repro-

* Corresponding author: Department of Aeronautical and Automotive Engineering, Loughborough University, Loughborough, Leicestershire LE11 3TU. email: a.gazis@lboro.ac.uk

duce in-cylinder-pressure profile characteristics from ion current data [23–28]. If successful, the advantages are obvious. The high cost of the pressure sensor can be bypassed with just the cost of relatively cheap electronics.

The most obvious way to apply a voltage inside a cylinder is to use two already existing electrodes, the spark plug tips. This approach has some inherent problems. In most engines there is one plug per cylinder which has to generate a spark as well as to measure ion current. Because the spark-generating voltage is substantially higher than the typical voltages applied in the ion-current-measuring circuit, the latter has to be protected somehow. This has been accomplished for example by either measuring from the low-voltage side of the ignition circuit or by switching the measuring circuit in and out of the high-voltage side. Both these approaches complicate matters, the former because of increased noise and bandwidth filtering by the coils, and the latter because of the intricacy of such a dedicated circuit. Furthermore, all approaches that measure ion current signals from the ignition spark plug suffer from the fact that no meaningful information can be gathered until the ignition circuit has been fully discharged. As a result, the initial stage of the combustion, which corresponds to the chemical phase of the ion current signal, cannot be recorded [29, 30].

Another significant problem of measuring ion current through the firing spark plug is that, since the initial stage of the combustion cannot be well measured, the best signal is derived from the ion current signal's thermal phase. This, however, becomes less significant with reduced load and can disappear for load settings less than 75 per cent, thus severely limiting the usefulness of the ion current signal.

In order to address these issues, ion current sensing from dedicated sensors can be employed (remote sensing), introducing significant advantages. On the technical side, signal quality is greatly improved since data acquisition (DAQ) does not need to be interrupted. This continuous measurement allows for acquisition of ion current data throughout the combustion process. This enables a much greater volume of information to be extracted from the signal at higher signal-to-noise ratios. Since this signal potentially holds much information to be extracted, sophisticated signal processing strategies need to be employed.

On the cost side, this approach offers the opportunity for simpler, more robust and therefore more cost-efficient designs for the measuring circuit, since there is no consideration of coupling with the ignition circuit to be taken into account.

Finally, signal quality is greatly improved using remote sensing, thus permitting true cycle-to-cycle engine diagnosis and control. Thus, the need for averaging is eliminated, which reduces computational and time requirements.

It might, at first, seem as a significant complication to introduce dedicated ion sensors on mass production engines. However, companies that already offer head gaskets with multiple ion collectors exist. This makes modifications to the cylinder head and engine block unnecessary [31, 32].

Thus, this research focuses on the examination of the potential of ion current based mainly on the benefits of better signal quality, cheaper electronics, and use of computationally inexpensive signal-processing algorithms that are made possible through remote sensing.

After examining the relations between the ion current and cylinder pressure and investigating the characteristics of these two signals, artificial neural network (ANN) techniques are used to deduce the cylinder pressure information from the ion current measurement and knowledge of the operating conditions. To reduce the implementation difficulties, a simple and computationally inexpensive adaptive linear element (ADALINE) type of network is chosen for this purpose. Then the networks are trained with a number of data sets for different operating conditions. The trained networks can deduce the cylinder pressure information required for engine monitoring and cycle-to-cycle closed-loop engine control from the ion current measurement and the operating conditions such as speed and load. To verify the effectiveness of the proposed techniques, experiments are designed to compare the deduced pressure yielded by the networks using ion current measurement with the actual in-cylinder pressure.

ANNs have been used before to interpret ion current signals. These are most commonly of the perceptron type, a standard ANN for general usage. ADALINES are networks widely used in industrial applications too; however, their use for ion current interpretation has not been witnessed by the present authors in the relevant literature. ANNs offer a promising tool for this type of task, however, for the reasons outlined in section 4, ADALINES are chosen as the best candidate.

2 EXPERIMENTAL SET-UP

The engine employed in the investigation is a single-cylinder four-stroke research engine. The basic parameters are listed in Table 1. It features variable

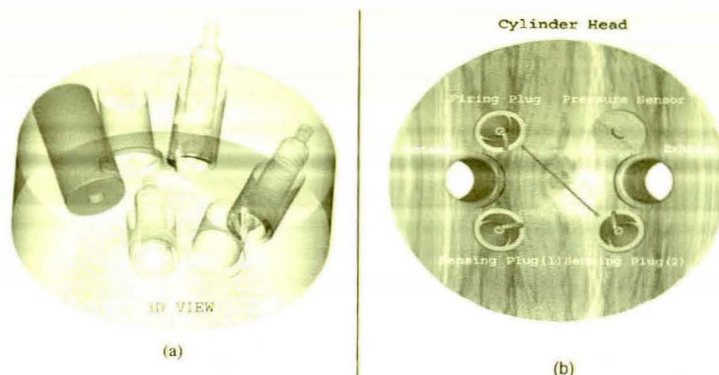


Fig. 1 Configuration of cylinder head

Table 1 Engine parameters

Bore	80 mm
Stroke	100 mm
Capacity	0.503 l
Inlet valve opening	12° before top dead centre (BTDC)
Inlet valve closing	64° after bottom dead centre
Exhaust valve opening	64° before bottom dead centre
Exhaust valve closing	12° after top dead centre (ATDC)
Compression ratio	4.5:1-13:1
Ignition timing	55° BTDC, 20° ATDC
Maximum speed	4500 r/min
Maximum power	16 bhp

compression ratio, variable ignition timing, variable AFR, variable valve timings, and four access points on the cylinder head for up to three spark plugs and one pressure sensor to be located.

Figure 1 shows the configuration of the cylinder head. There are four access points. One was fitted with a firing spark plug (bottom left). The next two were equipped with two sensing spark plugs (top and bottom right). The ion current was detected by these two remotely located spark plugs. The fourth access point was fitted with a pressure transducer.

The tips of the sensing spark plugs were assigned as the positive electrodes while the spark plug body together with the rest of the combustion chamber were used as the negative side. This was convenient since the original engine polarity was preserved.

The voltage source shown in Fig. 2 produces a voltage of 5 V, to the DAQ, for an infinite resistance between the ion sensor electrodes. This voltage reduces in an inversely proportional manner to any measured ion current signal, building in DAQ protection.

In order to reveal the true ion current signal, the measure voltage signal has been re-inverted by a voltage divider before feeding into the computer DAQ board. The DAQ sampling rate was one sample per 2° of crank angle (CA) at all engine speeds, thus making it easily implemented for mass production purposes. The ion current signals from the two sensing plugs were fed into the DAQ board, as shown in Fig. 2. Therefore, an ion current signal from either sensor or their sum can be presented and analysed.

Use of this set-up presents the whole flame-front

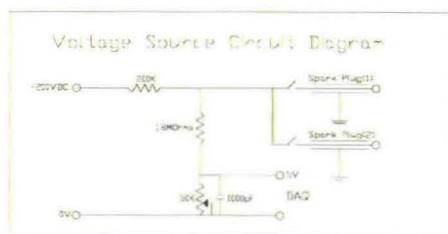


Fig. 2 DC voltage source

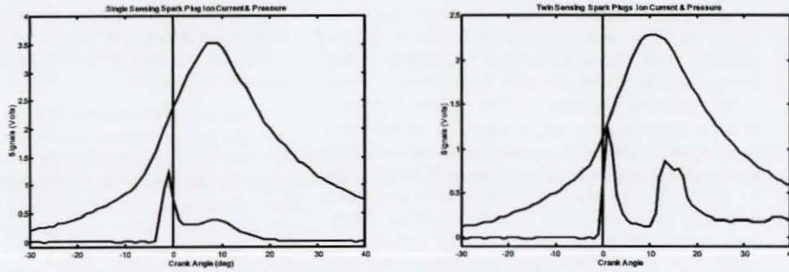


Fig. 3 Examples of pressure and ion current logs

profile as measured while it sweeps past the plugs as opposed to measuring the back of it as it recedes from the plug in a typical set-up.

Examples of pressure and ion current logs using one or both sensors can be seen in Fig. 3. Results obtained using both sensors contain more information, thus generally produce higher correlations. Throughout the rest of the paper, only results obtained using both sensors are discussed.

3 SIGNAL INTERPRETATION

The experimental data consist of two signals. The first is the in-cylinder pressure, measured from the pressure sensor. The second is the ion current signal measured from the two measuring plugs. Both of these signals are sampled every 2° CA. Figure 4 shows them together for a typical combustion event.

The leftmost vertical line indicates inlet valve closing (IVC). The next line indicates ignition timing

advance (ITA). The line at x-axis zero indicates top dead centre (TDC). The rightmost line indicates exhaust valve opening (EVO).

3.1 Measurants

The pressure signal is simpler than the ion current signal. In order to describe it numerically, four characteristics or 'measurants' are extracted for every combustion event. Figure 5 shows a typical pressure curve and associated measurants.

The measurants for the pressure curves are as follows:

- (a) the peak pressure position (x axis);
- (b) the peak pressure magnitude (y axis);
- (c) the width of the curve at half its height;
- (d) the area of the curve between IVC and EVO.

The ion current is a much more interesting signal. Because it is measured from two different plugs at different distances from the firing plug, there are two

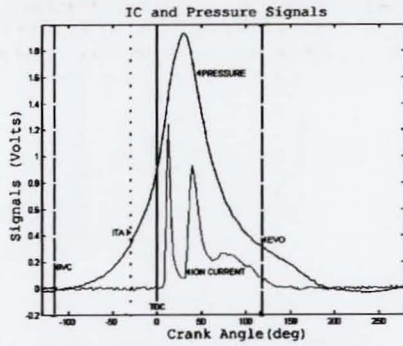


Fig. 4 Pressure and ion current signals

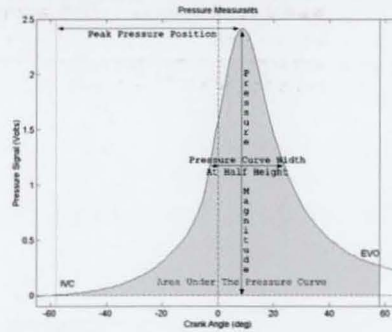


Fig. 5 Typical pressure curve and associated measurants

distinct spikes. This is because the flame front will sweep through the measuring electrodes at slightly different times. After the second spike there is the hump associated with the post-flame phase.

One point to consider is how signals from two sensing plugs create a single trace. The circuit used simply adds up the two signals and so what is seen is the sum of the ion current on both plugs. This would lead to the expectation that the second spike is heavily affected by the post-flame phase, since both measuring plugs are registering at that time (whereas, for the first spike, the flame has only reached the first plug), degrading its information content. This, however, is not the case. Figure 6 shows a close-up of an ion current trace with only one measuring plug and the engine operating highly throttled so as to minimize the post-flame hump. These are the conditions that create the most problems when measuring from the firing plug, as is the usual practice. Hellring *et al.* [24] mentioned that 'the post-flame peak essentially vanishes if the load is less than 20 per cent of the maximum load'. It is evident from Figs 3 and 4 that the first spike only lasts for about 10° CA. The post-flame phase is missing completely since ionization due to compression of the gases is low owing to the low-load conditions. Employing remote sensing eliminates the dependence on the post-flame signal. Employing two remote sensors adds further signal information.

The third phase (thermal post-flame hump) is a less-localized lower-magnitude event. Although the time window available for post-flame signal acquisition is reduced when using the sum of the signal from the two sensors, the results obtained are superior.

As in the pressure curve, some measurants are needed to describe the ion current signal for a combustion event. In the case of ion current there are 13

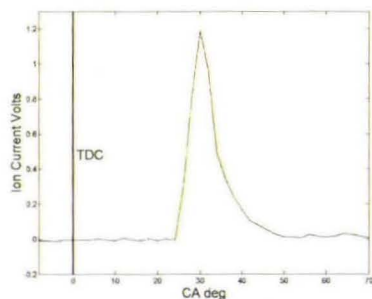


Fig. 6 Single plug trace

such measurants. A typical ion current signal and its associated measurants are shown in Fig. 7.

The measurants for the ion current signals are as follows:

- (a) the x-axis position of the start of the signal;
- (b) the x-axis position of the first spike;
- (c) the x-axis position of the second spike;
- (d) the magnitude of the first spike;
- (e) the magnitude of the second spike;
- (f) the slope of the curve between the signal start and the first spike peak;
- (g) the slope of the curve between the first spike peak and the minimum between the spikes;
- (h) the slope of the curve between the minimum between the spikes and the second spike peak;
- (i) the slope of the curve between the second spike peak and a point on the curve at the same x-axis distance as used for the previous slope;
- (j) the area under the first spike;
- (k) the area under the second spike;
- (l) the area under the post-flame section;
- (m) The x-axis position of the end of the signal.

After comparative tests, these measurants were chosen as carriers of adequate information to describe this signal. Of these, the various x-axis positions proved the most useful, since they are related to flame development. However, all selected measurants contribute to increasing the accuracy of the results.

3.2 Feature relations

Given the measurants extracted, the easiest way to look for relations is to plot them against each other. Ideally, a strong relation between an ion current

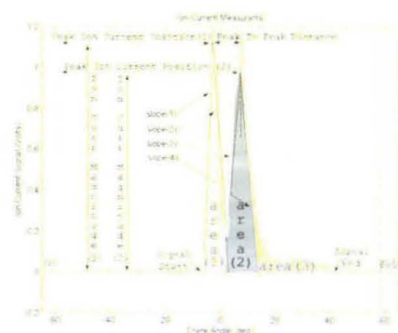


Fig. 7 Typical ion current signal and associated measurants

measurand and one or more pressure measurands will settle the case in favour of ion current. However, it is not that simple. There are conclusions to be drawn by averaging over a number of cycles, which is the technique used routinely in treating such signals. These, however, are not helpful when developing a tool; this should, in practice, be able to help to control cycle-to-cycle engine operation, which is the aim of this investigation.

Figures 8 to 10 show some cases of strongly related measurands. Ion current measurands are on the x-axis; pressure measurands are on the y-axis. These data are logged over a varying compression ratio loop, therefore each data point batch corresponds to a compression ratio between 4.5:1 and 11.2:1.

Figures 8 and 9 are matches for the peak pressure position with the positions of the first and second ion current spikes respectively. It shows good correlation with both measurands and that a delayed combustion event results in a late pressure peak position. Another point to note is that delayed combustion

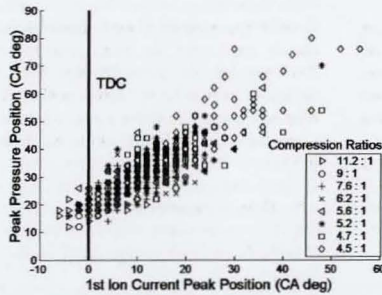


Fig. 8 Relationship between the first peak ion current and the peak cylinder pressure position

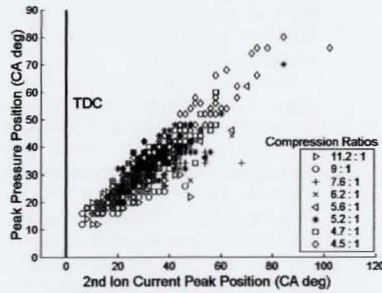


Fig. 9 Relationship between the second peak ion current and the peak cylinder pressure position

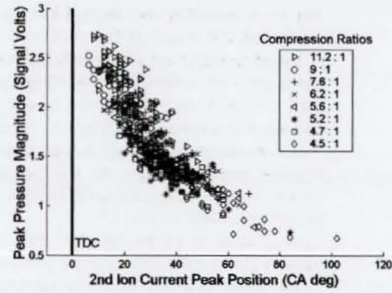


Fig. 10 Relationship between second peak ion current and the peak cylinder pressure

results in a greater uncertainty in the peak pressure position. This arises because delayed combustion is more unstable, resulting in higher cycle-to-cycle variation.

Figure 10 is a match between peak pressure magnitude and the position of the second ion current spike. It can be seen that the second peak ion current position has a strong relationship with the peak cylinder pressure magnitude, too. When the second ion current spike occurs late, the flame reaches the second sensing plug late, which indicates late combustion. Therefore the peak cylinder pressure magnitude is reduced.

Although the relationships between the first and second ion current spikes with the combustion event are strong, as can be seen in Figs 8 to 10, there is an uncertainty of the order of 10° CA relating to the peak pressure position and of the order of 0.4 V relating to the peak pressure magnitude. These uncertainties are not acceptable for engineering implementation of the use of the ion current as an alternative means of measuring the cylinder pressure. For this reason, a more sophisticated strategy has to be developed and employed for ion current signal interpretation in order to improve its correlation with the pressure signal.

4 PREDICTIONS

4.1 Artificial neural networks

ANNs are a good candidate for tackling this kind of problem [14, 22, 23]. These are computational constructs, used in a variety of applications for dealing with complicated inputs. The notion behind them is loosely modelled on real neural networks. Each artificial neuron is a node that takes a number of inputs.

These are weighed and then summed as illustrated on the left-hand side of Fig. 11.

The idea is that an input with a strong relation to the output will have a relatively large weight associated with it. Thus, fluctuations in important inputs will result in significant changes to the weighted sum.

Finally, the weighed sum is then passed through a transfer function to give the final output. There are various traditionally used transfer functions, some of which are shown in Fig. 12.

Their role is to 'summarize' the inputs of the neuron into a value. The simple form of Fig. 12(a) is a step function which basically translates to on and off states for the artificial neuron. Figures 12(a) to (d) are variations on the same theme, making a smoother transition so that information is not lost in the grey area where the weighted sum does not translate clearly into the on or off areas.

A collection of artificial neurons is what is termed the artificial neural network as illustrated in Fig. 13. The inputs are taken in by the input layer of artificial neurons. These are then processed through successive layers until they reach the final 'output' layer.

The main tasks when designing an ANN is to decide upon the architecture best suited to the task, e.g. number of layers and type of transfer functions, and then to tune its parameters, e.g. the various weights. There are many different types of training

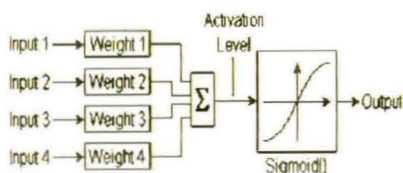


Fig. 11 Schematic representation of an artificial neuron

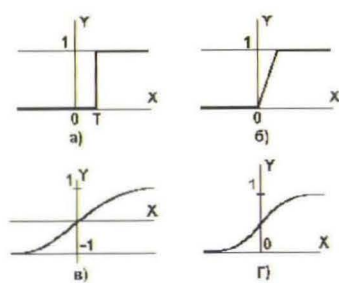


Fig. 12 Sample transfer functions

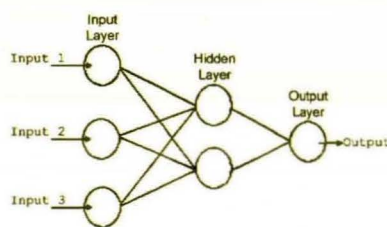


Fig. 13 A simple ANN

algorithm for this task. Most of these are recursive where a network is presented with successive sets of inputs; small alterations are made each time according to its response compared with the desired values until at some point tuning is decided to be adequate for the task.

In the case of this experiment, the following considerations are taken into account.

First, the network has to be as uncomplicated as possible. If the model is to be usable on a cycle-to-cycle basis by an engine controller, all computations have to be completed sufficiently rapidly to provide timely results for the next cycle for every cylinder. The simpler the network that does this, the less demand there is on the signal-processing electronics that will carry out those computations.

Second, the network or some further algorithm behind it must produce continuous output. This is important as the measurants are numbers that cannot be represented by an on-off state. To code for such states using step transfer functions requires a large amount of output artificial neurons for each output.

Third, the network must be easy to train with a reasonably small amount of data. In engineering applications, it is impractical to require a vast amount of data to train a neural network owing to the cost and time needed to collect these. The goal was to use as few as 70 combustion events per engine operating condition.

There are several network families to choose from. Keeping the above points in mind, ADALINES were chosen. These ADALINES are among the classic types of ANN. An ADALINE neuron takes a weighted sum of its inputs but, instead of passing it through a transfer function, sends it straight to its output. This is also helpful for producing continuous output since a single output artificial neuron can produce any real value. The main limitation of ADALINES is that they will tackle linear relations but will not be very useful beyond these. Looking at the data in Figs 8 to 10, both linear and non-linear relationships are

indicated. However, the window of engine operating conditions tested is strongly exaggerated compared with normal operation. Despite this and the fact that linear approximations were used, the obtained results are well within the scope of closed-loop engine control implementation. In addition, the range of operating conditions spanned by a production engine is such that the data produced would be in relations even more adequately modelled as linear.

Finally, for training purposes, ADALINES can be trained using the least-mean-squares (LMS) algorithm. This is a very important consideration given the low-data-volume requirement. The strength of the LMS algorithm lies in that it competently handles this case where the data are limited. The way that LMS trains the network is as follows: given a set of inputs and a set of desired outputs, the error is defined as the difference between the actual output and the desired output. LMS minimizes the average of the sum of the square of these errors. Since this is a quadratic function, it will have at most one minimum. Thus, for a given set of inputs, LMS will tune the network so that their averaged squared errors are minimized. In this research, two sets of networks have been developed and tested. To test these, some data sets were set aside and used afterwards to assess performance under unknown inputs.

4.2 Measurant-predicting network

The first network is the smallest in terms of artificial neurons. It is a layer of four artificial neurons (ADALINES are single-layer networks), each of which takes the 13 ion current measurants as inputs and produces one of the predicted pressure measurants as an output. Each input is multiplied by a weight factor and all weighted inputs are then summed into what becomes the output.

Figure 14 shows the network architecture. The 13 ion current measurants are the set of circles at top

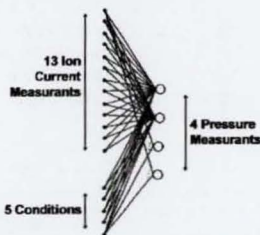


Fig. 14 Schematic representation of the network

left. The set under them, labelled 5 Conditions is a string of numbers (constant for each input file) that describes the operating conditions of the engine at the time. These conditions are throttle position, engine speed, engine load, AFR, ignition timing advance, and compression ratio.

Training is carried out as follows. When data were logged, one of the aforementioned operating conditions was varied and a number of files logged for various values of that condition with everything else kept the same. This created 'families' of files, the compression ratio family, the ignition timing family, etc. Of these families, one member is selected to be the 'test set', the set of values to be shown to the network after training to test performance. The rest of the family is then used to train the network. Thus, when testing the network, it is given values not encountered during its training. By choosing the test set to be somewhere in the 'middle' of the variable condition range, the network arrives at the correct results since these lie within its training window. The results of this process can be seen in Figs 15 to 18.

The entries on the x axis are the measured values of the measurant, and the entries on the y axis are

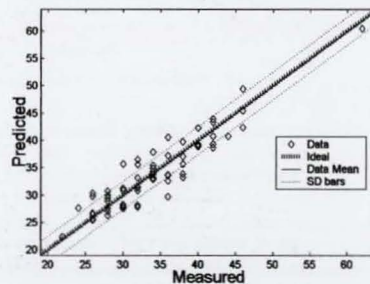


Fig. 15 Predictions for peak pressure position

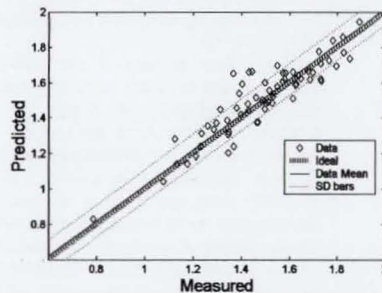


Fig. 16 Predictions for peak pressure magnitude

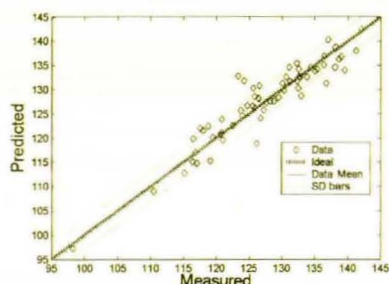


Fig. 17 Predictions for pressure curve area

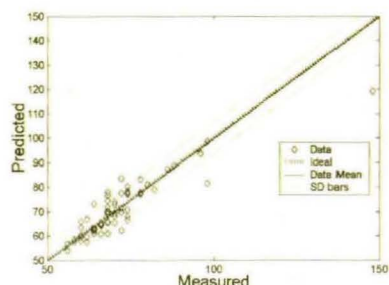


Fig. 18 Predictions for pressure curve width

the predicted values. Thus, a perfect prediction would plot a diagonal line. This is the 'ideal' line mentioned in the keys and is used for reference. The solid line indicates the data mean. It often coincides to a great extent with the 'ideal' line, which indicates a good match between measurements and predictions. The two outer dotted lines indicate the standard deviations (SDs) of the data. In these four figures, the network performs so well that the mean of the predictions and the diagonal are almost identical. The only figure in which they can be seen separately is Fig. 16.

Of the four outputs of the network, the most important are the peak pressure position and peak pressure magnitude which give the x and y coordinates respectively of the pressure curve's peak. Figure 15 shows the predictions for peak pressure position. The mean of the predicted values is shifted by 0.062° from the mean of the actual values and the standard deviation of the predictions is 2.55° . A similar degree of accuracy was obtained for the rest of the in cylinder pressure measurand predictions. Given that the ion current signal is sampled every 2° CA, this result is satisfactory.

The predictions in these figures are calculated from a mixed training set. The families used are the compression ratio family with various compression ratios and the speed and load families with various speeds and loads. The compression ratios for the first family are 11.2:1, 7.6:1, 6.2:1, 5.2:1, 4.7:1, and 4.5:1. The speed-load settings for the second family are 33 per cent at 1400 r/min, 75 per cent at 1400 r/min, wide-open throttle at 1400 r/min, 33 per cent at 1750 r/min, and 75 per cent at 1700 r/min. The test set is a member of the compression ratio family with a compression ratio of 5.6:1. Ignition timing for these was kept constant at 30° BTDC.

What is worth noting is that the network gives better results when the families are mixed together than when the training is performed on each individual family. This is a satisfactory result, demonstrating how the network can interpolate and select the right predictions for the test set, the operating conditions that it has not encountered at all during training.

4.3 Curve-predicting network

Given the satisfactory performance of the simple ADALINE in tackling the 13-input by four-output measurand predictions, a new network was tested predicting the whole pressure curve. Again an ADALINE was used, but this time with the whole ion current signal as the input and the whole pressure signal as the output. More specifically, each cycle is examined between IVC and EVO. Given the sampling rate and the valve timing, this gives a data string of 117 elements for both ion current and pressure. Thus the network consists of 117 artificial neurons, each of which is connected to all inputs and which produces one output, corresponding to a point on the predicted pressure curve. Figure 19 shows the measured and predicted pressure curves resulting from

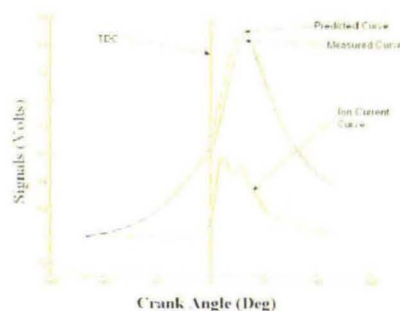


Fig. 19 Averaged actual and predicted pressure curves

this network averaged over the whole of the test set. The training set and test set are the same as for the previous network.

Again, the averaged ADALINE follows the target quite closely even though the compression ratio of the test data has never been encountered in its training. However, the measurants extracted from the predicted curves are not as good as for the previous network. Figure 20 shows the actual and predicted values for the peak pressure position. The mean of the predicted values is shifted by 1.69° (compared with 0.062 for the previous network) and the standard deviation is 5.45° (compared with 2.55 for the previous network).

Similar results are true for the rest of the measurants, with uncertainty increasing roughly twofold compared with the previous network.

This network is created with the task of matching the curve point to point. The objective of training the network is to minimize the average difference between the actual and predicted curves, which may result in the fact that the error between the predicted and actual in-cylinder pressure peak positions is not minimum.

5 DISCUSSION

The results reported here showed how ion current data can be treated using simple techniques to predict various features of the in-cylinder pressure. Of the two networks presented, the most likely to be suitable for the task of engine control is the first (measurant prediction). This is by far the cheapest computationally and is specialized in predicting the most important aspect of the pressure curve, the location of its peak. This should be a welcome result for the further development of engine control systems striving to employ fast and simple algorithms

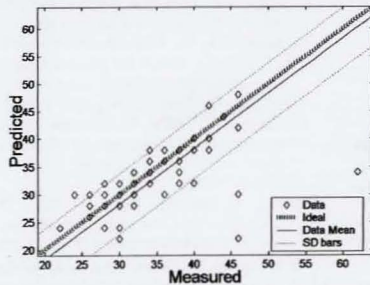


Fig. 20 Predictions for pressure curve peak position

for changing engine parameters on cycle-to-cycle timescales. One drawback of this approach is that, even though the network used is itself extremely simple, its inputs are the results of some data processing since the ion current measurants used are themselves the product of various operations. Even though these operations are well within the capabilities of modern electronics, they can be more expensive computationally than the operation of the network itself, a factor that will have to be taken into account when designing such a system.

Another feature to take into account regarding measurants is the y-axis data of the ion current signal. All the measurants strongly affecting the pressure curve results were those on the ion current signal x axis, in other words related to the timing, and not the magnitude, of the ion current events. Figure 4 shows an ion current signal. What should be noted is the sharp slopes leading up to the two peaks. In some cases, there could be two to four data points from bottom to top of the ion current spike. Therefore, the ion current signal might contain frequencies which are too high for our sampling rate. This might be an additional factor to explain why ion current magnitudes never showed any strong relation to any pressure measurants in the measurant-to-measurant plots.

The ADALINEs employed in this research manage their predictions based mostly on x-axis ion current measurants. It might be possible that higher sampling rates can improve the results further as the significance of y-axis ion current measurants will be taken into account. However, other researchers [29] have pointed out that large cyclic fluctuations are a typical problem with ion current measurements anyway. Thus, by not relying on ion current magnitude but rather on ion current timing (made easy by measuring from the remote plugs) this problem can be avoided to some extent.

Apart from the most important position of the peak of the pressure curve an ADALINE has been found to be able to tackle quite competently the task of predicting the pressure curve itself. Normally, such tasks are best left to more specialized (and more computationally expensive) tools such as radial basis functions. An important point to consider in this second network is that the input is passed to it 'raw' as it were, with no need for preprocessing to extract ion current measurants. There is a cost to pay at the output as pressure measurants are extracted from it but it is a much simpler task as there are only four measurants involved in the pressure curve as opposed to 13 in the ion current signal. However, this

network is not as effective in locating the peak of the pressure curve.

It might seem to be a logical step to design an ADALINE accepting a 'raw' ion current signal and producing pressure curve measurants as output. Variations on this have been tried with poor results. It seems that, for this kind of task, simple networks such as the ADALINE can no longer keep up.

Finally, not all data are necessarily in linear relations. Figure 10 is an example of two measurants that seem to indicate rather strongly that a non-linear relation exists between them. Modified networks have been tried to see whether performance can be improved by passing the inputs through a function, thus making the curve resemble a more linear form. The most important measurants, peak pressure position and magnitude, sometimes improved by as little as 2–3 per cent. This is not a particularly strong case for adding computational cost to the system. It seems that, given the uncertainty in the data and the short segment of curve in question, a linear approximation is best suited to dealing with it.

6 CONCLUSION

The results of this research demonstrate the feasibility of bypassing the use of a pressure transducer as a means of in-cylinder data gathering.

Through the use of the ion current signal, manipulated by computationally inexpensive ANNs, the peak pressure position has been predicted to a best resolution of 2.55° CA at a sampling rate of one sample per 2° CA.

Coupled with the robustness and significantly lower cost of the ion-current-sensing apparatus, this performance is indicative of the importance of ion current sensing as a tool in the development of future closed-loop controllers needing to acquire fast cycle-per-cycle combustion information.

REFERENCES

- 1 Schnauffer, K. Engine cylinder flame propagation studies by new methods. SAE technical paper, 1934.
- 2 Iinuma, K. Studies of engine combustion processes by ionization current. *Bull. of JSME*, 1961, 4(4), 352–357.
- 3 Bytner, S., Rognvaldsson, T., and Wickstrom, N. Estimation of combustion variability using in-cylinder ionization measurements. SAE technical paper 2001-01-3485, 2001.
- 4 Yoshiyama, S., Tomita, E., and Hamamoto, Y. Fundamental study on combustion diagnostics using a spark plug as ion probe. SAE technical paper 2000-01-2828, 2000.
- 5 Shimasaki, Y., Maki, H., Sakaguchi, J., Nishizawa, K., Kato, A., Suzuki, H., Kondo, N., and Yamada, T. Study on combustion monitoring system for formula one engines using ionic current measurement. SAE technical paper 2004-01-1921, 2004.
- 6 Yoshiyama, S., Tomita, E., and Hamamoto, Y. Fundamental study on combustion diagnostics using a spark plug as ion probe. SAE technical paper 2000-01-2828, 2000.
- 7 Aithal, S. M., White, A. R., Subramaniam, V. V., Babu, V., and Rizzoni, G. A chemical kinetics model of current signatures in an ionization sensor. <http://www.cis.ohio-state.edu/~saday/894/spark9.doc>.
- 8 Forster, J., Gunther, A., Ketterer, M., and Wald, K. Ion current sensing for spark ignition engines. SAE technical paper 1999-01-0204, 1999.
- 9 VanDyne, E. A., Burckmyer, C. L., and Wahl, A. M. Misfire detection from ionization feedback utilizing the smartfire plasma ignition technology. SAE technical paper 2000-01-1377, 2000.
- 10 Lundsstrom, D. and Schagerberg, S. Misfire detection for prechamber SI engines using ion-sensing and rotational speed measurements. SAE technical paper 2001-01-0993, 2001.
- 11 Raymond, R., Andre, S., and Fabian, M. Local air-fuel ratio measurements using the spark plug as an ionization sensor. SAE technical paper 970856, 1997.
- 12 Devesh, U. and Giorgio, R. AFR control on a single cylinder engine using the ionization current. SAE technical paper 980203, 1998.
- 13 Balles, E. N., VanDyne, E. A., Wahl, A. M., Ratton, K., and Lai, M. In-cylinder air-fuel ratio approximation using spark gap ionization sensing. SAE technical paper 980166, 1998.
- 14 Hellring, M., Munther, T., Rognvaldsson, T., Wickstrom, N., Carlsson, C., Larsson, M., and Nytomt, J. Robust AFR estimation using the ion current and neural networks. SAE technical paper 1999-01-1161, 1999.
- 15 Schneider, D. and Lai, M. D. Real-time air/fuel ratio control in a small SI engine using the ionic current signal. SAE technical paper 1999-01-3323, 1999.
- 16 Klovmark, H., Rask, P., and Forssell, U. Estimating the air/fuel ratio from gaussian parametrizations of the ionization currents in internal combustion SI engines. SAE technical paper 2000-01-1245, 2000.
- 17 Ohashi, Y., Fukui, W., Tanabe, E., and Ueda, A. The application of ionic current detection system for the combustion limit control. SAE technical paper 980171, 1998.
- 18 Bie, T., Ericsson, M., and Rask, P. A novel start algorithm for CNG engines using ion sense technology. SAE technical paper 2000-01-2800, 2000.
- 19 Eriksson, L., Nielsen, L., and Glavenius, M. Closed loop ignition control by ionization current interpretation. SAE technical paper 970854, 1998.

- 20 Asano, M., Kuma, T., Kajitani, M., and Takeuchi, M. Development of new ion current combustion control system. SAE technical paper 980162, 1998.
- 21 Franke, A., Einewall, P., Johansson, B., and Reinmann, R. Employing an ionization sensor for combustion diagnostics in a lean burn natural gas engine. SAE technical paper 2001-01-0992, 2001.
- 22 Hellring, M., Munther, T., Rognvaldsson, T., and Wickstrom, N. Spark advance control using the ion current and neural soft sensors. SAE technical paper 1999-01-1162, 1999.
- 23 Wickstrom, N., Taveniku, M., Linde, A., Larsson, M., and Svensson, B. Estimating peak pressure position and air-fuel ratio using the ionization current and artificial neural networks. In Proceedings of the IEEE Conference on *Intelligent transportation systems*, Boston, 1997 (IEEE, New York).
- 24 Saitzkoff, A., Reinmann, R., and Mauss, F. In-cylinder pressure measurements using the spark plug as an ionization sensor. SAE technical paper 970857, 1997.
- 25 Hellring, M. and Holmberg, U. An ion current based peak-finding algorithm for pressure peak position estimation. SAE technical paper 2000-01-2829, 2000.
- 26 Hellring, M., Rognvaldsson, T., Wickstrom, N., and Larsson, M. Ion current based pressure peak detection under different air humidity conditions. In *Advanced microsystems for automotive applications (AMAA)* (Eds S. Krueger and W. Gessner), 2000 (Springer, Berlin).
- 27 Eriksson, L. Spark-advance control by ion-sensing and interpretation. <http://www.vehicular.isy.liu.se/~larer/Projects/main.html>.
- 28 Malaczynski, G. W. and Baker, M. E. Real-time digital signal processing of ionization current for engine diagnostic and control. SAE technical paper 2003-01-1119, 2003.
- 29 Peron, L., Charlet, A., Higelin, P., Moreau, B., and Burg, J. F. Limitations of ionization current sensors and comparison with cylinder pressure sensors. SAE technical paper 2000-01-2830, 2000.
- 30 Asano, M., Ito, A., Kuma, T., Kajitani, M., Takeuchi, M., Fukumura, Y., and Izumi, M. Further development of an ion current combustion control system. SAE technical paper 2001-01-0266, 2001.
- 31 Russ, S., Peet, G., and Stockhausen, W. Measurements of the effect of in-cylinder motion on flame development and cycle-to-cycle variations using an ionization probe head gasket. SAE technical paper 970507, 1997.
- 32 SMETEC GmbH, <http://www.smetec.de>.

Using Ion-current Sensing to Interpret Gasoline HCCI Combustion Processes

Dimitris Panousakis, Andreas Gazis, Jill Patterson and Rui Chen
Loughborough University

Jamie Turner, Nebosja Milovanovic and David Blundel
Lotus Engineering

Copyright © 2006 SAE International

ABSTRACT

Homogeneous charge compression ignition (HCCI), combustion has the potential to be highly efficient and to produce low NO_x, carbon dioxide and particulate matter emissions, but experiences problems with cold start, running at idle and producing high power density. A solution to these is to operate the engine in a 'hybrid mode', where the engine operates in spark ignition mode at cold start, idle and high loads and HCCI mode elsewhere during the drive cycle, demanding a seamless transition between the two modes of combustion through spark assisted controlled auto ignition. Moreover, HCCI requires considerable control to maintain consistent start of combustion and heat release rate, which has thus far limited HCCI's practical application.

In order to provide a suitable control method, a feedback signal is required. This paper will investigate the use of an ion-current sensor in HCCI combustion in order to extract and quantify combustion measurants, with particular reference to control applications. A presentation of results of ion-current sensing for monitoring combustion under steady state operation, over a variety of speeds and trapped residual gas amounts is made. The results show that estimation of cylinder pressure parameters through the ion signal with promising accuracy is shown, and ion-current is proven to be a cost effective and adequately informative feedback signal for both SI and HCCI engine control.

INTRODUCTION

Homogeneous charge compression ignition (HCCI), has the potential to be highly efficient and to produce low NO_x, carbon dioxide and particulate matter emissions, but experiences problems with cold start, running at idle and also at producing high power density. A solution to these problems is to operate the engine in a 'hybrid mode', where the engine operates in HCCI mode at low and medium loads while switching to spark ignition (SI) mode at a cold start, idle and higher loads. In order to

achieve acceptable drivability a seamless transition between the two modes of combustion must be attained. In addition, HCCI requires considerable control to maintain consistent start of combustion (SoC) and heat release rate (dQ), especially during transient performance. Because no cost efficient control method has been found that would allow the aforementioned problems to be solved, HCCI's practical applications have been limited.

In order to provide a suitable control method, it is clear that a feedback signal is required but existing production engine sensors are inadequate for this task. The most straightforward answer would be to use a cylinder pressure sensor, but there are issues of high cost and low long-term reliability with this method. Alternatively, an ion-current sensor could be used as it is the most cost effective in-cylinder combustion sensor available.

Ion-current signals have long been investigated as a combustion diagnostic tool [1-6]. In SI engines the prevailing conditions during combustion cause ionization of the gases inside the cylinder. This ionization occurs mainly in two phases. The first phase occurs during combustion as fuel reacts with oxygen, and is defined as the chemical phase. The second phase is defined as the thermal phase, and occurs due to compression of burnt gases when fuel further away from the spark plug is burned [7]. By applying a voltage through these gases, a current will be produced since the ionized gasses are conductive, and further information can then be deduced from this ion-current signal [6, 8].

The most obvious way to apply a voltage inside the cylinder is to use two existing electrodes; the spark plug tips; but this approach has some inherent problems. In most engines there is one plug per cylinder, which must generate the spark as well as measure the ion-current. Because the spark generating voltage is substantially higher than the typical voltages used in an ion-current measuring circuit, the latter has to be protected somehow. Furthermore; all approaches that measure ion-current signals from the ignition spark plug suffer

from the fact that no meaningful information can be gathered until the ignition circuit has been fully discharged. Consequently, the initial stage of combustion, which corresponds to the start of the chemical phase of the ion-current signal, cannot be recorded [9, 10]. This becomes even worse at high speeds where less time is available for the coil ringing to 'dump down' [11]. Another significant problem of measuring ion-current through the firing spark plug is that since the initial stage of the combustion cannot be well measured, the best signal is derived from the thermal phase of the signal. However, this becomes less significant with reduced load and can disappear for load settings less than 75%, thus severely limiting the usefulness of the ion-current signal.

All this becomes even more exacerbated by the fact that for HCCI combustion, the signal acquired displays only one peak. Given the relatively low engine cycle temperature, the ion-current from this type of engine is thought to come mainly from chemi-ionization [12]. Since in HCCI there are low concentrations of NO_x, the ion-current signal results from ions in the reacting gas, i.e. when the electrode gap is in the reaction zone. The reaction zone might be created either due to flame propagation, (low TRG%), due to auto-ignition, (high TRG%), or a combination of the two in medium TRG%. Provided these problems can be overcome, ion-current becomes a suitable and computationally inexpensive means of acquiring data from the HCCI combustion process.

This paper will investigate the potential of using an ion-current sensor (in a separate location to the spark plug) in HCCI combustion in order to extract and quantify combustion measurants, with particular reference to control applications. A presentation of results of ion-current sensing for monitoring combustion under steady state operation, over a variety of speeds and trapped residual gas amounts is made. The results show that the ion signal is sufficiently high to be used during HCCI under all speeds and loads. Estimation of cylinder pressure parameters through the ion signal with promising accuracy is shown. Overall, ion-current is proven to be a cost effective and adequately informative feedback signal for both SI and HCCI engine control.

EXPERIMENTAL STUDY

The engine employed in this research was a single cylinder, gasoline port fuel injected, 4-stroke research engine based on a GM Family One, 1.8L series architecture, shown by the photograph of Figure 1. A standard 4-cylinder head is mounted on top of a water cooled barrel, with a custom made bottom end. Only the front cylinder of the head is operational. A fully variable valve timing system named Active Valve Train (AVT); manufactured by Lotus Engineering; was fitted to allow a variable valve timing strategy. Variable quantities of trapped residual gas (TRG) can be captured in this way. For this investigation, the CR was set at 10.5:1. (It is

worth noting that intake air temperature was maintained at a room temperature of 20 degrees Celsius)

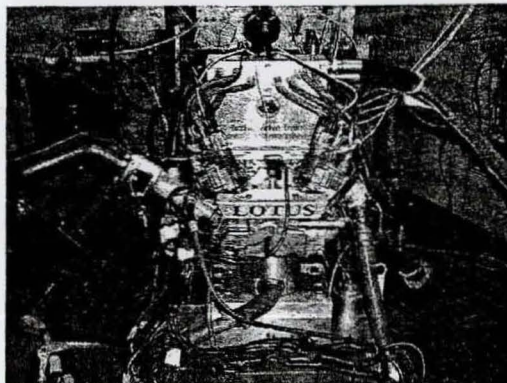


Figure 1. Single-cylinder research engine with AVT system

The engine was connected to a Froude AG30 30kW eddy-current dynamometer. A redline ACAP data acquisition system from DSP Technologies Inc. together with a Kistler 6123 piezoelectric pressure transducer and a Horiba MEXA 7100 DEGR emissions analyzer. Port fuel injection was employed, managed by a conventional Lotus V8 engine controller. High speed data were sampled at one degree crank angle intervals. This sample rate is sufficiently high to obtain the salient features of the ion-current signal (as a combustion performance indicator), whilst coarse enough to be realistically used as part of a real time engine control strategy that is compatible with conventional car electronics.

Three combustion regimes were investigated; SI, HCCI and SA-CAI (which occurs in transition regions between SI and HCCI) and where a spark is used to position heat release in the correct time window. This region is not the same as HCCI where ignition occurs due to compression. To enable this investigation, the valve strategy involved two separate profiles, one for CAI/HCCI and one for SI operation. The CAI/HCCI profile had a fixed lift of 2.5mm and fixed duration but variable overlap, which was changed from positive to negative in variable step sizes until the misfire limit was reached. For high power SI operation a high lift (8mm), long duration valve profile was used. During HCCI operation the load was controlled by changing the overlap, so the engine manifold was unthrottled. During SI operation an electronic throttle was used to adjust load. The throttle is also responsible for controlling the engine load during immediate transitions from SI to HCCI and back to SI.

In order to acquire the ion-current signal an ionization probe was located in the four-valve cylinder head between one of the inlet and one of the exhaust valves as shown in Figure 2. The probe was electrically isolated from the cylinder head by means of a ceramic sleeve.

The diameter of the sensing element was slightly less than 1mm, and the tip protrusion into the combustion chamber was approximately 3.5 mm.

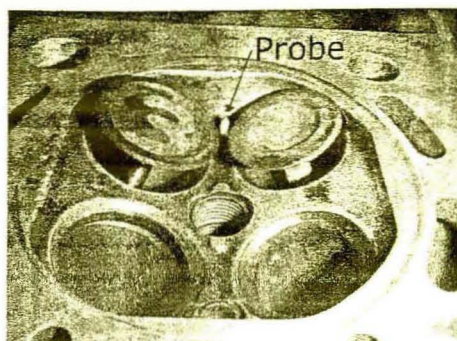


Figure 2. Photograph of cylinder head showing the location of the ionisation probe

Since the mass of positive ions, such as H_3O^+ , is approximately 30,000 times larger than that of an electron (negative charge), the light electrons can be accelerated much more easily towards the positive electrode than the heavy ions [13], when driven by an applied electromagnetic field. The voltage polarity at the gap of sensing spark plugs was therefore selected such that the small area centre electrode was positive, and the rest of the combustion chamber was negative. This coincides conveniently with the original engine polarity where the engine block is negative.

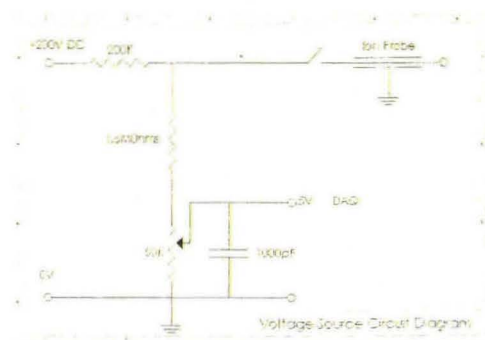


Figure 3. Voltage source circuit diagram

A one-off DC voltage source shown in Figure 3, was used to power the measuring probe. The DAQ board was fed the output of the voltage divider as the ion-current signal, which was inversely proportional to the sensed ion-current (i.e. 5V for zero ion-current and 0V for infinite) to avoid the possibility of damage caused due to excessive voltage. The signal was then inverted during the post processing phase.

Issues like fuel additive effects and carbon contamination of the sensor were not examined. However, other studies [11] have shown that fuel additives affect mainly the amplitude and not the shape of the ion signal curve. As such, it was reported that they can be overcome through data normalization. Soot contamination, although not a major problem in gasoline engines, could be resolved through techniques like auto-calibration by measuring the resistance of the ion sensor prior to combustion [14].

RESULTS AND DISCUSSION

HCCI COMBUSTION

The fuel used throughout this experimental study was commercial gasoline (95ON) having a carbon to hydrogen ratio of 1.79, whilst the AFR was kept at a stoichiometric ratio. The engine was initially tested under conventional SI operation mode. Then TRG quantity was gradually increased, thus moving from pure flame propagation, to SA-CAI, and then to HCCI as shown in Figure 4.

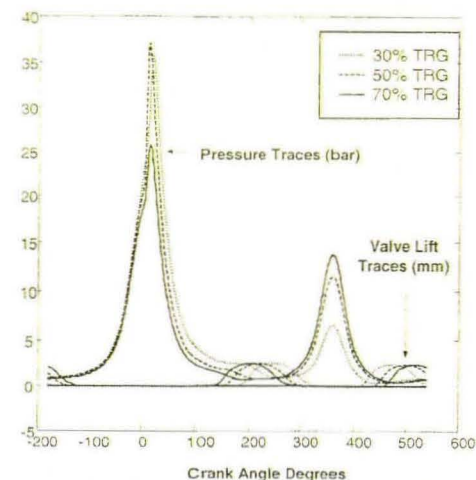


Figure 4. Typical pressure signals and valve profiles at various TRG levels

The amount of TRG noted in this paper is the molar ratio of fresh charge to exhaust gasses, it was calculated using a zero dimensional thermodynamic model and equation (1).

$$\%TRG = \frac{\text{Charge_Moles}}{(\text{Charge_Moles} + \text{TRG_Moles})} \times 100 \quad (1)$$

Charge is calculated through measurements of the air and fuel mass flows. TRG is calculated through the

application of the ideal gas law $PV = NRT$ at exhaust valve closure. P and V are both known, while temperature is taken from a reading of the exhaust gases, and N in this case is the amount of TRG moles. The slow response nature of the thermocouple and the effects of the expansion into the exhaust imply an underestimation of the temperature, and hence an overestimation of the number of moles of TRG. However, its usage without any correction factors guarantees the production of *nominal* values which still correctly capture the *changes* among TRG levels without suffering the problems that plague NVO-related methods (which, for example, neglects speed).

The maximum amount of TRG that the engine will accept depends on the engine speed. Thus an amount of TRG that is on the edge of HCCI at one speed might be in the middle of the operating region, at another. As such, it does not always make sense to speak in absolute terms of TRG%, especially as TRG tolerance is a very engine specific issue. In this paper, TRG% will be described as low, medium or high, rather than assigning absolute values that cannot be extrapolated to different research.

The entire HCCI and SA-CALI operating range was investigated varying the speed over a range between 1500rpm to 3500rpm. In the area surrounding this range, SI operation was used. Figure 5, shows the speed and load, (in terms of IMEP), and the corresponding amount of TRG that was used for load control, where negative valve overlap (NVO) is limited by zero TRG and misfire. It can be seen that NVO, the controlling parameter of TRG, can't be the same in all speeds, and that the IMEP with HCCI can't be the same at all speeds.

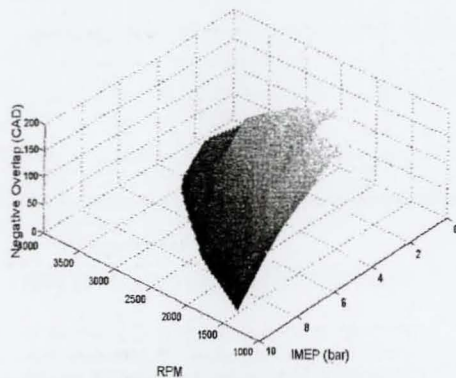


Figure 5. HCCI operating range

ION-CURRENT SIGNAL INTERPRETATION

In a gasoline engine operating in dual mode, four groups of parameters must be known in order to control the combustion process. These are; misfire and preignition

detection (so that operating conditions leading to unstable combustion can be avoided); calculation of TRG levels (as load is controlled in HCCI mode through TRG); combustion performance parameters (so that the engine performance can be monitored); and finally ITA (which is used for engine control) outside the HCCI envelope). Each of these groups will now be examined.

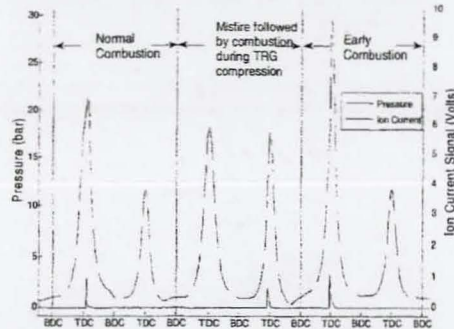


Figure 6. Cylinder pressure trace and corresponding ion-current signal

In order to control a gasoline engine operating in HCCI mode, a number of features must be monitored on a cycle by cycle basis. The simplest of these are misfire and preignition detection. In Figure 6, three consecutive cycles are shown during unstable SA-CALI operation. In the first cycle where the ion-current signal starts after TDC, the peak pressure of combustion is within normal levels and position. In the next cycle a misfire happens and no ion-current is present, (providing a simple way to monitor the engine for this event). However, during the following TRG compression and expansion, the mixture ignites, and is manifested by the presence of ion-current signal during that period [18]. Additional mixing of the charge and TRG during expansion and exhaust stroke (or at least the part of the exhaust stroke that the exhaust valve is open) results in ignition during TRG compression, due to better mixing and increased time history of high pressures and temperatures that break up the fuel. In the third cycle, the ion-current signal starts before TDC since an early combustion, an elevated in-cylinder pressure and early peak pressure position (PPP) occurs. After a TRG compression and expansion that experiences heat release, it is usual for early combustion to occur in the next cycle, due to the very high temperature of the TRG gases which result in early ignition of the fresh charge.

COMBUSTION PERFORMANCE AND ION-CURRENT SIGNAL

Although important conclusions regarding the combustion process can be drawn by inspection, and

simple diagnostics can be performed directly through the ion-current signal, more detailed analysis yields greater insight. In order to do this, four basic characteristics of the ion signal curve were extracted and compared to combustion parameters. As shown in Figure 7, these are the signal start, the signal slope, the ion-current 50% position and the signal peak. It has to be noted here that the signal peak includes two measurants, the signal strength, and the signal peak position (X and Y coordinates).

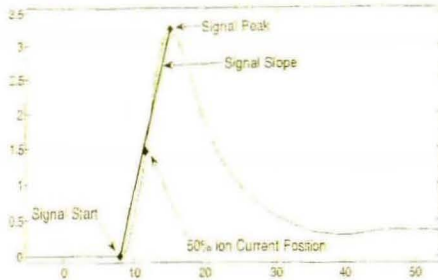


Figure 7. Signal Measurants from ion-current signal

Ion-current can also be used to determine PPP, or similar combustion parameters like MFB50 and maximum rate of heat release (dQ MAX). Determining any of these is important in any engine, however in HCCI (where control of SoC and heat release rate are notoriously difficult), it is almost essential. It has to be noted here that in gasoline HCCI engines, combustion modes change from flame propagation only (low TRG%) to flame propagation with end-gas auto ignition (medium TRG%) and finally bulk auto ignition (high TRG%). As these modes change, different relationships occur between PPP, MFB50 and dQ MAX, in contrast to SI engines where their correlation is far simpler.

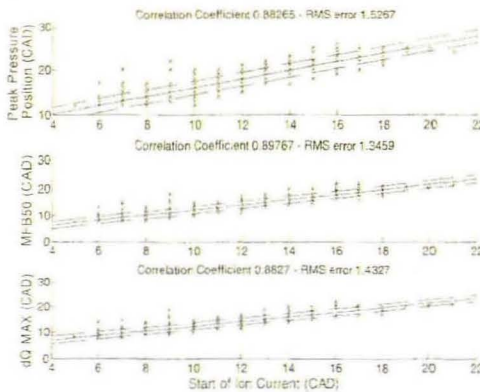


Figure 8. Start of ion-current vs. combustion characteristics

The second method is to correlate the 50% ion-current signal as suggested by [15], and the third method is to correlate the position of signal peak. In all three methods, a linear correlation is used and the resulting PPP estimation has an RMS error of less than 2 CAD. However, the estimation is improved when using the peak ion-current position as the signal is stronger and thus the signal to noise ratio (SNR) is better. Figure 9 and Figure 10 show the 50% and peak signal correlations with PPP respectively, again at 3000rpm medium TRG%.

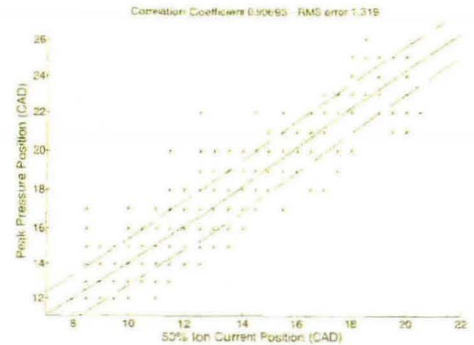


Figure 9. Position of 50% ion-current vs. PPP

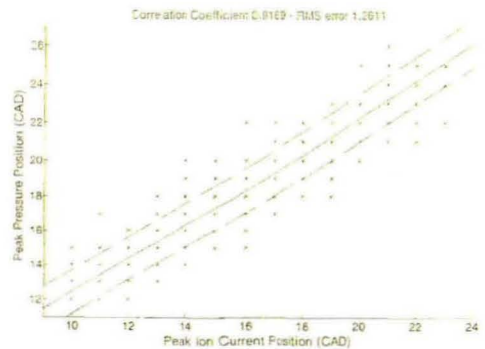


Figure 10. Peak ion-current position vs. PPP

Although a linear estimation is a simple technique and yields acceptable results, it becomes more difficult to implement when a greater range of engine operation is examined, such as varying amounts of TRG. Figure 11 shows the average start of ion-current signal and PPP averaged from 500 cycles across the whole HCCI operating region between 1500 rpm and 3500 rpm, and from SI to maximum TRG% (misfire limit). The same trends are repeated if 50% ion-current or peak ion-current were plotted instead of start of ion-current.

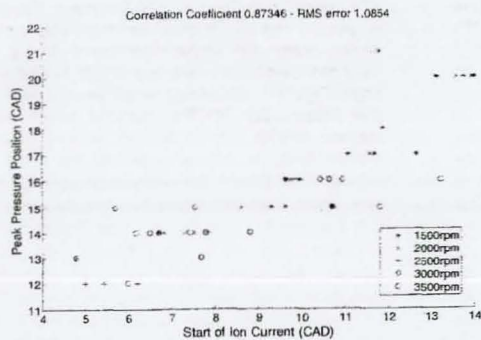


Figure 11. Start of ion-current signal and PPP at various speed

It is obvious that the estimation accuracy reduces if the same linear equation is used for the whole TRG spectrum, regardless of the correlation parameter employed. This is because combustion modes change with varying amounts of TRG thus affecting the signal in more than one way, so estimation precision could be further increased through the use of more advanced signal interpretation techniques correlating more than one ion-current characteristic to PPP, such as ion-current slope. Nevertheless; correlation coefficients remain high, even with the simple linear approach. This indicates that ion-current could, if computational power is an issue, be directly/linearly correlated for combustion analysis purposes.

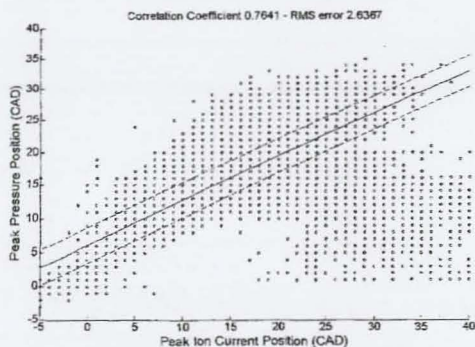


Figure 12. Cycle to cycle peak ion-current vs. PPP

On a cycle to cycle basis and considering the whole HCCI operating envelope, the graphs seem a lot less attractive. Figures 12 and 13 show the correlation of PPP to peak ion-current position and highlight the problem that early peak cylinder pressures show on the zero line. This can be overcome by using a different mesurant (e.g. MFB50), but for a real time control application, it is quicker and more straightforward to extract signal peaks. Despite these issues, the correlation coefficient is still

high, and the RMS error is only increased to 2.64 deg CAD.

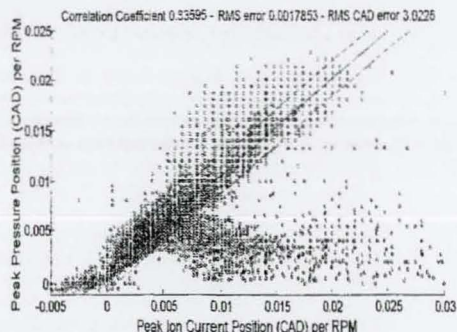


Figure 13. Cycle to cycle peak ion-current vs. PPP

Transforming the acquired signals on time domain, (by dividing them by RPM) provides a better insight into this problem as data from different speeds are better separated. As can be seen in both cycle to cycle figures however (Figure 12 and Figure 13), there is a "leg" of data points that breaks off the main diagonal correlation. Although not easily identifiable on the graph, analysis showed that the percentage of data points on this "leg" are relatively small (<5%), so this is not a major source of error.

A possible explanation for this feature might be that the different knocking modes, that result in different acoustic or oscillation modes that may occur in a combustion chamber depend on mixture distribution, which can vary, even under the same operating conditions [16]. These modes can vary between circumferential and radial and also have different shapes, within their domain. More advanced interpretation technique will improve results by taking in account more than one ion-current parameters, i.e. by not looking at peak position of ion-current alone. However, the only way to radically improve accuracy would be to use more than one ion-current sensor. This would give a more complete, and less localized, picture of the combustion process.

From the foregoing discussion, it becomes apparent that ion-current lends itself to an easy and cost effective solution to combustion diagnostics, during HCCI operation. A simple integration of the signal can reveal misfires, while the position of the start, 50% or maximum of the signal can be used to determine more intricate combustion properties like peak pressure, MFB50 or dQmax positions. Its strength or slope can determine dilution levels. Irregular positioning of the signal, like very early or very late in the combustion cycle, can reveal pre-ignition or partial late combustion, and its absence indicates misfire.

Using a simple linear relationship between the ion-current measurants and combustion parameters will

provide fast and computationally feasible prediction capabilities, of adequate precision, which could be used in a cycle to cycle control strategy. Results of less than 3 CAD RMS combustion prediction error were obtained. For comparison, a current map based ignition system for SI engines is capable of controlling PPP to about the same value, on a new engine.

TRG LEVELS AND ION-CURRENT SIGNAL

For combustion phasing within a reasonable operating window (as employed in a commercial engine), a quite important feature of the slope of the ion current signal is that it can be used to determine the TRG%. The positioning of the combustion phasing can be trimmed by varying ITA and verified using ion-current start, peak (or other chosen measurants) as a feedback signal. It is worth emphasizing again that during all but a few 'pure-HCCI' operating points, a spark was used to position heat release during the desired time window. The PPP values for the data in figures 14 and 15 ranged over 8 CAD, thus within this relatively small operating window, both signal strength and slope of ion-current signal show a very good relation to TRG levels.

In practice this is highly important because variation of intake air temperatures, manifold absolute pressures, coolant temperatures, air humidity and a host of other unknowns such as engine wear, might change the amount of TRG, and this is difficult to express with mathematical models and knowledge of valve timing. By having an in-cylinder sensor, what can be termed as the "effective TRG" can be determined via one of two simple methods.

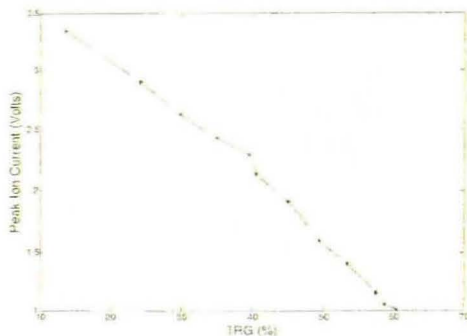


Figure 14. Ion-current signal strength as a function of TRG% at 3000rpm

The first method of finding TRG level is by measuring the ion-current signal strength, shown in Figure 14. Increasing TRG quantity results in a decrease in the measured ion-current signal, and a linear correlation is exhibited between the two parameters. It is important to note that in spite of this decrease, the ion-current signal always remains within measurable range. Moreover,

higher sensor voltages or signal amplification could be used in applications where signal strength becomes an issue.

The second method of determining the effective TRG levels is through the acquisition of the ion-current signal slope. Again, the slope decreases as the TRG amount increases, although not in a linear fashion, as shown in Figure 15. By assuming a simple model that considers the signal start as the point of which the ion-current sensor detects any ion activity within a close range of its vicinity and the signal peak as the point of which full activity is apparent, the slope becomes a measure of the time taken between these two events. With this in mind it can be inferred that fast combustion will be presented as a steep slope while slow combustion will give milder slopes. As such, TRG amounts that result in fast combustion will give the steepest slopes. This happens half way between pure SI and pure HCCI operation, the exact point depending on factors such as compression ratio and combustion chamber design. Pure SI operation is slow because it is solely deflagration and pure HCCI operation is slow because of the high dilution. The region between spark assisted SA-CAL and HCCI is the region where the exhaust gasses have very high temperatures and are of adequate quantity to induce large scale or complete, vigorous detonation.

It has to be noted here that other parameters affecting the speed of combustion, mainly AFR, will also affect the ion-current slope, so the AFR should be held constant for the ion-current slope to be only a function of TRG. In addition, the effect of TRG on the slope of ion-current is not as pronounced if the signal is normalized against its maximum value. This implies that the TRG effect on slope is amplified due to the dependency of the signal strength on TRG, before normalization.

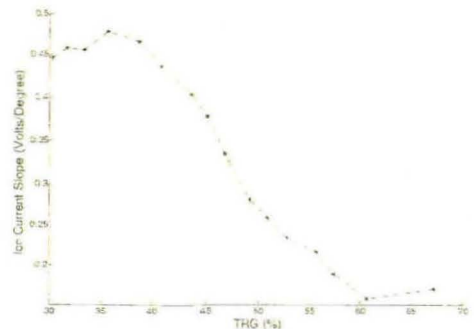


Figure 15. Ion-current signal slope as a function of TRG% at 2000rpm

ITA EFFECT ON ION-CURRENT SIGNAL

Since spark assistance is used to control PPP in all but the few pure HCCI cases, it is important to determine the effect that the ignition timing advance (ITA) will have on

the SoC and thus PPP and ion-current signal. SI operation is directly dictated by ITA, while in pure HCCI it has a minor effect. It is thus logical to show here a mid-way TRG% scenario. In Figure 16, the effects of an ignition timing sweep are shown against start of ion-current signal and PPP at 2200rpm with medium TRG%. Once again, a close correlation of pressure to ion-current measurants can be seen. As PPP delays in crank angle terms, as ITA is retarded, the ion-current signal start delays too. It is clear that the ITA does have an effect on both PPP and ion-current signal. Both are retarded as ITA is retarded in a close correlation.

A 'cross over' point appears when ITA equals -10 CAD-BTDC, (where combustion is delayed beyond the point that would be observed in practical applications). A possible explanation of this phenomenon is that when the spark is delayed enough to allow the fuel time to chemically break up and auto-ignite, the result is a sharper pressure rise and hence advanced PPP. On the contrary, if the spark is early enough to consume a considerable portion of the combustible mixture, before auto-ignition pressure rise will be gentler. This explanation is plausible if the mixture is considered as inhomogeneous.

According to the mixing model of [17] referring to a gasoline HCCI engine with almost identical valve strategy, the charge around the spark plug is less diluted with EGR, as there is a higher concentration of 'fresh charge' near the top of the combustion chamber, whereas TRG will be mostly concentrated at the bottom. If this is so, it will be the fresh charge near the spark plug that will combust most vigorously once auto-ignited. However, if the fresh charge is consumed by SI flame propagation, the heat release will be slower during both the flame propagation phase and the auto-ignition phase that will occur at the more diluted end gasses.

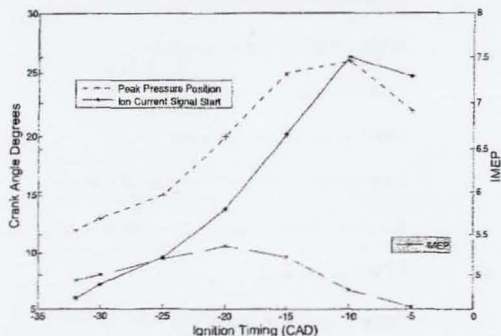


Figure 16. Ignition timing effect on start of ion-current and PPP

HCCI engines are complicated in that the load has to be controlled by the amount of TRG and with load varying almost continuously; the automotive engine must have the flexibility to adjust TRG whilst also controlling

combustion timing. Effectively, when the engine is operating in the HCCI region, the throttle pedal angle needs to be interpreted to a torque requirement. This requirement will then command an increased or decreased negative valve overlap, translating to an appropriate TRG%. The ion-current measurants during these transients can be used to control combustion in terms of timing, through ignition timing advance (ITA). If SoC is too late, the ignition can be advanced and vice versa. During steady state operation, ITA has enough control over the combustion event to time it appropriately. However, during transients it might be necessary to use other means of control. There exist two possible events when a sudden change in torque demand occurs.

1. In the case where there is a decrease in demanded torque, more TRG will have to be used. This will mean that hot gases from a low or medium TRG combustion will suddenly be used in larger amounts leading to early combustion. Retarding ITA might help: except where early auto ignition occurs regardless of ITA. In this case the valve timing transition has to be delayed.

2. Where an increase in torque is required, cold TRG from highly diluted combustion will be required to combust with a lot more fresh charge, since a decrease in TRG will be necessary. Late combustion might be prevented by advancing ITA and lower amounts of TRG equates to higher combustion control through the spark. If this measure proves inadequate, switching to SI operation can rescue the situation.

So under all conditions the ion-current signal can be used by an engine control system to decide on advancing or retarding ITA; or if this strategy is inadequate, to adjust valve timing. By using the ion-current signal, all this is possible on a cycle-to-cycle basis with no averaging requirements. This is especially helpful during transients, or unstable combustion.

CONCLUSION

An experimental study of ion-current sensing in a gasoline HCCI engine was conducted. From these experiments, it can be concluded that ion-current can be used to monitor HCCI combustion events. Ion-current is an attractive proposition for a cost effective sensor, and it has been shown that the signal can be processed with adequate accuracy and speed for feedback closed loop control.

Results of monitoring combustion under steady state operation, over a variety of speeds and trapped residual gas amounts were discussed. The results show that the ion signal is sufficiently high during HCCI under all speeds and loads.

Misfire detection, pre-ignition detection, and estimation of TRG% were shown possible with trivial mathematical approaches.

PPP, MFB50 and dQmax were all determined with RMS errors less than 2 deg CAD, when a specific engine operating condition was examined. When a linear relationship that would cover the whole HCCI operating spectrum, from 0% TRG to maximum TRG, was derived, the maximum error rose to 2.64 deg CAD, remaining accurate enough for feedback purposes.

A straightforward monitoring of the effect of ITA on PPP is possible through ion-current signal monitoring.

Overall, ion-current was proven to be a cost effective and adequately informative feedback signal for both SI and HCCI engine control.

REFERENCES

1. Calcote, H.F. Ion production and recombination in flames. in 8th Symposium on Combustion. 1962.
2. Calcote, H.F. Ion and electron profiles in flames. in 9th Symposium on Combustion. 1963.
3. Shuler, K.E., Ionization in High-Temperature Gases, Academic Press. (1963)
4. Shimasaki, Y., M. Kanehiro, S. Baba, S. Maruyama, T. Hisaki, and S. Miyata, Spark plug voltage analysis for monitoring combustion in an internal combustion engine, SAE Technical Paper Series. 930461:(1993).
5. Saitzkoff, A., R. Reinmann, T. Berglind, and M. Glavmo, An ionization equilibrium analysis of the spark plug as an ionization sensor, SAE Technical Paper Series. 960337:(1996).
6. Yoshiyama, S., E. Tomita, and Y. Hamamoto, Fundamental Study on Combustion Diagnostics Using a Spark Plug as Ion Probe, SAE Technical Paper Series. 2000-01-2828:(2000).
7. Reinmann, R., A. Saitzkoff, F. Mauss, and M. Glavmo, Local Air-Fuel Ratio Measurements Using the Spark Plug as an Ionization Sensor, SAE Technical Paper Series. 970856:(1997).
8. Aithal, S.M., A.R. White, V.V. Subramaniam, V. Babu, and G. Rizzoni, A Chemical Kinetics Model of Current Signatures in an Ionization Sensor, AIAA Plasmadynamics and Lasers Conference. AIAA-1999-3606:(1999).
9. Peron, L., A. Charlet, P. Higlen, B. Moreau, and J. Burq, Limitations of Ionization-current Sensors and Comparison with Cylinder Pressure Sensors, SAE Technical Paper Series. 2000-01-2830:(2000).
10. Asano, M., A. Ito, T. Kuma, M. Kajitani, M. Takeuchi, Y. Fukumura, and M. Izumi, Further Development of an Ion-current Combustion Control System, SAE Technical Paper Series. 2001-01-0256:(2001).
11. Malaczynski, G.W. and M.E. Baker, Real-Time Digital Signal Processing of Ionization-Current for Engine Diagnostics and Control, SAE Technical Paper Series. 2003-01-1119:(2003).
12. Strandh, P., M. Christensen, J. Bengtsson, R. Johansson, A. Vressner, P. Tunestal, and B. Johansson, Ion-Current Sensing for HCCI Combustion Feedback, SAE Technical Paper Series. 2003-01-3216:(2003).

13. Kiencke, U. and L. Nielsen, Automotive Control Systems. SAE International. (2000)
14. Glavmo, M., P. Spadafora, and R. Bosch, Closed Loop Start of Combustion Control Utilizing Ionization Sensing in a Diesel Engine, SAE Technical Paper Series. 1999-01-0549:(1999).
15. Strandh, P., J. Bengtsson, R. Johansson, P. Tunestal, and B. Johansson, Cycle-to-cycle Control of a Dual-Fuel HCCI Engine, SAE Technical Paper Series. 2004-01-0941:(2004).
16. Coricione, F.E., M. Vaglieco, and S. Merola, Evaluation of Knocking Combustion by an Ion-current System and Optical Diagnostics of Radical Species. in The Sixth International Symposium on diagnostics and Modelling of Combustion in Internal Combustion Engines. 2004. COMODIA 2004.
17. Zhao, H., J. Li, T. Ma, and N. Ladommatos, Performance and Analysis of a Four Stroke Multi-cylinder Gasoline Engine with CAI Combustion, SAE Technical Paper Series. 2002-01-0420:(2002).
18. Koopmans, L., Backlund, O. and Denbratt, I., Cycle to cycle variations: Their influence on cycle resolved gas temperature and unburned hydrocarbons from a camless gasoline compression ignition engine. SAE Technical Paper Series, 2002-01-0110: (2002)

ABBREVIATIONS

- AFR: Air Fuel Ratio
- CAD: Crank Angle Degrees
- dQ: Rate of Heat Released
- dQMAX: Maximum Rate of Heat Release
- HCCI: Homogenous Charge Compression Ignition
- ITA: Ignition Timing Advance
- MFB50: 50% Mass Fraction Burned
- NOx: Oxides of Nitrogen
- NVO: Negative Valve Overlap
- PPP: Position of Peak cylinder Pressure
- RMS: Root Mean Squared
- RPM: Engine Revolutions Per Minute
- SA-CAI: Spark Assisted Controlled Auto ignition
- SI: Spark Ignition
- SNR: Signal to Noise Ratio
- SoC: Start of Combustion
- TRG: Trapped Residual Gas

Ion Current Signal Interpretation via Artificial Neural Networks for Gasoline HCCI Control

Dimosthenis Panousakis, Andreas Gazis, Jill Paterson,
Wen-Hua Chen and Rui Chen
Loughborough University

Jamie Turner and Nebojsa Milovanovic
Lotus Engineering

Copyright © 2006 SAE International

Abstract

The control of Homogeneous Charge Compression Ignition (HCCI) (also known as Controlled Auto Ignition (CAI)) has been a major research topic recently, since this type of combustion has the potential to be highly efficient and to produce low NO_x and particulate matter emissions.

Ion current has proven itself as a closed loop control feedback for SI engines. Based on previous work by the authors, ion current was acquired through HCCI operation too, with promising results. However, for best utilization of this feedback signal, advanced interpretation techniques such as artificial neural networks can be used.

In this paper the use of these advanced techniques on experimental data is explored and discussed. The experiments are performed on a single cylinder camless (equipped with a Fully Variable Valve Timing (FVVT) system) research engine fueled with commercially available gasoline (95 ON). The results obtained display an improvement in the correlation between characteristics of ion current and cylinder pressure, thus allowing superior monitoring and control of the engine. Peak pressure position can be estimated with sufficient precision for practical applications, thus pushing the HCCI operation closer to its limits.

KEYWORDS: Homogeneous Charge Compression Ignition, Ion Current, Artificial Neural Networks

Abbreviations

AFR	Air Fuel Ratio
ADALINEs	Adaptive Linear Elements
ADALINE	Adaptive Linear Element
ANN	Artificial Neural Network
ANNs	Artificial Neural Networks
AVT	Active Valve Train
CAD	Crank Angle Degrees
CAI	Controlled Auto Ignition
CR	Compression Ratio
DWT	Discrete Wavelet Transform
EGR	Exhaust Gas Recirculation
EVC	Exhaust Valve Closing time
FVVT	Fully Variable Valve Timing
GRNNs	Generalised Regression Neural Networks
GRNN	Generalised Regression Neural Network
HCCI	Homogeneous Charge Compression Ignition
MLP	Multi-Layer Perceptron
PPP	Peak Pressure Position
RBF	Radial Basis Function
RBFs	Radial Basis Functions
RPM	Revolutions per minute
SI	Spark Ignition
TRG	Trapped Residual Gas

1 Introduction

The use of ion current as a combustion diagnostic tool has been long investigated [1] for a variety of internal combustion engine applications [2, 3, 4]. The decoding of the information inherent in its signal has been implemented in various ways. Of these methods, the use of Artificial Neural Networks (ANNs) is being often used with promising results by researchers [5, 6].

Past research by the authors has demonstrated the possibility of using very lightweight ANNs to treat the ion current signal on SI engines [7]. This research intends to expand on the same idea on Homogeneous Charge Compression Ignition (HCCI) engines. What is being investigated is the strategy behind the building of a specific algorithm for extracting combustion information from the ion current signal of an HCCI engine.

The ideas presented here are based on the following design criteria. On the hardware side, the ion current signal is given a dedicated circuit. This ensures a good quality signal throughout a cycle, with none of the problems associated with using a spark plug as an ion current sensor.

On the software side, the algorithm must be implemented on a cycle to cycle basis with no averaging involved. The rationale is to evaluate the performance of the algorithms at a demanding level.

The next consideration are the algorithms themselves. The use of the Adaptive Linear Elements (ADALINEs) type of Artificial Neural Network (ANN) has been used by the authors in the past with good results, so it is a candidate as it is a very lightweight, robust ANN despite it being uncomplicated. A commonly used ANN for this kind of task is the Multi-Layer Perceptron (MLP) [8]. To test possible alternatives to the MLP this paper focuses on the use of ADALINEs as a starting point

and then explores the use of Generalised Regression Neural Networks (GRNNs). The advantages of both ADALINEs and GRNNs lies in the relative simplicity of their architecture, which offers little room for ambiguity over the optimum design. GRNNs are very similar to Radial Basis Functions (RBFs). For the data used in this research, GRNNs generally outperformed RBFs so were chosen instead.

The final consideration is the choice of preprocessing techniques. A classic approach is to use signal processing algorithms in order to extract various characteristic measurants from the ion current signal to be used as input to the ANNs. To this end, the use of wavelet algorithms has been evaluated. Wavelets are a signal processing tool that is being used in a variety of applications [9], ion current signal processing being an ideal candidate [10]. An interesting advantage of wavelets is that the treated signal can be reduced in size, thus making the use of the wavelet output directly into the ANN a possibility. This approach is also investigated.

2 Experimental Setup

The engine employed in this research was a single cylinder, gasoline port fuel injected, 4-stroke research engine based on a GM Family One, 1.8L series architecture, as shown by the photograph in figure 1. It has a production piston and stroke, with a standard 4-cylinder head on top of a water cooled barrel and a custom made bottom end. Only the front cylinder of the head is operational. A Lotus Engineering Fully Variable Valve Timing (FVVT) system named Active Valve Train Active Valve Train (AVT) is fitted to allow a variable valve timing strategy. Variable quantities of Trapped Residual Gas (TRG) can be captured in this way. It has to be pointed out here that AVT gives the capability of trapping the residual gas in the cylinder through early Exhaust Valve Closing time (EVC) as opposed to recirculating it through the inlet. Because this strat-

egy has been employed throughout this research, the Trapped Residual Gas (TRG) is being used as opposed to the commonly employed Exhaust Gas Recirculation (EGR). For this investigation, the Compression Ratio (CR) was set to 10.5:1.

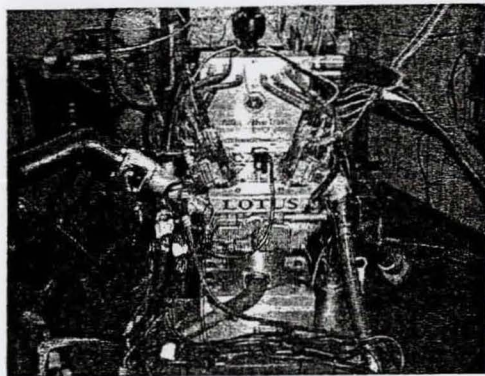


Figure 1: Single-cylinder research engine with AVT system

The engine was connected to a Froude AG30 30kW eddy-current dynamometer. A redline ACAP data acquisition system from DSP Technologies Inc. was used, together with a Kistler 6123 piezoelectric pressure transducer and a Horiba MEXA 7100 DEGR emissions analyzer. Port fuel injection was employed, managed by a conventional Lotus V8 engine controller.

In order to acquire the ion-current signal an ionization probe was located in the four-valve cylinder head between one of the inlet and one of the exhaust valves as shown in Figure 2. The probe was electrically isolated from the cylinder head by means of a ceramic sleeve. The diameter of the sensing element was slightly less than 1mm, and the tip protrusion into the combustion chamber was approximately 3.5 mm.

Since the mass of positive ions, such as H_3O^+ , is approximately 30,000 times larger than that of an electron (negative charge), the light electrons can be accelerated much more easily towards the positive electrode than the heavy ions [11], when driven

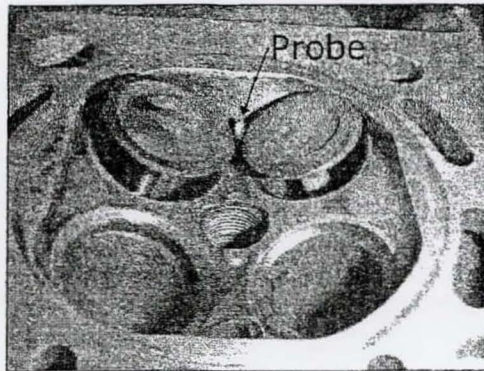


Figure 2: Photograph of cylinder head showing the location of the ionisation probe

by an applied electromagnetic field. The voltage polarity at the gap of sensing spark plugs was therefore selected such that the small area centre electrode was positive, and the rest of the combustion chamber was negative. This coincides conveniently with the original engine polarity where the engine block is negative.

A one-off DC voltage source shown in Figure 3, was used to power the measuring probe. The DAQ board was fed the output of the voltage divider as the ion-current signal, which was inversely proportional to the sensed ion-current (i.e. 5V for zero ion-current and 0V for infinite) to avoid the possibility of damage caused due to excessive voltage. The signal was then inverted during the post processing phase.

Using a dedicated probe and circuit, avoids the problems of circuit switching, bandwidth filtering, circuit ringing and so on which are common with other ion current measuring techniques [12, 13, 14].

The data was sampled once per Crank Angle Degrees (CAD).

The data used in this research are based on stoichiometric, HCCI combustion using 95 ON commercial gasoline.

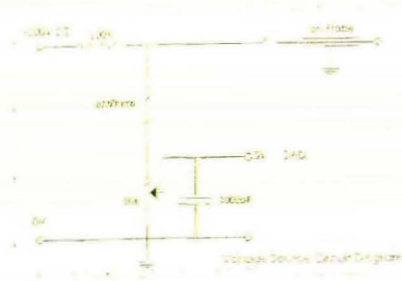


Figure 3: Voltage source circuit diagram

3 Ion Current Signal and Treatment

The ion current signal in both SI and HCCI is usually in the form of a sharp spike, sometimes followed by a hump (figure 4). The spike is associated with the flame arriving in the vicinity of the sensor (chemical ionisation). It is the most obvious feature of the signal and is always present if combustion occurs in the chamber. The hump is associated with the increased temperatures and pressures following the combustion (thermal ionisation) and is hence a good indicator of Peak Pressure Position (PPP). However, because of the need for increased temperatures and pressures, it is most prominent in high load SI. In the lower loads and temperatures associated with HCCI operation, this feature is greatly suppressed. Since this paper focuses on HCCI combustion, where this feature is hardly noticeable as seen in the figure, only the initial spike is considered. For this initial spike to be properly recorded under all conditions a dedicated circuit is needed.

The treatment of the signal requires certain operations to be performed upon it in order to extract certain characteristic measurants that will be used in order to quantify its features. This process is, in effect, a compression of the information contained in the signal into a small number of key variables.

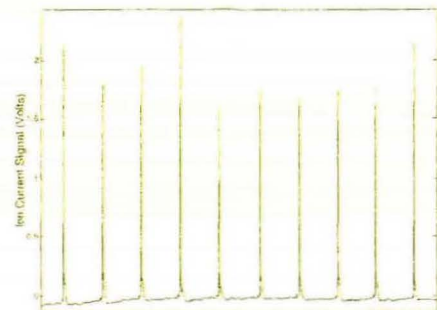


Figure 4: Typical HCCI ion current signal

This has the advantage that, in the first instance, they can be directly investigated for correlation to corresponding measurants of the pressure trace (e.g. peak pressure position) and also that these can be used as a much reduced data source when using further algorithms, e.g. ANNs.

3.1 Ion Current Measurant Extraction

The breakdown of the measurants extracted from the ion current signal are shown in figure 5.

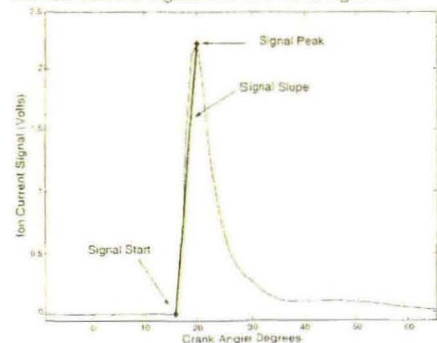


Figure 5: The ion current measurants

These are:

1. The start of the signal
2. The slope of the signal
3. The maximum of the signal
4. The position of the maximum of the signal

The easiest to extract and one of the most information rich is position and magnitude of the spike's peak, which is simply extracted by means of a maximum search. The timing of this has been shown [7] to be a good approximate indicator of combustion timing, having a strong relation with pressure measurants such as PPP.

Another important ion current measurant is the position of the start of the signal. Coupled with the coordinates of the peak, it can lead to an estimation of the slope of the spike. Previous research on SI operation has established a correlation between this slope and Air Fuel Ratio (AFR) [15, 5, 16]. In HCCI, this effect is further complicated by the presence of TRG but still, slope information can be a valuable tool. Thus, in order to acquire it, an estimation of the start of the signal is required.

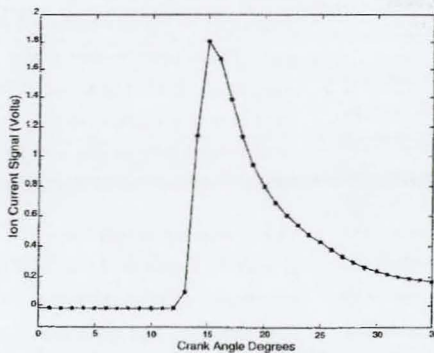


Figure 6: Example of sudden spike rise

While the spike's peak is very straightforward to extract, its start can be more problematic. This is mainly because the base of the ion current signal can be a very noisy region. Added to that, is the

fact that, because HCCI combustion is very sudden compared to SI, the spike can rise in a very short time. typical values can be as low as 3 data points (data is sampled every 1 degree CAD) as is demonstrated in figure 6. Hence, an uncertainty of even one or two degrees can have a big effect on the final value for the spike rise duration and hence the slope.

Matters are complicated further by the fact that the start of the signal can be concealed by noise as is shown in figure 7. This should not normally be a problem as the spikes are usually high enough to easily rise above the noise. However, to guarantee a safe detection through a simple technique such as a static trigger level for example, compromises have to be made that will erroneously classify certain cycles.

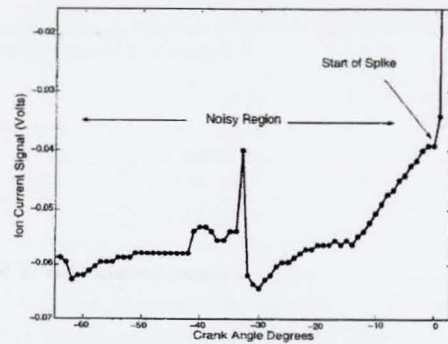


Figure 7: Detail of noisy region before spike

Another problem is that the ion current signal can suffer from a noticeable base drift, an extreme example of which can be seen in figure 8. Coupled with the problem of noise and potentially weak spikes, this makes the use of a static trigger inappropriate.

To counter these problems, two different techniques have been tried out. One, designed for maximum speed, is based on classic concepts and employs a dynamic trigger to judge how to classify each candidate point. The other, designed as a more rigorous approach, is based on wavelet analysis and classifies points by processing the high frequency part of the

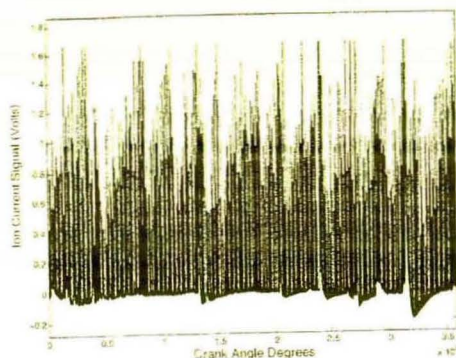


Figure 8: Example of base drift

ion current signal. Both these techniques are outlined in the following section.

3.1.1 Classic Estimation of Signal Start

The classic approach is based upon certain assumptions which work well for the type of signal encountered during this research. These are that there is no combustion in the first 100 data points and that the base drift is not fast enough to affect the signal within a cycle. The algorithm employed uses the initial 100 data points of each cycle to work out the value for the base of the signal and to gauge its background noise by taking their standard deviation. A dynamic trigger level can then be established by setting a tolerance window around the base level (in this research and for this signal, set to 10 standard deviations).

The algorithm then starts from the position of the spike's peak and goes backwards towards the cycle's start. The criterion for classifying a point as the spike's start is for it to have dropped within the tolerance window. The value of ten standard deviations quoted might seem as unacceptably high. However, due to the sharpness of the spike, this value has been found to be appropriate.

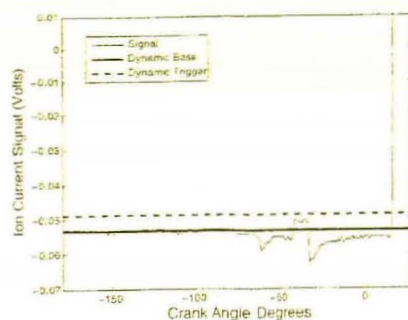


Figure 9: Ion current signal showing base and trigger level

Another variation of this technique can consider a rolling window instead of single points. This is essentially the same concept, looking at individual points backwards from the spike's maximum. In this scenario however, the average value and standard deviation of all the points previous to the point being considered is being estimated and used as a criterion. This variation also yields good results. However, since both these variations can be tuned to yield almost identical results, only the first one will be discussed here as it is obviously the fastest of the two.

The advantage of this technique is that, because the processing starts at the peak of the signal, it usually terminates after considering very few points, given that the start and peak are normally very close together. It can be further speeded up by considering fewer initial points in order to estimate the dynamic base and trigger level.

The disadvantage is that it needs to be presented with the whole signal since it needs to establish the position of the spike's peak first. This is a problem when considering real time, cycle to cycle implementation on a working engine. However, the magnitude of the spike for a non misfiring cycle is normally such that, even a simplistic static trigger approach should pick it out of the noisy signal (assuming the quality

of the signal can remain similar to that encountered in this research, during real time implementation). If that is given, the processing for the estimation of the start of the spike can start immediately after the trigger level has been reached, even if the actual peak has not yet been recorded.

3.1.2 Wavelet Based Estimation of Signal Start

The second technique used for estimating the start of the ion current signal is based on wavelet decomposition. Wavelets are a very promising tool for signal analysis which has been implemented in the context of ion current interpretation [10]. Given this particular problem, their strength lies in being able to establish the exact location of various frequency components of a complicated signal. The results described in this research have all been implemented using the Wavelet toolbox in MATLAB.

Traditionally, a wavelet transform works by taking a given waveform (wavelet) scaling it to different wavelengths and comparing it to the signal across the signal's length. This analysis gives a very thorough overview of the signal composition. However, it is unrealistically time consuming for the task at hand. Thus, a faster algorithm can be employed, the Discrete Wavelet Transform (DWT), which in essence works by splitting the signal into a high and low frequency part, where the choice of wavelet acts as the kind of filter to be used. In wavelet analysis, these two low and high frequency components of the signal are often referred to as *approximation* and *details*. Through a process called downsampling, these are reduced to approximately half the length of the original signal.

Although, this process can be repeated to decompose the signal to deeper levels, in this case we are only interested in the high frequency, *details*, part and one level of decomposition is adequate.

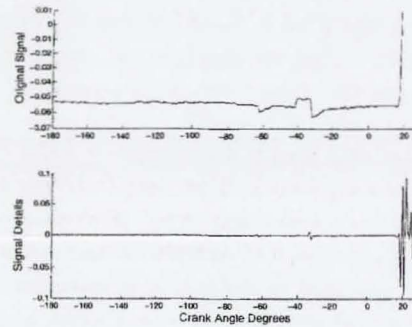


Figure 10: Original ion current signal and DWT generated details

Figure 10 shows the original signal zoomed in before the start of the spike, occurring around 20 CAD, along with its *details* after one decomposition. It is obvious how the *details* easily mark the start of the spike.

This behaviour lends itself to very easy identification of the spike start by simply working backwards from the maximum value of the *details* signal until reaching a "calm" region (implemented by checking that all members of a fixed size window are below a static trigger value) without need for a dynamic trigger. A major advantage, visible in figure 10 is that the *details* are not affected by the base drift, since the latter has very long wavelength. This is why a static trigger can be successfully implemented in the case of the algorithm employing wavelet decomposition.

Of the available wavelets, the *Daubechies* and *Symlet* families produce results that most readily resemble the results of the classic algorithm. In fact, the best agreement comes from the *Daubechies 1* (also Haar) wavelet, where the average error between their results is less than 1 CAD. It has to be pointed out though that the results of the classic algorithm are not necessarily a "correct" target to be met. In most of the ambiguous cases, the precise start of the signal

is open to interpretation, even by a human. Having been the first to be developed, the classic algorithm has been the one most closely tuned to return agreeable bulk results. Hence, agreement with it is a good indicator of performance but is by no means a definitive test since the algorithm can always be tuned to yield even "better" results for a particular wavelet.

This very elegant implementation hides the major processing that is done behind the scenes by the discrete wavelet transform. However, a real time implementation of such a technique can potentially be optimised for the task to an extent much greater than was done in this research where readily available, general purpose functions from the MATLAB wavelet toolbox were used. In addition, the implementation can and indeed must, be narrowed down to a specific window of interest in a real time implementation. In this case, tested as proof of concept on the whole length of the signal, it performed approximately 20 times slower than the classic algorithm, which is a stripped down procedure designed strictly for identifying the signal start. As pointed out however, this is not by any means representative of the relative computational speed a purpose built wavelet based algorithm could achieve. For a real time, cycle to cycle implementation, the major concern has to be speed and at this point, this particular implementation of wavelets seems to be at a disadvantage. However, the possibility of treating additional information inherent in the wavelet decomposed signal, coupled with the ability to process the reduced size *approximation* and *details* signals make wavelets a promising tool for analysis of the ion current signal as is described below.

3.2 The Wavelet Decomposition of the Ion Current Signal Procedure

A major strength of the wavelet decomposition lies in the reduction in signal size. The mesurant extraction method described previously, explicitly re-

duces the original signal to a few numbers describing geometrical characteristics. However, decomposing the signal through employing the DWT algorithm, reduces the signal while retaining significant information. Figure 11 shows an ion current signal and the subsequent two levels of decomposition. The figure highlights how varying levels of decomposition reduce the signal length while retaining the main features.

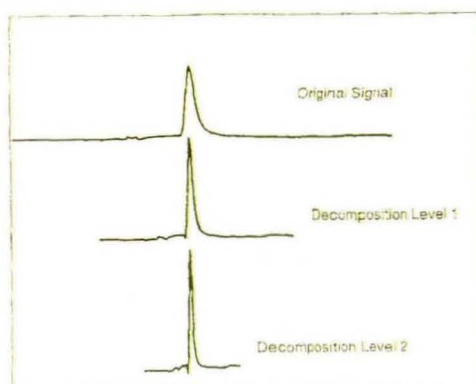


Figure 11: Example of two levels of wavelet decomposition of ion current signal

By reducing the signal size in this way, an ANN can be designed whose input layer will be much shorter than would be needed if the whole signal was to be used as an input. Thus, the reduced size ANN will be much faster. However, deeper levels of decomposition take more time on the DWT. Also, deeper decomposition of the signal can potentially degrade the ANN output.

Hence, there is a tradeoff between time spent on the DWT, time spent on the ANN and the overall performance. All these issues need to be taken into account when designing a system that should, in principle, be able to process cycle to cycle information from the ion current signal.

4 Artificial Neural Network Based Predictions

4.1 Types of Input

In order to test the feasibility of a control system having ion current based information for the pressure measurants, the data extracted by the procedures described previously are presented to various different ANNs. The aim is to get the best predictions possible from as uncomplicated ANNs as possible for a great range of operating conditions. The two types of ANNs investigated are ADALINEs, and GRNNs. These have been implemented through the corresponding functions supplied by the MATLAB Neural Network Toolbox.

ADALINEs are classic single layer ANNs, which use a linear transfer function. Their strength lies in their Least Mean Square training rule, which will always minimise the error of data presented in the training set, thus avoiding the ambiguity over the completeness of training that might be an issue with other ANN training algorithms. Their weakness lies in that they are, in effect, a system of linear equations and are thus not well equipped to respond to non linear relationships. Previous research by the authors on the ion current signal on SI engines indicates that ADALINEs' responses for handling ion current data seem satisfactory for their strengths to compensate for their weaknesses.

GRNNs are two layer ANNs, with a Radial Basis Function (RBF) first layer and a linear second layer. Initial trials demonstrated that GRNNs give promising results. The question is to establish if their increased complexity, which incurs performance penalties, is worth their possible performance benefits.

The ANNs fall into two categories, depending on what kind of inputs they accept. On one hand, the inputs consist of the extracted measurants as de-

scribed in section 3.1. In this case, the ANN input layer size is the 4 extracted ion current measurants plus any additional information on engine operating conditions such as RPM. On the other hand, the input consists of the wavelet decomposed signal, normally the *approximation*, plus any engine operating conditions. In this case, the input layer is variable depending on the decomposition level.

In the case of the extracted measurant data, certain additional tests have to be carried out. Before the data is presented to the ANNs, it goes through a final selection process. The data is organised in matrices where a set of inputs and corresponding set of outputs take up a row. Certain rows may represent cycles where one of these numbers has not been established, most likely because of a misfire, in which case ion current information is unavailable. In that case, the whole cycle is removed by deleting the respective row in the matrix. The other part of the selection involves outliers. Again, cycles which are problematic for any reason can either fool the extraction algorithms into returning unrealistic values or the cycles themselves have uncharacteristic values. This is treated by doing a histogram of the data and identifying the left and right edges at which points a certain percentage of the total data is present (set to 1.5% in this research). Data outside the region specified by these edges are discarded.

It has to be noted that none of these techniques have to be employed in a real time implementation. Cycles that return no ion current signal up to a certain point can be quickly classified as misfires anyway. Similarly, predefined triggers based on the operational conditions for the allowable range of values can be employed on the extracted measurants to decide very fast if a cycle is to be considered as normal before proceeding with the processing of its data.

In the case of the ANNs using the whole decomposed signal as an input, no such processing is carried out. This can be considered as a token of added robustness, since there is no intermediary algorithm, other

than the DWT itself, which might complicate the process.

The output of the ANNs is always PPP. In reality, there is a host of pressure related measurants that can be derived from a pressure trace, such as start of combustion, combustion duration etc. However, PPP is preferred because its extraction algorithm, which is simply maximum point search, is simple to the point of guaranteed perfect accuracy. This is important since there is uncertainty on the input side, especially where the mesurant extraction algorithms are concerned. Adding uncertainty on the output side through using a harder to extract mesurant, such as start of combustion for example, will yield results that are more unrepresentative. Since the scope of this research is to analyse the relative merits of different techniques, the chosen output used as measure is PPP. It has to be pointed out, however, that in principle, an ANN can be designed to predict any pressure related mesurant.

4.2 ANN Testing within Different Speed Sites

The first kind of data to be treated consists of steady state data collected at different engine speeds. TRG sweeps are carried out at each speed. All are WOT, with $\lambda=1$. Spark advance varies among members of the same speed site. The Revolutions per minute (RPM) range covered is from 1500 to 3500.

To test performance of the algorithms described above, the initial test is done within the members of each speed site. The reasoning is that, at the very least, a control system switching between ANNs, each one trained for a certain RPM region, can be implemented for steady state operation¹.

¹A question that might arise here is why classify the data according to RPM and not TRG. The reason is that, unlike RPM, TRG is not directly measurable. For a given valve setting, the engine will trap a different amount of TRG at different RPM. Note that, in this throttleless valve strategy, load is adjusted via TRG, hence the RPM - TRG space is equivalent to the speed and load space.

Each training point corresponds to a cycle. The data points are randomly split into a training and a test group with the training group taking up 80% of the total sample. The ANN is then tested on the test sample, which is made up of the remaining 20%. Because of the random nature of the selection of the test sample, no two consecutive tests will give the same result. For that reason, the numbers quoted throughout this research are averages of multiple tests. This scheme has been favoured over simpler ones, such as taking the first 20% of data from each data log for example. The reason for this is that, in logs which exhibit areas of localised behaviour, such as a series of unstable cycles, these might not be sampled, or not sampled at a representative fraction. By making the selection random, the test sample is spread evenly over the whole of the data.

The errors quoted throughout are RMS errors of the difference between the ANN prediction and the actual value of the output. The units are always in CAD. The percentage errors quoted correspond to the percentage of the error as a fraction of the overall spread of the actual values of the output.

4.2.1 Performance of Mesurant Based ANNs

The results presented here correspond to the ANNs taking extracted ion current measurants as inputs. These initial trials do not supply the ANN with information on any other operating conditions.

The performance of the ADALINE over the different speed sites is presented on table 1, which summarises the errors for PPP for each engine speed. The "Error Classic" and "Error Wavelet" refer to the CAD error for the speed group, depending on whether classic or wavelet techniques are used to extract the ion current measurants. The number in brackets is the respective percentage error.

Table 1: ADALINE performance for each speed site, only ion current measurant inputs

RPM	Error Classic (%)	Error Wavelet (%)
1500	2.34 (8)	2.35 (9)
2000	1.46 (6)	1.71 (8)
2500	2.19 (9)	2.23 (9)
3000	2.56 (10)	2.26 (10)
3500	3.08 (13)	3.53 (15)

The same trials, carried out on GRNNs are displayed on table 2.

Table 2: GRNN performance for each speed site, only ion current measurant inputs

RPM	Error Classic (%)	Error Wavelet (%)
1500	2.31 (9)	2.42 (9)
2000	1.46 (6)	1.40 (6)
2500	2.42 (5)	1.50 (6)
3000	2.14 (9)	1.86 (8)
3500	2.28 (10)	2.57 (11)

These trials demonstrate any differences between both the wavelet and classic ion current measurant extraction techniques as well as the relative performance of ADALINEs and GRNNs. The differences between classic and wavelet measurant extraction methods generally appear small enough to be negligible. As far as the ANNs are concerned, the GRNNs seem to offer a slight advantage as well. However, it has to be noted that the GRNN takes approximately 7 times as long to process the same input.

Table 3 is aimed at gauging the performance improvement of ANNs over conventional methods. The prediction method in this case is a simple linear fit of the data for an ion current measurant against PPP. The error quoted in the table prediction is based on either of two measurants which exhibit good correlation with PPP, the position of the signal's maximum or the position of the signal's start (see figure 5).

One point to note here is that all results seem to indicate a best performance at 2000 RPM. This is in agreement with the fact that engine operation has been very smooth at this speed, reflected by the lowest PPP variance of all speed sites.

Table 3: Performance of conventional linear fit method for two different ion current measurants

RPM	Signal Max Pos.	Signal Start Pos.
1500	2.96	3.19
2000	2.21	2.64
2500	2.50	2.53
3000	3.70	3.62
3500	2.93	2.95

4.2.2 Performance of Decomposed Signal Based ANNs

To get a better understanding of the relative merits of the different ANN designs, the same tests are carried out using the decomposed ion current signal. Table 4 displays the performance of these ANNs.

Table 4: ANN performance for each speed site, decomposed ion current signal as input

RPM	ADALINE (%)	GRNN (%)
1500	4.04 (14)	4.02 (15)
2000	3.22 (13)	3.24 (15)
2500	3.62 (15)	3.5 (14)
3000	4.04 (16)	4.05 (16)
3500	3.30 (14)	3.33 (14)

These results were produced through ANNs at various decomposition levels. The ion current signal decomposition was carried out using the "db2" wavelet and the levels varied between 1 and 5. The errors quoted are the best results, however, the results did not vary for more than 7% across the decomposition levels in the case of these tests within RPM speed groups. The analysis of the relation between error, computational time and decomposition level is presented in detail in section 4.3.2.

The tests presented here are only carried out to investigate the capabilities of the ANNs on separated sets of data. The most important test, however, is to test performance of a single ANN across the RPM range as well. The feasibility of such an ANN can greatly enhance the performance of a cycle to cycle control system.

4.3 ANN Testing Across Different Speed Sites

Having tested that the performance of the ANNs seems promising within single RPM speed groups, the next step is to test it across the span of RPM. As in the previous section, the results are split between the measurant based and decomposed signal based ANNs.

4.3.1 Performance of Measurant Based ANNs

At this stage, the effect of adding operating condition information to the ANNs is assessed. In the first instance an ADALINE and a GRNN are trained and tested on the whole of the RPM range. In the second instance, apart from the ion current measurants, additional information is supplied to the ANNs in the form of the following:

1. RPM
2. Negative overlap
3. Ignition timing
4. Airflow

The negative overlap is one way of measuring amount of TRG. However, it is not directly representative of the actual mass of TRG, as this also depends on volumetric efficiency, a function of engine speed. It is however, an easy way of getting a handle of the TRG. Similarly, the airflow is a rough measure of each cycle's energy intake. Since for all these data $\lambda = 1$, logged at WOT, the power output is regulated by the TRG amount (which is in turn regulated by the negative overlap), which has a direct impact on the airflow.

Again, to account for statistical error arising from the random nature of the selection of the training

and test sets, a series of tests have been performed for each case and the average results quoted. One point worth mentioning here is that care has to be taken when quoting the error across mixed speed groups. There are two factors that can contribute to unequal effects of each group's error on the final value. First, is the fact that not all groups have the same amount of logs in them. This will be reflected in the overall sample, making groups with larger populations dominate the result. Second, is the random selection process of the test points. Despite being superior, the disadvantage is that it adds fuzziness to the amount of cycles taken from each group. To address these concerns, the test points have been labelled according to the speed group they belong to and at the end, errors have been calculated for each individual group. The final error quoted is the mean of these, thus each group contributes equally to it irrespective of how many of its members make it to the test sample.

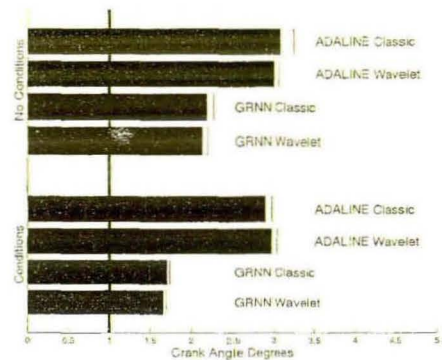


Figure 12: Comparative results of different measurant based ANNs

Figure 12 shows the various strategies tested and their associated outcomes. The horizontal bars show the errors for each ANN design. The thin line at the edge of each bar shows the standard deviation encountered between the successive test performed on each design. The thick vertical line at $x=1$ marks the sampling rate.

The bars are split into two groups, depending on whether the ANNs have operating condition information among their inputs. Within these groups, they are further split into ADALINEs and GRNNs. Finally, each type of ANN is classified depending on whether the measurant extraction procedure employs classic or wavelet methods.

Hence, the top four bars show the cases where no operating condition information is presented to the ANNs. GRNNs outperform ADALINEs, while the type of measurant extraction technique (wavelet or classic) does not have any significant influence on the results.

The bottom four bars show that ADALINEs do not yield any significant improvement by adding operating condition information to their inputs. On the contrary, GRNNs respond with a noticeable improvement in performance.

4.3.2 Performance of Wavelet Decomposed Signal Based ANNs

The second series of tests across speed groups involves the use of the ion current signal decomposed to some level through wavelet decomposition. In this case, certain additional factors need to be taken into account since the decomposition introduces new parameters.

The first parameter is which wavelet to choose for the decomposition. In the case of measurant extraction, the "db1" or "haar" wavelet gave good results. In the case of decomposing the signal, it seems that moving from "db1" to "db2" yields slightly better results. This is possibly due to the fact that the "db1" wavelet, being in essence a step function, generates a less faithful *approximation* signal than the "db2" which is a more sophisticated wavelet. When identifying measurants, the rough results of "db1" are probably best suited for the task. However, when using the decomposed signal as an input, "db2" outperforms "db1".

The other parameter that has to be determined is the level of decomposition. As discussed in section 3.2, a deeper level will take more time spent on the decomposition itself but less time on the ANN since the input layer is reduced in size. Clearly, a balance has to be struck. Figures 13 and 14 demonstrate these considerations.

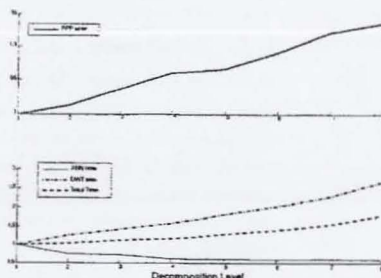


Figure 13: Breakdown of ADALINE design parameters

The x-axis on these figures represents the decomposition level of the ion current signal. The lines represent the error, and the times spent on calculating the DWT and ANN response to the test input. The y-axis represents these quantities normalised by dividing by their initial (i.e. at decomposition level 1) values.

On figure 13, which corresponds to the Adaptive Linear Element (ADALINE), the total time spent on both DWT and ANN is clearly dominated by the DWT time. This is because the ADALINE response calculation is a very lightweight process. The error on the other hand shows a clear trend to increase monotonically as the decomposition level increases.

On the contrary, figure 14 shows that, in the Generalised Regression Neural Network (GRNN) case, the total computational time is dominated by the ANN response calculation. Meanwhile, the error is not as strongly affected by the depth of the decomposition as it was in the case of the ADALINE.

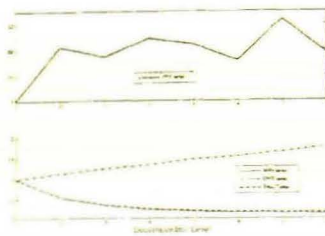


Figure 14: Breakdown of GRNN design parameters

These tests highlight the relative concerns of design within the ANN types. Figure 15 shows the comparisons between the designs. In this figure, the bars representing errors are black and their values are indicated on the bottom x-axis. The white bars represent total time (DWT plus ANN) for each design. These have been scaled by dividing by the maximum value among them, hence showing their relative values. Their values are indicated on the top x-axis.

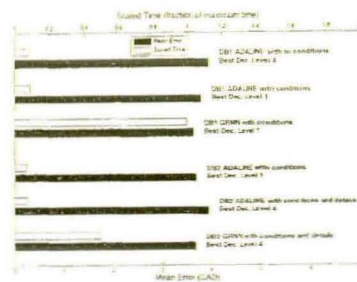


Figure 15: Comparative results of different decomposed ion current based ANNs

Starting from the top, the first three correspond to designs based on "db1" decomposition. They represent two ADALINES, one with and one without operating conditions added to the input, followed by a GRNN with conditions added to the input. Quoted also are the decomposition levels where these designs

performed best.

The second three correspond to designs based on "db2" decomposition. The first one is an ADALINE with operating conditions added to the input. The second and third are an ADALINE and GRNN where, apart from operating conditions, the *details* part of the decomposition has been added to the input. In terms of size, this has the effect of making the input double, effectively taking the decomposition up one level. Thus, these ANNs, both whose decomposition level is quoted as 4, have the same size input layers as ANNs whose decomposition level is 3.

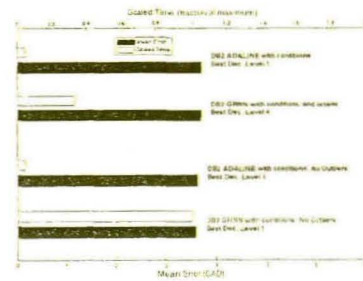


Figure 16: Comparative results of different decomposed ion current based ANNs

The ANNs in this section are trained on all data available in the sample since normally there is no input measurant extraction process through which to classify outliers. To compare more objectively with the ANNs which accept extracted ion current measurants as input, a series of trials were performed where the same cycles were removed from both. The results are presented in figure 16. The top two bars are the same as the 4th and 6th from figure 15, while the bottom two represent trials of similar design ANNs with the outlier cycles removed. The removal of the cycles does not result in a notable improvement.

5 Conclusion

Two different approaches to ANN design have been described and evaluated. One is based upon extraction of relevant measurants from the ion current signal in order to present them to the ANN. The other relies upon the reduction in size which is achieved through wavelet decomposition in order to achieve a small and fast ANN.

The two approaches that have been tried were organised in two different ways. In the first instance, the data is presented in various groups and an ANN is trained specifically for each case. In the second instance, data is not classified according to speed but is presented to the ANN as a whole, with and without information on operating conditions as part of the input.

Two types of ANNs have been tested, ADALINEs and GRNNs.

The results from the trials within the same speed groups are as follows:

Both types of ANN achieve an RMS error between 1.5 and 3 CAD, depending on RPM, for the ANNs whose input is based upon measurants extracted from the ion current signal².

Both types of ANN achieve an RMS error between 3 and 4 CAD when their input is the wavelet decomposed ion current signal itself³.

The results from the trials where testing is done across all data are as follows:

On ANNs whose input is based upon extracted ion current measurants, with no information on operating conditions as part of the input, GRNNs outperform ADALINEs by achieving an RMS error of around 2.2 CAD as opposed to around 3 CAD for ADALINEs. When information on operating condi-

tions is added to the inputs, the error drops to under 3 CAD for ADALINEs and to around 1.7 CAD for GRNNs⁴.

On ANNs whose input is the wavelet decomposed ion current signal, the error always remains between 3.5 and 4 CAD, largely independent of the type of ANN, the presence of operating conditions in the input, choice of wavelet, or removal of potentially problematic cycles from the data⁵.

From the above, it follows that the ANNs whose inputs are based upon extracted ion current measurants outperform the ANNs whose input is the wavelet decomposed ion current signal. Hence, for the particular task at hand, it is preferable to expend the computational resources required for the extraction of measurants from the signal if the ANN of choice is the ADALINE or the GRNN.

The performance of both these types of ANN using extracted measurant inputs is all the more noteworthy, considering that no averaging takes place and the results at their best performance are only 50% above the sampling rate (best performance around 1.5 CAD with a sampling rate of 1 CAD). Thus, either of these ANNs could potentially be a strong candidate as part of a control system for the steady state operation of an HCCI engine

References

- [1] K. Iinuma. Ionization current in spark-ignition engines. Technical Report 3, Report of the Technical College, 1958.
- [2] M. Hellring *et al.* Spark advance control using the ion current and neural soft sensors. *SAE Technical Paper Series*, (1999-01-1162), 1999.
- [3] L. Eriksson, L. Nielsen, and M. Glavenius. Closed loop ignition control by ionization cur-

²Tables 1 and 2

³Table 4

⁴Figure 12

⁵Figure 16

- rent interpretation. *SAE Technical Paper Series*, (970854), 1998.
- [4] C. Daniels. The comparison of mass fraction burned obtained from the cylinder pressure signal and spark plug ion signal. *SAE Technical Paper*, (980140), 1998.
- [5] N. Wickstrom *et al.* Estimating peak pressure position and air-fuel ratio using the ionization current and artificial neural networks. In *Proceedings of IEEE Conference on Intelligent Transportation Systems*, 1997.
- [6] M. Hellring *et al.* Spark advance control using the ion current and neural soft sensors. *SAE*, (99P-78), 1998.
- [7] A. Gazis and D. Panousakis *et al.* *Computationally inexpensive methods of ion current signal manipulation for predicting characteristics of engine in-cylinder pressure*. International Journal of Engine Research, 2005. [IN PRESS].
- [8] M. Hellring and U. Holmberg. An ion current based peak-finding algorithm for pressure peak position estimation. *SAE Technical Paper Series*, (2000-01-2829), 2000.
- [9] A. L. Graps. An introduction to wavelets. *IEEE Computational Sciences and Engineering*, 2(2):50-61, 1995.
- [10] G. W. Malaczynski and M. E. Baker. Real-time digital signal processing of ionization current for engine diagnostic and control. *SAE Technical Paper Series*, (2003-01-1119), 2003.
- [11] U. Kiencke and L. Nielsen. *Automotive Control Systems*. Springer-Verlag.
- [12] L. Peron *et al.* Limitations of ionization current sensors and comparison with cylinder pressure sensors. *SAE Technical Paper Series*, (2000-01-2830), 2000.
- [13] M. Asano *et al.* Further development of an ion current combustion control system. *SAE Technical Paper Series*, (2001-01-0266), 2001.
- [14] D. Panousakis and A. Gazis *et al.* Analysis of SI combustion diagnostics methods using ion current sensing techniques. *SAE*, SAE 06P-214 [IN PRESS], 2006.
- [15] D. Schneider and M. D. Lai. Real-time air/fuel ratio control in a small si engine using the ionic current signal. *SAE Technical Paper Series*, (1999-01-3323), 1999.
- [16] E. N. Balles *et al.* In-cylinder air-fuel ratio approximation using spark gap ionization sensing. *SAE Technical Paper Series*, (980166), 1998.

